Nordic Concrete
Research

Nordic
Concrete
Federation

NORDIC CONCRETE RESEARCH

Preface

Nordic Concrete Research is since 1982 the leading scientific journal concerning concrete research in the five Nordic countries, e.g., Denmark, Finland, Iceland, Norway and Sweden. The content of Nordic Concrete Research reflects the major trends in the concrete research.

Nordic Concrete Research is published by the Nordic Concrete Federation that beside the publication activity also organizes the Nordic Concrete Research Symposia that have constituted a continuous series since 1953 in Stockholm. The Symposium circulates between the five countries and takes place every third year. The XXI Symposium on Nordic Concrete Research and Development to be held in Hämeenlinna, Finland from 30 May to 1 June 2011. Information can be found on www.nordicconcrete2011.fi.

Since 1982, 365 papers have been published in the journal. Since 1994 the abstracts and from 1998 both the abstracts and the full papers can be found on the Nordic Concrete Federation's homepage: www.nordicconcrete.org

Vodskov, December 2010

Dirch H. Bager
Editor, Nordic Concrete Research

CONTENTS

Investigating Salt Frost Scaling by using Statistical Methods

Marianne Tange Hasholt
Assistant professor, M.Sc., Ph.D.
Department of Civil Engineering
Technical University of Denmark
E-mail: matah@byg.dtu.dk

Line H. Clemmensen
Assistant professor, M.Sc., Ph.D.
Department of Informatics and Mathematical Modelling
Technical University of Denmark
E-mail: lhc@imm.dtu.dk

ABSTRACT

A large data set comprising data for 118 concrete mixes on mix design, air void structure, and the outcome of freeze/thaw testing according to SS 13 72 44 has been analysed by use of statistical methods. The results show that with regard to mix composition, the most important parameter is the equivalent water to cement ratio (w/c_{eq}). Regarding the importance of the air void structure, the most important parameter turned out to be the total surface area of air voids. The impact of this parameter is statistically more significant than the impact of the spacing factor, and it raises the question if total surface area of air voids is a more appropriate evaluation criterion than the spacing factor, which is normally used.

Key words: Salt frost scaling, frost resistance, mix design, air void structure, ANOVA, regression.

1.   INTRODUCTION

The starting point of the present study dates 10 years back: An analysis was performed on a data set comprising more than 100 concrete mixes by using artificial neural network (ANN) [1]. The objective was to establish a relation between on one hand mix design and air voids structure and on the other hand the resulting frost resistance, measured as scaling in a freeze-thaw test. The

analysis led to the surprising conclusion that the spacing factor could not be used as evaluation criterion when examining the air void structure and its ability to protect concrete against frost attack. This has puzzled one of the authors ever since. Therefore, the analysis is repeated on the same set of data, but now by using common statistical methods.

2. BACKGROUND

The neural network of the human brain is unique in the way it can process information on reason (input) and consequence (output) and learn relations between them. An artificial neural network (ANN) is an analyzing tool, where a software package is used to establish a network that can imitate the human brain in a very simplified way. The ANN is trained by presenting it to sets of input and output data. When the network is trained, it can be used to predict the output of other sets of input data, where the answer is unknown. By studying how the ANN makes predictions, i.e. by varying input variables one at a time and registering the impact on the output, it is also possible to gain knowledge on the input/output relation.

Previously, an artificial neural network has been designed to investigate the influence of different parameters on the salt frost resistance of concrete [1]. The aim was twofold: The general objective was to demonstrate that ANN analysis is applicable for predicting concrete durability, using salt frost scaling as an example. For salt frost scaling, the specific objective was to study if the critical spacing factor is a function of mix design parameters.

Different ANN configurations were trained with input and output data from literature. Data were gathered from 12 Scandinavian research and development projects, see reference list in [2]. The data comprised mixes with 1-, 2-, and 3-powder combinations and *w/b* ranging from 0.24-0.75. There were both air entrained and non-air entrained mixes. Approximately 40 % of the mixes showed scaling after 56 freeze-thaw cycles that exceeded 0.5 kg/m².

The most successful network, i.e. the network with minimum average difference between predictions and actual outcome of a salt frost scaling test according to SS 13 72 44 [3], used the following input parameters:

- Water/binder ratio [-]
- Air content [% of total concrete volume]
- Content of fly ash [% of powder by mass]
- Content of silica fume [% of powder by mass]
- Specific surface of air voids [mm^{-1}]

When this network were tested on data, which had not been used during training, it was used to classify concrete into groups with good frost resistance (scaling < 0.5 kg/m²) and poor frost resistance (scaling ≥ 0.5 kg/m²). The classification was correct for 23 of 32 concrete mixes (classification error 0.2813).

The analysis showed that water/binder ratio and air content were the most significant input parameters. The binder combination had some effect (silica fume improves frost resistance, whereas fly ash tends to lower it). The specific surface also had some effect, though the effect was minor compared to the effect of total air content.

The above mentioned network was superior to network configurations using the spacing factor as input parameter. No clear relation between spacing factor and salt frost scaling was established (and for this reason it was not possible to link critical spacing factor to mix design either). This was a very surprising finding, as the spacing factor is often used as decisive parameter when evaluating if the air void structure of concrete is adequate to protect the concrete against frost deterioration. This is e.g. normal practice in Denmark [4]. However, the ANN software is to some extent a black box, and what happens inside can be difficult to follow. It was speculated that the lack of relation between spacing factor and salt frost scaling could be due to a mathematical peculiarity, and as such the ANN analysis could only be seen as a preliminary analysis. The findings would have to be validated by other methods, e.g. statistical methods.

3.   STATISTICAL METHODS

The statistical toolbox is large, but in this study we have only used two different methods: Analysis of variance (ANOVA) and regression analysis. They are two relatively simple yet powerful methods. Below is given a short introduction to the two methods. For a thorough description, please refer to textbooks in statistics, e.g. [5, 6].

3.1   Analysis of variance (ANOVA)

Student's t test is one of the most commonly used statistical methods to test the null hypothesis that the means of two populations A and B are equal. But what is actually investigated is the variance: If the variances within population A and population B, respectively, are of the same size as the variance of the joint population A+B, then it is very likely, that A and B belong to the same population, in which case their means are equal. But if the variances within the two populations are smaller than the variance of the joint population, it is more likely that their mean values differ. The test can e.g. be used to test the effect of two different treatments (e.g. 'low temperature' and 'high temperature'). If the test supports that the two populations have the same mean (e.g. compressive strength after 3 days), then the treatments have the same effect. Figure 1 shows an example, where treatments A and B most likely have different effects.

Analysis of variance (ANOVA) is a formalized way to test variances in a data set to compare the effect of two or more treatments – in the case of only two treatments the ANOVA is identical to the Student's t test. The calculated p-value is the probability that populations are the same, i.e. a low p-value indicates that populations are distinct.

When comparing groups, it is important that only the treatment differs, whereas everything else is equal. In the case of testing the effect of temperature on compressive strength, groups have to be comparable regarding e.g. mix proportions, quality of constituents, mix procedures etc.
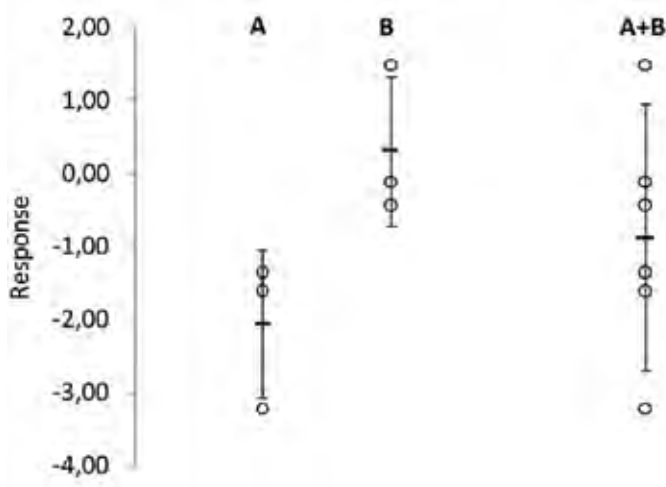
Figure 1: Example of two treatments, A and B, each tested on a group of 3. ○ marks measured response, whereas the bar shows mean and standard deviation in each population. As the variance in the joint population A+B is larger than the variance in both A and B, it is very likely that A and B are two distinct populations with different means.

3.2 Regression analysis

In regression analysis, the aim is to study the relation between a dependent variable Y and one or more independent variables $(x_1, \ldots, x_p)$. It is assumed that Y is a linear function of $x_1, \ldots, x_p$:

$$Y_i = a_0 + \sum_{j=1}^{p} a_j x_{ij} \qquad (1)$$

but from the starting point, constants $a_0, \ldots, a_p$ in the function are unknown. The constants are calibrated by fitting the function to sub data sets of specific $x_1, \ldots, x_p$ and the observed response y. For each sub data set, there will be a difference (error or residual) ε between the value of the regression function Y and the observed response y. It is assumed that the best regression function is the one, which minimises the sum of the squared errors. Therefore with n observations, the constants a_j are fitted to minimize:

$$\sum_{i=1}^{n} (y_i - Y_i)^2 = \min \qquad (2)$$

For this reason, regression analysis is also called least squares modelling. The total data set has to contain at least as many sub data sets as the number of constants which are to be calibrated $(n \text{-> } p + 1)$.

In the simplest form, the regression function is a straight line $Y = a_0 + a_1 \cdot x$. However, the regression function does not necessarily fit the template $Y = a_0 + a_1 \cdot x_1 + \ldots + a_p \cdot x_p$. But it is a

necessary precondition, that the problem to be described by the regression function can be linearised in a way so independent variables are separated, e.g.:

$$Y = a_0 + a_1 \cdot x_1^3 + a_2 \cdot \sqrt{x_2} + a_3 \cdot \exp(x_3) \tag{3}$$

If it from the physical nature of the problem seems reasonable to include combinations of variables, e.g. the product $x_1 \cdot x_2$, then the combination can be introduced as a new independent variable, $x_4 = x_1 \cdot x_2$.

For each constant $a_0, ..., a_p$ a p-value is calculated. The p-value is the probability that the hypothesis $a_j = 0$ is true. If the p-value is high, it is very likely that a_j is 0 and the variable x_j is only of little importance for the observed outcome. On the contrary, if the p-value is low, x_j does have a significant impact on the value of the residual of the current model. A p-value is also calculated for the entire regression function. It equals the probability that the model is not significant.

4.   IMPORTANCE OF MIX DESIGN

The influence of mix design on salt frost scaling can be documented by using ANOVA, where the treatments e.g. are different water to cement ratios or different levels of fly ash addition. The ANOVA is performed on data from selected studies, i.e. on subsets of the total data set. This is done, because then it is easier to divide data into groups, where everything but the treatment is the same, for example the raw materials are the same within the same study. The philosophy is that if a trend is present in a subset of data, then it is plausible that the trend will also be present in the complete data set, which the subset is a part of.

4.1   Water/binder ratio (w/b)

In the original data set the largest subset of data origins from [7]. Here mix designs are tested with

- different water to binder ratio, *w/b*: 0.30, 0.35, 0.40, 0.50, 0.75
- with and without air entraining agent
- different binder combinations:
  - CEM I
  - CEM I + 5 % b.w. silica fume
  - CEM II with limestone filler
  - CEM I + 30 % b.w. ground blast furnace slag
  - CEM III with approximately 70 % slag

(Results for mixes with slag were not included in the ANN analysis, as this would have necessitated the introduction of a new input variable, and the aim was to keep the number of input variables low.)

Mixes with air entrainment showed very little scaling, and for this reason it is difficult to see the effect of other variables. Results for mixes without air entraining agent are shown in table 1:

Table 1: Salt frost scaling [kg/m²] according to SS 13 72 44 for concrete mixes without air entrainment [7].

w/b	0.30	0.35	0.40	0.50	0.75
CEM I	0.26	4.39	7.92	14.45	> 15
CEM I + 5 % SF	0.20	0.89	3.25	4.61	6.58

An ANOVA can be performed, where *w/b* is the treatment and ln(*scaling*) as the response (*w/b* = 0.75 is omitted as there is no exact scaling value for binder combination CEM I). The p-value of the ANOVA is 0.0326, i.e. the effect of *w/b* is significant on 5 % level of significance.

Treatment and response is plotted in figure 2 as well as deviations between individual measurements and average values for treatments.
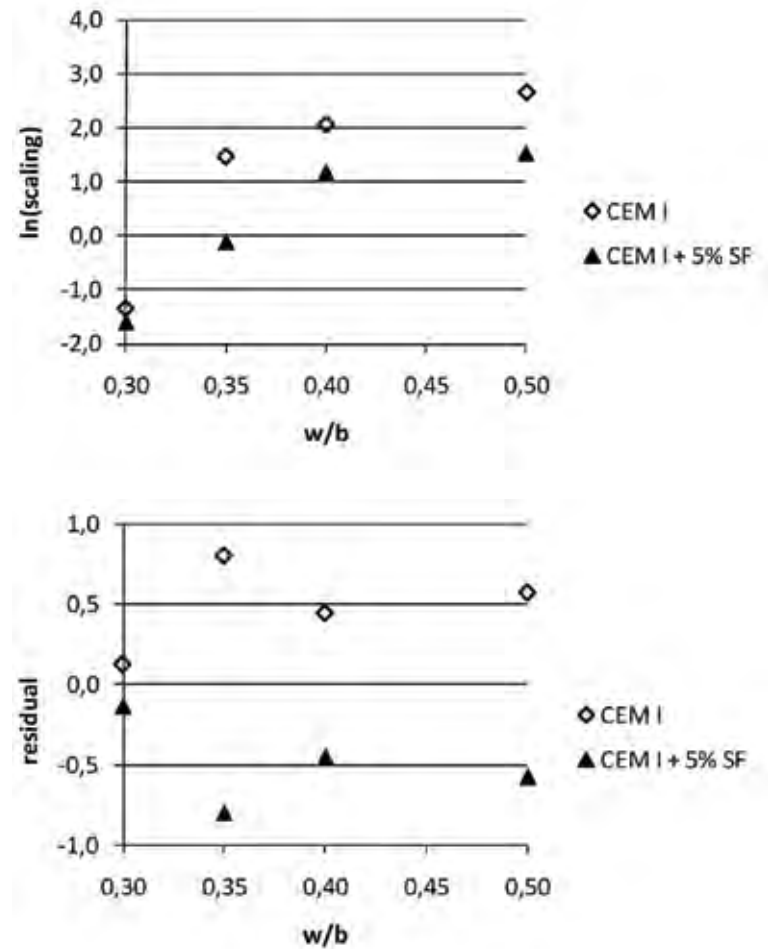

Figure 2: Results from [7]. Top: ln(scaling) vs w/b. Bottom: Residuals, when single measurements are compared to the average for each w/b.

4.2 Silica fume

In figure 2, top, it can be seen that there is a systematic trend, where concrete mixes with silica fume has lower scaling than mixes without silica fume. If a 2-factor ANOVA is performed on data in table 1, where w/b is one factor and silica fume content is the other, then the p-value for w/b is 0.0087 and the p-value for silica fume content is 0.0395, i.e. both factors are significant. This is in accordance with conclusions in [7] regarding the influence of w/b and silica fume.

4.3 Fly ash

Regarding the influence of fly ash on salt frost resistance, there are two studies in the original data set, which are suitable for ANOVA. The criteria are that they contain a sufficient number of data and it is possible to divide data into groups, where level of fly ash addition is the only difference (treatment) and the groups are otherwise comparable:

- Pedersen and Haugaard [8]: 6 mixes, which all have w/c_{eq} = 0.40. They are based on 3 different types of cement, and each type of cement is tested with 0 % and 15 % fly ash (% of powder weight). The equivalent water to cement ration w/c_{eq} is calculated according to equation (4).
- Terje F. Rønning [9]: 6 mixes with w/b 0.40 and 0.45 are mixed with three different types of cement, where one of them contains 20 % fly ash.

The equivalent water to cement ratio w/c_{eq} is calculated the following way:

$$w/c_{eq} = \frac{m_{water}}{m_{cement} + \frac{1}{2} \cdot m_{flyash} + 2 \cdot m_{silicafume}} \tag{4}$$

where m_{water}, m_{cement}, $m_{fly\,ash}$, and $m_{silica\,fume}$ are masses of water, cement, fly ash, and silica fume, respectively.

If results from [8] are divided into groups with 0 % and 15 % fly ash, respectively, then the p-value of the ANOVA is 0.7664, i.e. fly ash has no significant effect on salt frost scaling. If results from [9] are divided into groups with CEM I and CEM II (with 20 % fly ash), then the p-value is 0.0044, i.e. fly ash has a significant effect on salt frost scaling (and it is a negative effect, where fly ash increases scaling).

The results from analysis of data from [8] and [9] seem contradictory. However, the explanation can probably be found in different preconditions. In [8], w/c_{eq} is constant, whereas in [9], w/b is constant. This means that in [8], the negative effect of fly ash is accounted for by the activity factor ½ for fly ash compared to the activity factor 1 for cement, just like the activity factors accounts for that fly ash has a negative effect on concrete strength, if cement is replaced by fly ash 1:1 by weight.

5. IMPORTANCE OF AIR VOID STRUCTURE

The ANOVA approach showed very useful to study the influence of different mix design parameters. Unfortunately, it is not possible to follow the same path when pursuing the

importance of parameters describing the air void structure. The reason is that it is impossible to divide the data set into groups with well defined treatments. If e.g. dividing the overall dataset into two groups with different air contents, high and low, respectively, then they will most likely also have very different spacing factors (concrete with low total air content is often poorly air entrained or not air entrained at all, and then it will have a high spacing factor, and vice versa). So if the ANOVA reveals that the difference in salt frost scaling in the two groups are statistically significant, then it is not possible to discriminate if this is due to the difference in air content or the difference in spacing factor – or the difference in a third unknown factor.

In this case the regression analysis is more appropriate. It is possible to include different independent variables at the same time (e.g. total air content, spacing factor and specific surface), and then observe if the calibrated regression function puts any weight on them.

5.1   Stepwise regression analysis

In this study, we have used stepwise regression analysis to establish a regression function. This is a convenient approach, if the regression function is not established from an underlying theory. Instead, the starting point is a long list of potential independent variables.

The first step is for each of the variables on the long list to calculate the correlation with the dependent variable (y). Based on these results, the most significant variable is selected. In the next step, the partial correlation is calculated for each of the variables on the list with the dependent variable, given the variable already in the model. Now the most significant variable is chosen. The stepwise selection at each step chooses the variable with the lowest p-value and then recalculates the model. After each selection step, an elimination step is carried out. In the elimination step, a t-test is calculated for the coefficients in the model of all the selected variables. If one or more of them is not significantly different from zero they will be removed from the model. More steps are performed in the same line, until the improvement of the regression function by adding more variables is below a critical value (stop criteria for the procedure), and it is then concluded that the remaining variables on the list are not significant. In this study we have used a 5% level of significance as a threshold both for selecting and removing variables.

The stepwise procedure is automated in different software packages. In this study, we have used MATLAB with the add-in Statistics Toolbox.

5.2   List of independent variables

When preparing the long list of potential variables, both parameters regarding mix design and parameters regarding air void structure were included. The reason for including e.g. powder combination, though the effect of e.g. silica fume has already been verified, is to clear the data set for effects of powder combination, so the effect of air void structure will stand out stronger.

The first list was made from 11 basic variables, which also were used when training the neural network in [1]:

- Powder:
    - cement content, C [kg/m³ concrete]

- fly ash content, *FA* [kg/m³ concrete]
- silica fume content, *SF* [kg/m³ concrete]
- Water:
  - water content, *W* [kg/m³ concrete]
  - water to cement ratio, *w/c* [kg/kg]
  - water to binder ratio, *w/b* [kg/kg]
  - equivalent water to cement ratio, *w/c$_{eq}$* [kg/kg], calculated as shown in section 4.3.
- Paste content including air [m³/m³ concrete]
- Air void structure
  - Total air content, *A* [% of concrete volume]
  - Powers' spacing factor, *L* [mm]
  - Specific surface, *S* [mm^{-1}]

The cement type was also included by adding 4 variables, which could take the value 0 or 1, corresponding to the following cement types:

A. CEM I, strength class 42.5
B. CEM I, strength class 52.5
C. CEM II with fly ash
D. CEM II with limestone filler

The artificial neural network in [1] was trained and tested using data from 123 different concrete mixes. For 5 of the mixes, the cement type was not stated in the original source, and therefore the data set was reduced to 118 concrete mixes.

5.3   Regression functions

The logarithm of measured scaling after 56 freeze-thaw cycles ln*(scaling)* is used as the observed response. The reason for this, and for not just using measured scaling, is that it is more important to get an accurate model in the range of 0-2 kg scaling per m² test surface, because it is in this range we have accept criteria to distinguish between concrete with good and poor frost resistance [3]. The accuracy for higher scaling values is considered less important. For example it is not important if the scaling is 3 or 5 kg/m² as in both cases the scaling is unacceptable. The difference between high scaling values is toned down by using the logarithm (this procedure was also applied when training the neural network [1]).

A significance level of 0.05 was used as stop criteria. This resulted in the following regression function, see equation 5:

$$
\begin{aligned}
\ln(scaling) \ = \ & 1.2329 \\
& - 0.0296 \cdot W \\
& + 12.7160 \cdot w/c_{eq} \\
& - 0.4085 \cdot A \\
& - 0.0492 \cdot S
\end{aligned}
\tag{5}
$$

When evaluating the importance of each variable, one has to take the range of the variable into account. For example, in the data set *w/c$_{eq}$* ranges from 0.23 to 0.75, and the 10 % and 90 %

fractiles are 0.32 and 0.50, respectively. If changing the value of w/c_{eq} in the regression function from 0.32 to 0.50, then ln(*scaling*) is increased by the value of 2.29. For the specific surface S, the 10 % and 90 % fractiles are 12 and 35 mm^{-1}, and this can change the value of ln(*scaling*) 1.13. Like this, w/c_{eq} seems to be more important than S.

In equation 5 w/c_{eq} and A are the most important parameters, and the specific surface S also has some importance, whereas the spacing factor L is not included in the list of independent variables which are statistically significant. This corresponds well with the findings of the artificial neural network. The regression function also indicates that an increase in water content W will result in a decrease in scaling. There is no obvious explanation for this, and it may even seem illogical, as e.g. the water content increases, when the paste content increases, and normally this will also lead to increased scaling. However, it may be because the relation between ln(*scaling*) and w/c_{eq} is not perfectly linear for constant A and S, and this is to some degree fixed by including the water content.

The experimental results presented by Lindmark [10] indicate that the total surface area of air voids is a better evaluation criterion than the spacing factor. The total surface area of air voids is proportional to the cross product $S·A$, so 'total surface area' can be used as the physical interpretation of $S·A$. Inspired by Lindmark, the variable $S·A$ was also put on the long list, which now consisted of 16 variables. Stepwise regression analysis led to the following regression function:

$$
\begin{aligned}
\ln(scaling) \;=\; & -0.6120 \\
& -0.0252 \cdot W \\
& +12.5298 \cdot w/c_{eq} \\
& -0.0163 \cdot S \cdot A
\end{aligned}
\tag{6}
$$

The software package offers the opportunity to force specific variables into the model. If the spacing factor L is forced into the model, the following regression function is obtained:

$$
\begin{aligned}
\ln(scaling) \;=\; & 1.6839 \\
& -0.0288 \cdot W \\
& +12.8157 \cdot w/c_{eq} \\
& +0.0602 \cdot S \\
& +1.2677 \cdot L \\
& -0.0195 \cdot S \cdot A
\end{aligned}
\tag{7}
$$

Even when forcing L into the model, it does not oust $S·A$, and the result is a much more complex model with 5 variables. It was presumed that the reason for the superiority of $S·A$ to L could be because the linearization was more favourable to $S·A$ than to L. At high air contents, $1/L$ is proportional to $(S·A)$, so therefore $1/L$ was added to the list of variables. However, this variable was not naturally selected, $1/L$ only appeared in the regression function, if it was forced into it:

$$\ln(scaling) = 1.0017$$
$$-0.0320 \cdot W$$
$$+12.9570 \cdot w/c_{eq} \qquad (8)$$
$$-0.2793 \cdot A$$
$$-0.2793 \cdot 1/L$$

$1/L$ seemed to work slightly better than L. It was tested if this could be used as the single variable describing air void structure, in the same way as $S \cdot A$ is the only variable describing air void structure in equation (6). For this test A, S, L, and $S \cdot A$ were removed from the list of variables:

$$\ln(scaling) = -0.2076$$
$$-0.0266 \cdot W$$
$$+12.3671 \cdot w/c_{eq} \qquad (9)$$
$$-0.3990 \cdot 1/L$$

The performance of the different regression functions are compared in table 2:

Table 2: Comparison of regression functions.

Equation	Independent variables	p-value	Residual mean square error	Classification error
5	W, w/c$_{eq}$, A, S	$4.30 \cdot 10^{-9}$	1.6930	22.03 %
6	W, w/c$_{eq}$, S·A	$8.35 \cdot 10^{-10}$	1.6844	20.34 %
7	W, w/c$_{eq}$, S, L, S·A	$2.2239 \cdot 10^{-9}$	1.6682	20.34 %
8	W, w/c$_{eq}$, A, 1/L	$2.0367 \cdot 10^{-9}$	1.6815	20.34 %
9	W, w/c$_{eq}$, 1/L	$2.1567 \cdot 10^{-8}$	1.7340	26.27 %

Table 2 shows that even though the regression function in equation 6 only has 3 variables, it performs better than equation 5, 7, and 8 with 4-5 variables. The function in equation 6 has the lowest p-value, whereas the residual mean square error is at the same level for equation 5-8. It has been tested, if the regression functions can be used to classify concrete into groups with good frost resistance (scaling < 0.5 kg/m³) and poor frost resistance (scaling ≥ 0.5 kg/m³). The classification error is identical for equation 6, 7, and 8, and it is slightly higher for equation 5

Equation 6 also performs better than the other regression function with 3 variables, i.e. equation 9: The p-value is lower, the residual mean square error is lower, and the classification error is lower.
For all the presented regression functions, residuals have been plotted versus the selected variables, see example in figure 3. These plots are made to test if there is a systematic variation of residuals, for example if residuals are larger for small values of the variable than for high values. If such trends are present, they indicate a possibility of improving the regression function by transforming the variable, for example by using $\ln(X)$ as variable instead of X. However, no systematic variations were detected.
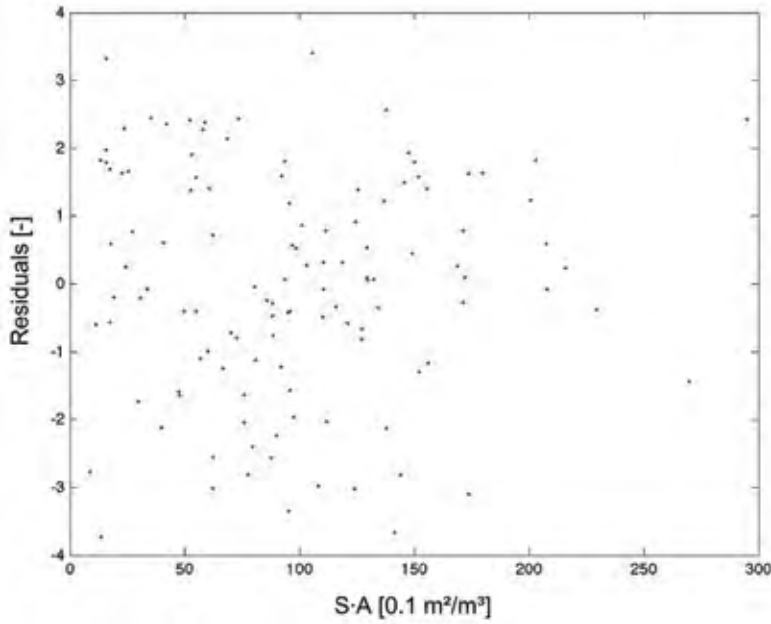
Figure 3: Residual plot (residuals vs. S·A) for regression function presented in equation (6).

Finally, to check for combined effects, the list of potential variables was expanded with the squares of the 11 basic variables, cross products of the 11 basic variables (55 cross products) and products of the basic variables and cement types variables (44 products). This results in a list with 125 potential variables.

This resulted in the following regression function:

$$
\begin{aligned}
\ln(scaling) \quad = \quad & -2.7549 \\
& +11.937 \cdot w/c_{eq} \\
& +0.0672 \cdot A^2 \\
& -0.0010 \cdot SF \cdot paste \\
& -0.0074 \cdot W \cdot A \\
& +1.3618 \cdot L \cdot cementtype A
\end{aligned}
\tag{10}
$$

Again, the w/c_{eq} and the air content A showed to be statistically significant. There is no physical explanation for the combined variables, e.g. the cross product of spacing factor and cement type A. It may be a combination of two effects, which are both weak, but joint they are stronger than other effects.

Comparing with the regression functions presented in table 2, the regression function in equation (10) has a p-value of $3.6671 \cdot 10^{-13}$ and a residual mean square error of 1.5385. Assessing the regression functions based on these values, it looks like this regression function is an improvement, but the classification error is 21.19 %, so in reality not much is gained. In the

neural network analysis, there is a risk of getting a network that that does not generalise, and instead it memorises data, if the network has too many input variables and too many connections. In regression analysis, there is a similar risk of over-fitting data, when using many input variables. It is possible that the complex variables in equation (10) are a symptom of over-fitting.

6. DISCUSSION

Analysis of variance (ANOVA) has been performed on data from selected studies. This shows that salt frost scaling is affected by the following parameters:

- *w/b* (increased scaling, when *w/b* is high)
- content of silica fume (silica fume addition decreases scaling)
- content of fly ash (fly ash addition increases scaling)

When this pattern is found in studies that are subsets of a bigger data set, then it is also expected that the same pattern is present in the big data set.

Automated stepwise regression analysis has been performed on the complete data set to get the first regression function, and then this function has been refined manually. This showed a statistically significant effect of:

- water content W
- equivalent water to cement ratio w/c_{eq}
- the product of specific surface area S and total air content A (which is proportional to the total surface area of air voids)

The effects of fly ash and silica fume are not statistically significant in the regression analysis. It is probably because they are accounted for by the efficiency factors used to calculate the equivalent water to cement ratio (½ for fly ash and 2 for silica fume, respectively). The cement type did not show statistical significance as sole parameter. However, in a test of combined effects, it did show significance in combination with other variables, so the result may indicate that the frost resistance of concrete produced with CEM I, strength class 42.5 is slightly lower than concrete produced with the other types of cement in the data set.

The findings regarding the effect of *w/b* (or w/c_{eq}), fly ash and silica fume are not surprising, as they have been documented before, and also in studies that are not included in the present data set (for a literature review on this subject, see e.g.[11]). But the effect of the total surface of air voids and especially the observation of the spacing factor not being statistically significant, if the air content and the specific surface area of air voids or their cross product were possible input parameters, are probably more controversial. This is against prevailing practice, where the spacing factor is used as evaluation criterion when assessing the adequacy of the air void structure. To the knowledge of the authors, the effect of the total air void surface has only been reported once before, by Lindmark [10].

6.1   Tools for analysis

The statistical processing of the data set in this paper supports all the findings of the artificial neural network in [1]. However, in that paper a question mark was put to artificial neural network as analyzing tool, because the finding of the spacing factor having no importance was contradictory to "what we all know about the spacing factor". It was questioned if this particular finding was entirely a consequence of the tool used for analysis and not an actual pattern of the data set? But as this statistical evaluation supports the findings of the ANN, there is no reason to believe that the ANN itself leads to odd conclusions.

There is some similarity between regression analysis and ANN. For both methods the result is a model (a trained network or a calibrated regression function), which can be used for future predictions. When comparing the tools of analysis, it points out the strengths and weaknesses of each method.

When using a machine learning approach as ANN, a relatively large data set is needed. If the data set is too small, the model will just memorize data instead of extracting general trends. And there are no explanations for the findings.

A purely mathematical approach as regression analysis can be performed on fewer data, which is obviously an advantage, and it is easier to interpret the regression model than the ANN model. But for the regression approach data alone is not enough, it is also necessary to make some assumptions about the variables in the regression function, and that is the Achilles heel of this method, as there is always a risk of missing important variables. In this project, the spacing factor would have turned out to be statistically significant, if it had been the only variable describing the air void structure in the regression function, and the significance of $S \cdot A$ had not been discovered, if it had not been tested. Manual optimization of the regression function is very laborious and certainly puts a limitation to that (together with the statistical skills of the person performing it!). The procedure in stepwise regression to some extent repairs this weak point of regression analysis, as it makes it possible to screen a large number of possible variables. However, including not only variables but also variants of variables (x, $1/x$, x^3, $\ln(x)$, etc.) makes an endless list, which cannot be processed, so stepwise regression analysis is not complete either. But a combination of stepwise regression with manual optimization of the regression function will often result in a satisfactory data analysis.

6.2   The data set

Now, where the conclusions in [1] do not seem questionable due to the method used, it can still be questioned if the trends found in the data set with ANN and now also statistical methods are general trends for all concrete, or trends which are biased due to the composition of the data set.

When the data set was originally established, the aim was to collect as many data from literature as possible, where at the same time the mix composition, the air void structure of the hardened concrete and the result of a SS 13 72 44 freeze-thaw test were available. In that respect the data set is just what we happened to get – also known as happenstance data.

The discussion of the validity of results from happenstance data is classical in statistics, and there are some hazards to look out for:

- *Inconsistent data*: Data may not be consistent and comparable. For example, the oldest data are from 1989 and the newest from 2001. During that 12 year span, the test standard has been revised, and if the test procedure has changed, then results are not directly comparable. Moreover, data are obtained at different laboratories, and though they all follow the same standard for testing, there may be differences in equipment and execution.
- *Range of variables*: When a variable is included in a model (ANN or regression function), there has to be examples in the data set, where this variable takes a range of different values. If the variable always takes the same value, it is not possible to observe an effect on the outcome. For example, it would be difficult to establish a reliable model from production data. Normally concrete that will be exposed to frost during its service life is produced with a relatively high air content obtained by air entrainment, so in the data set there will be no examples of concrete with low air content.
- *Nonsense correlation*: Just because there is established a significant relation between y and x_i in a model, it does not provide evidence that y and x_i are causally related. Except for the variables for cement type, we have no variables characterizing the raw materials. If all samples with fly ash are from the same study, and this study happens to be with aggregates that are frost susceptible, then we will see a negative effect of fly ash in the model, though it is actually due to a problem with the aggregates.

We have examined the data set critically regarding these hazards. For example there are only few production data in the data set (from demonstration projects), most data are from research projects, which represents both concrete with good and poor frost resistance. 11 out of 12 studies include supplementary cementitious materials (fly ash or silica fume), these data are not collected from one source only. Like this, we have no suspicion that conclusions are due to a distorted picture from the data set, and that it would have been different, if the analysis was based on a series of experiments targeted at this purpose.

7. CONCLUSION

Results obtained by the artificial neural network analysis have been confirmed by using statistical methods, regarding the influence of *w/b*, fly ash and silica fume on salt frost scaling:

- Scaling decreases when *w/b* (or w/c_{eq}) decreases
- Scaling increases, when cement is replaced by fly ash and it decreases, when cement is replaced by silica fume. This is indirectly accounted for when using w/c_{eq} as variable in the model.

The statistical analysis also supports that when characterizing the air void structure as part of an evaluation of frost resistance, then the spacing factor L is not the most relevant parameter. The ANN analysis performed in an earlier study [1] pointed to total air content A and specific surface area S. The regression analysis in this study points to a combination of the two, $S \cdot A$. If the variable $S \cdot A$ is transformed to the unit m^2/m^3, it equals the total surface area of air voids per volume of concrete.

ACKNOWLEDGMENT

The first attempt to apply statistical methods on a complex dataset originally gathered for training an artificial neural network was made ahead of a presentation at the NCR Mini Seminar on Freeze-thaw testing of concrete [12]. A contribution to the proceedings was not completed, however, the discussions at the seminar were very fruitful, and the inspiration from fellow colleagues in the Nordic countries is very much acknowledged. A special thank to Dirch H. Bager for organising the NCR Mini Seminar, for showing interest in this project, and for his friendly push to finalize this paper.

REFERENCES

1. Marianne Tange Jepsen: *Predicting concrete durability by using artificial neural network*, Proceedings, Nordic miniseminar: Durability of exposed concrete containing secondary cementitious materials, Hirtshals, Denmark, 21-23 November, 2001, editor: D. H. Bager, Nordic Concrete Federation, Oslo, pp. 277-288 (2002).
2. Marianne Tange Hasholt: *Salt frost scaling – interaction of transport mechanisms and ice formation in concrete*, Ph.D. thesis, Danish Technological Institute, Taastrup (2002).
3. SS 13 72 44: *Concrete testing – Hardened concrete – Scaling at freezing*, Swedish Standards Institution, Stockholm (1995).
4. DS 2426: *Concrete - Materials - Rules for application of EN 206-1 in Denmark*, Danish Standard, Charlottenlund (2009).
5. George E.P. Box, William G.Hunter and J. Stuart Hunter: *Statistics for experimenters. An introduction to design, data analysis, and model building*, John Wiley & Sons, New York (1978).
6. Alvin C. Rencher: *Methods of Multivariate Analysis*, 2nd edition, John Wiley & Sons, New York (2002).
7. Peter Utgenannt: *Frost resistance of concrete – Experience from three field exposure sites*, SP report 2001:30, Swedish National Testing Institute, Borås, Sweden (2001).
8. Erik J. Pedersen and Marlene Haugaard: *New cement types. Basis for evaluation of the applicability of cement with lime stone filler for concrete intended for moderate and aggressive environment* (in Danish: *Nye cementtyper. Grundlag for bedømmelse af Basis-cements anvendelighed i beton til moderat og aggressiv miljøklasse*), client report, Concrete Centre, Danish Technological Institute, Taastrup (1994).
9. Terje F. Rønning: *Freeze-thaw resistance of concrete. Effect of: curing conditions, moisture exchange and materials*, Dr. Ing thesis, report 2001:4, Department of Structural Enginerring, Norwegian University of Science and Technology, Trondheim (2001).
10. Sture Lindmark: *On the relation between air void system parameters and salt frost scaling*, Proceedings, Nordic miniseminar on Freeze-thaw testing of concrete, 4-5 March 2010, Vedbæk, Denmark, editor Dirch H. Bager, Nordic Concrete Federation, Oslo, pp. 41-58 (2010).
11. John J. Valenza II and George W. Scherer: *A review of salt scaling: I. Phenomenology*, Cement and Concrete Research, vol. 37, no. 7, pp. 1007-1021 (2007).
12. Proceedings, Nordic miniseminar on Freeze-thaw testing of concrete, 4-5 March 2010, Vedbæk, Denmark, editor Dirch H. Bager, Nordic Concrete Federation, Oslo (2010).

Nonlinear modelling of packing of aggregates of four sizes with fixed compaction effort

Abhay Bulsari, Dr.
Nonlinear Solutions Oy
Kaivokatu 10 A 21, Fin-20520 Turku
E-mail: abulsari@abo.fi

Klaus Juvas
Lic.Sc.Tech.
Consolis Technology Oy Ab
Box 72, Fin-21291 Rusko
E-mail: klaus.juvas@consolis.com

ABSTRACT

Packing of particles of different sizes is of enhanced interest to concrete industries these days, particularly to be able to reduce cement consumption. It is not easy to mathematically describe the packing of particles of more than two different sizes, especially when the particle shape too might be difficult to describe. In the real world, each "size" or aggregate actually implies a particle size distribution which can be fairly wide, and overlapping with sizes of the other aggregates.

In 2008, the authors presented a solution for packing of particles of three sizes, indicating how the minimum voidage can be calculated. Packing of particles of four sizes is more interesting from a scientific point of view, as well as from the industrial point of view. As this paper makes it clear, the optimal packing of particles of four sizes is at least as good as the optimal packing of three sizes, and usually better. This means that one can usually save more cement by optimally mixing particles of four sizes than by mixing only three sizes.

It is difficult to develop physical models predicting the packing characteristics of particles of three or more sizes. Empirical modelling is a good approach if nonlinearities are taken into account. New techniques of nonlinear modelling, however, make this kind of model development feasible. From a limited amount of experimental data, one can develop nonlinear models of a good accuracy.

This paper illustrates with an example how nonlinear models can describe sufficiently well the packing of aggregates of four sizes with a wide variation in their diameters.

Key words: mix design, nonlinear modelling, aggregate packing

1. INTRODUCTION

The problem of particle packing is of interest in several applications, such as production of ceramic products, cemented carbide inserts of cutting tools and rock drills, particle suspensions with high solid contents, food materials including milk chocolates, medical tablets, coal and metal powders for their flowability, concretes and asphalt for minimising the binder content. The cost of the final product can be reduced if the volume of a high cost component such as bitumen or cement can be minimized by optimizing the low-cost aggregate fraction to the highest possible packing density.

In industries, attempts to minimise voidage are often based on trial and error experiments. In order to reduce the number of required experiments and to locate the real optimum, it is advantageous to develop mathematical models for the packing so that the optimum can be calculated with a modest effort.

Aggregates exhibit variable particle size distributions and particle shapes. The attempt to predict packing by simple packing density of the individual components is very crude. Packing properties of a single component can be measured easily, but those three or four numbers do not contain enough information to be able to predict the behaviour of mixes of three or four sizes. Therefore, a method for combining a reasonable number of accurate measurements with a suitable mathematical model is highly desirable.

Figure 1 - The gyratory compactor used for this work

Packing of particles has been a subject of research for a long time. In the early 1930s, Furnas [1] was among the first to report a mathematical study of the packing of broken solids, and developed models for binary and ternary systems. In the 1960s, McGeary [2] measured steel shot packing of binary mixtures by air pluviation and with moderate knocking of the test vessel. Farris [3] studied the viscosities of suspensions of a mix of particles with different sizes. More

recently, Golterman *et al.* [4] measured packing of concrete aggregate combinations by compacting the mixes on a vibratory table. Based on these measurements a ternary mix model was presented. These models are simplistic and have their limitations. The empirical models which are based on pre-specified nonlinearities cannot approximate the function as efficiently as those based on free-form nonlinearities. The authors' earlier work [5] has been on packing of particles of three sizes, which has resulted in an automated solution.

The objective of the work was to determine the optimal packing recipe for four selected aggregates from experimental data. Experiments were planned to measure the relative volume and voidage of aggregate mixes of different compositions after a fixed compaction effort. The experimental data was then utilised to develop a nonlinear model, from which the optimal recipe was calculated. The nonlinear model creation procedure has now been automated.

Figure 1 show the gyratory compactor (called an IC tester) used for this experimental work. In a gyratory compactor, a cylindrical container undergoes gyratory motion with a certain pressure applied from the top. This results in repeatable compaction efforts and consequently repeatable results of voidage or relative volume. These IC testers have shown higher accuracy and reproducibility in characterization of the properties of aggregate mixes. Based on the structure of nonlinear empirical models, the number of experiments needed to obtain a desired accuracy in the location of the optimum or the accurate value of the optimal degree of packing, can be roughly estimated.

2. NONLINEAR MODELLING

Nonlinear modelling has been around for more than fifteen years [7, 8]. It has been successfully utilised by various industries for a variety of purposes from quality control, product development and process guidance to software sensors and fault detection.

Nonlinear modelling can be roughly defined as empirical modelling which takes at least some nonlinearity into account. Nonlinear modelling can be performed in many ways. The simpler ways include polynomial regression and linear regression with nonlinear terms. One can also use basis functions and splines, and in cases where the form of the nonlinearities is known, nonlinear regression can also be used. New techniques of nonlinear modelling are based on free-form nonlinearities and do not require the knowledge of the form of nonlinearities in advance. Artificial neural networks are a set of efficient tools for nonlinear modelling, for reasons mentioned earlier, and particularly the universal approximation capability of feed-forward neural networks [6].
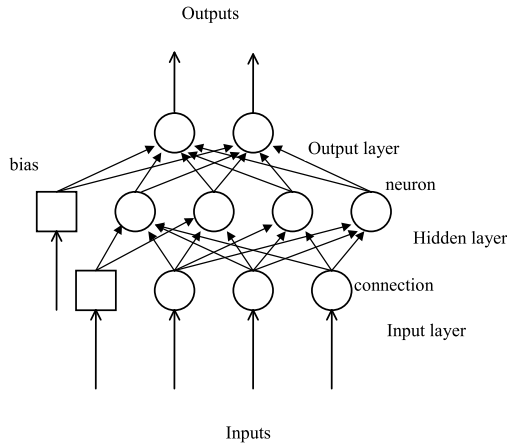
Figure 2 - A typical feed-forward neural network [7, 8].

Artificial neural networks usually consist of neurons in layers directionally connected to others in the adjacent layers (see Figure 2).

Mathematical models represent knowledge of quantitative effects of relevant variables in a concise and precise form. They can be used instead of experimentation if they are reliable enough. Mathematical models also permit the user to carry out various kinds of calculations, like optimisation, which can be used to improve quality or increase production rate. Mathematical modelling can be performed in various ways, and different ways are suitable in different situations.

It is not possible to use physical modelling in many situations. Even if it is possible, physical models tend to compute the output more slowly than empirical or semi-empirical models. Development of physical models is time consuming. Nonlinear modelling tends to be expensive, but physical modelling usually costs even more. Physical models involve assumptions and simplifications. Thus empirical modelling is often a better alternative.

Traditional empirical modelling is based on linear statistical techniques. Nothing in nature is absolutely linear. So it helps to take nonlinearities into account rather than ignore them. If the range of variables is small, linear techniques are sometimes sufficient. New techniques of nonlinear modelling based on artificial neural networks allow us to approximate nonlinearities without specifying in detail the nonlinearities to be accounted for. They allow for free form nonlinearities, unlike linear and nonlinear regression methods.

There are many different types of neural networks, and some of them have practical uses in process industries [7, 8]. Feed-forward neural networks have been in use in process industries for over fifteen years [9]. Most neural network applications in industries [9-16] ranging from concrete [11] to optical fibre cables [15] are based on them. The multilayer perception (Figure 2) is a kind of a feed-forward neural network.

The output of each neuron i in a feed-forward neural network is given by

$$z_i = \sigma\left(\sum_{j=0}^{N} w_{ij} x_j\right) \tag{1}$$

where the activation function is often the logistic sigmoid, given by

$$\sigma(a) = \frac{1}{1 + e^{-a}} \tag{2}$$

The incoming signals to the neuron are x_j, and w_{ij} are the weights for each connection from the incoming signals to the ith neuron. The w_{i0} terms are called biases. This results in a set of algebraic equations which relate the input variables to the output variables. Thus, for each observation (a set of input and output variables), the outputs can be predicted from these equations based on a given set of weights. The training procedure (Figure 3) aims at determining the weights which result in the smallest sum of squares of prediction errors. There are a variety of training methods in use today. It is also possible to combine neural networks with physical models or other empirical models, which often lead to better solutions.

3. EXPERIMENTAL DATA

The aggregates available for the precast concrete plant in Rusko in Finland were taken to the laboratory and dried. Since we have four sizes of particles classes, we will refer to them as fines, small particles, medium sized particles and coarse particles. The fine particles were sub-millimetre limestone powder. Small particles were slightly larger filler material. The medium sized particles were 0 to 8 mm, the coarse were 6 to 12 mm. With regards to particle size, the last two classes had considerable overlap.

A total of 35 experiments were planned (see Table 1) and aggregates were separately weighed for each of the experiments. These were then lightly mixed manually before being loaded into the gyratory compactor or the IC tester (see Figure 1). After a constant compaction effort of 10 cycles, the bulk density was recorded from each of the experiments, and the relative volume was calculated. The packing density increases a little with compaction effort, partly due to the grinding of some of the particles, and this will be the topic of another paper in future.
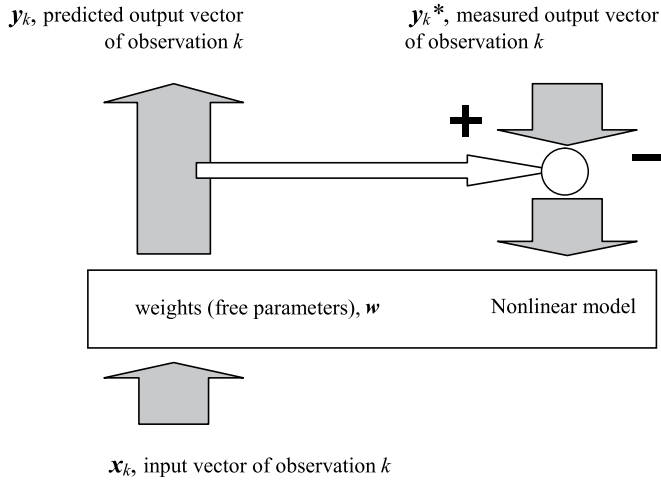
Figure 3 - Training is the process of determining the weights, the free parameters of the model.

Like the triangular plots used for ternary systems, pyramidal plots can be used for quaternary systems. They are more complicated to plot, but can be shown nicely in "slices" of triangles at different heights. In Figure 4, the four corners represent fines, small, medium and coarse. The proportion of each perpendicular to the side opposite a given vertex, from any given point represents its fraction. The 35 experiments are on the points shown in the plot of Figure 4. The points at the bottom are without a coarse fraction. The points above those are with a coarse content of 0.25, the six points at half height with a coarse content of 0.5 and the three points above that are with a coarse content of 0.75. The uppermost point is plain 100% coarse.

Figure 4 - The 35 points of the experiment plan on a pyramidal plot; each of the 4 faces of the pyramid has a minimum; each of the 6 edges has a minimum; the minimum inside is the lowest.

3.1. Analysis and pre-processing of data

Before model development is attempted, usually the data is analysed and pre-processed. It is more important for production data, but experimental data should also be analysed and pre-processed.
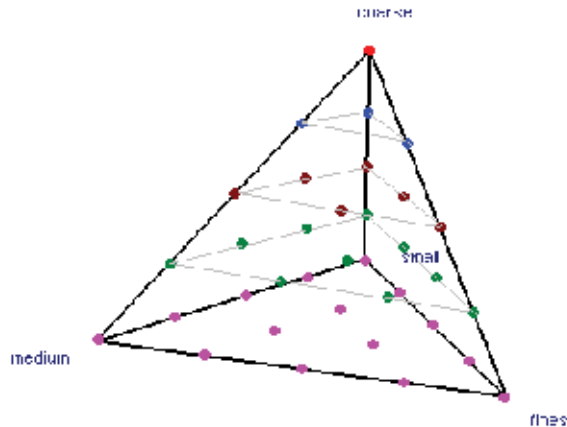
The experimental data was pre-processed and analysed by a pre-processing software, which has several facilities, including simpler things like calculating the basic statistics of the data set, filtering observations with missing measurements or variables beyond the range of interest, calculation of correlation matrices, showing the plots of every variable against every other, etc. It also has more advanced features like clustering, calculating sets of observations with maximum or minimum similarity, and dividing the data into training, test and validation sets required for nonlinear modelling, with desired forms of imbalance in the division.

The plots often reveal some relevant things, like variables which are binary or variable pairs which show a high correlation. Correlation matrices also reveal pairs of variables with high correlations. High correlations between input variables cause inconvenience during modelling, and sometimes one of them has to be excluded. No such problems were found in this data set. High correlations between two output variables, on the hand, is usually very welcome, since such variables can sometimes be treated together as two outputs in the same model.

The occupied volume divided by the volume of the solids is defined as relative volume, and is used as the output variable of the models, instead of total volume or voidage. Figure 5 shows a plot of relative volume against fraction of coarse particles with medium (no small or fines, diamonds), with small (no medium or fines, squares), with fines (no medium or small, triangles). It is easy to see that there is a minimum in each of these combinations. In each combination of three particles too, there is a non-trivial minimum. Similarly, for a mix of four sizes also, there is a non-trivial minimum. The objective of developing a nonlinear model is primarily to determine the minimum. The rightmost points in Figure 5 indicate the relative volume of just the coarse aggregate.

Table 1 - The plan of 35 experiments as shown in Figure 4

fraction of fines	small	medium	coarse
1	0	0	0
0.75	0.25	0	0
0.5	0.5	0	0
0.25	0.75	0	0
0	1	0	0
0.75	0	0.25	0
0.5	0.25	0.25	0
0.25	0.5	0.25	0
0	0.75	0.25	0
0.5	0	0.5	0
0.25	0.25	0.5	0
0	0.5	0.5	0
0.25	0	0.75	0
0	0.25	0.75	0
0	0	1	0
0.75	0	0	0.25
0.5	0.25	0	0.25
0.25	0.5	0	0.25
0	0.75	0	0.25
0.5	0	0.25	0.25
0.25	0.25	0.25	0.25
0	0.5	0.25	0.25
0.25	0	0.5	0.25
0	0.25	0.5	0.25
0	0	0.75	0.25
0.5	0	0	0.5
0.25	0.25	0	0.5
0	0.5	0	0.5
0.25	0	0.25	0.5
0	0.25	0.25	0.5
0	0	0.5	0.5
0.25	0	0	0.75
0	0.25	0	0.75
0	0	0.25	0.75
0	0	0	1

The data from these experiments were then pre-processed and analysed before model development was attempted. The data set was divided into 29 observations for model development and 6 observations for testing. It would be nice to have an equal number of observations in the training as well as the test sets, but there have to be a good number of observations in the training set to allow us to develop nonlinear models with a sufficient number of free parameters. Therefore, if we want 25 observations in each, it would mean 50 experiments. In this case, we had planned 35 experiments, so we can barely afford too many observations for the test set.

Table 2 shows the ranges of variables used in the experiments and the resulting range of relative volumes. The fraction of coarse particles is not included as an input variable since it is redundant. It can be calculated from the three other fractions, since the sum of the four has to be 1.
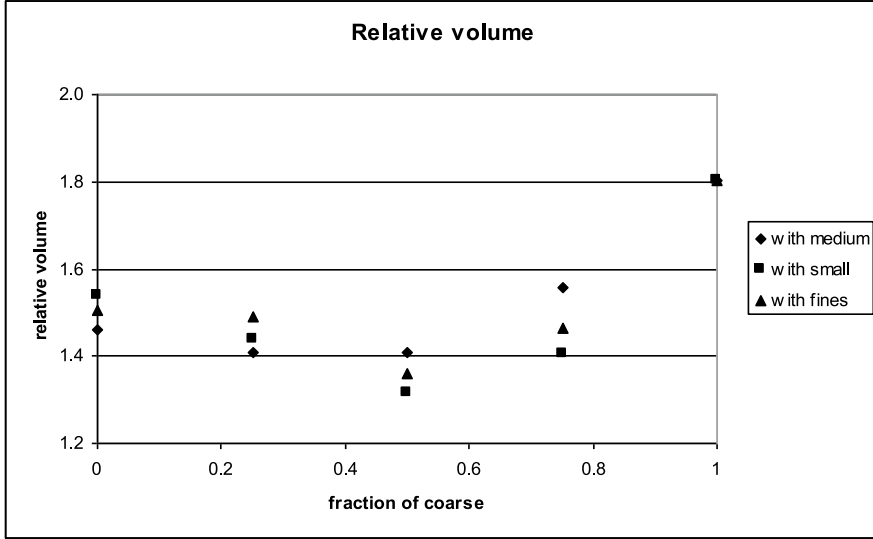
Figure 5 - A plot of relative volume against fraction of coarse particles with either no fines, no small or no medium fractions

Table 2 - Variables and their ranges

Variable	minimum	maximum	average in training set	average in whole set
fraction of fines	0	1	0.2500	0.2500
fraction of small	0	1	0.2241	0.2500
fraction of medium	0	1	0.2328	0.2500
relative volume	1.2591	1.8025	1.4085	1.3961

Earlier experience has shown that relative volume is a better variable than voidage for models of packing, so this work is based on relative volumes. The same procedure can be applied to voidage as well, but nonlinear models of relative volume have turned out to be slightly better because of slightly weaker nonlinearities on the edges of the input variable space. Relative volume is the total volume occupied by the mix of particles divided by the volume of the solids. Voidage, ε, is thus related to relative volume.

$$\varepsilon = 1 - \frac{1}{relative\_volume} \qquad\qquad relative\_volume = \frac{1}{1-\varepsilon} \quad (3)$$

4. RESULTS

Figure 6 illustrates the structure of the attempted nonlinear models. There are three input variables, the fraction of fines, the fraction of small particles, and the fraction of medium sized particles. As mentioned earlier, the fraction of coarse particles is not an independent variable, and is redundant. The nonlinear model development and their characteristics are described in the sequel.
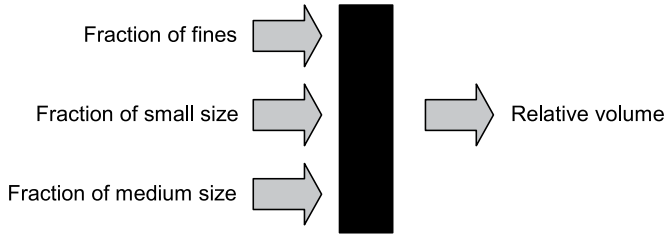

Figure 6 - Relative volume depends on the fractions of particles of each size

A large number of feed-forward neural network models were developed using NLS 031 software. Most of the runs do not produce the best models that one can produce with a given model configuration. However, after several runs, the result which is the best becomes clearer. These results are recorded in Table 3. Larger models cannot be attempted because there are only 29 observations available in the training set. It turns out that larger models are not quite necessary for this problem.

The lowest rms (root mean square) error on the test set occurs with three nodes in the hidden layer. Among the models in Table 3, (3,3,1) is probably the best model. However, still better models with more complicated structures can be developed. This is beyond the range of this paper which is likely to be read primarily by experts in field of concretes. The best model shows a very good prediction and generalisation capability. Figure 7 shows a comparison of the measured values with the values predicted by the nonlinear model. The measured values are on the horizontal axis, while the predicted values are on the vertical axis.

Table 3 - Prediction errors for feed-forward neural networks of different configurations

Model configuration	rms error (training set)	rms error (test set)	number of parameters
(3,1,1)	0.08640	0.07000	6
(3,2,1)	0.06536	0.13222	11
(3,3,1)	0.02448	0.03011	16
(3,4,1)	0.00539	0.05457	21
(3,5,1)	0.00389	0.05429	26
(3,2,2,1)	0.04767	0.05746	19
(3,3,2,1)	0.02479	0.04787	23
(3,3,3,1)	0.01726	0.03380	28

Based on this feed-forward neural network model, the optimal fractions of the fines, small and medium were calculated to be 0.1633, 0.1699 and 0.3992 respectively, where the relative volume is 1.2406. The contours are shown on a triangular plot in Figure 8. Unlike with three sizes, the triangular plot is not so efficient for four sizes because there are three independent

variables and the value of the third variable cannot be read from these plots. Therefore, Figure 8 shows only the values of the fines and small at the optimum depicted by a little rectangle inside the lowest contour. The actual value of the third variable, fraction of medium sized particles, is constant at 0.3992, which also means that the right edge of the triangle has total fractions well above 1, and is of no interest.

NLS 031 nonlinear modelling software
Licensed by Nonlinear Solutions Oy, Finland
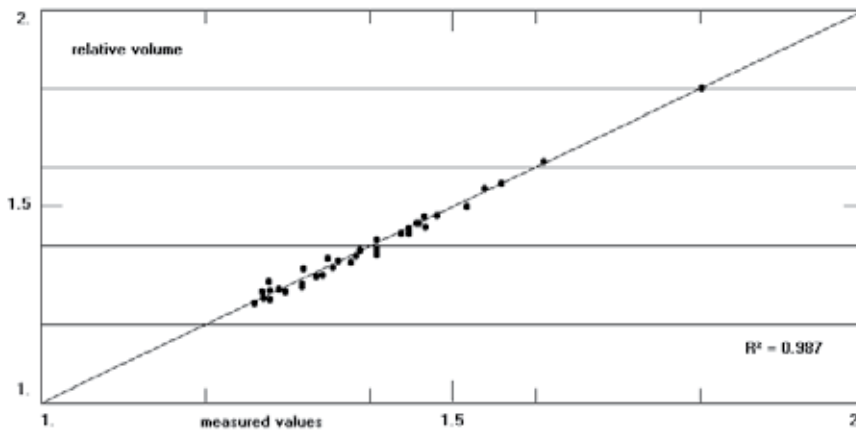
Figure 7 - A comparison of the measured values with the values predicted by the nonlinear model

All the four combinations of three of these four aggregates lead to minimum relative volumes which are not as low as 1.2406, the minimum obtained by mixing all the four aggregates. An optimal mix of fines, small and medium has a minimum relative volume of 1.2764. An optimal mix of fines, small and coarse has a minimum relative volume of 1.2869. An optimal mix of fines, medium and coarse has a minimum relative volume of 1.2545. An optimal mix of small, medium and coarse has a minimum relative volume of 1.2579 according to the nonlinear model for the four aggregates.

LUMET system
Licensed by Nonlinear Solutions Oy. Finland

Horizontal axis

lines

Minimum 0

Maximum 1

Vertical axis

small

Minimum 0

Maximum 1

Contours of

relative volume

Minimum 1.240604

Maximum 1.503366

medium

coarse

fine

Figure 8 - Contours of relative volume as predicted by the nonlinear model.

5. CONCLUSIONS

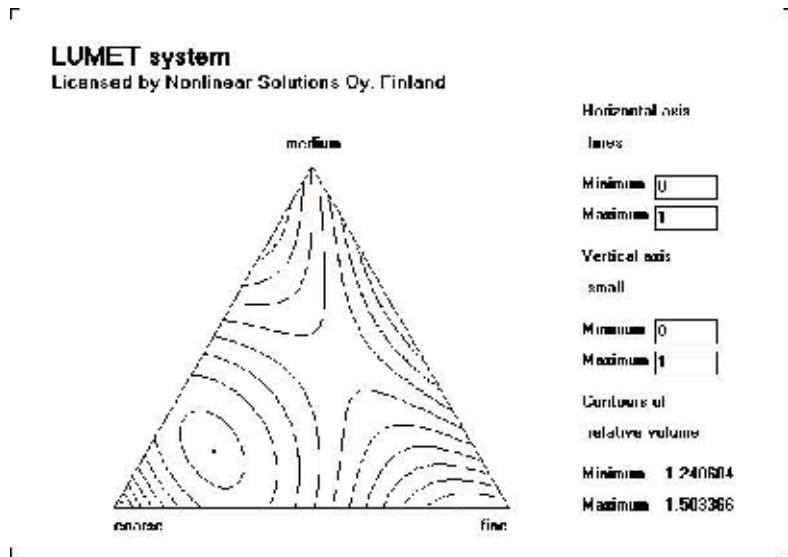Optimal packing of particles is important to minimise the amount of cement consumption. When there are particles of three or more sizes, it is not trivial to determine the optimal amounts of each fraction of the particles. Development of mathematical models of a good quality to predict the bulk density or relative volume for packing of four particle sizes has been considered to be very difficult. Physical modelling is not feasible. Conventional linear statistical techniques of empirical modelling are not suitable either because of the strong nonlinearities in the relations. New techniques of nonlinear modelling like feed-forward neural networks, however, have shown to be very capable of describing this kind of relations from a limited amount of experimental data.

In this work, nonlinear models were developed for one actual case of packing of aggregates of four sizes. Nonlinear models showed excellent statistical characteristics, with very good correlations. It was easy to determine the minimum relative volume from the nonlinear model. This demonstrated that the procedure of measuring the relative volumes from a gyratory compactor for several different mixes with a fixed compaction effort, followed by development of nonlinear models, and optimisation of relative volume, is a technically and an economically efficient way of determining the best mix of four aggregates.

REFERENCES

1. C. C. Furnas, Grading aggregates I-mathematical relations for beds of broken solids of maximum density. Industrial and Engineering Chemistry, Vol. 23, No. 9 (1931), pp. 1052

2. R. K. McGeary, Mechanical packing of spherical particles. Journal of the American Ceramic Society, Vol. 44 (1961), p. 513.

3. J. Farris, Prediction of the viscosity of multimodal suspensions from unimodal viscosity data. Transactions of the Society of Rheology, Vol. 12, No. 2 (1968), pp. 281–301

4. P. Goltermann, V. Johansen and L. Palbol, Packing of aggregates: an alternative tool to determine the optimal aggregate mix. ACI Mater. J. September–October (1997), pp. 435–443.

5. A. Bulsari and K. Juvas, Nonlinear modelling of packing of aggregates of three sizes for minimising cement consumption, presented at the 20th symposium on Nordic concrete research and development, Bålsta, Sweden, June 2008

6. K. Hornik, M. Stinchcombe, and H. White, "Multilayer feed forward networks are universal approximators," Neural Networks, Vol. 2, (1989) 359-366.

7. A. Bulsari (ed.), *Neural Networks for Chemical Engineers*, Elsevier, Amsterdam, Netherlands, 1995.

8. A. Bulsari, "Quality of nonlinear models in process industries", Internal Report NLS/1998/2.

9. A. Bulsari *et al.*, "Nonlinear modelling paves the way to bespoke polymers", British Plastics and Rubber, December 2002, 4-5.

10. A. Bulsari, J. Fredriksson and T. Lehtinen, "Neural networks for quality control in the wire rod industry", Wire Industry, Vol. 67 (March 2000) 253-258.

11. A. Bulsari and A. Käppi, "Prediction of compressive strength and compaction degree of concrete", Proceedings of the International Conference EANN '98, 181-184.

12. A. Bulsari *et al.*, "Uuden sukupolven laatujärjestelmät sisältävät epälineaarisia malleja", Vuoriteollisuus, No. 1/1999, 38-41.

13. P. Myllykoski, "Prediction of formability of steel sheets", Proceedings of the International Conference EANN '98, 221-224.

14. A. Bulsari, H. Rajainmäki, O. Naukkarinen, "Improving cryogenic grade copper with nonlinear models", Wire Industry, Vol. 69 (May 2002) 292-298

15. A. Bulsari and M. Lahti, "Nonlinear models guide secondary coating of OFCs", Wire and Cable Technology International, Vol. 29, No. 5 (September 2001) 40-43

16. A. Bulsari and P. Hooli, "More accurate alloying with neural networks", Stainless Steel World, Vol. 12 (November 2000) 54-57

Experience Using the Norwegian 38°C Concrete Prism Test to Evaluate the Alkali Reactivity of Aggregates, Concrete Mixes and Binder Combinations

Jan Lindgård
Senior Scientist
SINTEF Building and Infrastructure
Richard Birkelandsvei 3, NO 7465 Trondheim
E-mail: jan.lindgard@sintef.no

Bård Pedersen
Technology Manager
NorStone Heidelberg Cement
PO Box 60, NO 4301 Sandnes
E-mail: bard.pedersen@norstone.no

Sigrun K. Bremseth
Senior Engineer
Norcem Heidelberg Cement
NO 3950 Brevik
E-mail: sigrun.bremseth@norcem.no

Per Arne Dahl
Senior Scientist
SINTEF Building and Infrastructure
Richard Birkelandsvei 3, NO 7465 Trondheim
E-mail: per.dahl@sintef.no

Terje F. Rønning
R&D Manager
Norcem Heidelberg Cement
NO 3950 Brevik
E-mail: terje.ronning@norcem.no

ABSTRACT

Three test methods have been applied in Norway for 20 years to classify the alkali reactivity of concrete aggregates. The Norwegian 38°C concrete prism test was in 1996 also specified in the Norwegian guidelines for performance testing of concrete mixes and/or binders. Since then, more than 160 such performance tests have been carried out in Norway. The main objective with this paper is to discuss the experiences gained from these tests. The Norwegian concrete industry has successfully used the performance test as a flexible tool to be able to utilize alkali reactive aggregates.

Key words: alkali-silica reactions, performance testing, Norwegian experiences, critical alkali limit

1   INTRODUCTION

1.1   Background

Alkali-Silica Reaction (ASR) was recognized as a deterioration problem in Norway about 1990. Since then, several comprehensive national research projects have been carried out on this subject. These projects have strongly focused on test methods for aggregates and corresponding criteria for the prediction of ASR as observed on Norwegian concrete structures.

The research projects have resulted in reasonably reproducible test methods regarding ASR of Norwegian aggregates. Three methods have been applied since the early 90's, the *petrographic method* (similar to the RILEM AAR-1 method [1]), the *80°C accelerated mortar bar test* (AMBT, similar to the RILEM AAR-2 method [2]; exposure time 14 days; prism size 40x40x160 mm) and the *Norwegian 38°C concrete prism test* (NCPT; similar to the old Canadian CPT [3]; exposure time one to two years; unwrapped prisms of size 100x100x450 mm). These methods are included in the current Norwegian regulations for handling the alkali reactivity problem, see section 1.2 [4,5,6].

About 20 years of commercial testing of aggregates with respect to potential ASR have provided SINTEF a very good overview over the alkali reactivity of Norwegian aggregates. In most parts of Norway, alkali silica reactive rock types are present in varying quantities in many commonly used concrete aggregates. To be able to utilize these alkali-silica reactive aggregates for production of durable concretes, there is a need for a reliable performance test to evaluate the alkali reactivity of concrete mixes and/or binders resistant to alkali aggregate reactions. Several such performance tests have been used world wide for at least 15 years, mainly to evaluate supplementary cementing materials (SCMs) and lithium as means to avoid damaging ASR in concrete. Thomas et al. [7] have recently provided a critical evaluation of different test methods. The authors conclude that none of the currently available or commonly used test methods meet all the criteria for an ideal performance test. For example, the main shortcoming of the Canadian 38°C concrete prism test (prism size 75x75x250 mm) [8] is the duration of the test (2 years) and that addition of alkalis are required to compensate for alkali leaching effects. Thus the method cannot be used to determine the "critical" alkali content for an alkali reactive aggregate, nor determine how the minimum level of a SCM changes with the concrete alkali content. However, research are going on towards improving current test methods and to develop alternative tests, for instance within the RILEM technical committee "TC 219- ACS" (2007-2012). Similar work has also been initiated in USA by the U.S. Department of Transportation [9].

The NCPT [5] was in 1996 also specified in the Norwegian guidelines [10] for performance testing of concrete mixes and/or binders (i.e. various cements added any SCMs or other mineral admixtures). Since then, a large number of "job mixes" (i.e. real concrete recipes) and binders have been "performance tested", mainly on a commercial basis. The main objective with this paper is to discuss the experiences gained from these tests, rather than presenting detailed results. The Norwegian concrete industry has successfully used the performance test as a flexible tool to be able to utilize alkali reactive aggregates. Such aggregates may be found in most parts of Norway.

1.2   The Norwegian system for approval based on performance testing

In 1996, the Norwegian Concrete Association published a national guideline on ASR ("NB 21") [10]. Based on knowledge gained after 1996, and the fact that the publication now is a harmonised normative reference document to the new concrete materials standard, NS-EN 206-1 [11], a revised version of the publication was provided in 2004 [4,6].

The 2004 edition of "NB21" is divided into two major parts. Part 1, "Specifications", describes in formal terms the mandate and the use of the publication, and how concrete constituents and concrete recipes shall be tested and evaluated with respect to potential ASR. Individual aggregates and blends of aggregates shall be evaluated by the petrographic analysis as a first step. The evaluation based on results from these analyses can be reassessed by the 80°C AMBT, while the 38°C CPT can be used to reassess the evaluation from any of these tests. For the evaluation of binders and concrete compositions (incl. mortars and shotcrete), only the CPT can be used.

The three methods are described in detail in a corresponding publication from the Norwegian Concrete Association ("NB32") [5]. "NB32" also gives rather detailed requirements to laboratories that aim to be approved to run the Norwegian ASR tests.

Part 2 of "NB21" gives advisory guidelines for how the concrete industry can fulfil the requirements given in part 1. It also provides a survey of binders and corresponding alkali contents documented to be suitable for production of ASR resistant concrete containing all types and amounts of Norwegian reactive aggregates. This survey is updated whenever new binders obtain satisfactory documentation – see www.betong.net (*comment: click on "Publikasjoner"*).

Based on extensive laboratory performance testing and comprehensive calibration of results against field behaviour [12,13], "NB21" states that all CEM I binders shall be considered to be suited for production of non-reactive concrete containing all types of alkali reactive Norwegian aggregates up to an alkali content of 3.0 kg Na_2O_{eq}/m^3 of concrete (see section 3.5). If alkali reactive aggregates are to be used in CEM I based concretes with a higher alkali content or in concretes containing other binders, the Norwegian regulations require performance testing of the actual "job mix" or the actual binder. In such general testing of different binders' ability to prevent development of alkali silica reactions, the binders are tested in concrete containing a specified aggregate composition [5] (see Table 1) that for Norwegian conditions is considered to be "worst case" with respect to alkali reactivity (i.e. reacts at low alkali levels and gives a very high prism expansion when tested in the NCPT).

The validity of documentation supplied by performance testing is limited to concrete with composition considered to be no more reactive than was the concrete used for the testing. The reactivity is considered to increase if:
- The concrete alkali content increases *(comment: For performance tested materials, extra fly ash or silica fume may be added the cement or the concrete mix without any further documentation, even if these additions contribute with supplement alkalis).*
- The content of pozzolanic material or other SCMs decreases.
- The content of reactive rock types increases more than the upper limit specified in the publication *(comment: No pessimum effects have been documented for any Norwegian aggregate – opposite to the experience gained e.g. in Denmark with opaline flint [21]).*

The acceptance criteria for different types of binders and concrete recipes are differentiated when NCPT results are assessed. In general it can be said that:

- CEM I binders and CEM I based concrete compositions containing no pozzolans or other SCMs shall be considered non-reactive if showing 1 year expansion less than 0.050 %.
- CEM I based concrete compositions containing silica fume, concretes based on the fly ash blended CEM II/A-V cement produced by Norcem in Norway (co-grinding of PFA and clinker) and / or blends of this cement and CEM I shall be considered non-reactive if showing 1 year expansion less than 0.030 %.
- Concrete recipes based on other binders than those mentioned above shall be considered non-reactive if showing 1 year expansion less than 0.030 % and at the same time 2 years expansion less than 0.060 %.

A performance test shall be based on one or more mixes. If based on more than one mix, test results shall be plotted in an expansion versus alkali content-diagram as illustrated by Figure 1. Based on the assumption that a linear relation exists between expansion and alkali content, straight lines connecting the points shall be drawn. If a connecting line and the line illustrating the accepted limit for expansion cross each other, the alkali content limit value for acceptance of non-reactivity is given by the alkali content at the point of intersection subtracted a "safety factor" amounting to 0.2 kg Na_2O_{eq}/m^3 of concrete. If the above-mentioned crossing of lines does not occur, the alkali content limit value for acceptance of non-reactivity shall be:

- 3.0 kg Na_2O_{eq}/m^3 when all the mixes show expansions exceeding the acceptance value.
- Equal to the highest individual alkali content used within the mixes involved when all the mixes show expansions less than the acceptance value.
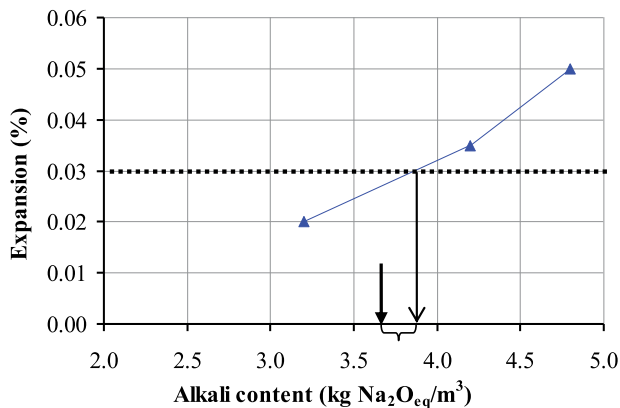
Figure 1 -   Principle diagram for determination of acceptance limit for alkali content based on performance testing according to Norwegian regulations. The dotted line represents the critical expansion limit for PFA binders after one year of exposure. The bracket represents the "safety factor" amounting to 0.2 kg Na_2O_{eq}/m^3 of concrete. In the current example, the critical alkali limit is (3.85-0.20) 3.65 kg Na_2O_{eq}/m^3 of concrete.

Internationally, a too high extent of alkali leaching is reported to be one of the main sources of error in connection with accelerated performance testing (see e.g. Thomas et al. [7]), leading to a correspondingly reduced alkali content within the test prisms during the test. Consequently, a

too low expansion may be obtained, negatively influencing the laboratory/field correlation. Despite this fact, no specific "safety factor" (beyond the 0.2 kg Na_2O_{eq}/m^3 alkalis of concrete discussed above) is included in the Norwegian regulations to compensate for the (so far undocumented) amount of alkalis that may leach out from the test prisms in the NCPT during the one to two years exposure period. However, alkali leaching is currently focused on in on-going national research activities, as well as in the RILEM task group 219-ACS-P "Performance testing". This is also the case regarding the question if some aggregate types may release alkalis into the concrete pore water during the test period.

2   REVIEW OF NORWEGIAN PERFORMANCE TEST SERIES

2.1   Available test results

Since performance testing by use of the Norwegian 38°C CPT started in Norway in 1996, the detailed testing procedure has been unchanged [5]. Only a few testing laboratories are approved to perform such performance testing on a commercial basis. As part of the PhD study of Jan Lindgård, all available results from the performance test series performed by the two most experienced approved Norwegian laboratories, SINTEF Building and Infrastructure (Trondheim) and Norcem (Brevik) have been compiled and evaluated. SINTEF have primarily performed the testing on a commercial basis for the industry, while Norcem mainly have tested the performance of various cements in trade or under development [14,15,16,17,18]. All the about 30 concrete prisms test series being part of the PhD study of Bård Pedersen [19,20] are also included in the review. SINTEF performed all the test series in his study, focusing of the possible mitigating effects of different filler types on ASR.

In total, the review includes results from 161 performance test series. Table 1 and 2 give an overview of the different aggregate types and binder types tested. The duration for the 155 finalised test series have varied from one to twelve years.

Table 1 -   Overview of aggregate types included in the reviewed performance test series executed in Norway in the period 1996-2010

Aggregate type		Number of tests [1]
Fine (0-5 mm)	Coarse (5-20 mm)	
Reference-I (NR) [2]	Reference-II (R) [3]	26
Reference-III R [4]	Reference-II (R) [3]	49
Reference-IV R [5]	Reference-II (R) [3]	7
Reference-IV R [5]	Reference-I (NR) [2]	26
Different types [6]	Different types [6]	50
Recycled glass (R)	Recycled glass (R)	3
	Sum	161

[1] 119 of the tests are performed at SINTEFs laboratory (include the 29 tests being part of Bård Pedersens PhD study [19, 20]). The remaining 42 tests are performed by Norcem.

[2] Non-Reactive (NR) natural gneiss/granite aggregate.

[3] Reactive (R) chrushed cataclasite.

[4] Natural aggregate (R) with claystone, siltstone and phyllite as the main reactive rock types.

[5] Natural aggregate (R) with mylonite, cataclasite, greywacke and phyllite as the main reactive rock types.

[6] Primary alkali silica reactive aggregate types. 27 of the mixes include a crushed mylonite [19, 20].

Table 2 - Overview of binder types included in the reviewed performance test series executed in Norway in the period 1996-2010

Binder type	Total number of tests	Number of the tests added CSF [5]
CEM I [1]	51	8
CEM I + CEM II Portland fly ash cement [2]	45	22
CEM II Portland fly ash cement [2]	26	9
CEM II Portland slag cement [3]	7	---
CEM I + fly ash added separately	5	---
CEM I + added LWA fines	4	---
CEM I + added different filler types [4]	22	---
CEM I + other admixture added	1	---
Sum	161	39

[1] All the cements, except the Portland slag cement, are produced by Norcem (part of the Heidelberg Cement Group). Different types of CEM I have been tested.

[2] CEM II/A-V including about 20 weight-% fly ash of the binder.

[3] CEM II/B-S including at least 32 % ggbfs.

[4] Most filler types were produced from alkali reactive aggregates [19, 20].

[5] CSF = Condenced Silica Fume.

The 161 test series include some "job mixes" and some mixes to determine the critical alkali limit for various aggregate types. However, most of the performance test series have aimed to document different binder combinations ability to prevent ASR. Reference reactive aggregates were used in these tests series. In addition to different CEM I cements, the binders tested included pulverized fly ash (PFA), condensed silica fume (CSF), ground granulated blast furnace slag (ggbfs), light weight aggregate fines and/or different filler types (mainly produced from alkali silica reactive rock types). The water/binder ratio in the test series varied mainly between 0.45 and 0.48. If needed to boost the alkali content, NaOH was added to the mixes.

2.2   Alkali leaching

Since 2007, SINTEF have systematically performed analyses to document the extent of alkalis leached out from the prisms in the NCPT during the one to two years exposure period. To avoid contamination, all testing equipment and storage containers are washed properly and a new lining is applied before new test series are started. At every standard measuring points of time, a 20 ml sample of the water in the bottom of each storage container is collected. Before each sampling, the total amount of water is calculated by measuring the depth of the water in the centre of each container. A depth versus volume ratio was earlier established for the applied type of storage container by successively adding a known quantity of water and measure the corresponding water depth. If some of the water has evaporated since the last measurement, water is added after sampling.

The content of alkalis, Na^+ and K^+, has been measured by use of flame atomic absorption spectroscopy (FAAS). Based on these measurements, the total content of alkalis leached out from the concrete prisms has been calculated. As a quality control, five samples were parallel

tested in a laboratory at the Norwegian University of Science and Technology (NTNU) using inductively coupled plasma mass spectrometry (ICP-MS). A satisfactory correlation between the two methods was documented; on average about 5 % less alkalis were found by use of ICP.

3   RESULTS AND DISCUSSION

3.1   Repeatability and reproducibility of results

Spread in results obtained between individual prisms within one test series (repeatability)
To document the repeatability of the NCPT, standard deviations and coefficients of variation (c.o.v) for the measured expansions and the corresponding weight increases of the three prisms within one test series have been calculated. The outcome of these calculations is shown in Table 3 (mean results) and Figure 2 (detailed results for the expansion).

Two of the rows in Table 3 give the calculated mean standard deviations and c.o.v. for all 119 SINTEF test series included in the review (include 29 test series being part of the PhD study of Bård Pedersen [19,20]). In the other two rows and in Figure 2, all single test results with mean prism expansion lower than 0.010 % are left out, giving more meaningful results for the calculated c.o.v. for the expansion (calculation of c.o.v. becomes "meaningless" for very low expansion values; c.o.v. varies from about -200 to +200 %).

Table 3 -   NCPT - three parallel prisms within one test series; calculated mean standard deviations and mean c.o.v. for measured expansions and weight increases. The data is based on 119 test series performed in SINTEFs laboratory.

	Expansion			Weight increase			Comments
Exposure time (months)	6	12	24	6	12	24	
Standard Deviation (%)	0.002	0.005	0.008	0.030	0.034	0.035	Included all SINTEF results
	0.003	0.006	0.008	0.032	0.034	0.035	Excl. tests with expansion < 0.010 %
Coefficient of variaton (%)	6.2	14.0	6.8	8.0	6.7	5.3	Included all SINTEF results
	6.3	7.8	6.8	6.8	6.3	5.3	Excl. tests with expansion < 0.010 %

For test series with expansion higher than approximately 0.025 %, c.o.v. for the expansion is lower than 10 % for most test series (Figure 2). The corresponding mean values for c.o.v. are in the range 6 to 8 % (Table 3). Normally, a coefficient of variation in the repeatability of up to 20 % is regarded acceptable [21]. The repeatability for the NCPT is thus in general very good. However, as can be seen from Figure 2, a few exceptions exist.

In the precision trials within the European research project PARTNER [21], eight laboratories took part for each of the four test methods incorporated. The two CPTs included, RILEM AAR-3 [23] and RILEM AAR-4 Alternative [24], applied wrapped prisms. Each laboratory tested the same three aggregates types, prepared at one laboratory, before being distributed. Identical cement type was applied in all mixes. Mean c.o.v. for the expansions measured was in the range 14-21 % for RILEM AAR-3 and 9-16.5 % for RILEM AAR-4 Alternative, respectively. For ASTM C 1293 (38°C CPT, same prism size as the RILEM CPTs, but no wrapping of the prisms), c.o.v. has been found to be 12 % for average expansions of more than 0.020 % [25].

As shown, the repeatability for the Norwegian CPT is in general much better than reported for ASTM C 1293 and as documented in the PARTNER project applying two draft RILEM CPTs. This is mainly assumed to be due to a good quality control in SINTEF laboratory, combined with long term experience in performing expansion tests.
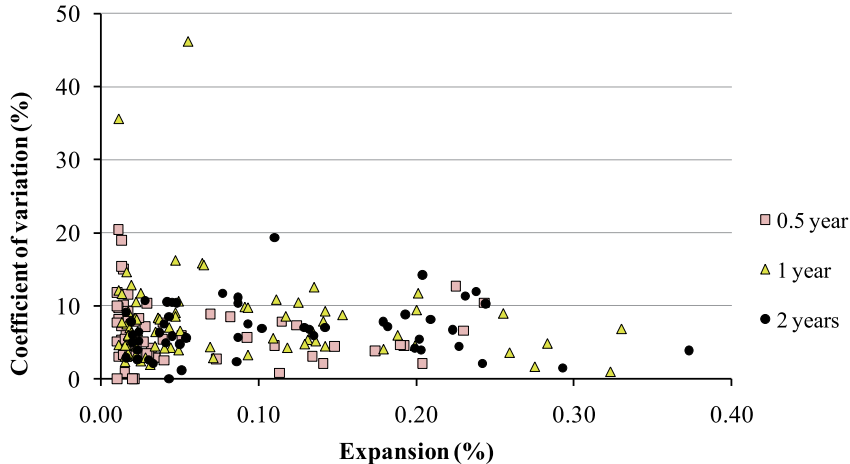

Figure 2 - NCPT; three parallel prisms within one test series; calculated c.o.v. for measured expansions versus corresponding mean expansions. The data is based on 119 test series performed in SINTEFs laboratory. All single test results with mean prism expansion lower *than 0.010 % are left out.*

Calculated c.o.v. for the weight increase is lower than 15 % for most test series (includes all SINTEF results). The corresponding mean values for c.o.v. are in the range 5.5-8 % (Table 3). The repeatability is thus acceptable with respect to measured weight increases, as well. In general, c.o.v. for the weight increase decreases with increasing weight increase.

Within laboratory – and multi laboratory variations (reproducibility)
Reproducibility of a concrete prism test is a measure to compare the difference in the mean value obtained between different laboratories when testing identical aggregate- and concrete compositions. In order to check the reproducibility of the NCPT, parallel tests have from time to time been performed by SINTEF and Norcem. Figure 3 shows the measured expansion versus exposure time for six such "pairs of concrete mixes" with identical concrete composition. For all these "pairs of mixes", except one, one of the test series was performed by SINTEF and the other test was performed by Norcem.

As shown in Figure 3, the corresponding graphs for all the six "pairs of mixes" are close. However, if the expansion is very close to the critical expansion limit, also small deviations between the two laboratories may lead to different conclusions from the testing. In Figure 3, this is the case for one of the six "pairs of mixes"; one of test series for a concrete with a highly reactive aggregate, fly ash cement and a total alkali content of 6.6 kg Na_2O_{eq}/m^3 of concrete expanded just above the critical limit after one year of exposure at SINTEF (0.031 %), while the expansion at Norcem was just below (0.025 %) the critical expansion limit (0.030 %) (the mix is marked with an open rectangle). After two years of exposure, the expansion was a little bit

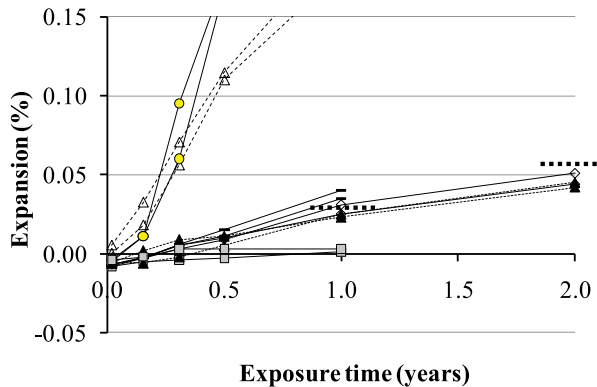below the critical expansion limit (0.060 %) at both laboratories (0.051 % and 0.044 %, respectively).

Figure 3 -   NCPT; expansion versus exposure time for six parallel concrete mixes. Each "pair of mixes" is marked with identical bullets. The dotted lines drawn at 1 and 2 years, respectively, represent Norwegian critical expansion limits for concretes with binders containing fly ash, condensed silica fume or ggbfs.

Also other test series (not included in the figure) confirm that SINTEF and Norcem produce corresponding results, among these the parallel tests performed by the two laboratories within the PARTNER project [22]. In the paper summarizing the PARTNER findings [21], the importance of experience is highlighted: "*There is also evidence that the experience of the laboratories with a particular method has a significant effect on the variability of results. Where laboratories were carrying out procedures with which they were very familiar, for example the Norwegian method carried out by Norcem and SINTEF, the expansion values were very close*".

Due to a limited number of laboratories applying the NCPT, the precision of the method is not documented by round robin testing as in the PARTNER project, in which the procedure in ISO 5725-94 [26] was followed. In the PARTNER project, the reproducibility for the RILEM AAR-3 method was quite poor [21]. Calculated c.o.v. for the mean expansions measured by the eight laboratories taking part was in the range 49-54 %, i.e. unacceptably high. Corresponding values for RILEM AAR-4 Alternative, was in the range 24-33%, i.e. somewhat better. It was concluded [21] that the precision of both RILEM concrete prism tests is sufficient to distinguish between pronounced non-reactive and reactive materials, but not between smaller differences of reactivity.

The precision of the ASTM C 1293 CPT [25], which is similar to the NCPT except application of smaller prisms, is, as discussed in [21], reported in a way which makes a direct comparison with the PARTNER results difficult: *For expansion levels less than 0.014%, the expected difference between laboratories should generally not exceed 0.009% (absolute percent). This means that if you sample an aggregate with an expected expansion of 0.014%, reduce it to several subsamples and send two of them to different laboratories, the expected expansion results (i.e. the average of three prisms) will most likely be between 0.023 and 0.005%. The multi-laboratory coefficient of variation for expansions greater than 0.014% is 23%.*

3.2   Expansion versus exposure time – overall results

Tables 1 and 2 give an overview of the different aggregate types and binder combinations included in the review of the Norwegian performance test series performed in the period 1996-2010. In Figure 4, all the measured mean expansions are plotted versus exposure time (up to 12 years).

75 of the total 161 performance test series have run for at least 2 years. Out of these, 38 concrete mixes have been exposed for 3-12 years. As shown in Figure 4, the general tendency is that the rather constant expansion rates for the most alkali reactive mixes (mainly reference mixes with high alkali content) decrease after an exposure time of approximately 0.5 year. The expansion rates for the medium reactive mixes, however, have shown to be rather constant up to about 2-3 years of exposure, before decreasing. For most mixes, the increase in expansion is very low or even non-appearing after the first two years of exposure.

One of the main reasons for the reduced expansion rate with time are assumed to be alkali leaching (see section 3.6) combined with consumption of alkalis in the alkali silica reaction, both reducing the pH of the concrete pore water.
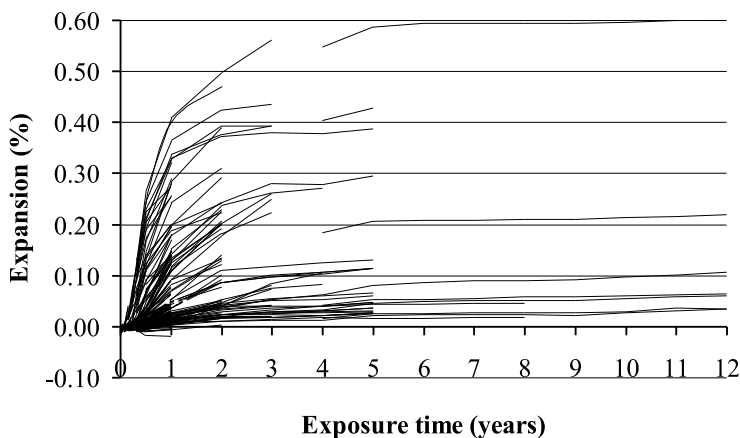

Figure 4 -   NCPT; expansion versus exposure time for 161 performance test series. Criterion expansion limits are given in Figure 3.

Some of the approved non-reactive mixes, i.e. mixes with a lower expansion than the critical limits given in the Norwegian regulations [4], have expanded beyond the critical expansion level(s) at later ages. However, most mixes showing non-reactivity after one year of exposure still show an expansion below the critical expansion level(s) even up to 12 years of exposure. Due to more alkali leaching with time, no further significant expansion is expected for these concrete mixes.

3.3   Weight increase as a quality control

Standard procedure in the Norwegian CPT, as in most comparable test methods, is to measure both expansion and weight increase of the prisms. The weight increase is rarely reported, but should act as an important quality control of the moisture conditions within the storage containers.

As shown in Figure 5, the prism weight typically increases with increasing prism expansion. However, no good correlation exists. This is not surprisingly, since the review includes concrete mixes with various aggregate- and binder types. The calculated correlation factors R^2 between the measured weight increases and the expansions were approximately 0.80 at the ages 2, 3 and 4 years. R^2 was somewhat lower at the ages 0.5 and 1 year.
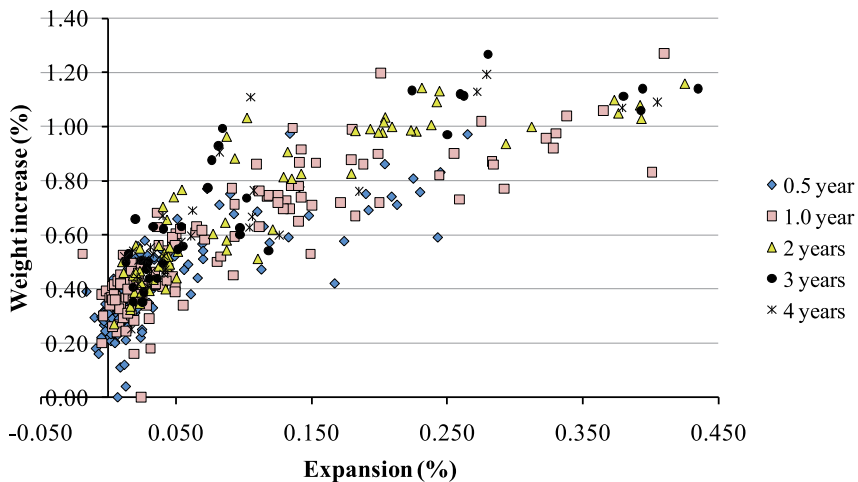

Figure 5 -   NCPT; weight increase versus expansion at ages 0.5-4 years. The data is based on 161 test series.

All the 161 test series, except three, revealed a one year weight increase in the range 0.20-1.30 %, even though some of these test series exhibited a slight shrinkage. The weight increase due to ASR is the total weight increase of the prisms, subtracted the weight gain due to water absorption by the aggregates and by the cement paste (in particular due to the on-going hydration). The weight increases show a reduced rate with time, as the expansions do (see Figure 4). The three test series with lower weight increase, in the range 0-0.20 % after 0.5-1 year of exposure, was performed at Norcem. The reason for this low gain in weight is not known.

According to the comprehensive experience gained with the Norwegian CPT, a minor weight loss may for some binders be recorded in the first few weeks of exposure, limited to maximum 0.20 %. If the prisms still show a significant weight loss after a longer time of exposure, this is most likely due to insufficient water present in the system. Thus, a too low prism expansion will be recorded. Example; in one test series performed at SINTEF, all the three prisms in the storage container lost some weight from one to two years of exposure. At the same time the expansion of the prisms decreased somewhat. By control of the storage containers, a crack was observed in

the cover, resulting in a moisture content within the storage container less than 100 % RH. Consequently, the test results had to be discarded.

In the RILEM CPTs, AAR-3 (38°C) [23] and AAR-4 (60°C) [24], a requirement is given to the recorded weight to ensure that sufficient water is present in the system. Until recently, the method descriptions stated that all the measurements related to a single test prism should be discarded if the weight loss recorded for the prism, with cross-section 75±5 mm and length 250±50 mm, was greater than 20 g. This means that a weight loss up to 0.4-0.8 % (depending on the prism size applied) compared to the starting reference weight should be accepted.

In light of the experience built up with the NCPT, where even prisms that exhibit shrinkage normally gain at least 0.2 % in weight after the first 0.5 year of exposure (Figure 5), this requirement seems far too little restrict. Based on a suggestion from SINTEF to the RILEM TC-219 ACS committee, the former requirement has now been sharpened. In the current method descriptions no weight reduction of the prisms, compared to the reference weight at start of testing, is allowed at the time of the final weight reading. If a net weight loss (i.e. without any cloth wrapping) is recorded at the time of executing the last length readings, the measurements relating to these prisms shall be discarded.

3.4   Performance testing of binders

As shown in Table 2, most of the performance test series have aimed to document different binder combinations ability to prevent ASR. About 70 of these test series have included Norcem "Standard FA" cement, a CEM II/A-V Portland - fly ash cement with a PFA content of approximately 20 % by weight of binder. All the fly ashes used the last 15 years are carefully selected in order to have good ASR mitigation properties. In contrast to usual CEM I - PFA combinations, the Norcem "Standard FA" cement is manufactured by co-grinding clinker and PFA, a process that has shown to enhance the well known ASR mitigating effect of fly ash [27]. An example of the effectiveness of this cement to suppress ASR is given in Figure 6. PFA constitutes about 80 kg/m^3 of the binder. All the alkalis in the fly ash are included in the calculated total alkali content of the concrete mixes. The expansion of these mixes increases with increasing alkali content from 5.0 to 8.5 kg Na$_2$O$_{eq}$ /m^3 of concrete, obtained by boosting with NaOH. Based on such performance testing, all the Norcem "Standard FA" cements with various selected fly ashes have given acceptance alkali limits equal to or higher than 6.5 kg Na$_2$O$_{eq}$/m^3 of concrete, and may thus be used in combination with all Norwegian concrete aggregates up to this documented alkali limit.

The influence on ASR from addition of different filler types produced from alkali reactive rock types was the issue of the PhD work of Bård Pedersen [19,20]. Selected results are given in Figure 7. The alkali content in all mixes was 5.0 kg Na$_2$O$_{eq}$/m^3 of concrete (excl. alkalis in the fly ash, in which constitute about 0.9 kg Na$_2$O$_{eq}$/m^3 of concrete). As shown, addition of about 85 kg filler per m^3 (of concrete) produced from Icelandic Rhyolite (earlier proven to be pozzolanic and thus able to mitigate ASR [28]) or recycled bottle glass (mitigation effect on ASR debated [19]), as well as addition of about 75 kg fly ash per m^3 of concrete (constitutes about 16 % of the binder), were able to suppress ASR below the critical expansion limit. The fly ash applied is the same type as included in the Norcem fly ash cement (see Figure 6). In contrast, none of the Norwegian filler types were able to suppress ASR. They all led to higher expansion than the reference mix added filler made of a non-reactive gneiss/granite.
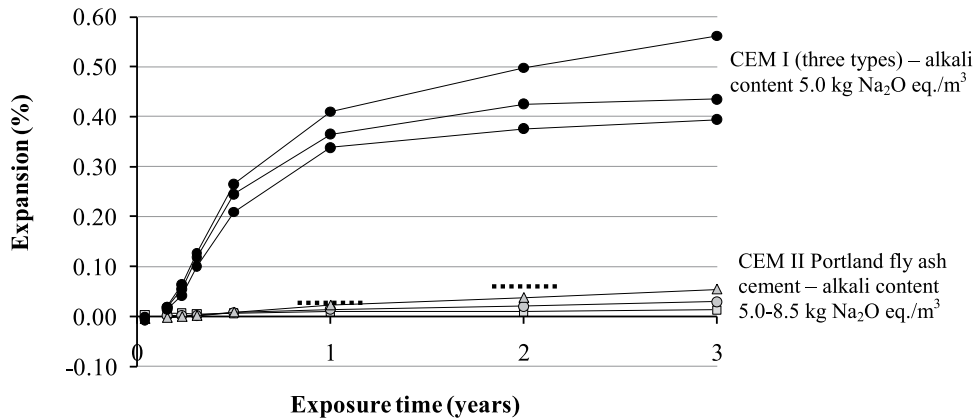
Figure 6 - Expansion versus exposure time for six binders tested with the aggregate combination Reference-I (non-reactive fine) + Reference-II (reactive coarse) - see Table 1. The CEM II Portland - fly ash cement contains 20 % PFA (80 kg/m³ of concrete). The dotted lines drawn at 1 and 2 years, respectively, represent critical limits for concretes with binders containing fly ash, condensed silica fume or ggbfs.

Figure 7 - Expansion versus exposure time for concretes containing different fillers (0/0.125 mm) and a reactive mylonite aggregate [19,20]. The number in ( ) is kg filler per m³ of concrete. The alkali content in all mixes was about 5.0 kg Na_2O_{eq}/m^3 of concrete. The dotted lines drawn at 1 and 2 years, respectively, represent Norwegian critical limits for concretes with binders containing fly ash, condensed silica fume or ggbfs.
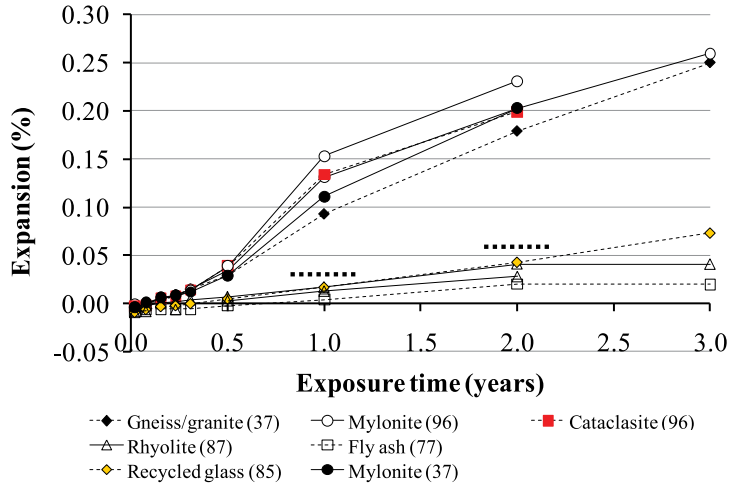
The Figures 6 and 7 show examples of application of the Norwegian performance test. Even though a one year testing time is required (two years for special binders – see section 1.2),

Norwegian cement – and concrete producers have frequently performed such tests. The aim has been to achieve approval for using different binder combinations (e.g. a CEM II Portland – fly ash cement) and/or possible new pozzolanic material (e.g. fillers produced from reactive rock types) in combination with various alkali reactive Norwegian aggregates. In this way, a number of commercial concrete recipes may be pre-documented, giving the concrete producers flexibility with respect to fulfilling the ASR requirements in the Norwegian regulations.

Normally a reference "worst case" reactive aggregate combination is used in these performance tests [5], giving a general approval for using the tested binders in combination with all Norwegian alkali reactive aggregates, which in general are assumed to be less reactive than the reference reactive aggregate combinations (see Table 1) applied in the performance tests.

3.5   Critical alkali limit for different aggregate types

Some of the alkali reactive aggregate types in common use in Norway for concrete production, have been "performance tested" to determine the critical alkali limit in combination with CEM I binder. Results from such testing of four aggregate combinations are shown in Figure 8. The lines drawn in the figure at the alkali content 3.0 kg Na_2O_{eq}/m^3 of concrete and the expansion 0.050 %, respectively, represent the Norwegian critical limits for a fine/coarse aggregate combination combined with CEM I cements (see section 1.2).
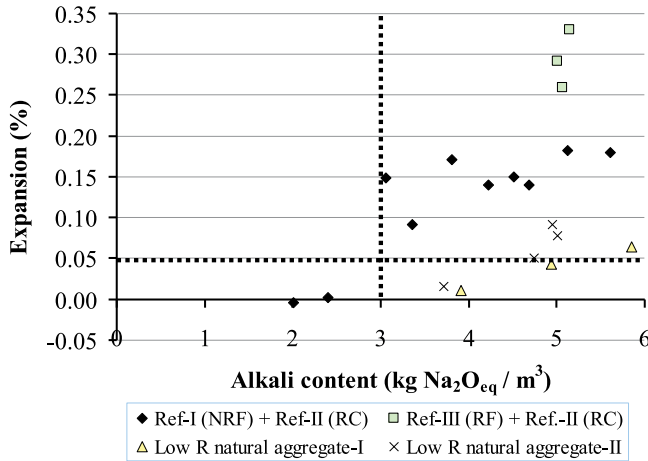
Figure 8 - Expansion versus alkali content for four Norwegian aggregate combinations after one year of exposure (R=Reactive, NR=Non-Reactive, F=Fine and C=Coarse aggregate). The dotted lines drawn at 3.0 kg Na_2O_{eq}/m^3 of concrete and 0.050 %, respectively, represent Norwegian critical limits.

One of the mixes with the highly reactive cataclasite ("Ref-II (RC)") revealed a disturbing high expansion at an alkali content of only 3.1 kg Na_2O_{eq}/m^3 of concrete. However, the cataclasite is very rarely used commercially in concrete, rather as a reference "worst case" coarse reactive aggregate [5]. Most alkali reactive aggregate types in common use in Norway are far less

reactive than this cataclasite. Thus, the general Norwegian acceptance alkali limit of 3.0 kg Na_2O_{eq}/m^3 of concrete for CEM I binders has been regarded as safe. Two examples of more moderate reactive Norwegian aggregates, with critical alkali limits between 4.5 and 4.8 kg Na_2O_{eq}/m^3 of concrete, respectively, are also shown in Figure 8.

3.6   Alkali leaching

According to Thomas et al. [7], the problem with alkali leaching from specimens stored over water in sealed specimens was first reported by Blanks and Meissner in 1946 [29]. They detected a build up of alkali ions in the water at the bottom of the containers in which mortar bars were stored, and explained this based on water condensing on the surface of the bars and running down the bars into the reservoir below, thereby providing transport of the alkalis. Due to this alkali leaching, the alkali content within the test prisms is reduced, leading to a drop in the pH of the pore water. Consequently, less silica is being dissolved from the aggregates and the extent of ASR is reduced, resulting in a too low prism expansion.

Several parameters may influence the extent of alkali leaching, among them prism size, storage conditions and concrete composition.

Tests performed by Bakker in the early 80'ties [30] showed that the larger the cross-section of a concrete prism, the greater the expansion, which was interpreted as being caused by higher extent of alkali leaching for the smaller specimens.

According to Bokern [31], intensive alkali leaching occurs in extremely humid conditions like in a fog chamber, as applied in the German CPT [32]. Even though prisms with a 100x100 mm cross section is applied, a loss of 20 % of a concretes initial soluble alkali content after 28 days and more than 30 % after 90 days is possible. Bokern [31] also states that concretes made of OPC or cement with ggbfs (20 %) seem to be particularly vulnerable to alkali leaching.

Rivard et al. [33] showed that for the same reactive mixture, concrete alkali leaching seemed to be greater for specimens containing higher alkali level (5.25 kg Na_2O_{eq}/m^3 of concrete) compared with specimens with lower alkali level (4.0 kg Na_2O_{eq}/m^3 of concrete). In these tests, the ASTM C 1293 CPT [25] was applied.

Figure 9 and 10 show the cumulative extent of alkali leaching for 30 SINTEF NCPT series. In Figure 9, the alkali content measured in the water in the bottom of the storage containers is recalculated to represent the reduction in alkali content in kg Na_2O_{eq}/m^3 of concrete compared to the total alkali content in the concrete at the time of mixing (includes all alkalis in the cement and in any mineral - and chemical admixtures, but excludes any alkalis that possibly may be released from the aggregates). Figure 10 shows a corresponding graph, but the reduction in alkali content is given as %. As can be seen, the rate of alkali leaching is highest the first three to six months of exposure. After one year of exposure, from 0.1 to 0.9 kg Na_2O_{eq} alkalis per m^3 of concrete are leached out from the prisms with size 100x100x450 mm, representing 2-17 % of the original alkali content in the concrete. Correspondingly, Thomas et al. [7] reported that 35 % of the alkalis originally in prisms of size 75x75x300 mm were leached out after 1 year, and as much as 20 % after just 90 days, i.e. about twice as much as the highest values from the NCPT prisms.

Figure 9 - NCPT; alkali content measured in the water in the bottom of storage containers, re-calculated to represent the reduction in alkali content in kg Na_2O_{eq}/m^3 of concrete compared to the total alkali content in the concrete at the time of mixing. The solid-drawn lines represent mixes in which NaOH is added to increase the alkali content. The dotted lines represent mixes without extra NaOH added. (* = "shotcrete")

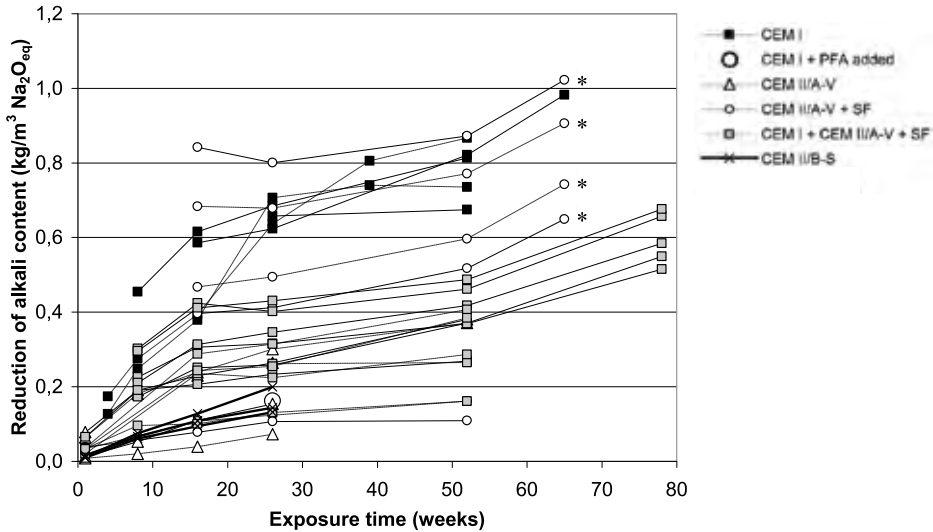*Figure 10 - NCPT; alkali content measured in the water in the bottom of storage containers, re-calculated to represent the reduction in alkali content in % compared to the total alkali content in the concrete at the time of mixing. The solid-drawn lines represent concrete mixes in which NaOH is added to increase the alkali content. The dotted lines represent concrete mixes without extra NaOH added. (* = "shotcrete")*
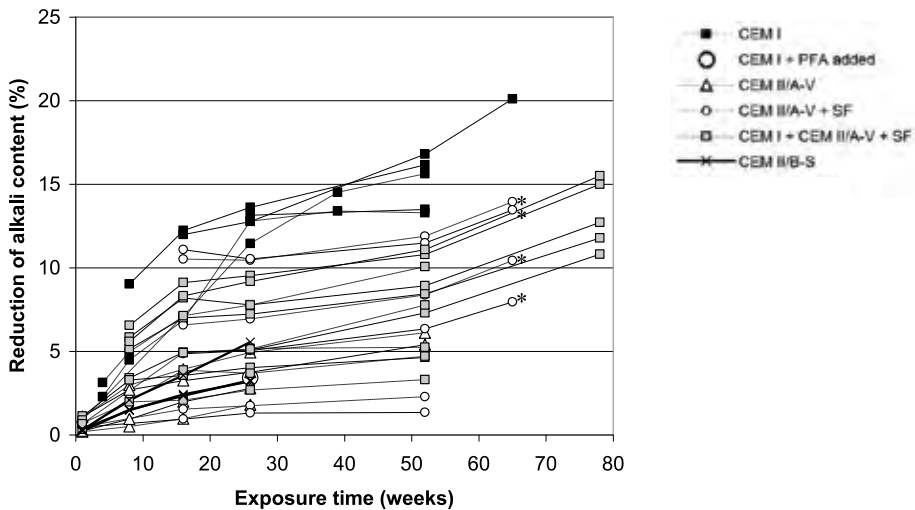
Any alkalis absorbed by the lining inside the storage containers are not included in the presented results. Later tests performed at SINTEF show that the extent of alkalis absorbed by the lining after one year of exposure constitutes less than 2.5 % of the total alkali content in the concrete at the time of mixing (CEM I, w/c-ratio 0.45).

Similar as Bokern [31] reported, OPC (CEM I) seems to be most vulnerable to alkali leaching, while some of the mixes with fly ash cement (CEM II/A-V) show the lowest extent of alkali leaching. Also mixes with the CEM II/B-S cement containing 33 % ggbfs show a low extent of alkali leaching (3-5 %) after 26 weeks of exposure.

Primarily due to higher binder content, some mortar prisms (simulating a shotcrete - marked with *) liberate relatively large amounts of alkalis to the water in the bottom of the storage container during the first 26 weeks of exposure (Figure 9). The alkali content in these mixes varied in the range 4.9-8.2 kg Na_2O_{eq}/m^3 of concrete. No alkali based accelerator was used, but the alkali content in some mixes was boosted by adding NaOH. In generals for all tests, no obvious differences in extent of alkali leaching were observed between concretes with – and without added NaOH.

The total extent of alkali leaching increases with time (see Figure 9) as the expansion does (see Figure 4). However, no tests are performed with aim to correlate the extent of alkali leaching versus total prism expansion applying the same binder type. Based on the tests performed (not focusing on alkali leaching), it is thus not possible to draw any conclusions regarding this relation. But, the extent of alkali leaching may be significant also for low expanding concretes. In some test series, up to 10 % of the alkalis present in the cement were leached out after one year of exposure, even though the prism expansion was lower than the critical expansion limit.

Most concretes tested had a water/binder ratio in the area 0.45-0.48. Thus, too little data is available to document the influence of water/binder ratio (i.e. changed diffusion properties) on the extent of alkali leaching.

In contrast to many laboratory results, the pore solution in field concrete is mostly not subject to alkali leaching (Rivard et al. [33]), except close to the concrete surface or close to any cracks. The problem with alkali leaching in many laboratory test methods is thus a big challenge. However, the presented results show that use of relatively large concrete prisms in the NCPT secure a rather low extent of alkali leaching compared to corresponding concrete prism tests applying smaller prisms. Still, the possible influence of alkali leaching on the measured expansions in the NCPT can not be neglected. Thus, the leaching issue should be looked further into.

As mentioned in section 1.2, no specific "safety factor" (beyond the 0.2 kg Na_2O_{eq}/m^3 alkalis of concrete discussed above) is so far included in the Norwegian regulations to compensate for any alkalis that may leach out from the concrete prisms during the one to two years exposure period. However, some extra security is already built in these regulations when testing binders, since most alkali reactive aggregate types in common use in Norway are far less reactive than the reference "worst case" alkali reactive aggregate combinations applied for performance testing of binders. In addition, most commercial concretes containing SCMs will normally contain less alkalis than the critical alkali limits documented for various binders. Norcem has also declared "upper alkali limits" for their cements to be used for calculating the concrete alkali content according to the Norwegian regulations.

4   CONCLUSIONS

During the last 15 years, about 160 performance tests have been performed by the two most experienced approved Norwegian laboratories at SINTEF (119) and Norcem (42). These tests include "job mixes" (i.e. real concrete recipes) and mixes to determine the critical alkali limit for different aggregate types. However, most of the performance tests have aimed at documenting different binder combinations ability to prevent ASR. In these tests, reference reactive aggregates are used. Based on the review of the results from these tests, the following conclusions may be drawn:

- Despite the long testing time required (1-2 years), the Norwegian system for performance testing has proven to be an advantageous and flexible tool to document critical alkali limits for binders and aggregates.
- The repeatability obtained at SINTEF for the Norwegian CPT is in general very good.
- In all parallel tests, SINTEF and Norcem produce results that are very close.
- In general, the expansion rates for all concrete mixes are highest in the first 0.5-2 years of exposure, before decreasing considerable or for several mixes become non-appearing. The main reason for this is assumed to be alkali leaching, combined with consumption of alkalis during the ASR. The expansion rates decrease earliest for the most alkali reactive mixes.
- Most approved non-reactive mixes still show an expansion below the critical expansion level(s) even up to 12 years of exposure.
- The prism weight increases with increasing expansions. In all SINTEF test series, the mean weight increase after one year was higher than 0.20 %, even for concrete mixes that shrunk. However, some of the mixes revealed a small weight loss during the first weeks.
- The review strengthens the importance of using weight measurements as a quality control of the moisture conditions within the storage containers.
- Even though one of the mixes with the highly reactive reference cataclasite (not in commercial use in concrete) revealed a disturbingly high one year expansion at an alkali content of only 3.1 kg Na_2O_{eq}/m^3 of concrete, the general Norwegian acceptance alkali limit of 3.0 kg Na_2O_{eq}/m^3 of concrete for CEM I binders in combination with all Norwegian aggregate types in common use has been regarded as a safe tool.
- By using the Norcem Standard-FA cement (CEM II/A-V), containing about 20 % PFA, a general acceptance alkali limit of 6.5 kg Na_2O_{eq}/m^3 of concrete (including all the alkalis in the fly ash) is approved in combination with all Norwegian aggregate types in common use.
- From 0.1 to 0.9 kg Na_2O_{eq} alkalis per m^3 of concrete are leached out of the NCPT prisms after one year of exposure, representing 2-17 % of the original concrete alkali content. The highest extent of alkali leaching measured from these NCPT prisms represents about half as much as reported from smaller prisms, e.g. as applied in ASTM C 1293 [25].
- The possible influence of alkali leaching on the measured expansions in the Norwegian CPT can not be neglected, even though rather large concrete prisms are used.
- No specific "safety factor" (beyond a "general safety factor") is included in the Norwegian regulations to compensate for any alkalis that may leach out from the prisms in the NCPT. However, some extra security is already built into these regulations when testing binders, since most alkali reactive aggregates in common use in Norway are far less reactive than the reference "worst case" alkali reactive aggregate combinations applied for performance testing of binders. In addition, most commercial concretes containing SCMs will normally contain less alkalis than the critical alkali limits documented for various binders. Norcem has also declared "upper alkali limits" for their cements to be used for calculating the concrete alkali content according to the Norwegian regulations.

5 ACKNOWLEDGEMENT

6 REFERENCES

1. RILEM, "AAR-1 - Detection of potential alkali-reactivity of aggregates – Petrographic method", *Materials and Structures*, Volume 36, 2003, pp. 480-496.
2. RILEM, "AAR-2 - Detection of potential alkali-reactivity of aggregates - the ultra-accelerated mortar bar test", *Materials and Structures*, Volume 33, 2000, pp. 283-289.
3. *CSA Standard*, "CAN3-A.23.2-M77 – Potential Expansivity of Cement Aggregate Combinations (Concrete Prism Expansion Method)", Supplement NO.2, 1986.
4. Norwegian Concrete Association, NB, "Durable concrete containing alkali reactive aggregates", *NB Publication* No. 21, Oslo, 2004, 34 p. including appendices.
5. Norwegian Concrete Association, NB, "Alkali aggregate reactions in concrete. Test methods and requirements to laboratories", *NB Publ.* No. 32, 2005, 39 p. incl. appendices.
6. Dahl, P.A., Lindgård, J., Danielsen, S.W., Hagby, C., Kompen, R., Pedersen, B. & Rønning, T.F., "Specifications and guidelines for production of AAR resistant concrete in Norway", in: Tang, M. and Deng, M. (Eds.), *Proceedings of the 12th International Conference on Alkali–Aggregate Reaction in Concrete*, Beijing, China, vol. 1, 2004, pp. 499–504.
7. Thomas, M., Fournier, B., Folliard, K., Ideker, J. & Shehata, M., "Test methods for evaluating preventive measures for controlling expansion due to alkali-silica reaction in concrete", *Cement and Concrete Research*, Volume 36, Issue 10, 2006, pp. 1842-1856.
8. CSA Standard A23.2-27A, "Standard practice to identify degree of alkali-reactivity of aggregates and to identify measures to avoid deleterious expansions in concrete", *CSA A23.2-00 Methods of Test for Concrete, Canadian Standards Association*, Toronto, Canada, 2000.
9. Allen Jr., C.L. & Brumfield, J.W., "Final report. ASR Benchmarking Workshop, August 2006", *Federal Highway Administration*, Washington D.C., USA, 2006.
10. Norwegian Concrete Association, NB, "Durable concrete containing alkali reactive aggregates", *NB Publication* No. 21, 1996, 32 p. including appendices. (In Norwegian).
11. *Norwegian Committee for Standardization*, NS-EN 206-1:2001, "Concrete Part 1: Specification, performance, production and conformity", (Amendment, in Norwegian, prA1:2003 incorporated), 2003, 90 p.
12. Lindgård, J. & Wigum, B.J., "Alkali Aggregate Reaction in Concrete – Field experiences", *SINTEF report* no. STF22 A02616, 2003, 127 p. + appendices. (In Norwegian).
13. Lindgård, J., Wigum, B.J., Haugen, M. & Skjølsvold, O., "Field experience from investigation of more than 100 Norwegian bridges with respect to Alkali Aggregate Reactions (AAR)", *Nordic Concrete Research*, No. 2/2004, pp. 114-128.
14. Lundevall, G., "Ressursvennlig Kvalitetsbetong, Bestandighet av betong, Alkalireaktivitet – Alkaligrenser", *Report 9D4/R97018 Norcem R&D*, Brevik, 1997, 16 p. + 4 appendices. (In Norwegian).
15. Bremseth, S.K., "Resultater av funksjonsprøving av alkalireaktiv sand, ikke-reaktiv stein og bindemiddel av CEM I og Norcem StdFA-sement", *Report 9D4/R05015, Norcem R&D*, Brevik, 2005, 9 p. (In Norwegian).
16. Bremseth, S.K., "Funksjonstest av betongprismer ifm ny FA fra Vliegasunie", *Report 9D4/R06031, Norcem R&D*, Brevik, 2006, 7 p. + 4 appendices. (In Norwegian).

17. Bremseth, S.K., "Resultater ifm langtidsforsøk i felt, sjø og 38°C i prosjektet Ressursvennlig Kvalitetsbetong", *Report 9D4/R08001, Norcem R&D*, Brevik, 2008, 10 p. + 8 appendices. (In Norwegian).
18. Kjellsen, K.O., Rønning, T.F. & Meland, I., "Prevention of Deleterious Alkali Aggregate reactions by use of Norwegian Portland fly Ash Cement", paper to the *Workshop "Durability of Exposed Concrete Containing Secondary Cementitious Materials"*, Hirtshals Denmark, 2001, 10 p. + 2 appendices.
19. Pedersen, B., "Alkali-reactive and inert fillers in concrete. Rheology of fresh mixtures and expansive reactions", *Doctoral Theses at NTNU* 2004:92, Trondheim, Norway, 2004, 198 p. + appendices.
20. Pedersen, B., "Effect of alkali-reactive crushed fillers on expansions due to ASR", in: Tang, M. and Deng, M. (Eds.), *Proceedings of the 12th International Conference on Alkali–Aggregate Reaction in Concrete*, Beijing, China, vol. 2, 2004, pp. 764–772.
21. Lindgård, J., Nixon, P.J., Borchers, I., Schouenborg, B., Wigum, B.J., Haugen, M. & Åkesson, U., "The EU "PARTNER" Project — European standard tests to prevent alkali reactions in aggregates: Final results and recommendations", *Cement and Concrete Research* 40, 2010, pp. 611-635.
22. Nixon, P. & Lane, S., "PARTNER Report No. 3.3: Experience from testing of the alkali reactivity of European aggregates according to several concrete prism test methods", *SINTEF Report* SBF52 A06021/ISBN 82-14-04081-7/978-82-14-04081-7, Trondheim, Norway, 2006, 35 p. + appendices.
23. RILEM, "AAR-3 - Detection of potential alkali-reactivity of aggregates - Method for aggregate combinations using concrete prisms", *Materials and Structures* 33, 2000, pp. 290-293.
24. *RILEM*, "AAR-4 - Detection of potential alkali-reactivity of aggregates: Accelerated (60°C) concrete prism test", draft 2006 (not published).
25. *ASTM International*, C 1293 – 08b, "Standard Test Method for Determination of Length Change of Concrete Due to Alkali-Silica Reaction", United States, 2008, 7 p.
26. *ISO* 5725-94, "Precision of test methods – determination of repeatability and reproducibility for a standard test method by inter-laboratory testing", 1994.
27. Internal Norcem results (not published yet).
28. Gudmundssson, G., "Investigations on Icelandic pozzolans", proceedings of the *Symposium on Alkali-Aggregate Reactions, preventive measures*, Reykjavik, Iceland, 1975.
29. Blanks, R.F. and Meissner, H.S., "The expansion test as a measure of alkali-aggregate reaction", *Journal of the American Concrete Institute* 17 (5), 1946, pp. 517–539.
30. Bakker, R.F.M., "The influence of test specimen dimensions on the expansion of alkali reactive aggregate in concrete", in: Idorn, G.M. and Rostam, S. (Eds.), *Proceedings of the 6th International Conference on Alkali-Aggregate Reaction in Concrete*, Denmark, 1983, pp. 369-375.
31. Bokern, J., "Concrete tests for ASR assessment: Effects of testing environment on preconditions for an ASR and transferability of test results", in: Broekmans, M.A.T.M. and Wigum, B.J. (Eds.), *Proceedings of the 13th International Conference on Alkali-Aggregate Reactions in Concrete*, Trondheim, Norway, 2008, pp. 511-520.
32. *Deutscher Ausschuss für Stahlbeton*, DAfStb (ed.), "Vorbeugende Maßnahmen gegen schädigende Alkalireaktion im Beton: Alkali-Richtlinie", Beuth, Berlin, 2001, (DAfStb-Richtlinie).
33. Rivard, P., Bérubé, M.A., Ollivier, J.P. and Ballivy, G., "Decrease of pore solution alkalinity in concrete tested for alkali-silica reaction", *Materials and Structures* 40, 2007, pp. 909–921.

Fly ash–limestone ternary composite cements: synergetic effect at 28 days.

Klaartje De Weerdt
M.Sc., Ph.D.-student
SINTEF Building and Infrastructure
NO-7465 Trondheim
E-mail: klaartje.de.weerdt@sintef.no

Harald Justnes
Ph.D., Adjunct Professor NTNU
SINTEF Building and Infrastructure
NO-7465 Trondheim
E-mail: harald.justnes@sintef.no

Knut O. Kjellsen
Ph.D., Adjunct Professor NTNU
Norcem Heidelberg Cement
NO-3908 Brevik
E-mail: knut.kjellsen@norcem.no

Erik Sellevold
Professor NTNU
Departement of Structural Engineering
NO-7491 Trondheim
Email: erik.sellevold@bygg.ntnu.no

ABSTRACT

Composite cements containing OPC, fly ash and limestone powder were tested in paste and mortar after 28 days of curing at 20ºC to verify a postulate claiming that calcium aluminate hydrates produced by the pozzolanic reaction of fly ash would react further with limestone to form calcium carboaluminate hydrates and thereby increase the total amount of hydrates and consequently strength. Thermogravimetric tests indicated indeed a change in hydration products when limestone powder was included in the system. This was also confirmed by X-ray diffraction showing the formation of calcium carboaluminate hydrates. It was demonstrated that this synergetic interaction between fly ash and limestone increases the compressive strength more than cement replacement by limestone alone.

Key words: ternary cement, fly ash, limestone, carboaluminate hydrate

1   INTRODUCTION

During cement production large amounts of CO_2 are emitted. In 2000, about 0.87 ton CO_2 per ton clinker was emitted on average, about 40% coming from fuel combustion, grinding and other operations, and 60% from the de-carbonation of limestone to form the clinker phases [1]. In order to reduce these emissions, cement factories have switched over to larger fractions of alternative fuels, optimized energy consumption (e.g. regeneration of heat, optimized the clinker with mineralisers, etc) [2].

The fact that, in the future, emitting CO_2 will come at a price, gives the cement producers a new incentive to reduce the emissions even more. One way of doing that on a short term is by replacing part of the clinker with other materials such as slag, limestone powder, fly ash, silica fume, natural pozzolans etc [3]. The type of replacement materials used depends on their availability (amount available, price, transportation …) and is therefore dependent on the geographical location of the cement plant.

The aim of this study is to contribute to the development of a novel all-round Portland composite cement for the Norwegian market. Currently the cements produced at the Norwegian cement plants are: CEM I [4] Portland cements containing up to 5% limestone powder and CEM II/A-V [4] Portland fly ash cements containing up to 20% fly ash but no limestone powder. In this study, the effect of increasing the replacement levels of the ordinary Portland cement (OPC) (up to 35%), and combining fly ash and limestone powder to replace OPC are investigated.

Limestone powder is known to accelerate the hydration of cement, especially the C_3S phase, by acting as nucleation surface for portlandite and CSH precipitation [5-7]. The accelerating effect can give rise to a slightly higher compressive strength at early age at moderate OPC replacements (<10%). At later age, replacing part of the OPC with limestone powder may result in a strength reduction, due to the replacement of the more reactive component, OPC, with less or non reactive one [8]. This effect is referred to as the dilution effect. Besides this physical effect, the calcium carbonate of the limestone powder is also known to interact with the aluminate phases of OPC [7, 9-13]. In the presence of small amounts of limestone powder, monosulphoaluminate hydrate is replaced by mono- or hemicarboaluminate hydrate and more ettringite. Due to this change in hydration products the volume of the hydration products formed can increase slightly [12-14]. This can in its turn lead to a slight increase in strength and a decrease in permeability. The effect is however limited due to the small amount of aluminate present in the OPC.

ASTM Class F fly ash [15] is a slow reacting pozzolan. It can take up to several weeks before it starts to react significantly at 20°C. The fly ash will not react noticeably during the so-called "incubation period" the length of which is believed to depend mainly on the alkalinity of the pore water [16, 17] and therefore also on the type of cement used [18]. Fly ash reduces early strength due to the dilution effect. However, it can contribute to a higher long-term strength, due to its pozzolanic reaction.

When combining limestone powder and fly ash, a synergetic effect between the two is expected to take place. Fly ash is an aluminate rich pozzolan, as it reacts it will introduce additional aluminates to the system, thereby decreasing the SO_3/Al_2O_3 ratio and amplifying the impact of the limestone powder on the hydration products. The increase of bound water and compressive strength gain resulting from a minor limestone powder addition is therefore is expected to be

greater for fly ash containing cements than for OPC. This was first postulated in the COIN application in 2005 (www.coinweb.no). The goal of the study is to validate this postulate concerning the synergetic effect between limestone powder and fly ash.

A preliminary study on fly ash-limestone-calcium hydroxide-alkaline solution [19]: showed a clear interaction between fly ash and limestone powder. More water was bound relative to the fly ash content and the hydration products formed were proven to contain calcium carboaluminate hydrate.

In literature many studies can be found on composite cements containing limestone powder and slag [20, 21], limestone powder and natural pozzolans [22] and even limestone powder and fly ash [23-26] have been investigated. However, these studies focused on heat of hydration, strength and durability, whereas the chemical interaction between the different components was not studied [24]. An exception is Hoshino at al. [27] who studied the addition of limestone powder to slag cements and linked the changes in the hydration phases observed by XRD with the increase in compressive strength. To the author's knowledge, the hydration mechanisms of composite cements containing both limestone powder and fly ash have not been fully investigated yet.

2   EXPERIMENTAL

2.1   Materials

The materials used in this project were: CEM I clinker, siliceous fly ash, limestone powder and natural gypsum. The composition of clinker, fly ash and limestone used as well as their density and specific surface are listed in Table 1. Table 2 gives the mineral composition of the clinker determined by Rietveld analysis. The clinker was interground with 3.7% of gypsum to form OPC, so that the total SO_3 content would be about 3% including the sulphates of the clinker. The gypsum contained 0.18% free water, and had a $CaSO_4 \cdot 2H_2O$ content of 91.39%. The particle size distribution of the different materials was determined with a Mastersizer from Malvern. The results are shown in Figure 1.

Table 1: *Chemical composition, density and Blaine specific surface of the clinker, fly ash and limestone powder*

	Clinker	Fly ash	Limestone
SiO_2	20.8	50.0	12.9
Al_2O_3	5.6	23.9	2.7
Fe_2O_3	3.2	6.0	2.0
CaO	63.0	6.3	42.3
MgO	3.0	2.1	1.8
SO_3	1.5	0.4	-
P_2O_5	0.1	1.1	-
K_2O	1.3	1.4	0.6
Na_2O	0.5	0.6	0.5
Na_2O Eq.	1.4	1.6	
LOI	0.3	3.6	37.7
Carbon	-	3.1	-
Chloride	0.05	-	-
Free CaO	1.9	-	-
Density [kg/m^3]	3150*	2490	2740
Blaine specific surface [m^2/kg]	500*	470	810

* for OPC = clinker + gypsum

Table 2: *Mineral composition of the clinker determined by Rietveld analysis*

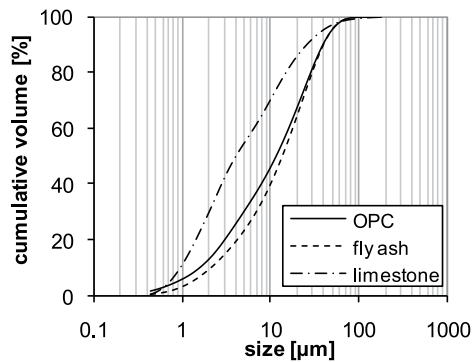| Minerals	%
C_2S	19
C_3S	54
C_3A	11
C_4AF	8

Figure 1: The particle size distribution of the materials used in this study determined by laser diffraction.

2.2 Testing

Table 3 shows the different composite cements which were tested. The experimental matrix can be divided into three main groups, together with the reference (mix 1). In the first group, OPC is gradually replaced by limestone powder, starting at 5% up to 35% in steps of 5% (mix 2 to mix 8). In the second group OPC is similarly replaced with fly ash (mix 9 to mix 15). In the third group different limestone powder and fly ash combinations were tested (mix 16 – mix 21) at a constant OPC replacement level of 35%, which is the potential replacement level for future commercial cements produced in Norway.

Table 3:   Composite cement combinations tested (replacement by mass)

mix	OPC	fly ash	limestone
1	100	/	0
2	95	/	5
3	90	/	10
4	85	/	15
5	80	/	20
6	75	/	25
7	70	/	30
8	65	/	35
9	95	5	/
10	90	10	/
11	85	15	/
12	80	20	/
13	75	25	/
14	70	30	/
15	65	35	/
16	65	30	5
17	65	25	10
18	65	20	15
19	65	15	20
20	65	10	25
21	65	5	30

The replacements are done by mass as this is most relevant for cement production. The aim of the study is to develop an all-round Portland composite cement which will be used at fixed w/c ratio's. Furthermore, additional tests showed little difference in compressive and flexural strength when OPC was replaced with crystalline quartz (considered inert material) either by mass or by volume (see Figure 2).
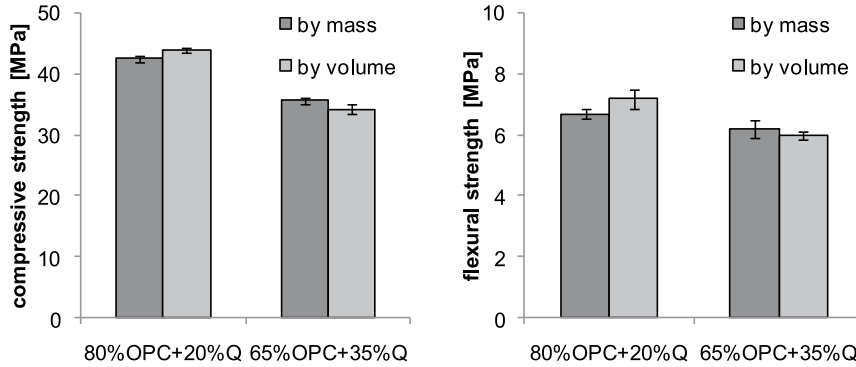
Figure 2: Comparison of the effect of replacement by mass and by volume on 28 day compressive and flexural strength results for two different combinations of OPC and crystalline quartz, Q (density 2700kg/m³).

Three mortar prisms of 40×40×160 mm were prepared for all the tested combinations according to NS-EN 196-1 (water-to-powder ratio 0.50, powder : sand = 1:3). The flexural and compressive strength was determined after 28 days of curing submerged in saturated lime water.

The volume of air voids in the mortars was determined according to [28]. The mortar samples are first dried in an oven at 105ºC for 1 week. Then their dry mass is determined. After this the samples are submerged in water for a week. When weighing the samples after this, the amount of water taken up due to capillary suction can be determined. During the last step of the procedure the samples are put into a pressure tank at 50 MPa for 2 days. From the mass of the samples weighed immediately after removing them from the pressure tank, one can calculate the volume of air voids in the samples assuming that the air voids fill under pressure, but can not fill by capillary suction due to their large radius.

The volume of air voids of the mortar samples was determined in order to take into account their effect on the compressive strength. The rule of thumb applied, is that a 1% increase in air void volume will lead to a 5% decrease in compressive strength [29]. The results were corrected relative to the average air porosity.

For all tested combinations, 300 ml of paste was made with a water-powder ratio of 0.50. The mixing water was distilled water. No admixtures were used, as all pastes were stable and mixable at this water-to- powder ratio. The pastes were mixed with a Braun MR5550CA high shear mixer. The mixing procedure consisted of mixing for half a minute, resting for five minutes and mixing again for one minute. The paste was poured into 15 ml glass vials and was stored under sealed conditions at 20°C.
To stop the hydration after 28 days, a sample of paste was crushed and washed twice with 150 ml ethanol. The suspension was filtrated. The remaining wet slurry was then poured into a glass vial which was sealed with a plastic lid to avoid evaporation of the ethanol.

Simultaneous TGA/SDTA analyses were performed on these wet slurries with a Mettler Toledo TGA/SDTA851. Samples of about 200mg were weighed into aluminium oxide crucibles. The samples were first dried inside the TGA/SDTA by purging them with N_2 for about 2 hours at 40ºC. The weight of the sample was monitored during drying and the analysis was started when

approximately constant weight was reached. This is however not a defined equilibrium condition. One might prefer to dry the samples at a certain RH until equilibrium is reached, but this might lead to carbonation during the handling the samples. By drying the samples in the TGA apparatus, carbonation could be limited to a minimum.

After this the samples were heated from 40ºC to 1,100ºC at a heating rate of 10ºC/min. During the analysis the oven was purged with N_2 at 50ml/min.

During a thermogravimetric analysis (TGA), the weight of the sample is monitored as a function of the temperature. The weight loss observed when the sample is heated from room temperature up to about 600ºC is due to the release of water bound in hydrates (H). Between 450ºC and 550ºC, a sharp weight loss step occurs. This is due to the decomposition of calcium hydroxide (CH). At temperatures above 600ºC carbonates decompose and weight losses are registered as the sample releases CO_2. The carbonates can originate from limestone powder if the sample contained limestone, any dehydrated calcium carboaluminate hydrate formed and/or carbonates which could have formed due to carbonation of the sample.

The weight losses were determined in two different temperature intervals. The weight loss due to the decomposition of CH, ranging from about 450ºC to 550ºC, and the weight loss corresponding to the release of bound water (H), measured between 50°C and about 550-600ºC. The start and ending of each temperature interval is determined for each sample based on the DTG-curve.

The standard deviation for the thermogravimetric measurements are 0.3% for the H measurements and 0.05% for the CH measurements. This data is based on the results of three independent experiments.

The weight losses are expressed as a % of the "dry sample mass" or OPC content. The "dry sample mass" is the weight at 600°C.

For some mixes of particular interest small amounts were dried gently over $CaCl_2$ in order to analyse them with an AXS D8 focus X-ray diffractometer. The diffractometer had a CuKα source and a 0.2 mm slit was used. An angular scan was performed for diffraction angles between 5 and 75° 2θ with an increment of 0.04° 2θ and a scanning speed of 0.3 s/step. The XRD-spectra give a qualitative idea of the crystalline hydration products formed, not a quantitative. The spectra are given as a function of the characteristic lattice distance, d.

3   RESULTS AND DISCUSSION

In
Table *4* the compressive and flexural strength, the air porosity and the corrected compressive strength for all tested combinations are given. One can see that fly ash containing cements have a tendency to lower the air content in the mortars. For limestone powder the opposite seems to be the case. This might be due to the effect of these materials on the compactibility of the mortars. Round fly ash particles are known to improve workability and fine limestone powder is known to stabilize and thicken mortars and concretes. By correcting the compressive strength for the air voids, the strength of the fly ash containing mixes is slightly reduced and the limestone containing blends is slightly increased. The trends observed in the results however do

not change whether or not the compressive strength is correct for the air content. For the following discussion the not-corrected results will be used.

Table 4: *The mean value and standard deviation of the compressive and flexural strength, the air porosity and the corrected compressive strength for all tested combinations after 28 days of curing at 20°C.*

mix	C	F	L	flexural			compressive			air porosity			compressive difference	corrected
	[%]			[MPa]			[MPa]			[%]			[%]	[MPa]
1	100	0	0	7.1	±	0.3	48.3	±	0.7	2.6	±	0.2	3.4	49.9
2	95	0	5	7.7	±	0.1	49.7	±	0.3	2.7	±	0.0	4.1	51.8
3	90	0	10	7.7	±	0.3	48.8	±	0.4	2.4	±	0.1	2.5	50.0
4	85	0	15	7.8	±	0.2	48.1	±	0.4	2.2	±	0.2	1.7	48.9
5	80	0	20	7.3	±	0.1	46.1	±	0.3	2.1	±	0.1	0.8	46.5
6	75	0	25	6.8	±	0.2	42.9	±	0.3	2.6	±	0.1	3.4	44.3
7	70	0	30	7.1	±	0.2	40.7	±	0.4	2.4	±	0.1	2.6	41.7
8	65	0	35	6.6	±	0.2	37.6	±	0.4	2.5	±	0.1	2.8	38.6
9	95	5	0	8.0	±	0.1	49.7	±	0.8	1.8	±	0.2	-0.3	49.6
10	90	10	0	7.9	±	0.2	49.2	±	1.0	1.5	±	0.1	-2.3	48.1
11	85	15	0	7.8	±	0.3	46.5	±	0.6	1.4	±	0.1	-2.4	45.3
12	80	20	0	7.6	±	0.2	45.2	±	0.4	1.4	±	0.1	-2.4	44.1
13	75	25	0	7.1	±	0.5	42.9	±	1.0	1.4	±	0.1	-2.4	41.8
14	70	30	0	7.0	±	0.3	41.2	±	1.0	1.5	±	0.2	-1.9	40.4
15	65	35	0	6.2	±	0.4	38.8	±	0.7	1.4	±	0.1	-2.7	37.8
16	65	30	5	7.3	±	0.1	42.4	±	0.7	1.6	±	0.1	-1.3	41.8
17	65	25	10	7.3	±	0.2	41.3	±	0.5	1.6	±	0.0	-1.4	40.7
18	65	20	15	7.3	±	0.2	40.7	±	0.4	1.7	±	0.0	-1.1	40.3
19	65	15	20	6.6	±	0.2	39.9	±	0.5	1.6	±	0.1	-1.6	39.2
20	65	10	25	6.8	±	0.2	39.2	±	0.4	1.8	±	0.0	-0.7	39.0
21	65	5	30	6.3	±	0.1	38.2	±	0.4	1.8	±	0.1	-0.6	38.0

In Figure 3 the compressive strength of cements containing different amounts of either fly ash or limestone powder are given. It can be seen that part of the OPC can be replaced with limestone powder without impairing the compressive strength after 28 days of hydration (up to 15%). Replacing 5% of the OPC by limestone even increases the compressive strength. A similar effect is observed for the fly ash. This might partly be due to better compaction properties of the mortars contain fly ash as the strength increase disappears when the strength is corrected for the air content. It seems as if fly ash has not reacted that much since the compressive strength of the mortars containing fly ash is similar to the ones containing limestone powder.

The flexural strengths of cements containing different amounts of either fly ash or limestone powder are given in Figure 4. The relative standard deviations of the results are large, up to 7%. Even so it can be seen that replacing part of the OPC with limestone powder or fly ash improves the flexural strength up to replacement levels of about 20%.
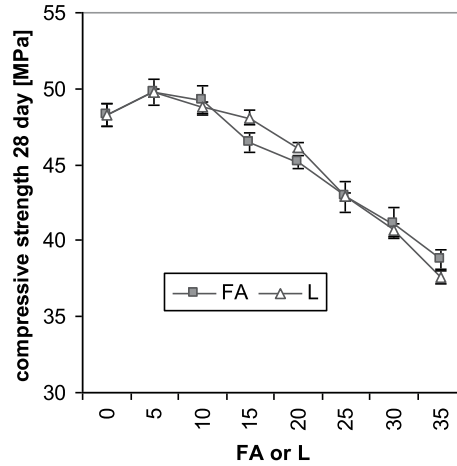
Figure 3: The 28 day compressive strength not-corrected for the air content for cements in which OPC is replaced by fly ash and limestone powder up to 35%.
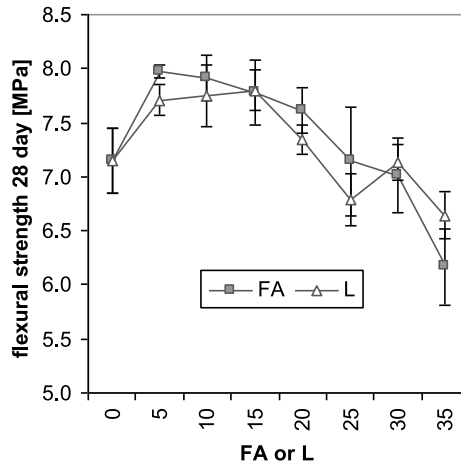

Figure 4: The 28 day flexural strength for cements in which OPC is replaced by fly ash and limestone powder up to 35%.

Figure 5 shows the compressive strength of composite cements in which 35% of the OPC is replaced by different combinations of fly ash and limestone powder. A significant compressive strength increase can be observed when instead of 35% fly ash, a combination of 5% limestone and 30% fly ash is used. This strength increase is about 4 MPa, which is approximately a 10% increase in compressive strength. This indicates that the postulated chemical synergic effect between fly ash and limestone plays a significant role. This beneficial effect on the compressive strength decreases with further increasing limestone powder content. In the corresponding flexural strength results a similar trend can be observed (see Figure 6).
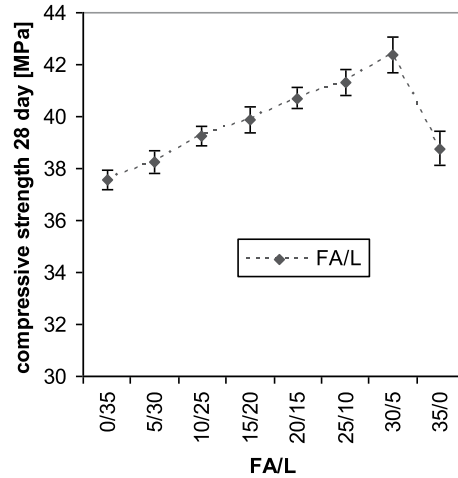
Figure 5:   The 28 day compressive strength for composite cements containing 65% OPC and different combination of fly ash and limestone powder.
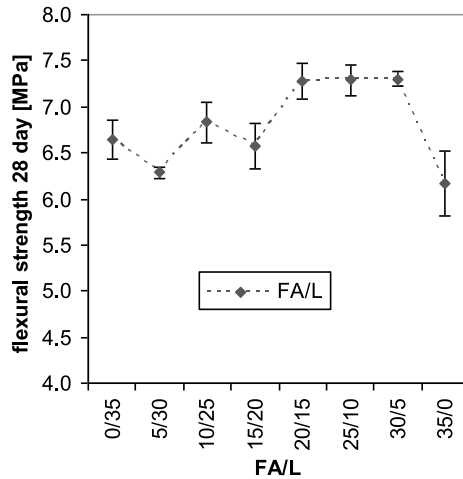

Figure 6:   The 28 day flexural strength for composite cements containing 65% OPC and different combination of fly ash and limestone powder.

The compressive strength results of the cements with only fly ash are compared with those of the composite cements containing different combinations of fly ash and limestone powder in Figure 7.

The fly ash curve with filled squares (FA) represents the compressive strength results for cements in which the OPC is replaced only by fly ash. The replacement levels go from 0% in the left of the graph to 35% in the right side in steps of 5%. The dotted with black diamonds (FA+L) represents cements containing 65%OPC and 35% of different combination of fly ash and limestone.

An interesting result is the fact that cement containing 30% fly ash and 70% OPC has a slightly lower compressive strength after 28 days than a cement containing 30% fly ash, 5% limestone and 65% OPC. This means that in this case replacing 5% of the OPC with 5% limestone powder results in a slightly higher compressive strength after 28 days. This result shows that the cement producers could burn 5% less clinker and instead add limestone powder. This is both economically and environmentally beneficial, as less energy is needed and less CO_2 will be emitted.
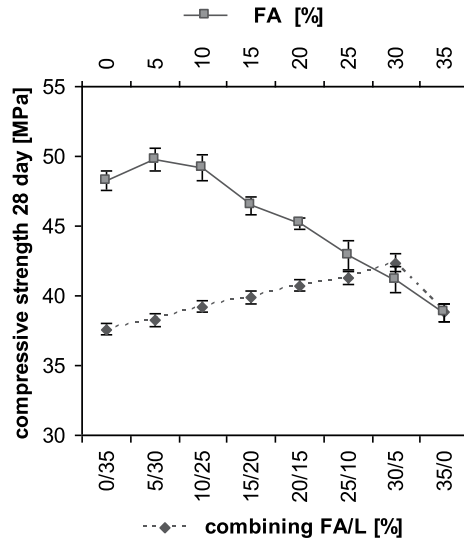

Figure 7:   Comparing the 28 day compressive strength of the composite cements with different combination of fly ash and limestone powder and 65% OPC (lower abscissa), and the cements in which OPC is gradually replaced by fly ash (upper abscissa). Different abscissae were used to be able to compare cements with different OPC content and evaluate whether part of the OPC can be replaced by limestone powder without impairing the strength.

In Figure 8 the compressive strength results are compared with the thermogravimetric (TG) results for different replacement levels of OPC with limestone powder.

The decrease in calcium hydroxide per *dry content*, when the OPC is increasingly replaced by limestone powder, is due to the dilution effect. OPC is the major reactive component, and as the amount of OPC decreases in the sample the amount of reaction products, such as CSH and CH, will also decrease.

More interesting is the observation that the amount of CH per *OPC content* decreases slightly when 5% and even 10% of OPC is replaced by limestone powder. Due to the filler effect of the limestone powder one would expect that the amount of CH would increase, but the amount of produced CH only starts to increase when 15% or more of the OPC is replaced by limestone powder.

When 5 % of OPC is replaced by limestone powder, the amount of bound water (H) per OPC and the compressive strength increases, but the CH content decreases. A strength increase should correspond to an increase in hydration products formed (H). Assuming the following reaction for the hydration of the main OPC mineral alite (C_3S):

$$C_3S + 2.3\ H \rightarrow C_{1.7}SH + 1.3\ CH \qquad (1)$$
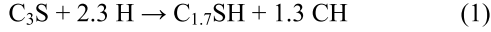
According to equation 1, a strength increase caused by an increase of hydration products like CSH would also implicate an increase in CH if the C/S of CSH remains constant. A decrease in the amount of CH and a corresponding increase in strength can only be explained by either the formation of CSH with a higher C/S ratio or the formation of other hydration products (e.g. alumina or iron rich hydration products) consuming CH.

The decrease in calcium hydroxide can be explained by the formation of calcium hemicarboaluminate hydrate ($C_3A \cdot 0.5CaCO_3 \cdot 0.5Ca(OH)_2 \cdot 11.5H_2O$) that in accordance with the formula will consume half a mole $Ca(OH)_2$ per mole $CaCO_3$ [7, 11, 27].

The amount of chemically bound water gives an indication about the degree of hydration, and therefore also for the strength development for a given cement. The compressive strength and amount of chemically bound water follow the same trend as they both increase when 5% of the OPC is replaced by limestone powder. For higher replacement levels (>5%) both properties decrease steadily (see Figure 8).

Figure 8: *Comparison between the compressive strength and the amount of calcium hydroxide (CH) and bound water (H) both relative to the dry samples mass and the OPC content for limestone cements after 28 days of curing at 20°C.*

In Figure 9 the compressive strength results are compared with the thermogravimetric (TG) results for different replacement levels of OPC with fly ash.

The amount of calcium hydroxide (CH) is given both relative to the dry sample mass and to the OPC content. The amount of CH relative to the dry sample mass, decreases due to the dilution effect. The amount of CH relative to the OPC content on the other hand increases due to the filler effect. Fly ash can react with the CH in a pozzolanic reaction and form hydration products similar to the ones of OPC. From the compressive strength results, it appeared that fly ash had

not reacted that much after 28 days of curing at 20°C. The strength of the fly ash cements was similar to the corresponding limestone cements. The amount of CH relative to the OPC content flattens out at replacement levels above 15% and even decreases a bit at 35%. This might indicate that the fly ash has reacted somewhat. As more fly ash is present some more CH has been consumed.

The compressive strength is compared with the amount of bound water in Figure 9. The results correlate quite well as both the compressive strength and amount of chemically bound water are quite similar for the reference up to the one containing 10% fly ash but then decrease with increasing replacement level. The decreasing trend is due to the dilution effect. The filler effect on the other hand is visible when the amount of chemically bound water is expressed relative to the amount of OPC. The amount of chemically bound water relative to the OPC content increases with increasing OPC replacement.

In Figure 10 and Figure 11 the compressive strength results are compared with the thermogravimetric (TG) results for different combinations of fly ash and limestone powder replacing 35% of the OPC.

When 5% to 15% of the fly ash is replaced by limestone, the amount of CH decreases compared to the cement with 35% fly ash. Initially one would expect the opposite as the fly ash should consume CH during its pozzolanic reaction. Therefore a higher amount of fly ash should lead to less CH. The amount of produced CH starts to increase only when 20% of the limestone powder or more is included in the system. The decrease in CH is accompanied by an increase in compressive strength. The reason is probably, as described for OPC/limestone, that calcium hemicarboaluminate hydrate is formed.
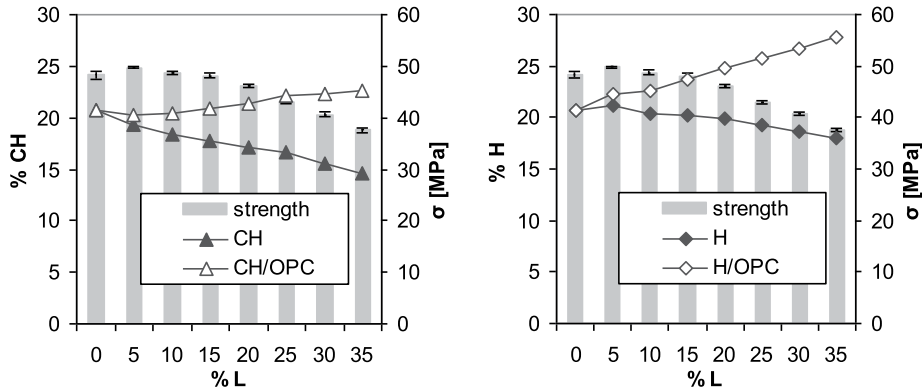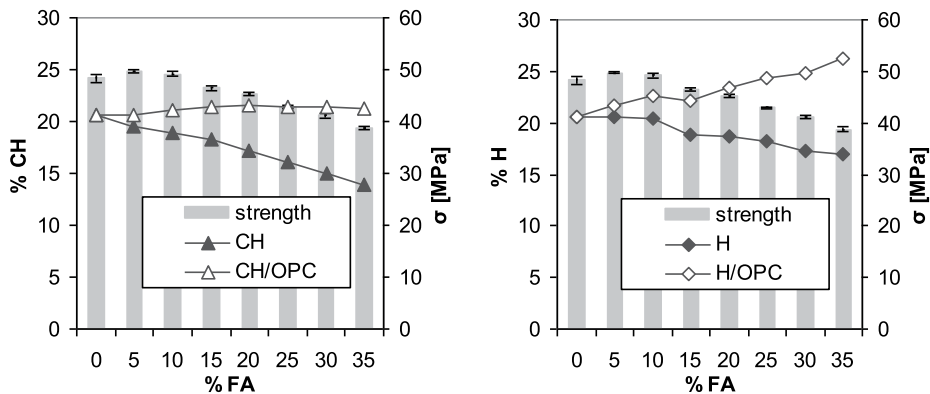

Figure 9:   Comparison between the compressive strength and the amount of calcium hydroxide (CH) and bound water (H) both relative to the dry samples mass and the OPC content for fly ash cements after 28 days of curing at 20°C.
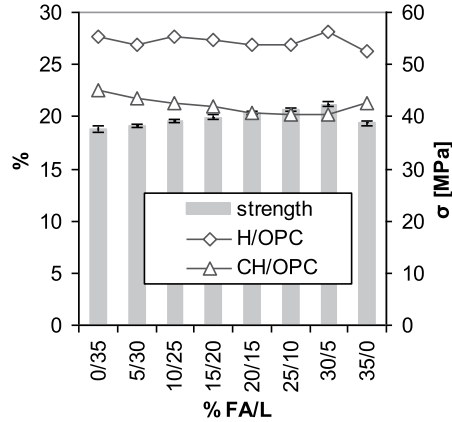
Figure 10: Comparison between the compressive strength and the amount of calcium hydroxide (CH) and bound water (H) relative to the OPC content for composite cements containing 65% OPC and a combination of fly ash and limestone powder after 28 days of curing at 20°C.
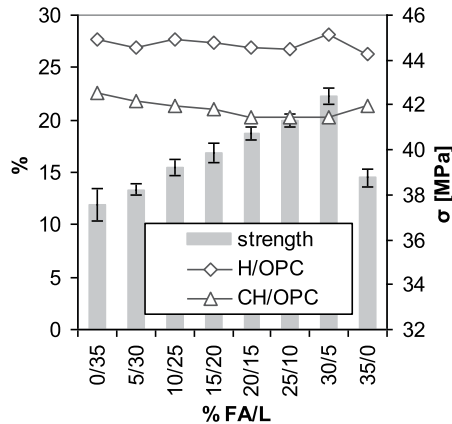
Figure 11: Magnification of the ordinate in Figure 10 in order to visualize the synergetic effect better.

From the previous results it can be concluded that an interesting phenomenon occurs when small amounts of limestone are used to replace both ordinary Portland cement and fly ash cement. The amount of CH decreases and the compressive strength increases. The effect on the fly ash cement seemed to be stronger than on the OPC, although the fly ash had not react that much. The thermogravimetric curves (TG-curves) and the differential thermogravimetric curves (DTG-curves) of some interesting combinations were compared in order to understand this phenomenon better. In Figure 12 the TG and DTG are depicted for 100%OPC cement and 100%OPC+5%L. Figure 13 shows the corresponding curves for 65%OPC+35%FA and 65%OPC+30%FA+5%L.

From Figure 12 it can be seen that the limestone containing cement binds about the same amount of water than the reference, as they reach about the same total weight loss at about

600°C. Some differences can be seen between the DTG-curves of the two cements. First there is the peak just above 100°C. This peak is partly due to the decomposition of ettringite. Limestone powder seems to stabilize the ettringite as expected. This peak should however always be interpreted with care as it is very sensitive to the preparation of the samples and the pre-drying. Secondly there is dissimilarity between 600°C and 800°C. This is due to the decomposition of the $CaCO_3$ present in the limestone powder. A remarkable difference between the two curves is the double peak for the reference around 180°C, which turns into a single peak when limestone is included in the system. The curves are also different between 200 and 400°C. The differences indicate that there is a change in hydration products when limestone powder is included in the system.

From Figure 13 it can be seen that when 5% of the fly ash is replaced by limestone powder more water is bound, as the total weight loss at about 600°C is larger. The DTG curves are fairly similar to the once shown in Figure 12, except for the weight changes at 750°C and higher, caused by the fly ash present in the system and the lower content of calcium hydroxide (between 400 and 500°C) due to the both dilution effect and slight pozzolanic reaction of the fly ash. Once more, the double peak around 180°C shown for the fly ash cement without limestone powder, turns into a single peak when limestone is included in the system and the ettringite appears to be stabilized.
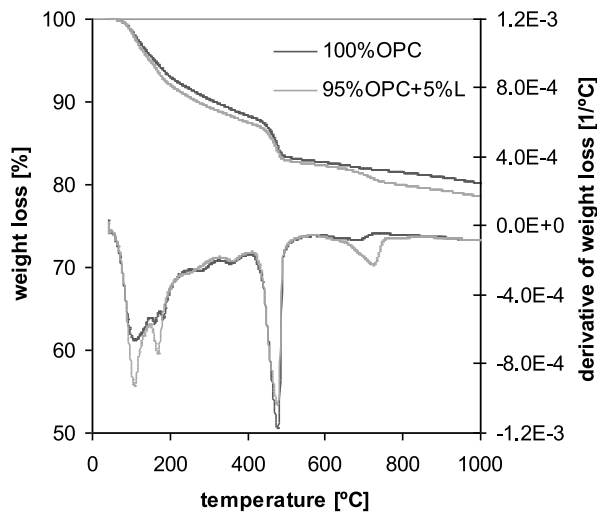

Figure 12: Thermogravimetric curves (TG) and differential thermogravimetric curves (DTG) for the reference (100% OPC) and a limestone cement (5% limestone powder + 95% OPC hydrated for 28 days).

In order to try to understand this change in hydration products X-ray diffraction analysis were performed. The cements tested were:

- 100% OPC (reference)
- 95% OPC + 5% limestone powder
- 65% OPC + 35% fly ash
- 65% OPC + 30% fly ash + 5% limestone powder

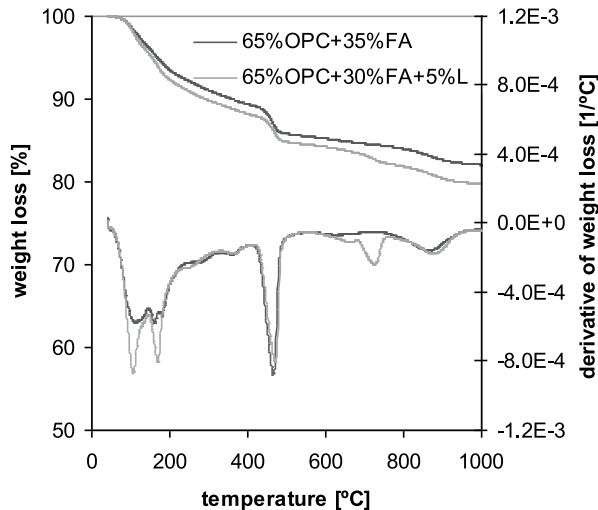The pastes had hydrated for 28 days at 20°C when they were analysed.

Figure 13: Thermogravimetric curves (TG) and differential thermogravimetric curves (DTG) for a fly ash cement containing 65% OPC and 35% fly ash and a composite cement containing 65% OPC, 5% limestone powder and 30% fly ash hydrated for 28 days.

In Figure 14 the XRD spectra of the tested cements are shown. The d-range of particular interest was enlarged and is shown in Figure 15. The main crystalline phases were:

- CH   portlandite $Ca(OH)_2$
- Q   quartz SiO_2
- C<u>C</u>   calcium carbonate $CaCO_3$
- E   ettringite $C_3A \cdot 3CaSO_4 \cdot 32H_2O$
- MS   calcium monosulphoaluminate hydrate $C_3A \cdot CaSO_4 \cdot 12H_2O$
- M<u>C</u>   calcium monocarboaluminate hydrate $C_3A \cdot CaCO_3 \cdot 11H_2O$
- H<u>C</u>   calcium hemicarboaluminate hydrate $C_3A \cdot 0.5CaCO_3 \cdot 0.5Ca(OH)_2 \cdot 11.5H_2O$

It can be seen that when limestone powder is present the calcium monosulphate hydrate disappears and instead ettringite, calcium monocarbonate hydrate and calcium hemicarbonate hydrate are formed.

The effect of small additions of limestone powder seemed to be more pronounced for the fly ash cements than for the ordinary Portland cement. This might be due to the liberation of additional aluminates by the fly ash. They cause a decrease of the sulphate/aluminate ratio of the system. Therefore relatively more calcium monosulphate hydrate than ettringite will form in the fly ash

blended cement. The presence of limestone will then have a larger impact as more calcium monosulphate hydrate will shift to ettringite in a fly ash containing cement as calcium monocarboaluminate hydrate and calcium hemicarboaluminate hydrate are formed. This process will lead to relatively more bound water and higher total volume of hydrates, which in turn will decrease porosity and increase strength even more in the case of fly ash blended cements compared to OPC. The chemistry of this synergy was recently elaborated by De Weerdt and Justnes [30] .

The applicability of this study is proven by a pilot project recently launched by the Norwegian cement manufacturer Norcem using a "low carbon", environmentally friendly cement containing 65%OPC, 30% fly ash and 5% limestone [31] .
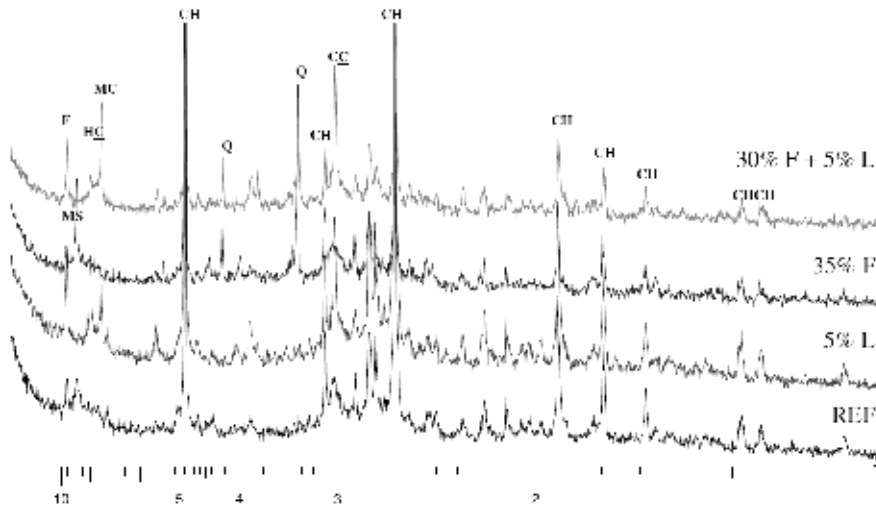

Figure 14: X-ray spectra for 100% OPC (REF), 95% OPC and 5% L (5% L), 65% OPC and 35% FA (35% F), and 65% OPC, 30% FA and 5% L (30% F + 5% L) all hydrated for 28 days at 20°C.
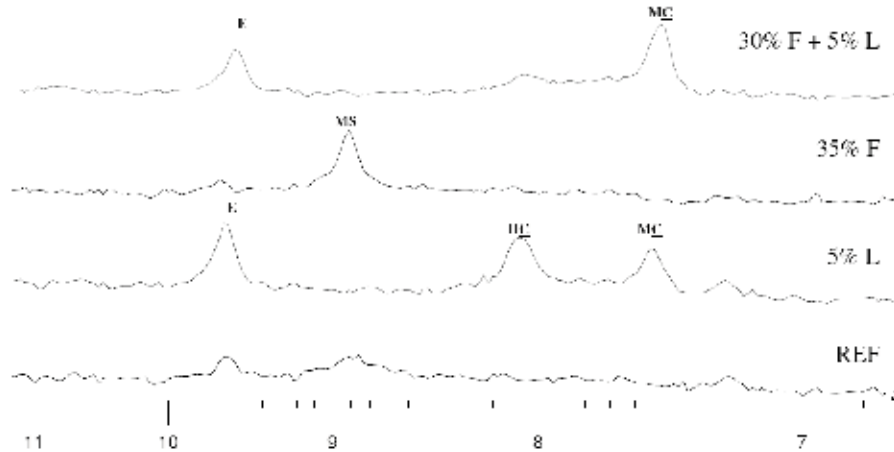
Figure 15: Zoomed in on the X-ray spectra for 100% OPC (REF), 95% OPC and 5% L (5% L), 65% OPC and 35% FA (35% F), and 65% OPC, 30% FA and 5% L (30% F + 5% L) all hydrated for 28 days at 20°C.

4   CONCLUSION

The compressive strength results at 28 days indicated a synergetic interaction between fly ash and limestone powder. Replacing 5% of fly ash with 5% of limestone powder in the 65% OPC + 35% FA cement resulted in a strength increase of about 10% (from 38 MPa to 42 MPa). The replacement of 5% OPC with limestone powder only resulted in a strength increase of about 4% (from 49.9 MPa to 51.8 MPa). Moreover, the combination 65% OPC + 30% FA + 5% L had a higher compressive strength after 28 days than the cement prepared with 70% OPC + 30% FA (41 MPa). This means that in this case it would be more beneficial to use 5% of limestone instead of 5% of OPC.

The thermogravimetric results showed that the hydration products change when limestone powder is included in the system. Moreover small additions of limestone resulted in a slight decrease of calcium hydroxide, indicating a possible formation of calcium hemicarboaluminate hydrate.

The X-ray diffraction results showed a change in crystalline hydration products. Calcium monosulphoaluminate hydrate disappears when limestone powder is present and instead ettringite, calcium monocarboaluminate hydrate and calcium hemicarboaluminate hydrate form.

It can be concluded that minor additions of limestone powder can have a beneficial effect on the strength development of Portland cement after 28 days of hydration most likely related to the interaction with the AFm and AFt phases. For fly ash containing cements this effect seems to be even greater.

Further research should be done to further explain this phenomenon. For example figuring out whether this is a pure chemical interaction or are there as well some physical effects playing a role in this, quantifying the chemical and physical effect etc. It is also important to look at how the interaction between fly ash and limestone powder evolves over time and how it will affect creep, shrinkage, durability, etc.

ACKNOWLEDGEMENTS

REFERENCES

[1]   Damtoft JS, Lukasik J, Herfort D, Sorrentino D, Gartner EM. Sustainable development and climate change initiatives. Cement and Concrete Research. 2008;38(2):115-127.

[2]   Justnes H. Principles of making cement with reduced CO_2 emission. COIN State of the art report, wwwcoinwebno; 2007.

[3]   Justnes H. Making cements with less clinker content. COIN State of the art report, wwwcoinwebno; 2007.

[4]   EN 197.1: 2000+A1. Part 1: Composition, specifications and conformity criteria for commen cements 2005.

[5]   Ramachandran VS. Thermal analyses of cement components hydrated in the presence of calcium carbonate. Thermochimica Acta. 1988;127:385-394.

[6]   Péra J, Husson S, Guilhot B. Influence of finely ground limestone on cement hydration. Cement and Concrete Composites. 1999;21(2):99-105.

[7]   Kakali G, Tsivilis S, Aggeli E, Bati M. Hydration products of C_3A, C_3S and Portland cement in the presence of $CaCO_3$. Cement and Concrete Research. 2000;30(7):1073-1077.

[8]   Soroka I, Stern N. Calcareous fillers and the compressive strength of portland cement. Cement and Concrete Research. 1976;6(3):367-376.

[9]   Kuzel HJ, Pöllmann H. Hydration of C_3A in the presence of $Ca(OH)_2$, $CaSO_4·2H_2O$ and $CaCO_3$. Cement and Concrete Research. 1991;21(5):885-895.

[10]   Vernet C, Noworyta G. Mechanisms of limestone fillers reactions in the system {C3A-CSH2-CH-CC-H}: Competition between calcium monocarbo- and monosulpho-aluminate hydrates formation. 9th ICCC. New Delhi, India; 1992. p. 430-436.

[11]   Bonavetti VL, Rahhal VF, Irassar EF. Studies on the carboaluminate formation in limestone filler-blended cements. Cement and Concrete Research. 2001;31(6):853-859.

[12]   Matschei T, Lothenbach B, Glasser FP. The AFm phase in Portland cement. Cement and Concrete Research. 2007;37(2):118-130.

[13]   Lothenbach B, Le Saout G, Gallucci E, Scrivener K. Influence of limestone on the hydration of Portland cements. Cement and Concrete Research. 2008;38(6):848-860.

[14]   Hirao H, Yamada K, Hoshino S, Yamashita H. The effect of limestone addition on the optimum sulphate levels of cements having various Al_2O_3 contents. 12th ICCC. Montreal; 2007.

[15]   ASTM C618-08a. Standard specification for coal fly ash and raw or calcined natural pozzolan for use in concrete. In: ASTM International WC, PA, 2008, DOI: 10.1520/C0618-08 editor.

[16]   Fraay ALA, Bijen JM, de Haan YM. The reaction of fly ash in concrete a critical examination. Cement and Concrete Research. 1989;19(2):235-246.

[17]   Fraay A, Bijen JM, Vogelaar P. Cement-stabilized fly ash base courses. Cement and Concrete Composites. 1990;12(4):279-291.

[18]   Pietersen HS. The reactivity of fly ash in cement geochemistry. Delft: TU Delft; 1993. p. 271.

[19]   De Weerdt K, Justnes H. Microstructure of binder from the pozzolanic reaction between lime and siliceous fly ash and the effect of limestone addition. In: Sun W, van Breugel

K, Miao C, Ye G, Chen H, editors. Microstructure Related Durability of Cementitious Composites Nanjing; 2008. p. 107-116.

[20]   Menéndez G, Bonavetti V, Irassar EF. Strength development of ternary blended cement with limestone filler and blast-furnace slag. Cement and Concrete Composites. 2003;25(1):61-67.

[21]   Carrasco MF, Menéndez G, Bonavetti V, Irassar EF. Strength optimization of "tailor-made cement" with limestone filler and blast furnace slag. Cement and Concrete Research. 2005;35(7):1324-1331.

[22]   Ghrici M, Kenai S, Said-Mansour M. Mechanical properties and durability of mortar and concrete containing natural pozzolana and limestone blended cements. Cement and Concrete Composites. 2007;29(7):542-549.

[23]   Elkhadiri I, Diouri A, Boukhari A, Aride J, Puertas F. Mechanical behaviour of various mortars made by combined fly ash and limestone in Moroccan Portland cement. Cement and Concrete Research. 2002;32(10):1597-1603.

[24]   Yilmaz B, Olgun A. Studies on cement and mortar containing low-calcium fly ash, limestone, and dolomitic limestone. Cement and Concrete Composites. 2008;30(3):194-201.

[25]   Sato T, Beaudoin JJ. The effect of nano-sized $CaCO_3$ addition on the hydration of cement paste containing high volumes of fly ash. 12th ICCC. Montreal; 2007. p. 1-12.

[26]   Härdtl R, Dietermann M, Schmidt K. Durability of blended cements with several main components. 12th ICCC. Montréal; 2007.

[27]   Hoshino S, Yamada K, Hirao H. XRD/Rietveld analysis of the hydration and strength development of slag and limestone blended cement. Journal of Advanced Concrete Technology. 2006;4(3):357-367.

[28]   Sellevold EJ, Farstad T. The PF-method - A simple was to estimate the w/c-ratio and air content of hardened concrete. ConMat'05. Vancouver, Canada; 2005. p. 10.

[29]   Neville AM. Properties of concrete - Fourth edition. Prentice Hall, Pearson Education Limited, 2000.

[30]   De Weerdt K, Justnes H. Synergic reactions in triple blended cements. 11th NCB International Seminar on Cement and Building Materials. New Delhi; 2009. p. 257-261.

[31]   Mathisen E. Green cement for the house of the future (in Norwegian). Cement Nå. Oslo, Norway: Norcem HeidelbergCement Group 2009. p. 3-6.

Capillary suction in concrete with analytical pipe model - part 1: Numerical study of flow conditions

Hung Thanh Nguyen
University of Tromsø, Department of physics, 9000 Tromsø, Norway &
Narvik University College, P. 8500 Narvik, Norway
E-mail: hung.thanh.nguyen@uit.no

Frank Melandsø
University of Tromsø, Department of physics, 9000 Tromsø, Norway
E-mail: frank.melandso@uit.no

Stefan Jacobsen
Norwegian University of Science and Techn., Dept. of Structural Engineering, 7491 Trondheim, Norway.
E-Mail: stefan.jacobsen@ntnu.no

ABSTRACT

Absorption of water in concrete is often described by the simple linear water uptake vs square- root-of-time law. However, a deviation from this behavior is frequently seen depending on factors such as initial water content, water/binder ratio and specimen thickness. The increasing deviation at increasing thickness is seen even for very dry specimens with a significant fraction of capillary pores when the specimen thickness increases from around 25 to around 100 mm. In this paper, we have combined Navier-Stokes flow equation with Laplaces law for suction created under a curved meniscus between air and water, and applied it to series of pipes with different lengths and radii, (the analytical model). The analytical model is in good agreement with the numerical models at abrupt reduction or increase of pipe radius, even at very small radii, and our analytical pipe model made with different radii and lengths thus works satisfactorily in terms of flow conditions.

Key Words: Concrete, capillary, surface tension, Analytical, and numerical modelling, Navier Stokes and Stokes models, pipe geometry.

1   INTRODUCTION

Capillary transport of water in porous materials like concrete has kept the attention of researchers world wide for many years. Capillary transport is considered a basic transport mechanism in concrete and similar porous materials [1] where suction is created under water meniscii in partly filled capillary pores. During the last decade an increasing portion of the applied concrete qualities have very little capillary porosity. This is due to the increasing use of high performance concrete and supplementing cementing materials that refine and make the pore structure less continuous [2]. However, in spite of the reduced capillary continuity of the pore system of HPC with low w/b and/or supplementary cementing materials like fly ash and condensed silica fume, such concretes may after some predrying show the typical nick point on the water uptake vs square root of time plots in one sided (unidirectional) capillary suction experiments. The severity

of drying has a very clear effect, and this has been found to relate to the degree of saturation of the pore system at start [3]. By re-plotting these results they actually fit well into the kind of saturation-sorptivity plots suggested [1] for use in solving Richards equation. However, in experiments there is a size effect on capillarity that is problematic compared to the capillary mechanism since there is an increasing deviation from the linear absorption vs square root of time relation of capillary theory as the sample thickness is increasing. The size dependant deviation from the square root-law effect has sometimes been ascribed to the replacement of interstitial water and subsequent swelling of the gel [1]. We believe that capillary discontinuities in the form of narrow passages or larger capillary voids along the flow path of the capillary pore system can be involved in the phenomenon (as some sort of pipe geometry effect on the water transport). This deviation from the square-root law has been observed in concrete with a significant amount of capillary porosity [4] as well as in materials with theoretically no capillary porosity, depending on the severity of the drying [3]. The deviation has also been observed in capillary absorption experiments with an organic fluid [5]. It is therefore probable that the proposed gel swelling [1] cannot be a general explanation for the anomaly. Figure 1 shows the results of one of our experiments on cylindrical mortar specimens with diameter 100 mm and w/c = 0.60 after drying at 105 C. The three graphs show how real capillary absorption deviates increasingly from the square-root of time law as the specimen thickness increases from 20 to 40 to 100 mm height. We also see how the nick-points vanish at increasing specimen height.
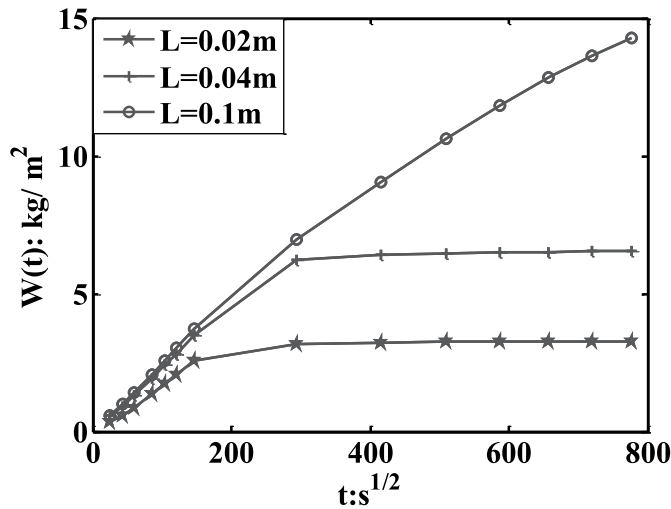
Figure 1- Capillary absorption in w/c 0.60 mortar with increasing deviation from linear absorption vs square-root-of-time law at increasing specimen thickness 20 to 40 to 100 mm.

The kind of narrowing and widening discontinuity-effects we propose may be compared with percolation thresholds which have so far mainly been used in diffusion studies [4]. That is, accounting only for transport in the capillaries and not in the very fine gel structure of the cement based material. For the very fine, nano sized gel pores molecular simulation is probably a suitable way of modelling the transport [6],[7]. To investigate to what extent the proposed capillary discontinuities affect the size dependant deviation from the linear square root time - absorption law, we have in this paper developed an analytical solution to a multiple pipe model. The objective has been to investigate the reliability of this model compared to a numerical solution of

the continuum approach. Then, in part 2 of this study we will calculate absorption with varying combinations of pipes and also compare the calculated pipe absorption with experiments from other researchers, as well as our own capillary absorption experiments. All capillary absorption experiments were made at ambient temperatures on specimens after drying at 50 or $105\,C$.

2   FLOW MODELS

Varying pipe flow approaches have been taken in earlier studies of this kind of problem. Some have been based on pipe flow according to Hagen-Poiselle with capillary suction due to the under-pressure caused by the surface tension between liquid and gas (l-g - water-air in our case) and the curvature of the water meniscus between air and the liquid wetting the pipe wall (concrete in our case). One example of pipe flow modelling can be found in [8] and early efforts to model capillary suction in sandstone and concrete in this way are [9],[10]. However, these studies did not analyze the reasons for the increasing deviation from the square root of time law.

2.1   Navier Stokes equation

As a starting point for our capillary system, we will assume an incompressible and stationary flow in an axial-symmetric pipe system. For such a system the mass conservation equation can be reduced to the incompressibility requirement

$$\frac{\partial u}{\partial x} + \frac{1}{r}\frac{\partial}{\partial r}(rv) = 0 \tag{1}$$

while the momentum conservation equations can be expressed as

$$\rho\left(u\frac{\partial u}{\partial x} + v\frac{\partial u}{\partial r}\right) = -\frac{\partial p}{\partial x} + \mu\left[\frac{\partial^2 u}{\partial x^2} + \frac{1}{r}\frac{\partial}{\partial r}\left(r\frac{\partial u}{\partial r}\right)\right] \tag{2}$$

and

$$\rho\left(u\frac{\partial v}{\partial x} + v\frac{\partial v}{\partial r}\right) = -\frac{\partial p}{\partial r} + \mu\left[\frac{\partial^2 v}{\partial x^2} + \frac{1}{r}\frac{\partial}{\partial r}(rv)\right]. \tag{3}$$

Here u and v are the velocity components in the axial direction (denoted by x) and radial directions (r), respectively, while p denotes the fluid pressure. The two other parameters ρ and μ describing the mass density and dynamic viscosity coefficient, are both assumed to be constants.

In the rest of the paper we will refer to Eqs. (1)-(3) as the Navier-Stokes equation (NSE), while the non-linear terms on the left hand side of Eqs. (2) and (3) will be referred to as the flow acceleration terms or the convective terms.

In order to obtain consistent solutions for the NSE, boundary conditions that incorporate the basic physics, have to be specified. For our case, a capillary suction or under-pressure p_c described above in front of the water column created at the meniscus is driving the flow trough the pipe

system. Such a driving force can be imposed through the pressures

$$p(r, x = 0) = 0 \quad and \quad p(r, x = L) = -p_c \tag{4}$$

at the pipe ends $x = 0$ and $x = L$. In addition, we also assume non-slip boundary conditions at the pipe wall at $r = r_x$, or

$$u(r = r_x, x) = 0 \quad and \quad v(r = r_x, x) = 0. \tag{5}$$

2.2 Stokes equation

For cases where the flow velocity is sufficiently small and well within the laminar regime, it is possible to approximate the NSE with models which are easier to handle both by numerical and analytical means. In Stokes approach for example, the convective terms in Eqs. (2) and (3) are neglected. This yields the Stokes equation (SE)

$$0 = -\frac{\partial p}{\partial x} + \mu \left[\frac{\partial^2 u}{\partial x^2} + \frac{1}{r} \frac{\partial}{\partial r} \left(r \frac{\partial u}{\partial r} \right) \right] \tag{6}$$

and

$$0 = -\frac{\partial p}{\partial r} + \mu \left[\frac{\partial^2 v}{\partial x^2} + \frac{1}{r} \frac{\partial}{\partial r} (rv) \right]. \tag{7}$$

2.3 Hagen-Poiseuilles equation

Further simplification may be possible, for example for pipes with constant radius where so-called fully developed flows will occure. Fully developed flows are characterized by both zero lateral velocity v and gradient of axial velocity component $(\partial u/\partial x)$. The latter velocity relates to the pressure p through Eq. (6), and gives

$$\frac{\partial p}{\partial x} = \mu \left[\frac{1}{r} \frac{\partial}{\partial r} \left(r \frac{\partial u}{\partial r} \right) \right]. \tag{8}$$

This equation points out a simple balance between shear and pressure forces in the flow [11].

It should be emphasized that Eq. (8) which is the basis for the Hagen-Poiseuille equation (HPE), also can be used as an approximation for pipes with a slowly changing radius, or in pipes with a stepwise changing radius. However, a Hagen-Poiseuille (HP) flow approximation requires that the changes are sufficiently small, or do not happen too often (for a stepwise change), so that a fully developed flow will dominate on a local scale. The latter assumption is also fundamental for the analytical theory presented in the next section.

2.4   Analytical equation: Pipe flow velocity - N-sized pipe model

In order to develop an analytical capillary model for a pipe system with a stepwise changing cross section, we will start with the two sized (binary) model shown in Fig. 2. This figure illustrates how a physical flow pattern shown in the upper Fig. 2(a), can be approximated with the stepwise model shown in the upper Fig. 2(b). For this binary model we assume a HP flow in both sections, which changes abruptly at the interface ($x = x_1$), and thereby neglecting the regions indicated with the darkest shading in the upper figures, where the flows are not fully developed. This approach will also lead to a stepwise flow velocity and a linear pressure as indicated in the lower Fig. 2(b), acting as approximation for the physical mean fields shown in the lower Fig. 2(a). The field u_x and p_x should be considered as mean values over the pipe cross section, given by the integrals

$$u_x = \frac{2}{r_x^2} \int_0^{r_x} u(r,x) r dr \qquad (9)$$

and

$$p_x = \frac{2}{r_x^2} \int_0^{r_x} p(r,x) r dr \qquad (10)$$

for an axial-symmetrical flow.

In addition to the radius parameter r_x which has the value r_1 and r_2 in section 1 and 2, respectively, the geometry is also characterized by the sections length l_1 and l_2, and h which is the current position for the water front.
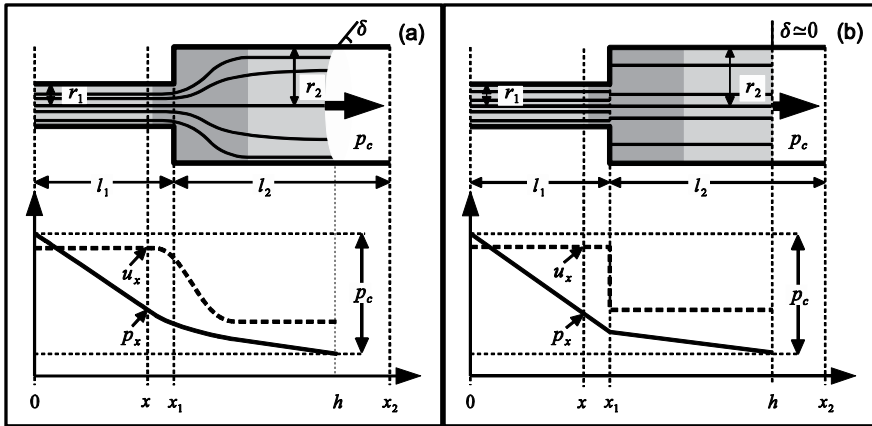

Figure 2- A circular tube divided into two sections and the balance force between the capillary force and the moving-body-force.

Local expressions for the HP flow now can be obtained by intergrating Eq. (8) twice and imposing the non-slip boundary conditions Eq. (5). This yields the well known parabolic profile [11]

$$u(x,r) = -\frac{1}{4\mu}\left(\frac{dp_x}{dx}\right)r_x^2\left[1-\left(\frac{r}{r_x}\right)^2\right] \qquad (11)$$

inside each pipe section.

The foregoing result may be used to determine the mean velocity of flow. After substituting Eq. (11) into Eq. (9) and integrating, we obtain

$$u_x = -\left(\frac{r_x^2}{8\mu}\right)\left(\frac{dp_x}{dx}\right). \qquad (12)$$

It should be emphasized that both the pipe radius, the pressure gradient and the velocity in Eq. (12) are local quantities changing between the individual pipe sections. Therefore, in order to determine the velocity at the fluid-front u_h based on Eq. (12), we need two additional constraints.

The first of these constraints can be found by looking at the total pressure fall from position $x = 0$ to h. This pressure fall has to be balanced by the capillary pressure p_c in the water front as shown in Fig. 2. The capillary pressure, on the other hand, can for fluids with moderate velocities, be approximated with the stationary pressure given by the Laplace equation

$$p_c = -\frac{2\sigma_{l-g}cos\delta}{r_h} \qquad (13)$$

obtained from static conditions. Here σ_{l-g} is the surface tension between water and air and δ the contact angle between the pipe wall and the wetting water front (see for example [1],[12]).

The second constraint can be imposed by assuming that the water flux entering the left hand side of the pipe interface, has to equal the right hand value. This constraint which has to be fulfilled in order to conserve the water mass in a stationary flow [13] , gives

$$u_x A_x = u_h A_h \Rightarrow u_x = u_h \frac{r_h^2}{r_x^2}. \qquad (14)$$

Here A_x and A_h are the cross section areas at position x and h, respectively, as shown in Fig. 2(b).

After rearranging Eq. (12) and then integrating from $x = 0$ to h we obtain

$$\int_0^h u_x \frac{dx}{r_x^2} = \frac{1}{8\mu}\left(-\int_{p_0}^{p_h} dp_x\right).$$

A further reformulation of this equation can be done by inserting expressions for the pressure $p_c = p_h - p_0$ and velocity u_x given by Eqs. (13) and (14), respectively. This yields

$$u_h = \frac{k}{f(h)r_h^3} \tag{15}$$

for the capillary front velocity where we have introduced a constant k as

$$k = \frac{\sigma_{l-g}cos\delta}{4\mu}. \tag{16}$$

and a function

$$f(h) = \int_0^h \frac{dx}{r_x^4} \tag{17}$$

which depends on the position h of the capillary front.

One should notice that the velocity u_h and radius r_h at the location h, are constants and that the evaluation of Eq. (17) involves integration of $f(h)$. In order to evaluate this function which may be interpreted as the area under the graph of $(1/r_x^4)$ from 0 to h, a numerical integration can be used [14]. However, in our approach where a step fuction is assumed, a simple analytical solution can be found, as

$$f(h) = l_1 \frac{1}{r_1^4} + (h - x_1)\frac{1}{r_2^4}. \tag{18}$$

Now, Eq. (18) can be substituted into Eq.(15), to give

$$u_h = \frac{k}{\left(\frac{r_2}{r_1}\right)^3 \frac{l_1}{r_1} + \left(\frac{r_2}{r_2} = 1\right)^3 \frac{h - x_1}{r_2}}. \tag{19}$$

In this equation the first terms in the denominator of Eq. (19) is a constant while the second term depends on the position h.

It is relatively straight forward to expand the two-pipe capillary model to a pipe system containing N sections. By repeating the previous steps for a N-pipe system, it can be shown that the velocity of the capillary front in an arbitrary section j, is

$$u_h = \frac{k}{f(h)r_h^3}. \tag{20}$$

This expression is identical to the one found for the two pipe model (Eq. (15)), but with $f(h)$ substituted with the general expression

$$f(h) = \int_0^h \frac{dx}{r_x^4} \quad = \frac{l_1}{r_1^4} + \cdots + \frac{l_{j-1}}{r_{j-1}^4} + \frac{h - x_{j-1}}{r_j^4}$$

$$= \sum_{i=1}^{j-1} f_i + \Delta f_j , \tag{21}$$

where

$$f_i = \frac{l_i}{r_i^4} \quad and \quad \Delta f_j = \frac{(h - x_{j-1})}{r_j^4} . \tag{22}$$

Here r_i and l_i are the pipe radius and pipe lengths, respectively for section i (expanding from position x_{i-1} to x_i) while h is the position of the capillary front assumed to be in pipe section j.

In many pipe geometries it is useful to describe the flow in terms of dimensional variables. For our case, we will introduce dimensionless variables α_i defined as

$$\alpha_i = \frac{r_i}{l_i} \quad for \quad i = 1, 2, \cdots, j-1, \quad and \quad \Delta \alpha_j = \frac{r_j}{h - x_{j-1}} \tag{23}$$

which provide information about how rapidly the cross sections change with respect to the pipe section lengths. Our approach which assumes Hagen-Poiseuille in all pipe sections and thereby neglecting the non-developed regions of the flow, are based upon sufficiently small α_i values. These parameters are therefore very useful when the breakdown of the analytical approach will be tested in the next section.

In addition to the α-parameters, we will introduce a set of β-parameters (also dimensionless) defined as

$$\beta_i = \left(\frac{r_j}{r_i} \right)^3 \quad for \quad i = 1, 2, \cdots, j . \tag{24}$$

The latter parameters relate the cross sections of previous pipe sections ($i = 1, 2, \ldots, j-1$) to the current section ($i = j$). It should be noticed that $\beta_j = 1$ due to its definition.

After inserting Eq. (23) and (24) into Eq. (20) and rearranging, the velocity can be expressed in terms of the new variables as

$$u_h = \frac{k}{\beta_1 / \alpha_1 + \beta_2 / \alpha_2 + \ldots + \beta_{j-1} / \alpha_{j-1} + \beta_j / \Delta \alpha_j} . \tag{25}$$

We call Eq. (25) the Analytical equation (AE).

3   RESULTS AND DISCUSSION

3.1   Flow velocity in contraction- and expansion sections

In order to evaluate the solution of the flow velocity for NSE, SE, and AE as shown in Eq. (25), we have introduced a testing model geometry as shown in Fig. 3. Here, the pipe has a contraction (model C) and expansion sections (model E). Data for the section length and radius are given in Tabs. 1 and 2 respectively. Figure 3- Tube with contraction and expansion sections.

Table   1- Geometry data for contraction-model

Idenfication	$r_1(m)$	$r_2(m)$	$l_1 = l_2 = l(m)$	α_1	α_2	β_1
$C_{l=10^{-2}}$	1×10^{-6}	0.5×10^{-6}	1×10^{-2}	0.0001	0.00005	0.125
$C_{l=10^{-3}}$	1×10^{-6}	0.5×10^{-6}	1×10^{-3}	0.001	0.0005	0.125
$C_{l=10^{-4}}$	1×10^{-6}	0.5×10^{-6}	1×10^{-4}	0.01	0.005	0.125
$C_{l=10^{-5}}$	1×10^{-6}	0.5×10^{-6}	1×10^{-5}	0.1	0.05	0.125
$C_{l=3.0\times10^{-6}}$	1×10^{-6}	0.5×10^{-6}	3.0766×10^{-6}	0.3250	0.1625	0.125
$C_{l=1.8\times10^{-6}}$	1×10^{-6}	0.5×10^{-6}	1.8180×10^{-6}	0.5500	0.2750	0.125
$C_{l=1.2\times10^{-6}}$	1×10^{-6}	0.5×10^{-6}	1.2902×10^{-6}	0.7750	0.3875	0.125
$C_{l=10^{-6}}$	1×10^{-6}	0.5×10^{-6}	1×10^{-6}	1.0	0.5	0.125

Results of velocity, where:

$$e_{NSE} = \frac{|u_h^{NSE} - u_h^{AE}|}{u_h^{NSE}} \; and \; e_{SE} = \frac{|u_h^{SE} - u_h^{AE}|}{u_h^{SE}}$$

Table   2: Geometry data for expansion-model

Idenfication	$r_1(m)$	$r_2(m)$	$l_1 = l_2 = l(m)$	α_1	α_2	β_1
$E_{l=10^{-2}}$	0.5×10^{-6}	1×10^{-6}	1×10^{-2}	0.00005	0.0001	8
$E_{l=10^{-3}}$	0.5×10^{-6}	1×10^{-6}	1×10^{-3}	0.0005	0.001	8
$E_{l=10^{-4}}$	0.5×10^{-6}	1×10^{-6}	1×10^{-4}	0.005	0.01	8
$E_{l=10^{-5}}$	0.5×10^{-6}	1×10^{-6}	1×10^{-5}	0.05	0.1	8
$E_{l=3.0\times10^{-6}}$	0.5×10^{-6}	1×10^{-6}	3.0766×10^{-6}	0.1625	0.3250	8
$E_{l=1.8\times10^{-6}}$	0.5×10^{-6}	1×10^{-6}	1.8180×10^{-6}	0.2750	0.5500	8
$E_{l=1.2\times10^{-6}}$	0.5×10^{-6}	1×10^{-6}	1.2902×10^{-6}	0.3875	0.7750	8
$E_{l=10^{-6}}$	0.5×10^{-6}	1×10^{-6}	1×10^{-6}	0.5	1.0	8

As shown in Tabs. 1 and 2, for both models C and E, we kept the radius of the sections constant, $r_1 = 10^{-6} m$, $r_2 = 0.5 \times 10^{-6} m$, while the lengths varied with the shortest and longest section $l_1 = l_2 = 10^{-6} m$ and $l_1 = l_2 = 10^{-2} m$. Hence, these section lengths give $\alpha_1 \in [10^{-4}, 1]$, $\alpha_2 \in [5 \times 10^{-5}, 0.5]$ or $\alpha_1 \in [5 \times 10^{-5}, 0.5]$, $\alpha_2 \in [10^{-4}, 1]$, for model C or E in Fig.3 respectively.
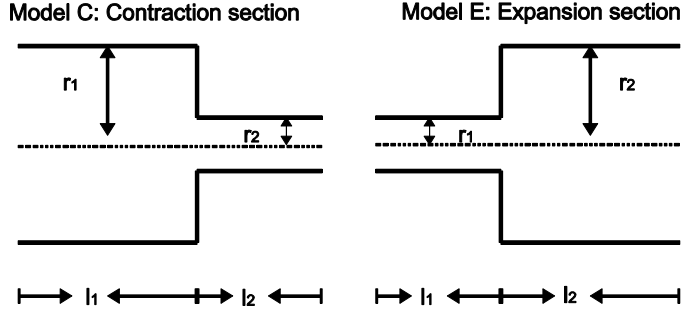

Figure 3- Tube with contraction and expansion sections

The results for NE, SE and AE presented in this section are based on $\rho = 1000 \; kg/m^3$, $\sigma_{l-g} = 0.073 \; mN/m$, $\mu = 0.001 \; kg/ms$, and the effect of the contact angle δ on AE is ignored by setting $\delta = 0$. Numerical solutions for NSE and SE were obtained using the FEM-based software [15]. The velocity results are based on the time for the flow front to reach the end of the last section (e.g section two).

In the following we have performed a series of parametric studies of the analytical model and compared with numerical solutions. The objective is to find out when the analytical models "break down" in terms of deviating from the numerical solutions of the not fully develop laminar flow shown at the darkest shading in Fig.2. This may happen when $\alpha_{1,2}$ increases or, as in our case, the section length is dramatically decreased with respect to the cross section area, for example $l_i \approx r_i$, $i = 1,2$.

Figure 4(a) and (b) illustrate the velocity as a function of α_2 for model C (where $\beta = 0.125$) and E (where $\beta = 8$), respectively. Tabs. 3 and 4 give the corresponding results of velocity in numbers and some other necessary information of the flow properties, like the Reynolds numbers for NSE. The $Re-$number is determined by the following equation [8]:

$$Re_i = \frac{u_i D_i}{\nu}; \; i = 1,2, \tag{26}$$

where u_i, and D_i are the mean velocity and diameter for section number i, while ν is the kinematic viscosity, $\nu = \dfrac{\mu}{\rho}$.

Table   3: Velocity for the NSE, SE and AE models, $C_{l=10^{-2}\to10^{-6}}$

Id.	$u_h^{NSE}(\frac{m}{s})$	$u_h^{SE}(\frac{m}{s})$	$u_h^{AE}(\frac{m}{s})$	e_{NSE}	e_{SE}	Re_1^{NSE}	Re_2^{NSE}
$C_{l=10^{-2}}$	0.00085	0.00085	0.00085	0.00001	0.00001	0.0004	0.0008
$C_{l=10^{-3}}$	0.00858	0.00858	0.00858	0.00016	0.00016	0.004	0.008
$C_{l=10^{-4}}$	0.08573	0.08574	0.08588	0.00166	0.00164	0.04	0.08
$C_{l=10^{-5}}$	0.84274	0.84473	0.85882	0.01908	0.01667	0.42	0.84
$C_{l=3.0\times10^{-6}}$	2.58647	2.64539	2.79137	0.07922	0.05518	1.29	2.58
$C_{l=1.8\times10^{-6}}$	4.07184	4.31063	4.72400	0.16016	0.09589	2.03	4.07
$C_{l=1.2\times10^{-6}}$	5.30450	5.85890	6.65611	0.25480	0.13606	2.65	5.30
$C_{l=10^{-6}}$	6.32553	7.31211	8.58823	0.35770	0.17452	3.16	6.32

Table   4: Velocity for the NSE, SE and AE models, $E_{l=10^{-2}\to10^{-6}}$

Id.	$u_h^{NSE}(\frac{m}{s})$	$u_h^{SE}(\frac{m}{s})$	$u_h^{AE}(\frac{m}{s})$	e_{NSE}	e_{SE}	Re_1^{NSE}	Re_2^{NSE}
$E_{l=10^{-2}}$	0.00010	0.00010	0.00010	0.00018	0.00019	0.00042	0.0002
$E_{l=10^{-3}}$	0.00107	0.00107	0.00107	0.00018	0.00019	0.00429	0.0021
$E_{l=10^{-4}}$	0.01071	0.01071	0.01071	0.00189	0.00190	0.04285	0.0214
$E_{l=10^{-5}}$	0.10548	0.10536	0.10736	0.01770	0.01888	0.42192	0.2109
$E_{l=3.0\times10^{-6}}$	0.33156	0.32789	0.34893	0.05237	0.06415	1.32623	0.6631
$E_{l=1.8\times10^{-6}}$	0.54748	0.53143	0.59005	0.07857	0.11114	2.18992	1.0949
$E_{l=1.2\times10^{-6}}$	0.75953	0.71846	0.83206	0.09548	0.15812	3.03841	1.5190
$E_{l=10^{-6}}$	0.97741	0.89257	1.07352	0.10196	0.20273	3.89716	1.9483

a) Models $C_{l:10^{-2} \to 10^{-6}}$ b) Models $E_{l:10^{-2} \to 10^{-6}}$
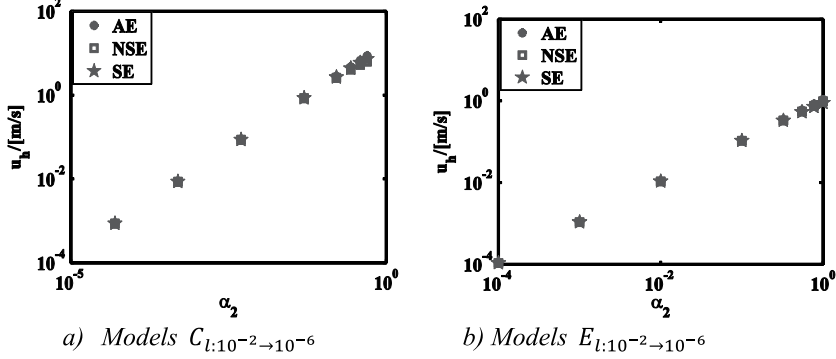
Figure 4: Velocity for contraction and expansion models, (as parameters $\alpha_i = r_i/l_i$) in log.-scala in both axis

We illustrate the velocity field for NSE and SE for some models in Figs. 5 and 6. As shown in Figs. 5(a-b-c) and (d-e-f), for model C and E respectively, the NSE-velocity field is regular or straight-lined for almost all section lengths $l_{1,2} = 10^{-3} \to 10^{-5}$, while irregular fields, are seen at a sudden change in section geometry as Figs.5(c) and (f) for $l_1 = l_2 \approx 10^{-6}$. This observation of the flow profile of SE are the same for model C and E as also shown in Figs. 6(a-b-c) and Figs. 6(d-e-f). That is, when the section length is too short the irregular flow region has a noticeable effect. Based on the Reynolds number, these results indicate that the flow velocity fields are still regular for Reynolds number of approximately $10^{-4} \leq Re_1^{NSE} \leq 2.65$ for section one and $8 \times 10^{-4} \leq Re_2^{NSE} \leq 5.30$ for section two. The velocity fields became irregular for $Re_1^{NSE} = 3.16$ to $Re_2^{NSE} = 6.32$. In other words, the irregular flow started at very small Reynolds numbers, (see Fig.5(c) and (f) for more detail).

The change of the laminar flow velocity profile at sudden contraction of cross sectional area was studied in [8]. Experiments using Laser-Doppler system (LDA) were employed for detailed velocity measurements of the incoming flow close to the change in the cross sectional area and also of the flow redeveloping in the smaller pipe (pipe material was glass and fluid consisted of warm oil and palatinol). The incoming flow had parabolic profile corresponding to a fully developed laminar flow. Only about one to two step-heights before the sudden change in cross sectional area, the longitudinal velocity profile starts to deform providing higher velocities in the center part of the test section. This work also showed the deformed velocity profiles redeveloping into a parabolic profile in subsequent longer section, for Reynolds number in the range $23 \leq Re_D \leq 1213$ for the large section and $42 \leq Re_d \leq 2294$ for the small section. With deformation of flow profile starting at $Re_D = 196$ and $Re_d = 371$. The authors also carried out LDA-measurements to obtain information of the geometry of the separation bubble developing just downstream of the inlet of the smaller pipe. The separation region started at a Reynolds number of approximately $Re_D = 300$. The actual pipe geometry was, however, very large: $r_D = 9.5mm, l_D = 720mm$ and $r_d = 5.1mm, l_d = 880mm$. (Or, $\alpha_D = 0.0132$ and $\alpha_d = 0.0058$). The author, found a good agreement between the experimental and numerical results for NSE for all Reynolds numbers but a small systematic deviation occurred just downstream of the plane of contraction in the region where the velocity overshoot occurs.

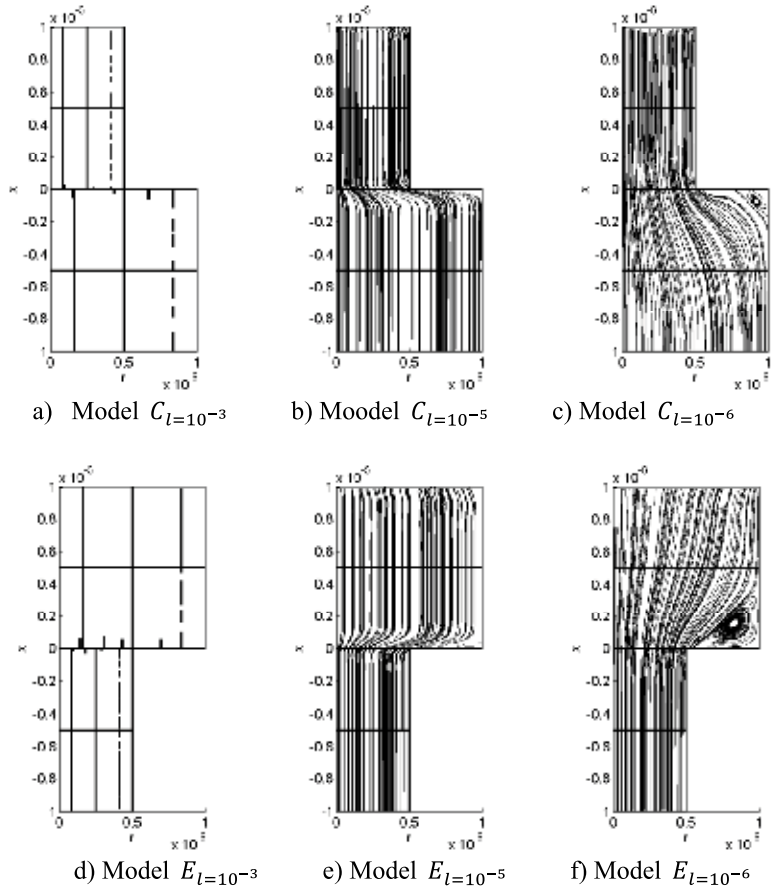a) Model $C_{l=10^{-3}}$ b) Moodel $C_{l=10^{-5}}$ c) Model $C_{l=10^{-6}}$

d) Model $E_{l=10^{-3}}$ e) Model $E_{l=10^{-5}}$ f) Model $E_{l=10^{-6}}$

Figure 5: NSE-Streamline velocity field for models C- $E_{l=10^{-3},10^{-5},10^{-6}}$, (water flows upwards)

a) Model $C_{l=10^{-3}}$ b) Model $C_{l=10^{-5}}$ c) Model $C_{l=10^{-6}}$

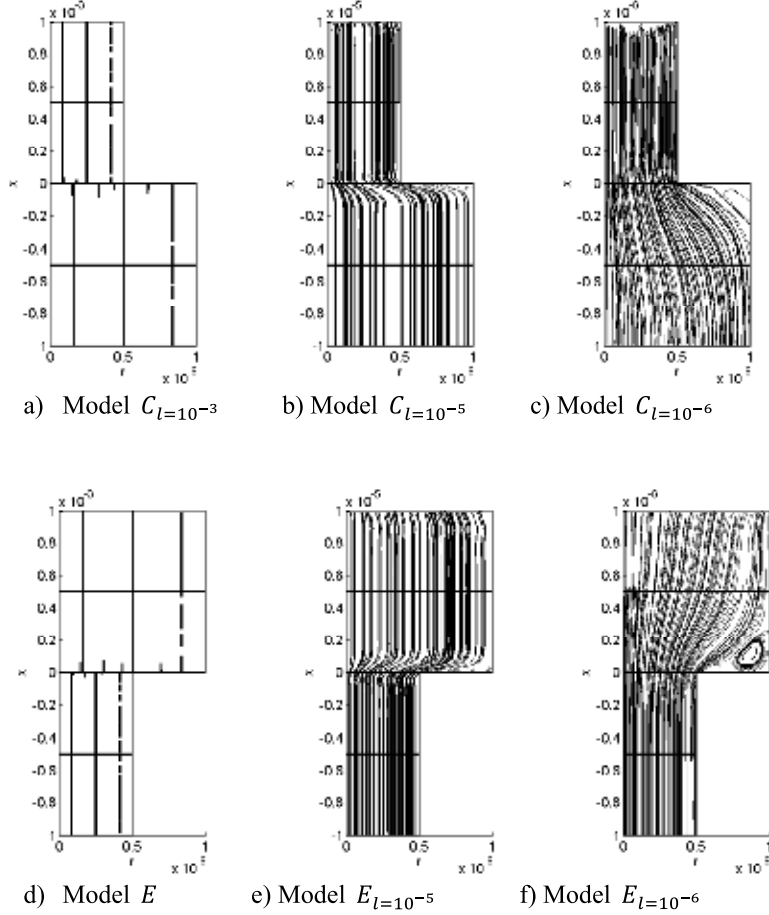d) Model E e) Model $E_{l=10^{-5}}$ f) Model $E_{l=10^{-6}}$

Figure 6: SE-Streamline velocity field for models C- E$_{l=10^{-3},10^{-5},10^{-6}}$

As shown in Fig. 4, the velocity of AE is in very good agreement with NSE and SE for almost all values of α_2, for both models C and E. However, a difference between the AE-velocity and the two other equations occurred as the section length is reduced to around $10^{-6}m$. Illustrated by numbers, for example, we have for model-C, when α_2 varies between 10^{-4} and 0.5 at equal section lengths and vary between 10^{-2} and 10^{-6} then the flow according to Navier Stokes u_h^{NSE} varies from 0.00085 to 6.32 m/s, whereas the flow according to Stokes u_h^{SE} varies from 0.00085 to 7.31 m/s, and the flow according to the analytical expression u_h^{AE} varies from 0.00085 to 8.58 m/s, The relative error-terms increase from $e_{NSE}=10\times10^{-5}$ to 0.35, and e_{SE} increase from 10×10^{-5} to 0.17, (see Tables 3 and 4 for more details). These results fall in line with the observation of the velocity fields of the NSE and the SE models. All velocities of the contraction models $C_{l=10^{-2}\rightarrow10^{-6}}$ are faster than the corresponding expansion models $E_{l=10^{-2}\rightarrow10^{-6}}$

That is, the suction at the front is more important than the flow resistance for the actual geometries.

Based on these results, it is clear that the AE is a very good model for the approximation of flow as the fluid passes section changes, for almost all the chosen pipe geometries in Tables 1 and 2. Figures 5 and 6 indicate that when the cross section of a pipe is relatively small for example r_1, r_2 $= (1 \times 10^{-6}, 0.5 \times 10^{-6} m)$, the flow still is laminar with a sudden contraction/expansion in cross sectional area, in spite of a large variation of the section length, $l_{1,2} = 10^{-3} \rightarrow 10^{-5} m$.

It is also worth noting that the velocity depends on the parameters α_i and β_i, $i = 1, 2$, with the AE-velocity being proportional to the logarithm of α_2 (Fig. 4). For the AE-velocity, it may be shown that the velocity function generally depends on the parameters α_i and β_i, by function analysis of u_h in Eq. (25).

3.2 Limiting pore size for capillary suction with Laplace equation

There is a possible physical limitation to the use of capillary rise simply calculated from the suction created in the pore water under the curved meniscus, Eq. (13). This limitation is the minimum size of a water meniscus when it is no longer possible to talk about a curved meniscus creating capillary suction.

The tensile strength of water $\sigma_{H_2 0}$ is a physical limitation to this problem. The net lifting force due to the capillary suction or under-pressure p_c of Eq. (13) is limited by the tensile strength of water which has been foud to be: $\sigma_{H_2 0} \approx 0.5 N/mm^2$ at $20^o C$ [16]. Equilibrium of vertical forces at the water surface, combined with Eq. (13) gives:

$$max \ p_c = \sigma_{H_2 o} = \frac{2\sigma_{l-g}}{r_{min}} \Rightarrow r_{min} = \frac{2\sigma_{l-g}}{\sigma_{H_2 o}} \tag{27}$$

giving

$$r_{min} = \frac{2 \times 0.073 \dfrac{N}{m}}{0.5 \dfrac{N}{mm^2}} \approx 3 \times 10^{-4} mm \approx 0.3 \mu m$$

The minimum capillary radius with a meniscus creating suction calculated this way is a bit smaller than the minimum radius used in the numerical examples in tables 1 and 2 and in figures 5 and 6. We therefore assume that capillary theory based on Laplaces law applies to our pipe models.

4 CONCLUSION

An analytical pore suction model was developed based on Navier-Stokes equation and Laplaces law with multiple sized pipes in series simulating the water flow in a porous material like concrete. The analytical model is very simple to apply to evaluate the dynamic capillary flow of

any other irregular well-defined pipe geometry. Furthermore, the parameters α_i and β_i are used in the model to account, for variations in pipe geometry in relation to the pressure-conditions under the meniscus at the water front.

The results of the analytical model were compared with numerical solutions of the Navier Stokes and Stokes models. This showed good agreement of the analytical model to the more complex flow at abrupt reduction or increase of pipe radius at very small radii. For the chosen geometries of contracting and expanding straight tube sections the maximum deviation in flow between analytical and numerical solutions were in the order of $20-35\%$ whereas the majority of geometries had practically equal flows, when comparing the analytical and numerical models. The analytical model was applied for pipes large enough to avoid tensile fracture of water (approximately $300nm$).

REFERENCES

[1]   Hoff, W. D.; Hall, C.(2002): Water transport in brick, stone and concrete. *Spon press London and New York.* , 318p.

[2]   Hazrathi , K. (1998): Etudes des mechanismes de transport de l'eau par absorption capillare dans des materiaux cimentarles conventionels et de haute performance.   PhD, Laval University.

[3]   Sellevold, E.J.; Punkki, J. (1994): Capillary suction in concrete: Effects of drying procedure.   Nordic Concrete Research.   15, 59--74.

[4]   Garboczi, E. Bentz, D. (1999): Computer simulation and percolation theory applied to concrete.   Annual reviews of computational Physics VII, World Sc. Publ. comp. 85--123. www.nist.gov.

[5]   Hansic, L. (2005): Capillarity in concrete.   PhD, University of Lubljana.

[6]   Martys, N.S.; Chen H. (1996): Simulation of multicomponent fluids in complex three-dimensional geometries by the lattice Bolzmann method.   Physical review E 53   1, 743--750.

[7]   Brennan, J.K.; Dong, W. (2003): Molecular simulation of the vapour-liquid phase behaviour of Lennard-Jones mixtures in porous solids.   Physical review E 67, 031503 , 1--6.

[8]   Durst, F.; Loy, T. (1985): Investigation of laminar flow in a pipe with sudden contraction of cross sectional areal.   Computers and Fluids.   13, 15--36.

[9]   Dullien, F. A. L.; El-Sayed, M. S.; Batra V. K. (1976): Rate of Capillary Rise in Porous Media with Nonuniform Pores.   Journal of Colloid and Interface Science.   60, 497--506.

[10]   Fagerlund, G.(1991): Unpublished data cited by E.J Sellevold in course compendium post graduate course Concrete Structure.   Norway Univ. Science and Technology.

[11]   Frank, P. Incropera; David, P. DeWitt (2002): Fundamental of Heat and Mass Transfer, Fifth Edition   *John Wiley and Sons. Inc*.

[12]   Chatterje, S. (2002): An explanation for the unsaturated state of water stored concrete. Cement and Concrete Composites.   26, 75--79.

[13]   Merle, C. Potter; David, C. Wiggert (1991): Mechanics of Fluid.   Prentice Hall, Inc.

[14]   Wen-Bin Young. (2004): Analysis of capillary flows in non-uniform cross-sectional capillaries.   Colloids and Surfaces A: Physicochem. Eng.   234, 123--128.

[15]   (2005): Comsol Multiphyscis 3.2.   COMSOL AB .

[16]   Crum, L. A. (1979): Tensile strength of water.   Nature.   278, 148--149.

Capillary suction in concrete with analytical pipe model - part 2: Expansion-, contraction- and random sized sections compared with experiments

Hung Thanh Nguyen
University of Tromsø, Department of physics, 9000 Tromsø, Norway &
Narvik University College, P. 8500 Narvik, Norway
E-mail: hung.thanh.nguyen@uit.no

Frank Melandsø
University of Tromsø, Department of physics, 9000 Tromsø, Norway
E-mail: frank.melandso@uit.no

Stefan Jacobsen
Norwegian University of Science and Techn., Dept. of Structural
Engineering, 7491 Trondheim, Norway.
E-Mail: stefan.jacobsen@ntnu.no

ABSTRACT

The Lucas-Washburn equation (LWE) is based on laminar flow within the simple geometry of a single pipe with a uniform radius. We studied the effect of different pipe geometries on capillary suction by modifying the LWE to be able to handle pipes with multiple sizes (the analytical model). To do this a complete second order equation describing the relation between the capillary suction and the suction time was developed. Varying geometries of the pipes of the capillary system were investigated including the effects on the flow rate of varying combination of lengths, radius and sequence (expansion $\rightarrow$ contraction and contraction $\rightarrow$ expansion series). The results showed that largest flow reductions occurred with very narrow sections causing a blocking, reducing the capillary flow rate vs. square root of time several ten folds compared to uniform pipes without diameter variations. Similar results were also obtained for the random size models. The often observed phenomenon of reduced flow below the straight line water uptake vs. square root of time could be simulated with the multiple diameter pipe model, as seen by comparing simulations with experiments with varying concrete qualities and sample thicknesses in simple capillary absorption tests.

Key Words: Concrete, Capillary absorption, Pore necks, Modeling and Experiments

1 INTRODUCTION

Following the suggested analytical model previously developed and investigated in terms of flow conditions [1] we here further investigate the capillary absorption in concrete. We particularly investigate the deviation from the square root time vs absorption law. This deviation or anomalous

capillary absorption has been observed and investigated by several, see for example [2],[3],[4] and [5]. In this second paper we proceed by investigating the behavior with our new model. This is done by investigating absorption vs square root of time relationships of three different types of pore- or pipe systems, contraction model (water going from large to small pore or pipe), expansion model (vice versa) and a random sized system where pipes of different radii and lengths follow each other up to a desired total length. The expansion- and contraction models are coupled in series so that they are repeated a sufficient number of times to give a desired total length, comparable to the thickness of a concrete specimen tested for capillary suction, without tortuousity network or branches etc.

The models investigated only consider straight pipes, which is a simplification since real concrete can have some kind of network with interconnections distributed at varying angles and lengths in space. Our straight pipe model is designed to investigate whether narrow passages between capillary size pores may slow down capillary suction rate and cause the anomalous absorption behavior discussed in part one of this study. Are such pore necks sufficient to explain the behavior often seen in experiments with increasing deviation from the straight line absorption vs square root time as specimen thickness and the number of necks increase?

Other effects have also been proposed as explanation. Air can be entrapped, compressed and/or dissolved in voids during capillary suction in concrete [6]. Furthermore, there is a significant volume fraction of gel pores in concrete that are too small for the capillary suction mechanism [7]. Neither effects of air nor gel are taken into account in our study. Still we believe that since the fraction of capillary active porosity in most concrete is quite large, the present model will give a useful illustration of the problem.

2   FLOWMODELS

Consider laminar flow in a circular pipe with with $N-$ subsections (Figure 1, where, r_i and l_i , $i = 1, 2, ..., N$ are section radius and length respectively). And, assume that the water front reaches the position h.
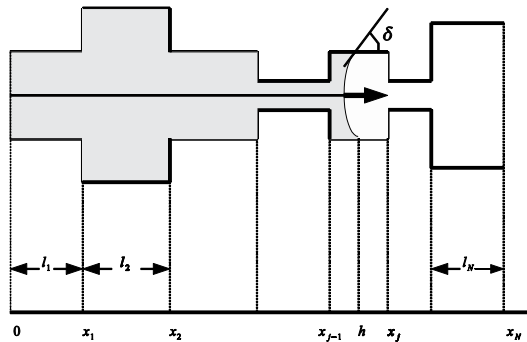

Figure 1- Pipe with $N-$ irregular subsections

Analyticale formulas for the capillary flow height $h(t)$ based on the velocity u_h were developed the previous paper [1]. The velocity of the water flow at the front in an arbitrary section j as

shown in Fig. 1, can be determined with the following equation

$$u_h = \frac{k}{f(h)r_h^3}$$ (1)

where

$$k = \frac{\sigma \cos\delta}{4\mu}$$ (2)

Here, σ is the surface tension between water and air, μ is viscosity coefficient and δ the contact angle between the pipe wall and the wetting water front (Figure 1). And

$$f(h) = \int_0^h \frac{dx}{r_x^4} \quad = \frac{l_1}{r_1^4} + \cdots + \frac{l_{j-1}}{r_{j-1}^4} + \frac{h - x_{j-1}}{r_j^4}$$
$$= \sum_{i=1}^{j-1} f_i + \Delta f_j,$$ (3)

$$f_i = \frac{l_i}{r_i^4} \quad and \quad \Delta f_j = \frac{(h - x_{j-1})}{r_j^4}.$$ (4)

The relation between the capillary velocity and the capillary height is given by the differential equation

$$u_h = \frac{dh}{dt}$$

which can be inserted in Eq. (1) and then integrated. This yields

$$\int_0^h r_s^3 f(s)ds = kt.$$ (5)

where s is an integration variable running over the tube sections with a stepwise changing radius r_s.

A solution of Eq. (5) will for a general variation in the cross section, require a numerical approach [8]. However, for a stepwise changing radius, it is possible to work out solutions by analytical means. We notice that the function $f(s)$ has to be continuous since it occurred from integrating a stepwise changing function [given by Eq. (3)], and linear in the individual tube sections as illustrated in Fig. 2. The left hand side of Eq. (5) may therefore be interpreted as the area under the graph $f(h)$ from 0 to h weighted by the section value r_h^3. With this in mind in addition to using the analytical formula for $f(h)$ [Eq.(3)] and for the area formula of a trapezoidal element, we get

$$\int_0^h r_s^3 f(s)ds = [r_1^3 A_1] + [r_2^3 A_2] + \cdots + [r_{j-1}^3 A_{j-1}] + [r_j^3 A_h]$$

$$= r_1^3 \left[\frac{1}{2} f_1 l_1 \right] + r_2^3 \left[f_1 l_2 + \frac{1}{2} f_2 l_2 \right] + \cdots$$

$$+ r_{j-1}^3 \left[(f_1 + f_2 + \cdots + f_{j-2}) l_{j-1} + \frac{1}{2} f_{j-1} l_{j-1} \right]$$

$$+ r_j^3 \left[(f_1 + f_2 + \cdots + f_{j-1}) + \frac{1}{2} \Delta f_j \right] (h - x_{j-1}) \qquad (6)$$

$$= \left[\sum_{i=1}^{j-1} r_i^3 l_i \left(\sum_{m=1}^{i-1} f_m + \frac{1}{2} f_i \right) \right] +$$

$$\left[r_j^3 (h - x_{j-1}) \left(\sum_{i=1}^{j-1} f_i + \frac{1}{2} \Delta f_j \right) \right].$$

From Eq. (6) we see that only the terms related to the front section or j-section, is a function of the capillary height h, while the other terms may be regarded as constants with respect to this parameter. Moreover, by inserting Eq. (6) into the left side of Eq. (5) and by substituting Δf_j from Eq. (4), we find that h and time t are related through the second order equation

$$\left[\sum_{i=1}^{j-1} r_i^3 l_i \left(\sum_{m=1}^{i-1} f_m + \frac{1}{2} f_i \right) \right] + \left(r_j^3 \sum_{i=1}^{j-1} f_i \right) \Delta h_j + \frac{1}{2r_j} (\Delta h_j)^2 = kt. \qquad (7)$$

As a short notation we have here introduced the relative height

$$\Delta h_j = h - x_{j-1}, \qquad (8)$$

measured from the starting position x_{j-1} from the last section. In addition, we will also introduce the parameters

$$C_{j-1} = \sum_{i=1}^{j-1} r_i^3 l_i \left(\sum_{m=1}^{i-1} f_m + \frac{1}{2} f_i \right) \qquad (9a)$$

$$B_j = r_j^3 \sum_{i=1}^{j-1} f_i \qquad (9b)$$

$$\overline{A_J} = \frac{1}{2r_j} \qquad (9c)$$

to put Eq. (7) into the quadratic form

$$C_j + B_j \Delta h_j + \overline{A_J} \Delta h_j^2 \qquad (10)$$

Equation (10) is particularly interesting since many useful results may be deduced from it. The equation gives, for example, the required filling time t

$$t = \frac{C_{j-1}}{k} + \frac{B_j \Delta h_j + \overline{A_J} \Delta h_j^2}{k} \qquad (11)$$

for all pipe section up to h, for cases where h is specified. Here the first term provides the filling

time for the first $(j-1)$ sections while the second term gives the time needed to fill up the last section up to position h.

On the other hand, if the total filling time t is known or specified, Δh_j may easily be obtained from using the quadratic solution formula on Eq. (10), to give

$$\Delta h_j(t) = \frac{-B_j + \sqrt{B_j^2 - 4\overline{A_j}(C_{j-1} - kt)}}{2\overline{A_j}} \tag{12}$$

It should be noticed that since the fluid height is a positive value, only the positive root of Eq. (10) should be considered here.

It is also possible to recalculate well known capillary formulas for tubes with a uniform radius r_U from Eq. (10). From $r_1 = r_2 = \cdots = r_j = r_U$ we find the well known equation

$$h(t) = \sqrt{2r_U kt} = \left[\sqrt{\frac{r_U \sigma \cos \delta}{2\mu}}\right]\sqrt{t} \tag{13}$$

often refereed to as the Lucas-Washburn equation [9],[10] .
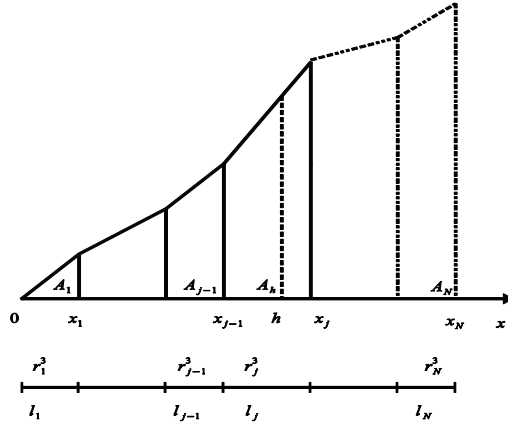

Figure 2- The areal under the graph of $f(h)$ from 0 to h, $A_1, \cdots, A_h$

Finally, we will show that the previously derived fluid velocity can be expressed in terms of the new notation, e.g. the $\overline{A}-$, $B-$ and $C-$ terms introduced in Eq. (9). This will give us an analytical expression for the velocity as a function of time. This time relation may be found by derivation of the flow height in Eq. (12) with respect to time, which yields

$$u_{\Delta h_j}(t) = \frac{d(\Delta h_j)}{dt} = \frac{d}{dt}\left[\frac{-B_j + \sqrt{B_j^2 - 4\bar{A}_j(C_{j-1} - kt)}}{2\overline{A_J}}\right] = \frac{k}{\sqrt{B_j^2 - 4\bar{A}_j(C_{j-1} - kt)}} \tag{14}$$

One should notice that this equation has to be identical to previous velocity expression given as a function of position u_h, for example, Eq. (1). To show this, the time t in Eq. (14) may be replaced by Eq. (11). This gives

$$u_h = \frac{k}{\sqrt{B_j^2 - 4\overline{A_J}\left(C_{j-1} - \left(C_{j-1} + B_j\Delta h_j + \overline{A_J}\Delta h_j^2\right)\right)}} = \frac{k}{B_j + 2\overline{A_J}\Delta h_j} = \frac{k}{f(h)r_h^3}$$

3   MODEL AND EXPERIMENTAL DATA

3.1   Contraction-expansion and expansion-contraction models

In order to study the influence of the pipe geometry on the absorption of water, we construct first several contraction-expansion sections (Model C) and expansion-contraction (Model E). Here the value of geometries are fixed as illustrated in Fig. 3. In addition a model with random geometries is investigated (Model R). As shown in Fig. 3, two different combinations of sections (a) and (b) give the structure of models C-E. Each combination has $(ns - N)$ sections.

When plotting the calculated absorption as (kg/m^2) vs square root time the absorption may simply be interpreted as a suction height to be compared with the results of Eqs.(12) - (14). To compare calculations with experiments where the pore volume varies depending on w/c, degree of hydration and fraction of cement paste (assuming non-porous aggregate) we could simply calculate the absorption in the form of weight. For this purpose we have calculated a mean pipe radius that we relate the degree of pore (or pipe-) filling to, for the C- and E-models, and for a random sized pore model,also taken into account the mean porosity.

For each set of models C or E, there is a corresponding model-U with the constant uniform mean volume radius r_U. We require the conservation of volume for these three models. Let V_C, V_E and V_U denote the volume for model C, model E and model U, respectively. In order to have the same volume for all three models, the radius r_U must satisfy the following condition:

$$V_C = V_E = V_U \Rightarrow \tfrac{1}{2}\pi(r_1^2 + r_2^2) = \pi r_U^2$$

or

$$r_U = \sqrt{\frac{r_1^2 + r_2^2}{2}}. \tag{15}$$

We observe that the radius r_U depends only on the radii r_1 and r_2 but not on the section lengths l_1 and l_2.

The volume (V) of the capillary absorbed water is calculated by the following equation
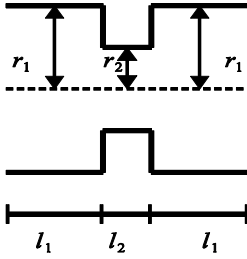
$$V(t) = \sum_{i=1}^{j-1} \pi r_i^2 l_i + \pi r_j^2 \Delta h_j(t) \qquad (16)$$
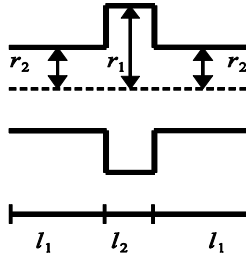
$\Delta h_j(t)$ is defined in Eq. (12).

The selection of data for the varying section lengths and section radii are given in Tables 1 and 2 respectively. Table 3 shows the relation between the value of radii r_1, r_2 and r_U.

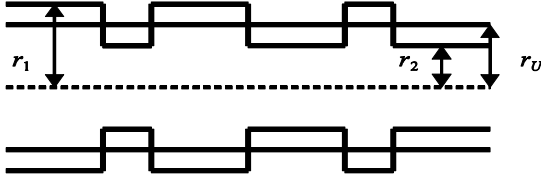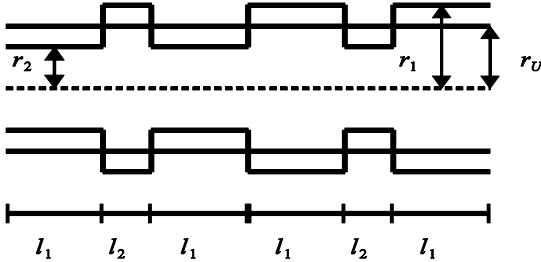*Figure 3- Model C, E with $ns = 3$, $N = 6$ sections and Model U with constant radius*

Table 1: Variation of section length for contraction-expansion and expansion-contraction series models

N	$L(m)$	$l_1(m)$	$l_2(m)$	$l_1:l_2$
6	0.04	0.0067	0.0067	1:1
6	0.04	0.005	0.01	1:2
6	0.04	0.008	0.004	2:1
30	0.04	0.0013	0.0013	1:1
30	0.04	0.0009	0.0018	1:2
30	0.04	0.0017	0.00086	2:1

Table 2: Variation of sections radii for contraction-expansion and expansion-contraction series models

$r_1(m)$	$r_2(m)$	$r_1:r_2$
1×10^{-6}	0.8×10^{-6}	1:0.8
1×10^{-6}	0.5×10^{-6}	1:0.5
1×10^{-6}	0.1×10^{-6}	1:0.1

Table 3: Relation between radii (r_1,r_2) *and* r_U

$r_1(m)$	$r_2(m)$	$r_U(m)$
1×10^{-6}	0.8×10^{-6}	0.905×10^{-6}
1×10^{-6}	0.5×10^{-6}	0.79×10^{-6}
1×10^{-6}	0.1×10^{-6}	0.71×10^{-6}

3.2 Experimental data

In addition to analyzing some capillary absorption data from the literature, a series of experiments with one sided capillary absorption was performed with two different concrete qualities. Specimens were produced from ordinary portland cement (ASTM Type II/CEM I 42,5 R) with blaine specific surface 384 m^2/kg, granitic aggregate with 8 mm maximum size, 9% fines less than $0.125mm$ and 0.5% absorption and a copolymer water reducer (Sika Viscocrete) added to obtain flowable consistency. Two different mortar mixes were made with $w/c = 0.45$ and 0.60, respectively. Both mixes had 39 percent cement paste and 2 percent air void. Fifty litre batches were made in an 80 liter horizontal rotating paddle mixer and cylindrical specimens with diameter 100 mm and height 200 mm were cast in two layers in steel molds with slight compaction on a vibrating table between each layer. The cylinders were de-moulded after 24 hours and cured in water at 20^oC for approximately four months. Then, slices with thickness 20, 40 and 100mm where cut normal to the cylinder axis. The slices were dried at 105^oC to constant weight, air cooled to room temperature and sealed on their lateral surfaces to ensure undirectional flow of water. For each material and thickness four specimens were weighed regularly. Plots of capillary absorption in weight vs square root of time $\left(W(t) - \sqrt{t} \; : \; [kg/m^2]\right)$ are shown in Fig. 4. We clearly see the vanishing nick points at increasing thickness and reduced w/c.
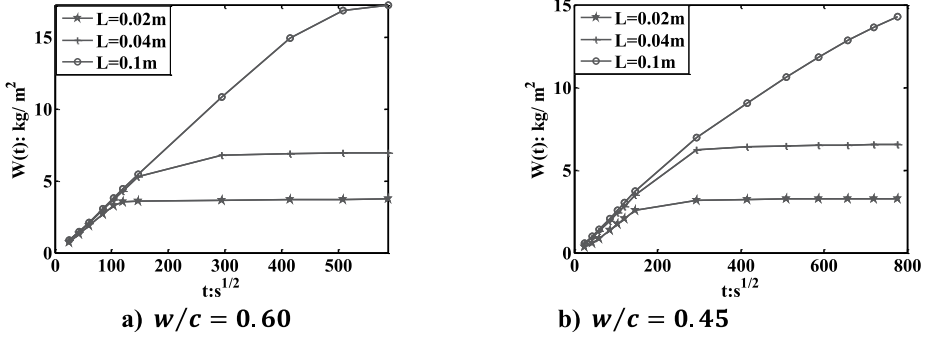
a) $w/c = 0.60$　　　　　b) $w/c = 0.45$

Figure 4- Experimental capillary suction for mortar specimens with ordinary Portland cement, $w/c = 0.60$ and 0.45, non-porous aggregate, and different thickness L as $20, 40$ and $100\ mm$.

The suction porosities of the specimens were measured following the capillary absorption test by total immersion until constant weight and determining volume by weighing in air and in water. Then hydration was calculated based on Powers model [7] and the formulae [11] $p_{tot} = (w/c - 0.172\alpha)/(w/c + 1/\rho_c)$, where α is degree of hydration and ρ_c is particle density of cement. Finally, the capillary porosities were determined according to Powers model with the following formula by [11], $p_{cap} = (w/c - 0.415\alpha)/(w/c + 1/\rho_c)$. Tab. 4 gives the results.

Table 4 indicates around 40% fraction of capillary porosity compared to the total porosity for our specimens according to the differentiation between gelpores (where meniscii do not exist)- and capillaries based on the sorption experiments of Powers and Brownyard [7]. Compared to our previous discussion about the tensile strength of water it means that around 60% of the pore volume could be filled by other suction mechanism than capillay suction mehanisms. Our interpretation of the results then excludes the filling of the other pores which is obviously a source of error. Nevertheless we believe that the approach presented in this paper can give information about the possibility that pore necks may cause the capillary absorption anomaly as discussed in the introduction.

Table 4: Total- and capillary porosity (m^3/m^3) and degree of hydration α in the mortar with $w/c = 45$ and 60 as measured and combination with caculated based on Power models for cement paste porosity and 39 volume $-\%$ cement paste in the mortar. Aggregate assumed non-absorbing.

w/c	p_{tot}	$p_{capillary}$	α
0.45	0.16	0.064	0.78
0.60	0.18	0.0678	1.0

We have also replotted experimental data from two other studies on capillary absorption and compared these with our model. In [4] the effect of initial moisture content was investigated, whereas in [3] a continuum modelling approach based on sorptivity and Richards equation was compared with absorption and NMR-measurements.

3.3   Random size pores model

In addition to models C and E we let the value of the section radii be random and section lengths be fixed. A uniform pseudorandom function generated a uniform distribution of random values on a specified interval , $r_i \in I = [r_{min}, r_{max}]$, [12].

Let n be the number selection of random of radii $(r_i)_1^N$ and assuming a uniform random distribution of radii in the interval $[r_{min}, r_{max}]$. The following matrices V and T express the capillary suction volume and time as

$$V = \begin{pmatrix} v_{1,1} & v_{1,2} & \cdots & v_{1,N} \\ v_{2,1} & v_{2,2} & \cdots & v_{2,N} \\ \vdots & & & \vdots \\ v_{n,1} & v_{n,2} & \cdots & v_{n,N} \end{pmatrix}$$

$$T = \begin{pmatrix} t_{1,1} & t_{1,2} & \cdots & t_{1,N} \\ t_{2,1} & t_{2,2} & \cdots & t_{2,N} \\ \vdots & & & \vdots \\ t_{n,1} & t_{n,2} & \cdots & t_{n,N} \end{pmatrix}$$

where $v_{i,j}$ is the capillary suction volume as the water front reaches the end of section number j (see Eq.(16)) at the selection nummer i, $i = 1,2,...,n$; $j = 1,2,...,N$. Hence, the corresponding suction time is $t_{i,j}$.

In practice, particularly for a random problem the mean value of V and T are most interesting. Now let $\overline{V}$ and $\overline{T}$ represent the mean value of V and T respectively. These new parameter are expressed by the following equation

$$\overline{V} = \overline{v}_j = \frac{1}{n}\sum_{i=1}^{n} v_{i,j} \quad and \quad \overline{T} = \overline{t}_j = \frac{1}{n}\sum_{i=1}^{n} t_{i,j} \quad j = 1,2,\cdots,N \tag{17}$$

Eq.(17) shows that the mean value of the matrix $\overline{V}$ is simply a row vector containing the mean value of each column $\overline{v}_j$, corresponding with the mean value of time $\overline{t}_j$. In the procedure which was presented in section 3.1, we introduced the model with uniform constant radius (Model U) which has the same capillary suction volume. Hence, if r_U is a radius to model U then the constant radius for model U is obtained from:

$$r_U = \sqrt{\frac{\overline{v}_N}{\pi L}} \tag{18}$$

where L is the length of pipe.

4 RESULTS AND DISCUSSION

The results for model capillary absorption calculated with the analytical expression (AE) presented in this section are based on density of water $\rho = 1000 \ kg/m^3$, surface tension between air and water $\sigma = 0.073 \ N/m$, viscosity of water $\mu = 0.001 \ kg/ms$, and contact angle between concrete and air-water surface $\delta = 0$. The calculated capillary suction results are based on the time for the flow front to reach the end of the last section (e.g section N). The capillary suction experiments are based on the regular weighing of specimens stored with one side in water and using total porosity to water measured on the same concrete specimens.

Calculation of absorption is based on the weight at the time $t_i, i = 1,2, \cdots$, of the different concrete specimens that we compare the models with, or

$$W(t) = \frac{W_i}{A} \tag{19}$$

where W_i is weight of absorbed water in time step t_i (kg), either caculated with one of the Analytical models C (Contraction), E (Expansion), U (Uniform) or R (Random) or measured during capillary expansion experiments. A is area of the actual concrete specimen tested, or $A = A_U/\rho_{tot}$ for Analytical models, where A_U is the area of $U-$model and ρ_{tot} is the actual total porosity.

Note that the capillary rise in the uniform tube (model U) (Fig. 3) is a straight line function of square root of time as described by the line $\left(W(t) - \sqrt{t}\right)$. By comparing the capillary suction of the varying models with this line, we can see how strong the effect of the different geometries are on the capillary rise.

Fig. 5 shows that the varying pipe geometries have large effects on the capillary suction. For constant section length (Fig. 5(a) to (c)) it seems that the capillary rise of models C-E practically stops when $[r_1:r_2]$ is reduced from $[1:0.8]$ to $[1:0.1]$, since models C and E used much more time to absorb as much as did model U. This is illustrated by keeping section length equal, $l_1 = l_2$. Then, the times for the three models to reach the total suction volume or capillary nick point L are $\sqrt{t_U} \approx 6.95\sqrt{s} < \sqrt{t_C} \approx 7.51\sqrt{s} < \sqrt{t_E} \approx 7.59\sqrt{s}$, when $[r_1:r_2]=[1:0.8]$, while $\sqrt{t_U} \approx 7.44 < \sqrt{t_C} \approx 14.30 < \sqrt{t_E} \approx 14.64$, when $[r_1:r_2] = [1:0.5]$, and $\sqrt{t_U} \approx 7.85 < \sqrt{t_C} \approx 326.46 < \sqrt{t_E} \approx 335.91$, when $[r_1:r_2] = [1:0.1]$. The latter capillary nick point times of around 300 - 400 square-root seconds are in the same order of magnitude as experimental nick points seen on slices made of normal weigh ordinary portland cement concrete with $w/c > 0.40$ and approximately $30mm$ thickness. The flow thus seems to more or less stop when passing one or several narrow/large contraction/ expansion sections. Clearly, there is some kind of blocking phenomenon (see Fig. 5). Also, combinations of varying both section length and section radius give very interesting capillary suction curves. When $l_1 = l_2$ and the ratio of radii vary from $[r_1:r_2] = [1:0.8]$ to $[1:0.1]$, the capillary suction curves for both models C-E are almost linear like the uniform pipe model as shown in Figs. 5 (a-b-c). On the other hand, when variation of section length is introduced, i.e. $[l_1:l_2]$ is changed from $[1:1]$ to $[1:2]$ for $[r_1:r_2] = [1:0.8]$, $[1:0.5]$ and $[1:0.1]$, the suction curve of model E obeys the linear behavior until the flow passes approximately 2/3 of the total suction volume, where-after the curves deviate from the linear behavior (as shown in Figs. 5 (d-e-f)). The same trend is observed for model C

where the sequence of the long and short pipe is switched for the contraction model for $[l_1:l_2]=$ $[1:1]$ and $[2:1]$. Apparently, the anomalous type of capillary suction curves we are interested in can be studied with both contraction and expansion models when the wide section are the longest, and are separated from each other with short, thin pipes. Reducing the radius of the small, short, pipe from 0.5:1 to 0.1:1 also makes the time scale of the analytical model similar to the time scale of capillary suction experiments shown in Figure 1 in part 1 and in the experimental data presented in the last figures of this paper.
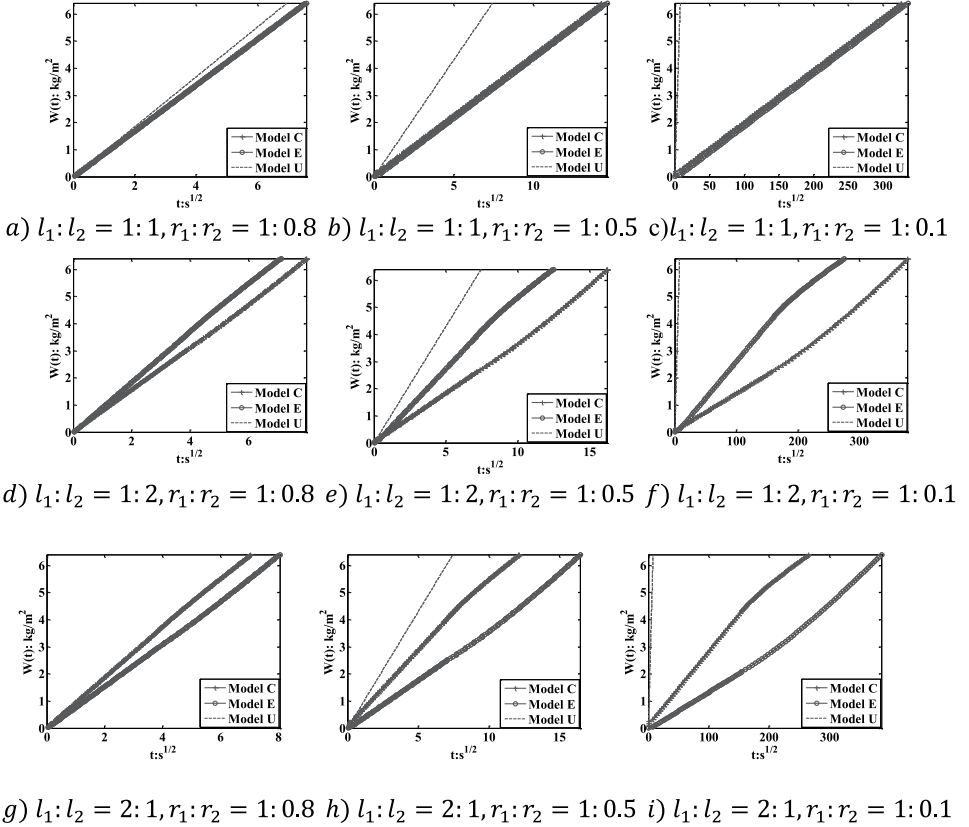

a) $l_1:l_2 = 1:1, r_1:r_2 = 1:0.8$ b) $l_1:l_2 = 1:1, r_1:r_2 = 1:0.5$ c) $l_1:l_2 = 1:1, r_1:r_2 = 1:0.1$

d) $l_1:l_2 = 1:2, r_1:r_2 = 1:0.8$ e) $l_1:l_2 = 1:2, r_1:r_2 = 1:0.5$ f) $l_1:l_2 = 1:2, r_1:r_2 = 1:0.1$

g) $l_1:l_2 = 2:1, r_1:r_2 = 1:0.8$ h) $l_1:l_2 = 2:1, r_1:r_2 = 1:0.5$ i) $l_1:l_2 = 2:1, r_1:r_2 = 1:0.1$

Figure 5- Analytical water absorption curves $\left(W(t) - \sqrt{t}\right)$ *for models C, E and U, where* $N = 30$, *and* $L = 0.04m$, *and* $\rho_{tot} = 0.16$.

Figure 6 shows the effect of the random sized pipes by comparing the capillary suction for model R and the corresponding model with constant radius (model U). The length of the large and the small pipes are 1:1 and 1:2, whereas the ratios of radii vary as 1:1, 0.5:1 and 0.1:1. We see that, just as for the Contraction and Expansion models, there is little effect on the capillary suction compared to the uniform model by varying the radius of the small pipe as the length of the large pipe is as short as $l_1:l_2 = 1:1$. In addition there is no effect of increased length $l_1:l_2 = 1:2$.
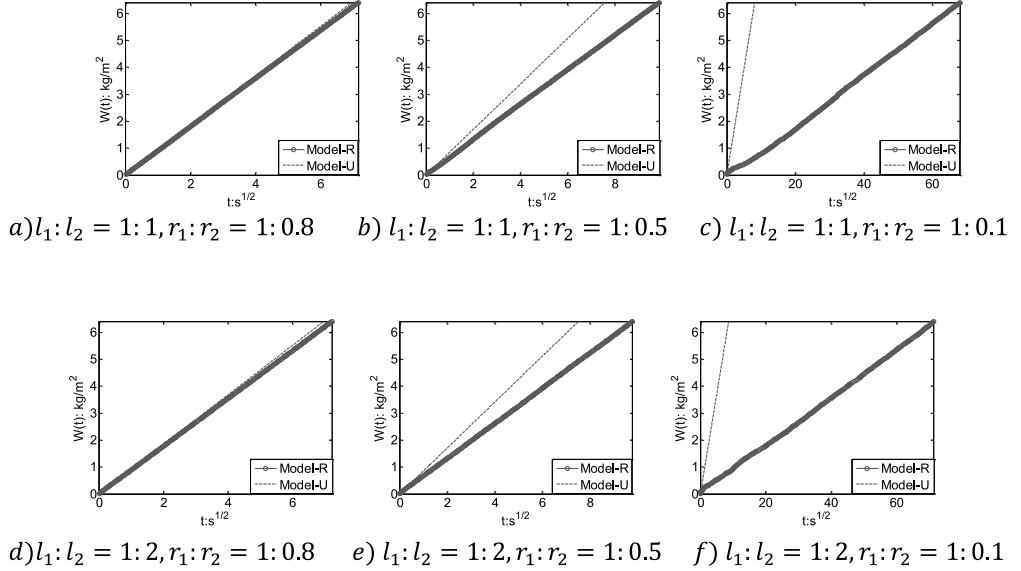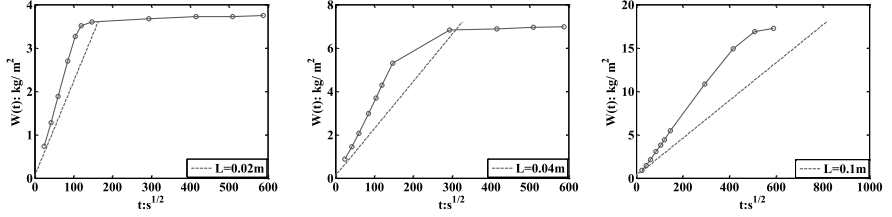
a) $l_1 : l_2 = 1 : 1, r_1 : r_2 = 1 : 0.8$ b) $l_1 : l_2 = 1 : 1, r_1 : r_2 = 1 : 0.5$ c) $l_1 : l_2 = 1 : 1, r_1 : r_2 = 1 : 0.1$

d) $l_1 : l_2 = 1 : 2, r_1 : r_2 = 1 : 0.8$ e) $l_1 : l_2 = 1 : 2, r_1 : r_2 = 1 : 0.5$ f) $l_1 : l_2 = 1 : 2, r_1 : r_2 = 1 : 0.1$

Figure 6- Analytical water absorption curves $\left(W(t) - \sqrt{t} \right)$ for models R (Random) and U where $N = 30$ and $n = 50$, and $p_{tot} = 0.16$.

We then compare the behavior observed in the AE-results with our own capillary absorption experiments as well as with the data from the literature.

Fig. 7 compares calculated capillary suction with two different pipe geometries for the $w/c = 0.60$ specimens were the ratio of radii between large and small pipes are always kept at $1 : 0.1$ or $1 \times 10^{-6} m : 0.1 \times 10^{-6} m$, based on the observations in Fig. 5. The main pipe geometry variable for the two plots is the length ratio between the large and the small pipes. From the plots we can see clearly how the calculated absorption approaches the measured absorption as the length ratio between the large and small pipes increases from $1:1$ to $2:1$. It is very interesting to note that the calculated capillary suction seems to give the right kind of increasing anomaly at increasing suction length, i.e at increasing specimen thickness. Apparently the increased number of necks has the right kind of effect compared to what is commonly seen in capillary suction experiments.

a) $l_1 : l_2 = 1 : 1, r_1 : r_2 = 1 : 0.1$ *b)* $l_1 : l_2 = 1 : 1, r_1 : r_2 = 1 : 0.1.$ *c)* $l_1 : l_2 = 1 : 1, r_1 : r_2$
            $= 1 : 0.1$ $= 1 : 0.1$
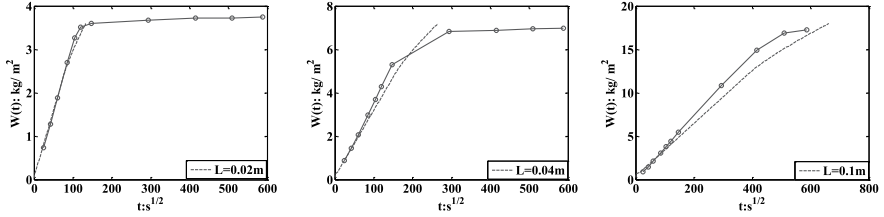
d) $l_1 : l_2 = 2 : 1, r_1 : r_2 = 1 : 0.1$ *e)* $l_1 : l_2 = 2 : 1, r_1 : r_2 = 1 : 0.1.$ *f)* $l_1 : l_2 = 2 : 1, r_1 : r_2$
            $= 1 : 0.1$ $= 1 : 0.1$

Figure 7- Analytical (dashed lines, Model C) and Experimental (full lines with circles) water absorption curves $\left(W(t) - \sqrt{t} \right)$ *for* $w/c = 0.60$, *and for three different pipe/specimens length/thickness, and* $p_{tol} = 0.18$.

Fig. 8 shows the same type of plots as in Fig. 7 with Ordinary Portland Cement specimens with $w/c = 0.45$. In this plot we see that a slightly different pipe geometry with similar length of the large and small pipes fits the measured absorption best of the two investigated geometries. Possibly a somewhat larger fraction of smaller pores in $w/c = 0.45$ with less continuity compared to $w/c = 0.60$ is represented by this geometry (figure 7).
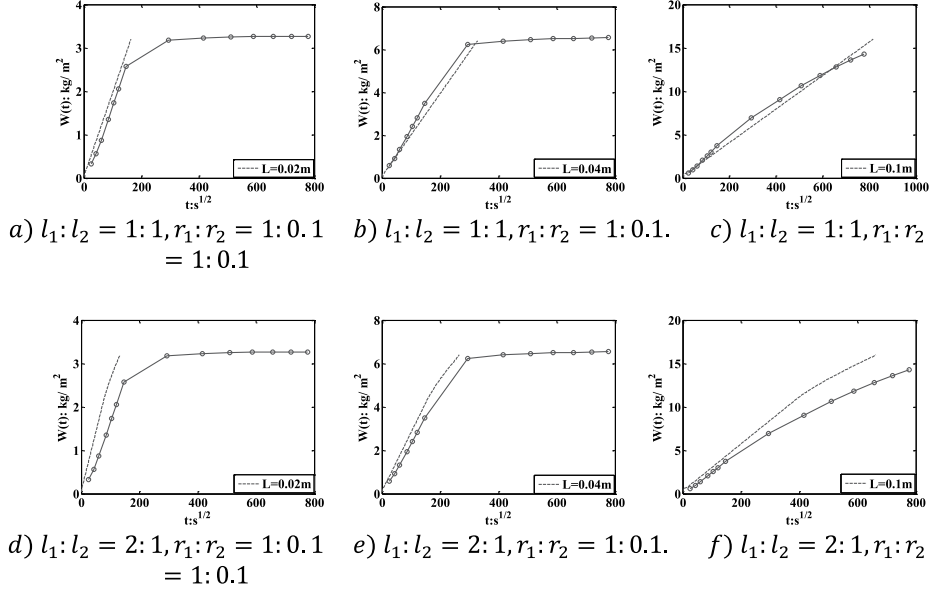
a) $l_1 : l_2 = 1 : 1, r_1 : r_2 = 1 : 0.1$
$= 1 : 0.1$

b) $l_1 : l_2 = 1 : 1, r_1 : r_2 = 1 : 0.1.$

c) $l_1 : l_2 = 1 : 1, r_1 : r_2$
$= 1 : 0.1$

d) $l_1 : l_2 = 2 : 1, r_1 : r_2 = 1 : 0.1$
$= 1 : 0.1$

e) $l_1 : l_2 = 2 : 1, r_1 : r_2 = 1 : 0.1.$

f) $l_1 : l_2 = 2 : 1, r_1 : r_2$
$= 1 : 0.1$

Figure 8- Analytical (dashed lines, Model C) and Experimental (full lines with circles) water absorption curves $\left(W(t) - \sqrt{t} \right)$ for w/c = 0.45 , and for three different pipe/specimen length/thickness, and $p_{tot} = 0.16$.

Fig. 9 shows experimental capillary suction data from the literature [4] together with the model. The actual concrete has w/b = 0.40 and two percent condensed silica fume, and so has a low fraction, if any, of capillary porosity according to Powers model. From the figure it can be seen that the changing of pipe geometry that worked successfully with high w/c in Fig. 7 with 1 : 0.1 ratio between radii and a bit longer large pipe -sections is less successful. The reason could be the slow capillary suction in these specimens due to more narrow necks at w/c = 0.45 compared to at w/c = 0.60 .
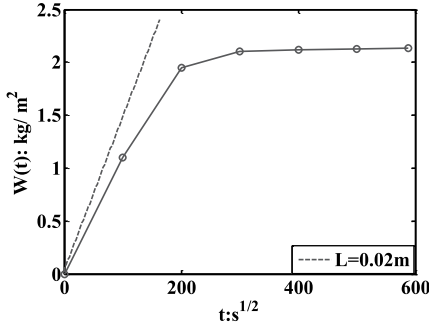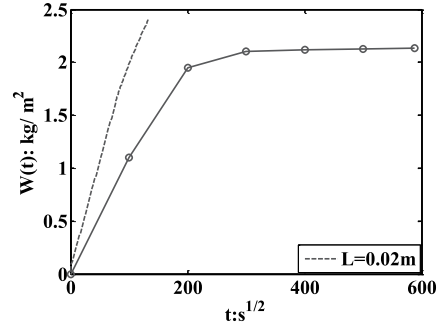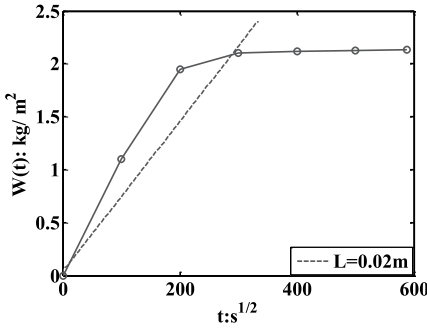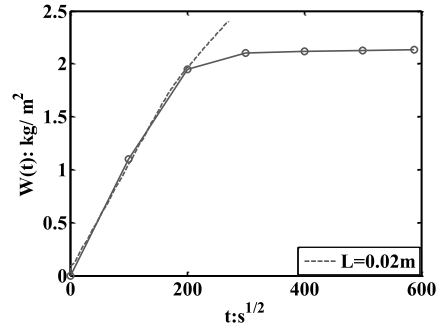
a) $l_1: l_2 = 1:1, r_1: r_2 = 1:0.1$

b) $l_1: l_2 = 2:1, r_1: r_2 = 1:0.1$

c) $l_1: l_2 = 1:1, r_1: r_2 = 1:0.07$

d) $l_1: l_2 = 2:1, r_1: r_2 = 1:0.07$

Figure 9- Experimental data [4] (full lines) and analytical (dashed lines) water absorption curves $\left(W(t) - \sqrt{t} \right)$ *and* $p_{tot} = 0.12$.

Fig. 10 shows experimental capillary suction data of ordinary portland cement mortar with $w/b = 0.40$ taken from [3] showing a similar tendency as in figure 9.
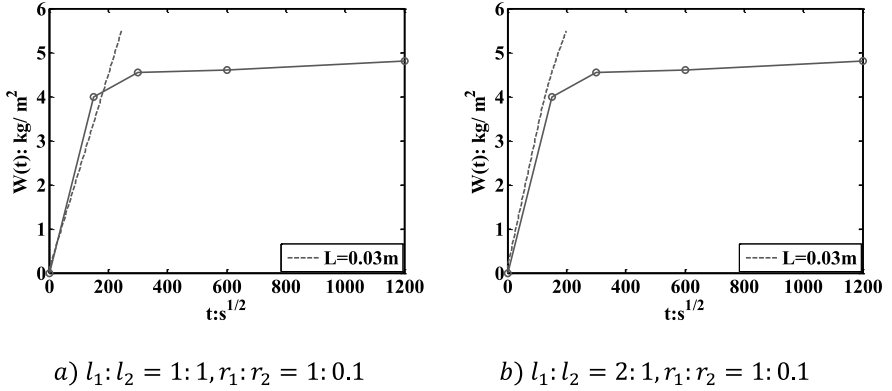
a) $l_1 : l_2 = 1 : 1, r_1 : r_2 = 1 : 0.1$ b) $l_1 : l_2 = 2 : 1, r_1 : r_2 = 1 : 0.1$

Figure 10- Experimental data [3] (full lines) and analytical (dashed lines) water absorption curves $\left(W(t) - \sqrt{t}\right)$ *for slices with* $w/c = 0.40$ *and* $p_{tot} = 0.18$.

The total length of the model pipes compared to the thickness of the specimen is a matter of uncertainly. We have in most of our comparisons between calculated and experimentally measured capillary suction assumed a total pipe length equal to the thickness of the specimens. Due to factors such as entrapment of air in a network and torturousity this may be wrong and we should expect the model suction to stop before the experimental suction. However, this is not always seen, for example in the 20 mm thickness slices of own data, and also in the data [3]. Clearly more work in the calculation of the correct total absorption should be made. We believe, however, that the present investigation has shown that the kind of narrowing or pore-neck effect proposed can at least partly explain the deviation from the square root time law often seen in concrete capillary suction experiments.

The present results also demonstrate a contradiction between the restriction of capillary theory due to the tensile strength of water (minimum capillary pore size approximately $3 \times 10^{-7} m$) and the application of a sort of "effective capillary radius" which can be as low as $10^{-11} m$ when applying Eq.13, see also [2], [4], [6], [13]-[15]. This scale problem is possibly solved to a large part by the accumulated effect of repeated necks with high flow resistance, possibly together with some kind of slow diffusion mechanism filling the gel-type pores smaller than those filled by the capillary mechanism. This could be further investigated in future modelling with some sort of overlapping diffusion-loss from the water in the pipe-shaped pores into the pipe walls made of gel-material. This introduction of a multi-scale mechanism would still keep the model on a relatively simple yet realistic and sound physical basis, proved that an algorithm or computational method requiring little computational power can be developed.

Finally we should also mention that the total porosity in the model absorption was taken as total porosity to water. The filling mechanisms is, however, only active in a fraction of the pore volume. This also has take to be taken better care of in more advanced modelling, possibly by the kind of multi-scale modelling mentioned above.

5 CONCLUSIONS

Comparison of capillary suction experiments on concrete with different binder qualities and

specimen thickness was made with a relatively simple pipe model consisting of a series of pipes with different diameter and length put together at regular intervals and also using random sized pipes.

The objective was to investigate to what extent the very slow capillary absorption with increasing deviation from the straight line square root of time law could be explained with narrow pore necks. Following the development and validation of the model on local flow conditions in part 1, we have here made a systematic comparison with real capillary absorption data from own experiments as well as some experimental data from the literature.

Realistic time scales for capillary filling can be obtained for series of pipes consisting of only large and small pipes of diameter in the order 1 and 0.1 microns, respectively. There has to be somewhat larger length than radius for the larger pipe in order to fit capillary suction for $w/c = 0.60$ compared to $w/c = 0.45$. The calculated capillary absorption then fits our experimentally measured absorption in slices with different thickness (20,40 and 100 mm), in line with the increased number of necks with increasing thickness and higher fraction of coarser capillary at heigh w/c. The comparison with experiments from the literature were in line with the comparisons with own experiments.

6 ACKNOWLEDGMENT

REFERENCES

[1]   Hung, Nguyen T.; Frank, Melandsø; Stefan, Jacobsen (2009): Analytical and numerical solution for capillary suction velocity and hight in pores with multiple sizes.   *Paper part 1, submitted together with this paper*.

[2]   Hoff, W. D.; Hall, C.(2002): Water transport in brick, stone and concrete.   Spon press London and New York.   , 318p.

[3]   Hazrathi , K. (1998): Etudes des mechanismes de transport de l'eau par absorption capillare dans des materiaux cimentaires conventionels et de haute performance.   PhD, Laval University.

[4]   Erik, J. Sellevold; Jonni, Punkki. (1994): Effects of drying procedure.   Nordic Concrete Research.   15, 59--74.

[5]   Hansic, L. (2005): Capillarity in concrete.   PhD, University of Lubljana.

[6]   Fagerlund, G. (1982): On the capillary of concrete.   Nordic Concrete Research.   1, 20p.

[7]   Powers, T. C.; Brownyard, T. L.(1948): Research Lab. Portland Cement Associantion. Bull.   22 .

[8]   Wen-Bin Young. (2004): Analysis of capillary flows in non-uniform cross-sectional capillaries.   Colloids and Surfaces A: Physicochem. Eng.   234, 123--128.

[9]   Karoglou, M.; Moropoulou, A.; Giakoumaki, A.; Krokida, M.K. (2005): Capillary rise kinetics of some building materials.   Colloids and Interface Science.   284, 260--264.

[10]   Barbare, Nikhil; Shukla, Arun; Bose, Arijit. (2003) : Uptake and loss of water in a cenosphere-concrete composite material.   Cement and Concrete Research.   33, 1681--1686.

[11]   Erik J. Sellevold; Tom Farstad (2005): The PF-method-A simple way to estimate the w/c-ratio and Air content of Hardened Concrete.   Mindess Symposium ConMat Conference, UBC, Vancouver Canada   .

[12]   Matlab versjon 7.4.0   .

[13]   Garboczi, E. B. D. (1999): Computer simulation and percolation theory applied to concrete. Annual reviews of computational Physics VII, World Sc. Publ. comp.   , 85--123.

[14]   Fagerlund, G.(1991): Unpublished data cited by E.J Sellevold in course compendium post graduate course Concrete Structure.   Norway Univ. Science and Technology.

[15]   Nicos, S. Martys; Chiara, F. Ferraris (1997): Capillary transport in mortars and concrete. Cement and Concrete Research   27, 747--760.

Testing of Ring Fibres – Measurements in Fresh and Hardened Concrete

Sindre Sandbakk, MSc, PhD-student
SINTEF Building and Infrastructure
NO-7465 Trondheim
E-mail: sindre.sandbakk@sintef.no

Lars Haugan, MSc
SINTEF Building and Infrastructure
NO-7465 Trondheim
E-mail: lars.haugan@sintef.no

Gunrid Kjellmark, MSc
SINTEF Building and Infrastructure
NO-7465 Trondheim
E-mail: gunrid.kjellmark@sintef.no

ABSTRACT

In the present paper, the effect of ring fibres in concrete is analyzed and discussed. The effect of ring fibres in both fresh and hardened phase is studied. In the fresh state, the loss of workability is studied by means of reduced slump and slump-flow with increasing fibre volume. In the hardened state, the ring fibre reinforced concrete's tensile strength and flexural tensile strength are investigated with different ring fibre content. The results from the experimental work show that adding ring fibres to the concrete does not reduce the workability more than acceptable, and that the hardened properties are improved.

Key words: Concrete, fibre reinforcement, ring fibres

1   INTRODUCTION

1.1   Background

All commercially available fibres are linear with different types of anchoring. Linear fibres have clear limitations in use since the dosage needed to change the concrete mechanical properties destroys workability of the concrete in large extent. Ordinary fibres are gradually pulled out of the concrete, a mechanism that results in an achieved tensile stress less than the fibre's fracture stress. Furthermore, ordinary fibres may take up less load the greater the deformations are, providing a material with strain-softening behaviour.

There is reason to believe that the ring-shaped fibres are better both for workability and mechanical influence of hardened concrete. Given the workability, there is reason to believe that fibre balling because of the end anchorage can be avoided. At high dosages fibre balling is a common problem. Considering the mechanical properties of hardened concrete, there is reason to believe that the rings are drawn out with greater resistance than ordinary fibres. There is also reason to believe that the fibre orientation will be more beneficial, since the circular fibres have the same capacity in two dimensions, as opposed to ordinary fibres which has that extension in only one dimension.

There is currently limited knowledge of such fibres in the literature. In 1974, Michael Tylor [1] studied the effect of fibres with a square look. These fibres were cut from a mesh reinforcement. The diameter of these fibres was 1.6 mm, with a side length of 25 mm. The experience from this study was that these fibres did not congest in the mix, and the fibres were able to increase the concretes ductility. Whether ductility increases more than corresponding amounts of ordinary fibres in concrete did not appear in this report. In 1984 Michael Tylor [2] compared straight fibres and circular fibres. In this study Tylor found that circular fibres reduced the variation in compressive strength and tensile strength, although the strength was not affected in particular. When the circular fibres were compared with ordinary straight fibres, Tylor concluded that the ring fibres had three times higher pull out resistance than straight fibres.

Stages & Minor [3], Gasparini & Faieta [4] and Choi & Lee [5] have also conducted surveys of circular fibres. Common to all the studies are:
- The risk of congesting of fibres is eliminated.
- The effect on mechanical properties is better than for equivalent amounts of ordinary straight fibres.

1.2   Objective

The aim of this pilot study was to investigate the effect of ring-shaped fibres in self-compacting concrete. It was of interest to investigate both the fresh properties and hardened properties.

Concerning fresh properties, it of interest to determine the maximum fibre content, and examine how increasing fibre content affects the concrete consistency.

With regard to hardened properties, it is of interest to examine tensile and bending strength after cracking. Compressive strength was tested to verify that the concrete from various mixtures are of equal quality.

2   EXECUTION

In the absence of commercially available ring fibres, key rings were used. Key rings were ordered in three different sizes, ring diameter 30 mm, 20 mm and 12 mm. Unfortunately, the material strength is not known. The test program was designed to give as much information as possible with the lowest amount of fibres. Figure 1 shows a principle drawing of the rings.
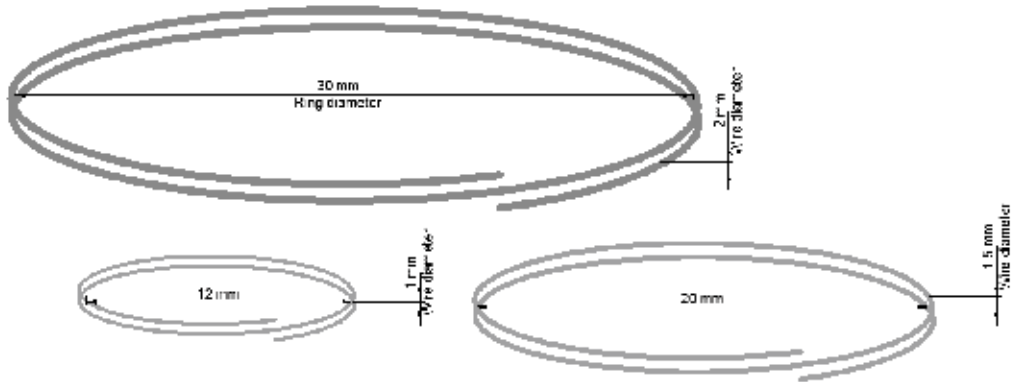

Figure 1 – Key rings used as ring fibres

2.1   Concrete mix

For these experiments, a reference concrete mix which previously has been used in many experiments on fibre reinforced concrete at SINTEF and NTNU were chosen. The mix does not provide a proper SCC, but it makes it possible to achieve a concrete with good workability at relatively high fibre content.   There were chosen to use a well known mix instead of a mix which gives a good SCC to make it possible to compare these results with other experiments performed on fibre reinforced concrete at SINTEF and NTNU. The reference mix is shown in Table 1.

Table 1 – Reference mix

Material	kg/m^3
Norcem Standard FA CEM II/A-V 42.5 R	367.8
Elkem Microsilica	22.1
Norcem Limestone powder	18.4
Årdal gravel 0-8 mm, natural gneissic granite	975
Årdal gravel 8-16 mm, natural gneissic granite	650
Sika ViscoCrete 3	1.9
Water (w/c=0.58; w/(c+∑fp)=0.52)	214.2

Elkem Microsilica has average particle size of approximately 15 μm, and 80 % of the particles have a particle size less than 5 μm [6]. The Norcem Limestone powder has a particle size from 1 μm to 200 μm, and 50 % of the particles have a particle size less than 20 μm. The particle size

distribution of Norcem Limestone powder is found by use of a Coulter Counter at SINTEF Materials and Chemistry.

Sika ViscoCrete 3 was used as superplasticizer since this admixture previously has turned out to be effective over a time period of at least 30 minutes. To complete the planned experiments it is required to have a concrete with stabile fresh properties the first 30 minutes after water addition.

2.2   Mixing procedure

For concrete mixing, the procedure given in Table 2 was used. The fibres were mixed in just after the rest period.

Table 2 – Mixing procedure

Interval	Duration [min]	Action
1	1	Dry mixing
2	2	Wet mixing
3	2	Resting
4	2	Wet mixing
Total mixing time	7	

2.3   Test method

To determine the maximum fibre content, 10 litres of concrete was mixed. Increasing amounts of fibre were added, and slump, slump-flow and a visual assessment were performed to determine the maximum possible fibre content.

To determine the increasing fibre amount's effect on the fresh concrete properties, slump, slump-flow, air content and density were measured at 0 %, 0.25 %, 0.5 % and 1 % (% = volume fibre/volume concrete). In these experiments fibres with diameter 30 mm were used.

To determine the effect of increasing fibre content on the hardened concrete properties, the following tests were performed:
- 3-point bending test, beams with dimension 100×100×1200 mm
- Tensile strength test, prisms with dimensions 100×100×600 mm
- Compressive strength
  - cylinders with diameter = 100 mm and height = 200 mm
  - cubes 100×100×100 mm

Fibres with diameter = 30 mm were used in these experiments, and fibre volumes were 0 %, 0.5 % and 1.0 %, respectively

In addition, a concrete with fibres of different diameters (30 mm, 20 mm and 12 mm) was mixed. Fresh properties were measured and test specimens were cast as described above for this concrete as well. The fibre content of this last series was:
- 0.5 % (268 g 30 mm fibre, 451 g 20 mm fibre and 451 g 12 mm fibre. Total 1170 g).
- 1.0 % (536 g 30 mm fibre, 902 g 20 mm fibre and 902 g 12 mm fibre. Total 2340 g).

The 3-point bending tests on 1200 mm long beams were performed according to a standardized SINTEF test procedure. This test procedure is normally used to analyze the toughness of different concrete mixes without fibre reinforcement. It was decided not to use the European test method for fibre reinforced concrete, EN 14651, because the volume of one EN 14651-beam is about 12 litres, and the shape of the beam makes it impossible to reuse the test specimen in for instance uniaxial tensile strength test.

The tensile strength tests were also performed according to a standardized SINTEF test procedure, while tests on compressive strength, slump, density, air content and slump-flow were performed according to EN 12390-3 [7], EN 12350-2 [8], EN 12350-6 [9] EN 12350-7 [10] and EN 12350-8 [11], respectively.

2.4   Casting order

The amount of available fibres was limited, and to be able to accomplish as many investigations as possible, the following casting program was performed.

Mix 1: 10 litres
The purpose of trial mix 1 was to find an upper limit for the amount of ring fibre the concrete can withstand before fibre balling or segregation takes place.

Mix 2: Reference 50 litres
The purpose of this mixture was to determine the loss of consistency as a function of time. The concrete was mixed without fibre, and slump, slump-flow, air content and density were measured 10 min, 20 min and 30 min after the water addition.

Three beams with dimension 100×100×1200 mm were cast. Bending tests were performed to determine the concrete's flexural tensile strength. When the bending tests were finished, the two remaining 100×100×600 mm prisms were used for tensile strength tests. The ends of each 1200 mm beam were not subjected to large stresses. From these two ends two cubes 100×100×100 mm, which were used for testing compressive strength, were cut out.

In addition, three cubes (100×100×100 mm) and 3 cylinders (diameter = 100 mm and height = 200 mm) were cast from the reference mixture for compressive strength tests. This also made it possible to determine whether measuring compressive strength on the cut-off ends from the beams gives a reliable result.

Mix 3: 0.25 % and 0.5 % ring fibre, diameter 30 mm
The purpose of this mixture was to determine the effect of 0.25 vol % and 0.5 vol % fibres on the fresh properties, and 0.5 vol % fibres on the hardened concrete properties.

The concrete was first mixed without fibre. Fresh properties were measured after 10 min. These measurements ensure that the concrete is equal to the reference concrete. 0.25 % fibres were then added and new measurements of fresh properties were performed 20 min after water addition. Additional amounts of fibres (0.25 %) were then added to give a total fibre content of 0.5 %, and measurements of fresh properties were performed 30 min after water addition.

Two beams with dimensions 100×100×1200 mm were cast from the concrete with 0.5 % fibres.

Mix 4: 0.5 % and 1.0 % ring fibre, diameter 30 mm
The purpose of this mixture was to determine the effect of 0.5 vol % and 1.0 vol % fibre on the fresh properties, and 1.0 vol % fibre on the hardened properties.

The mixing procedure was similar to mix 3, but with higher fibre content.

Mix 5: 0.5 % and 1.0 % ring fibre, diameter 30 mm, 20 mm and 12 mm
The purpose of this mixture was to investigate whether a combination of different ring diameters had better or worse effect on concrete. The distribution of the different ring diameters was:
- 30 mm: 22 %
- 20 mm: 39 %
- 10 mm: 39 %
- In total: 100 %

The mixing procedure was similar to mix 4. It may have been better to use 33 % of every fibre type, but due to shortage of 30 mm rings, the above-mentioned distribution was chosen.

3   RESULTS CONCERNING FRESH CONCRETE

3.1   Mix 1 – determination of maximum fibre volume

Too much SP was added in the first mixture. ViscoCrete RMC 630, which was in the original reference mix, is less effective than ViscoCrete 3 which was used in this test program. 0.6 % SP (% of cement weight) was added in Mixture 1, and the concrete was on the verge of segregation. The concrete segregated in the mixer, but not on the slump-flow table. Hence to this, the SP content was reduced to 0.5 % in the subsequent mixtures. The results of the tests are given in Table 3. Intermixture time for the fibres was set to 1 min.

Table 3 – Maximum amount of fibre

Mix 1	Amount of fibre in % and time after water addition in sec.				
	0.0 % t=10	0.5 % t=14	1.5 % t=20	2.5 % t=25	3.5 % t=33
Amount of fibre [g]	0	390	1170	1950	2731
Slump [mm]	Not measured	260	250	230	180
Slump-flow [mm]	610	580	540	480	410

The mixture's maximum fibre volume was reached at a fibre volume somewhere between 2.5 % and 3.5 %. There was a noticeable change in consistency, with a tendency to accumulation of fibre in the middle. Figure 2 to Figure 5 give a visual impression of concrete with different fibre contents.

Figure 2 – 0.5 % fibre

Figure 3 – 1.5 % fibre

Figure 4 – 2.5 % fibre

Figure 5 – 3.5 % fibre

3.2 Mix 2 – Reference concrete

Results from measurements of fresh properties of the reference concrete are summarized in Table 4 and shown graphically in Figure 6.

Table 4 – Results fresh properties, Reference concrete

Mix 2	Time after water addition [min]		
	10	20	30
Slump [mm]	260	260	250
Slump-flow [mm]	550	520	510
Air [%]	0.7	0.7	0.9
Density [g/l]	2340	2340	2340

As Table 4 show, the loss of consistency is relatively low. The concrete itself had low viscosity, but it was stable. Air content and density did not change significantly with increasing time after water addition.

Figure 6 to Figure 8 give a visual impression of the concrete at 10, 20 and 30 min after water addition.

Figure 6 – Reference concrete, 10 min after water, Slump-flow=550 mm

Figure 7 – Reference concrete, 20 min after water, Slump-flow =520 mm

Figure 8 – Reference concrete, 30 min after water, Slump-flow =510 mm

The results from this experiment show that the concrete was relatively stable with regard to slump and slump-flow the first 30 min after water addition. Loss of slump and loss of slump-flow 20 and 30 min after water addition were found to be as given in Table 5.

Table 5 – Loss of consistency, reference mixture

	Loss after 20 min[1]	Loss after 30 min[1]
Slump	0 mm / 0 %	10 mm / 4 %
Slump-flow	30 mm / 5 %	40 mm / 7 %

[1]Loss according to the values measured 10 min after water addition

The loss of consistency is calculated in percent of the "10 min values" so that it is possible to find the loss of consistency induced by increasing fibre contents in later mixes.

3.3 Mix 3 – 0.25 % and 0.5 % fibres

0.25 % fibres correspond to 585 g and 0.5 % fibres correspond to 1170 g. The results from the fresh properties of mixture 3 are summarized in Table 6.

Table 6 – Results fresh properties, Mix 3

Mix 3	Time after water addition [min]		
	10 (0 % fibre)	20 (0.25 % fibre)	30 (0.5 % fibre)
Slump [mm]	260	250	240
Slump-flow [mm]	540	440	440
Air [%]	0.7	1.3	2.0
Density [g/l]	2350	2350	2350

Figure 9 to 11 give a visual impression of the consistency of concrete, respectively with a fibre content of 0 %, 0.25 % and 0.5 %.

Figure 9 – Without fibre, Slump-flow=540 mm

Figure 10 – 0.25 % fibre, Slump-flow =440 mm

Figure 11 – 0.5 % fibre, Slump-flow =440 mm

Table 6 shows that the density is unaffected by intermixture of the fibres. Measurements on the reference mixture indicate that the air content was stable from 10 min to 30 min after water addition. This indicates that intermixture of fibres increases the air content. Values for loss of consistency are shown in Table 7. The values in Table 7 include loss of consistency due to increased time after water addition.

Table 7 – Loss of consistency inclusive time effect, Mix 3

	Loss at 0.25 % fibre[1]	Loss at 0.5 % fibre[1]
Slump	10 mm / 4 %	20 mm / 8 %
Slump-flow	100 mm / 19 %	100 mm / 19 %

[1]Loss according to values measured without fibres.

3.4   Mix 4 – 0.5 % and 1.0 % fibres

0.5 % fibre corresponds to 1170 g, and 1.0 % corresponds to 2340 g. The results from measurements of fresh properties in Mix 4 are summarized in Table 8.

Table 8 –   Results fresh properties, Mix 4

Mix 4	Time after water addition [min]		
	10	20	30
	(0 % fibre)	(0.5 % fibre)	(1.0 % fibre)
Slump [mm]	260	230	220
Slump-flow [mm]	520	430	390
Air [%]	0.7	1.3	2.0
Density [kg/m^3]	2360	2370	2380

Figure 12 to figure 14 give a visual impression of the concrete in Mix 4 at respectively 0 %, 0.5 % and 1.0 % fibre.

Figure 12 – 0 % fibre, Slump-flow =520 mm

Figure 13 – 0.5 % fibre, Slump-flow =430 mm

Figure 14 – 1.0 % fibre, Slump-flow =390 mm

In Mix 4 there was some increase in density as the fibre content increased. Also the air content increased with increasing fibre content. Theoretically, the relationship between fibre volume, V_f, air content (V_{air}) and concrete density (ρ_{FRC}) is:

$$\rho_{FRC} = (\rho_0 + V_f (\rho_f - \rho_0)) (1 - V_{air}) \tag{1}$$

where:

ρ_0 is the density of the concrete without fibres, measured for each concrete mix.

ρ_f is the density of the fibres, assumed to be 7800 kg/m^3.

From equation (1), the theoretical density is 2375 kg/m^3 and 2383 kg/m^3 for the concrete with 0.5 vol % fibre and 1.0 vol % fibre, respectively.

Loss of consistency is shown in Table 9.

Table 9 –   Loss of consistency inclusive time effect, Mix 4

	Loss at 0.5 % fibre[1]	Loss at 1.0 % fibre[1]
Slump	30 mm / 12 %	40 mm / 15 %
Slump-flow	90 mm / 17 %	130 mm / 25 %

[1] Loss according to values measured without fibres.

3.5   Mix 5 – combination of three different kinds of ring fibres

The following fibre content was added to the concrete at different times of measurement:
- 10 min: No fibres, 0 %
- 20 min: Total 1170 grams, 0.5 %
  - 30 mm ring fibres: 268 g
  - 20 mm ring fibres: 451 g
  - 12 mm ring fibres: 451 g
- 30 min: Total 2340 g, 1.0 %
  - 30 mm ring fibres: 536 g
  - 20 mm ring fibres: 902 g
  - 12 mm ring fibres: 902 g

Fresh properties of Mix 5 are shown in Table 10.

Table 10 – Results fresh properties, Mix 5

Mix 5	Time after water addition [min]		
	10 (0 % fibre)	20 (0.5 % fibre)	30 (1.0 % fibre)
Slump [mm]	260	250	230
Slump-flow [mm]	520	450	390
Air [%]	0.7	1.4	2.2
Density [kg/l]	2360	2370	2380

Figure 15 to Figure 17 give a visual impression of the concrete in Mix 5 at 0 %, 0.5 % and 1.0 % fibre, respectively.

Figure 15 – 0 % fibre, Slump-flow =520 mm

Figure 16 – 0.5 % fibre, Slump-flow =450 mm

Figure 17 – 1.0 % fibre, Slump-flow =390 mm

Also in Mix 5 there was an increase in density and air content as the fibre content increased. The theoretical density from equation (1) is 2370 kg/m^3 and 2378 kg/m^3 for the concrete with 0.5 vol % fibre and 1.0 vol % fibre, respectively.

Loss of consistency is shown in Table 11.

Table 11 –   Loss of consistency inclusive time effect, Mix 5

	Loss at 0.5 % fibre[1]	Loss at 1.0 % fibre[1]
Slump	10 mm / 4 %	30 mm / 12 %
Slump-flow	70 mm / 13 %	130 mm / 25 %

[1] Loss according to values measured without fibres.

4   COMPARISON MEASUREMENTS OF FRESH PROPERTIES

In order to relate the loss of slump and slump-flow to the increase of fibre volume, it is assumed that the percentage loss of slump and slump-flow with increasing time, as shown in Table 5, is the same for all mixtures. This loss was then deducted from the loss found with increasing time and increasing fibre content. In Figure 18 the loss of slump and slump-flow with regard to increasing fibre volume are shown.
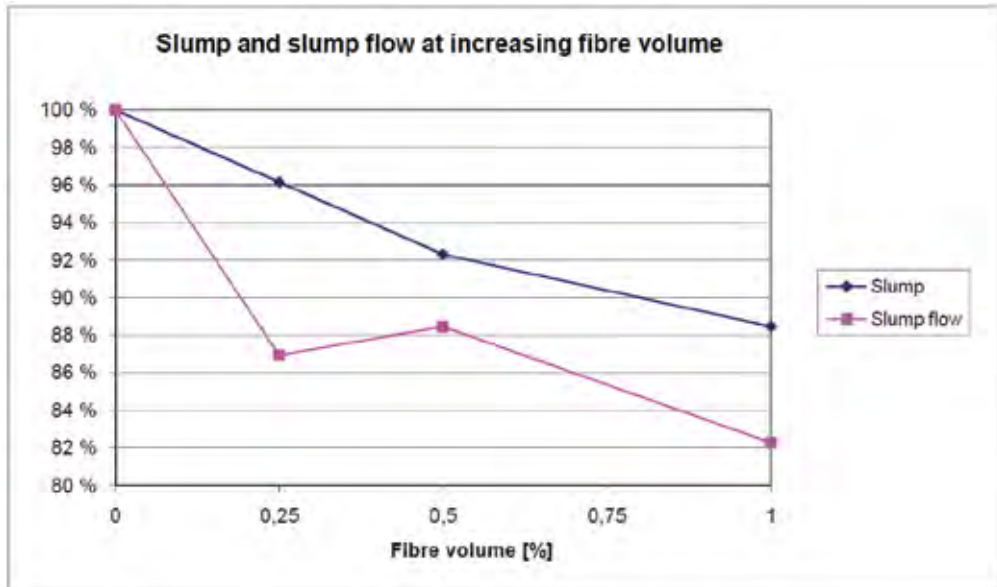
Figure 18 – Slump and slump-flow at increasing fibre content

The curves were calculated the following way:

> 1) The average measurement without fibre was calculated.
> 2) The percentage loss of slump and slump-flow with 0.25 % fibre content was found in Table 7, and the percentage loss of slump and slump-flow 20 min after water addition was found in Table 5. The difference was regarded to be the loss caused by increasing fibre content.
> 3) The average percentage loss of slump and slump-flow with 0.5 % fibre content was calculated from the results in Table 7 and Table 9, and corrected for the loss due to time after water addition found in Table 5.
> 4) The percentage loss of slump and slump-flow with 1.0 % fibre was found in Table 9, and compensated for the loss due to time after water addition found in Table 5.
> 5) The loss of slump and slump-flow was then calculated as percentage loss compared to the concrete without fibre.

The most interesting finding from figure 18 is the relatively low reduction in slump and slump-flow with a fibre content of 1 %. A reduction in slump from 260 mm to 220 mm (88 % reduction) should be acceptable if the hardened properties are largely improved.

5   RESULTS CONCERNING HARDENED CONCRETE

5.1   Strength.

Compressive strength was measured on cast cubes and cylinders from Mix 2 (the reference concrete), and on cut out cubes from bending and tensile prisms from all mixtures. The results are listed in Table 12 to Table 16. All tests are performed 28 days after casting.

Table 12 –   Density and compressive strength reference concrete – cast cubes/cylinders

Specimen	Density [kg/dm^3]	Strength [MPa]
0 % fibre – cast cube 1	2.36	60.7
0 % fibre – cast cube 2	2.38	60.4
0 % fibre – cast cube 3	2.35	60.1
Average cast cubes	**2.36**	**60.4**
Coefficient of variation	0.65 %	0.50 %
0 % fibre – cast cylinder 1	2.37	52.3
0 % fibre – cast cylinder 2	2.37	51.8
0 % fibre – cast cylinder 3	2.37	53.0
Average cast cylinders	**2.37**	**52.4**
Coefficient of variation	0.10 %	1.15 %

Table 13 – Density and compressive strength reference concrete – cut out cubes

Specimen	Density [kg/dm^3]	Strength [MPa]
0 % fibre 1	2.36	61.1
0 % fibre 2	2.39	62.0
0 % fibre 3	2.37	59.9
0 % fibre 4	2.39	61.1
0 % fibre 5	2.36	62.0
0 % fibre 6	2.38	62.6
Average	**2.38**	**61.5**
Coefficient of variation	0.64 %	1.56 %

Table 14 – Compressive strength and density, 0.5 % fibre – cut out cubes

Specimen	Density [kg/dm^3]	Strength [MPa]
0.5 % fibre 1	2.39	58.3
0.5 % fibre 2	2.40	60.9
0.5 % fibre 3	2.40	59.9
0.5 % fibre 4	2.39	59.5
Average	**2.39**	**59.7**
Coefficient of variation	0.31 %	1.80 %

'

Table 15 –   Compressive strength and density, 1 % fibre – cut out cubes

Specimen	Density [kg/dm^3]	Strength [MPa]
1 % fibre 1	2.44	60
1 % fibre 2	2.42	59.2
1 % fibre 3	2.46	62.3
1 % fibre 4	2.43	63
Average	**2.44**	**61.1**
Coefficient of variation	0.65 %	2.97 %

Table 16 –   Compressive strength and density, 1 % fibre combined – cut out cubes

Specimen	Density [kg/dm^3]	Strength [MPa]
1 % fibre 5	2.42	58.5
1 % fibre 6	2.45	59.6
1 % fibre 7	2.41	60.2
1 % fibre 8	2.45	58.3
Average	**2.43**	**59.2**
Coefficient of variation	0.83 %	1.53 %

As Table 12 and Table 13 show there is little difference in strength and density between the cast and cut out cubes. Further, when the values in Table 12 to Table 16 are compared, it is evident that strength is unaffected by the addition of fibre. The small variations that appear can be regarded as normal statistical variation. The observed increase in density is also as expected and already discussed in chapter 3.

When the concrete compressive strength is more or less constant in the different mixtures, there is reason to believe that the concrete is identical regardless of the mix number. Variations in the results of bending tests and tensile tests must then depend on different fibre content.

5.2 Bending tests of beams

The results from bending tests are summarized in Table 17 to Table 20. The results are discussed in chapter 5.4.

Table 17 – Bending tests, beams without fibres

Beam	Deflection at breakage [mm]	Deflection energy, G_f [Nm/m^2]	Maximum bending stress [MPa]
0 % fibre-1	0.69	71.5	3.81
0 % fibre-2	0.80	79.6	4.02
0 % fibre-3	1.22	108.5	4.18
Average	**0.90**	**86.6**	**4.00**
Coefficient of variation	31 %	22 %	5 %

Table 18 – Bending tests, beams with 0.5 % fibre

Beam	Deflection at breakage [mm]	Deflection energy. G_f [Nm/m^2]	Maximum bending stress [MPa]
0.5 % fibre-1	1.90	150.5	4.21
0.5 % fibre-2	1.14	105.8	4.34
Average	**1.52**	**128.2**	**4.27**
Coefficient of variation	35 %	25 %	2 %

Table 19 – Bending tests, beams with 1 % fibre

Beam	Deflection at breakage [mm]	Deflection energy. G_f [Nm/m^2]	Maximum bending stress [MPa]
1 % fibre-1	4.63	421.2	4.82
1 % fibre-2	6.38	537.9	4.35
Average	**5.50**	**479.6**	**4.59**
Coefficient of variation	22 %	17 %	7 %

Table 20 – Bending tests, beams with 1 % fibre combined

Beam	Deflection at breakage [mm]	Deflection energy. G_f [Nm/m^2]	Maximum bending stress [MPa]
1 % fibre combined-1	1.38	119.9	4.24
1 % fibre combined-2	1.45	126.6	4.25
Average	**1.42**	**123.3**	**4.25**
Coefficient of variation	3 %	4 %	0 %

5.3 Tensile tests of prisms

The results from the tension tests are shown in table 21 to table 24. The results are discussed in chapter 5.4.

Table 21 – Tension tests, prisms without fibres

Tensile prism	Strain at cracking [0/00]	Fracture stress [MPa]	E-modulus [GPa]
0 % fibre-1	0.13	3.32	29.4
0 % fibre-2	0.14	3.31	28.0
0 % fibre-3	0.11	2.80	27.8
0 % fibre-4	0.12	2.84	28.1
0 % fibre-5	0.11	2.72	27.9
0 % fibre-6	0.13	3.21	28.2
Average	**0.12**	**3.0**	**28.2**
Coefficient of variation	8 %	9 %	2 %

Table 22 – Tension tests, prisms with 0.5 % fibre

Tensile prism	Strain at cracking [0/00]	Fracture stress [MPa]	E-modulus [GPa]
0.5 % fibre-1	0.17	3.75	26.6
0.5 % fibre-2	0.13	3.40	28.5
0.5 % fibre-3	0.12	3.13	29.1
0.5 % fibre-4	0.14	3.33	27.8
Average	**0.14**	**3.4**	**28.0**
Coefficient of variation	14 %	7 %	4 %

Table 23 – Tension tests, prisms with 1 % fibre

Tensile prism	Strain at cracking [0/00]	Fracture stress [MPa]	E-modulus [GPa]
1 % fibre-1	0.10	3.15	37.7
1 % fibre-2	0.15	3.61	26.2
1 % fibre-3[1]	-	3.58	-
1 % fibre-4	0.14	3.56	29.2
Average	**0.13**	**3.5**	**31.0**
Coefficient of variation	20 %	6 %	19 %

[1]Untrustworthy strain-record. The stress-record is correct.

Table 24 – Tension tests, prisms with 1 % fibre combined

Tensile prism	Strain at cracking [0/00]	Fracture stress [MPa]	E-modulus [GPa]
1 % fibre combined-1	0.16	3.83	28.3
1 % fibre combined -2	0.15	3.52	28.1
1 % fibre combined -3	0.14	3.58	29.5
1 % fibre combined -4	0.14	3.54	29.1
Average	**0.15**	**3.6**	**28.7**
Coefficient of variation	6 %	4 %	2 %

5.4 ASSESSMENT OF RESULTS FROM BENDING AND TENSILE EXPERIMENTS

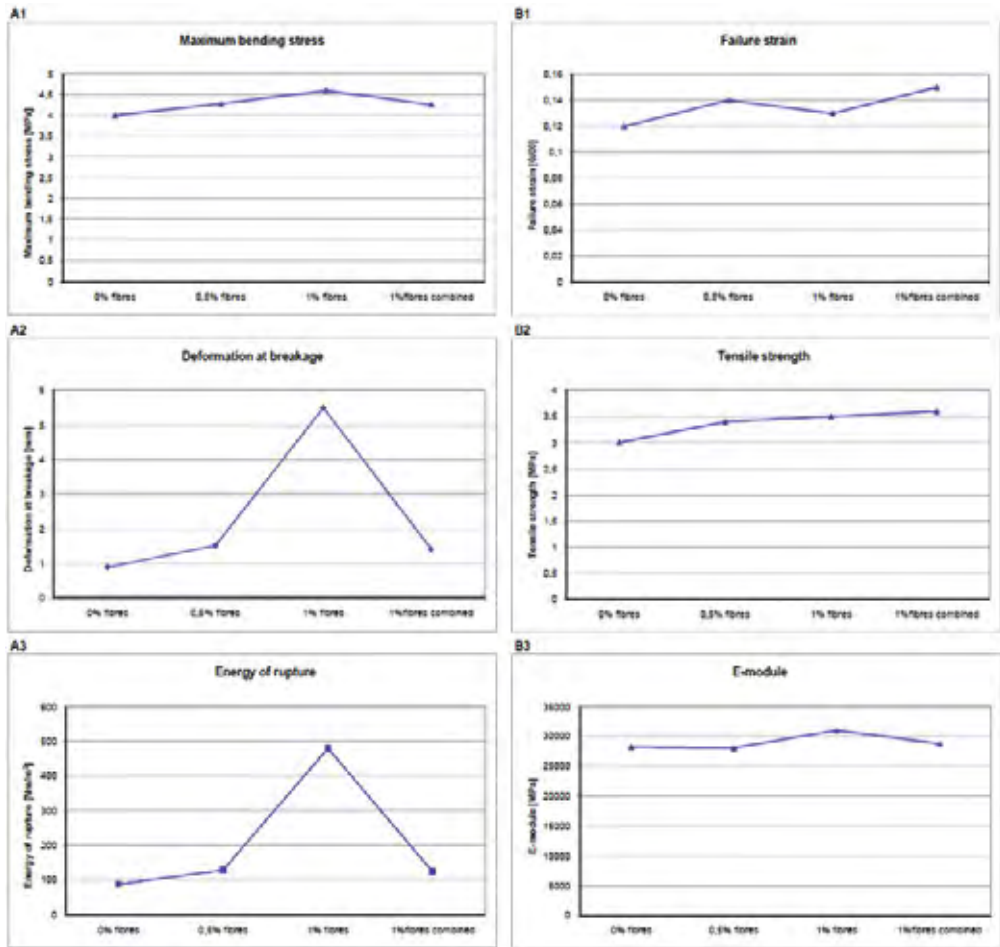Figure 19 shows the results from Table 17 to Table 24 in graphic form.

Figure 19 – Comparison of bending and tensile tests

It appears clearly that the fibres have a beneficial effect on the properties of concrete when the concrete is exposed to bending or tension.

From the bending stress tests, it appears that the combination of three diameters did not have the desired effect. The explanation may be that the rings need a diameter > d_{max} to be effective. d_{max} in this experiment was 16 mm, and the ring diameters was respectively 32, 20 and 12 mm. The amount of 20 and 32 mm fibres in 1 % fibres combined corresponds to respectively 0.23 % and 0.39 % of the concrete volume. That means that the volume of fibres with diameter > d_{max} was 0.62 %, and the results was with that comparable with the results from 0.5 % fibres.

From the tensile stress tests it appears that the tensile strength increases with increasing fibre volume. Average tensile strength for 1 % fibres is approximately 17 % higher than the reference concrete. Regarding ultimate strain and E-modulus, the connection is more complicated. Generally, the variation in results within a series is relatively large compared with the variation between the series, making it difficult to exclude normal statistical variation. However, it seems

that the addition of circular fibres increases both the tensile strength and the toughness of the concrete.

The ring fibres did not transfer stresses across a crack like ordinary fibre reinforcement. The cracks did always find a way around the ring fibres, so that the ring fibre acted more like large aggregate. If ring fibres should be able to transfer stresses across cracks, the wire diameter must most likely be less, so that a larger quantum of fibres are added for a given vol %.

6   CONCLUTIONS AND FURTHER WORK

The tests in this pilot study show that using key ring fibres in concrete has a beneficial effect on concrete properties when subjected to bending and tensile stress. There are no comparative studies with a commercially available straight fibre type, so whether the key rings are more or less effective than a common fibre types is not mapped. This aspect was neither emphasized during planning of the experiment, since key rings certainly not has the optimal geometry. The purpose of the experiment was to investigate whether circular fibres have a positive effect on bending and tensile strength, and also how the workability of the concrete is affected.

The easiest type of rings to obtain was common key rings, but these have probably not the optimal combination of geometry and strength. The rings had a diameter of 32 mm, 20 mm and 12 mm, with a corresponding a wire diameter of 2 mm, 1.5 mm and 1.0 mm, respectively. This gives a lot of metal per fibre, and thus a small number of fibres per vol %. It would probably be more beneficial if the wire was thinner and made of a material with higher strength and high ductility.

There is also reason to believe that the effect per ring will increase if the ring diameter increases, as long as the ring is not tore off at a too low deformation. Anyhow, the experiments indicate that the ring diameter must be larger than d_{max}.

The most important results from tests on fresh concrete are:
* The slump was reduced by 4 %, 8 % and 12 %, when adding 0.25 vol % fibres, 0.5 vol % fibres and 1.0 vol % fibres, respectively.
* The slump flow was reduced by 13 %, 12 % and 18 %, when adding 0.25 vol % fibres, 0.5 vol % fibres and 1.0 vol % fibres, respectively.
* The air content increases with increasing fibre amount.

The most important results from tests on hardened concrete are:
* Cast cubes and cut-out cubes have comparable compressive strength.
* The compressive strength is almost unaffected by the key ring content.
* Adding 1 vol % key rings increased the tensile strength by 17 %, and the maximum bending stress by 15 %.

Suggestions for further work:
* Performing similar experiments with more optimal fibre geometry, such as ring diameter / wire diameter corresponding to the l/*d*-ratio for ordinary straight fibres.
* Comparing the "optimal rings" influence on the concrete with ordinary straight fibres.

7 REFERENCES

[1]   Tylor, M., "Closed Loop Fibre Reinforcement for Concrete," *ACI Special Publication,* SP-44, 1974, pp. 299-316.   .

[2]   Tylor, M., "Comparison between closed-loop and straight metal fibres in concrete,"*Magazine of Concrete Research,* Vol. 36, 1984, pp 31-41.

[3]   Stages, A. H, and Minor, J., "Ring Fibre Reinforced Concrete," *ACI Journal,* September-October, 1981, pp.369-373

[4]   Gasparini, D.A. og Faieta, S., "A Comparison of Straight and Circular Fibres for Concrete," *American Society of Civil Engineers*, Serviceability and Durability of Construction Materials, 1990, pp 705-714.

[5]   Choi, O.C. og Lee, C., "Flexural performance of ring-type steel fibre-reinforced concrete," *Cement and Concrete Research 33,* 2003, pp.841-849.

[6]   Product data sheet, http://www.concrete.elkem.com/

[7]   EN 12390-3:2009 "Testing hardening concrete – Part 3: Compressive strength of test specimens", *European Standard*

[8]   EN 12350-2:2009 "Testing fresh concrete – Part 2: Slump-test", *European Standard*

[9]   EN 12350-6:2009 "Testing fresh concrete – Part 2: Density", *European Standard*

[10] EN 12350-7:2009 "Testing fresh concrete – Part 2: Air content – Pressure methods", *European Standard*

[11] EN 12350-8:2010 "Testing fresh concrete – Part 8: Self-compacting concrete – Slump-flow test", *European Standard*

Interfacial properties of steel fiber at mortars with different water and binder ratios: Backscattered electron image analysis and nanoindentation testing

Siaw Foon Lee
PhD, Postdoc
Department of Structural Engineering
Norwegian University of Science and Technology (NTNU)
NO-7491 Trondheim
Norway
E-mail: siaw.lee@ntnu.no

Xiao Hui Wang
PhD, Associate Professor
Department of Civil Engineering
Shanghai Jiaotong University
200240 Shanghai
China
E-mail: w_xiaoh@163.com

Stefan Jacobsen
PhD, Professor
Department of Structural Engineering
Norwegian University of Science and Technology (NTNU)
NO-7491 Trondheim
Norway
E-mail: stefan.jacobsen@ntnu.no

ABSTRACT

Backscattered electron image analysis (BSE-IA) and nanoindentation were adopted to study the properties in the interfacial transition zone (ITZ) of steel fiber with a diameter of 0.16 mm. Mortars with three different water and binder (w/b) ratios were made. A good sample preparation procedure that gave a surface roughness of less than 1 μm was used. It was found that the thickness of ITZ of steel fiber was 30 μm. BSE-IA and nanoindentation testing revealed that mortars with w/b 0.3 had less area % of porosity and higher hardness and elastic modulus at the ITZ than mortars with w/b 0.5. BSE-IA also showed that silica fume 10 % by cement weight did not densify the porosity in the ITZ as expected. This was in line with nanoindentation result which showed that mortar with 0 % silica fume had better interfacial bonding than mortar with 10 % silica fume for w/b 0.3.

1.   INTRODUCTION

Steel fiber-reinforced mortar is a heterogeneous composite material. Its properties depend on how well the cement paste, aggregate, steel fiber and admixtures distributing among each other during mixing. In the past, fiber-reinforced mortar was said to have three phases, which were aggregate, fiber and matrix. Lately, due to the discovery of the interfacial transition zone (ITZ) between aggregate and matrix or between fiber and matrix, the fiber-reinforced mortar is said to have four phases.

ITZ is defined as a region of transition (not a definite zone) because its formation is due to the "wall effect", where the packing of cement grains at the region close to the aggregate or steel is disturbed, mainly due to the presence of a relatively large and flat aggregate surface [1] or steel surface compared to the size of the cement grain. Depending on water and cement ratio [2] and binders such as silica fume or fly ash [1–6], its effective thickness ranges from 10 to 50 µm. The appearance of ITZ surrounding a single fiber also depends on the condition if the fiber's diameter is bigger or smaller than cement grains (typically < 80 µm). If the fiber's diameter is bigger than cement grains, the ITZ forms around the fiber is obvious with its thickness does not depend on the fiber's diameter [7, 8]. If the fiber's diameter is smaller than cement grains, for example carbon fibers with 7 µm, the ITZ forms around the fiber is as dense as the bulk matrix [9]. However, if the fibers bundle together, the ITZ only forms around the external fibers as the cement grains cannot penetrate into the fibers and the stress transfer from the matrix is merely through the contact of cement hydrates with the surfaces of external fibers [10].

A lot of research works have been carried out to study the effect of ITZ on the mechanical and durability properties of concrete during the last decades. Two contrary opinions on this problem were formed: some researchers argued that ITZ is a weakest link between the cement paste and the aggregate, so it has a significant role in determining the properties of all cementitious composites [11–13]; however, others [14] pointed out that there is no reason to assume the significant negative effects of ITZ on permeance or mechanical properties of concrete, even for concrete with a water/binder ratio of 0.5. Throughout those researches, Scanning Electron Microscopy (SEM) [13,14], Environmental Scanning Electron Microscopy (ESEM) [2] and Transmission Electron Microscopy (TEM) [15] have extensively been used. In order to quantify microstructural gradients across the ITZ, backscattered electron imaging and energy dispersive X-ray map [1, 16, 17] have also been adopted. Microindentation has also been used to determine the micro-mechanical characteristics such as hardness and elastic modulus of cement hydrates in various cement based composites [18–23]. Due to the limitations of microindentation, such as larger indent comparing with the thickness of ITZ [24], a new method which has already been used for many other materials [25], which is nanoindentation, has begun to be used in the cementitious composites. Until now, nanoindentation was widely used to measure elastic modulus and hardness of cement paste cured at different conditions [26–32]. Only few research works were focused on the studying of the ITZ between a rigid inclusion and matrix [33, 34].

In this study, backscattered electron image analysis and nanoindentation were adopted to study the ITZ properties between steel fiber and bulk matrix at steel fiber-reinforced mortars with 0.3 vol% steel fiber at w/b 0.3 and 0.5, with silica fume 0 and 10 % by cement weight. The diameter

and the length of the adopted steel fiber were 0.16 mm and 13 mm, respectively. The mix design, the rheological and the mechanical properties of the studied steel fiber-reinforced mortars were mentioned elsewhere [35]. The effects of different w/b on the area % of porosity and unhydrated cement in the ITZ, and on the nanomechanical properties (hardness and elastic modulus) of the microstructures in the ITZ of steel fiber are discussed in this paper.

2.   SAMPLE PREPARATION

A good sample preparation that produces a flat-polished surface with minimum artifacts is very important for the backscattered electrons imaging analysis (BSE-IA) and the nanoindentation study. For the BSE-IA, a clear topographical variation or severe artifact can appear as features that overlap with the studied features on the greyscale histogram, and this could lead to the misinterpretation of features in the image analysis. A rough surface could also increase scatter in the measured data by the nanoindentation [36]. In this study, we adopted the grinding and polishing procedure with minimum artifacts, which was presented in [37] by our group. Basically, three steps were involved in the sample preparation: grinding, epoxy vacuum impregnation and polishing. For the nanoindentation study, the step of epoxy impregnation was omitted. For the porosity quantification on cementitious materials using the BSE-IA technique, epoxy impregnation is necessary as epoxy with its low atomic number, $Z=6$ (contains mainly carbon), appears as black in the backscattered electron images, and thus separating pores from other phases.

A small cube of 16x16x16 mm was cut from the center of 40x40x160 mm prism (after 28day curing in water) using a low-speed diamond saw with water as a cooling agent. The cube was cleaned from any contamination and dried at the room temperature before it was cold-mounted into epoxy resin and cured for at least one day before proceeding to grinding and polishing. The epoxy resin used was Araldite Standard Epoxy resin with bas and hardener in ratio 1:1. The Struers TegraPol-31 grinding and polishing machine with adjustable rotational speed and polishing pressure, the Struers Silicon Carbide MD-Grinding disc and the MD-Polishing cloths were used. The detailed sample preparation procedure can be referred to [37].

3   BACKSCATTERED ELECTRON IMAGE ANALYSIS

Before the image acquisition using the Hitachi S-3400N LV-SEM equipped with Oxford INCA software, the examined surfaces of the specimens were sputter-coated with a layer of carbon using the Cressington 208Carbon High Vacuum Turbo Carbon Coater. The SEM was operated at an accelerating voltage of 5 kV, a working distance of about 8 mm and in low vacuum condition. The BSE images were taken at a magnification of 500x as it allowed half of the diameter of steel fiber being taken for the ITZ study. Each image was digitized at 2560x1920 pixels with a resolution of 0.1 μm per pixel.

Fig. 1 shows a typical greyscale histogram with the upper threshold cut-off value of 45 was used for the porosity at w/b 0.3 and 0.5. This upper threshold value was determined by visual-checking the colored area on the porosity in the BSE-image by manual adjusting the corresponding threshold setting in the OXFORD INCA Features software, although there are other means of doing that [38–40]. Since the threshold cut-off was performed by the same operator, the accuracy of the upper threshold setting for the porosity was maintained. The

aggregate, which was siliceous sand, shared the similar grey threshold as calcium silicate hydrate (CSH), see Fig. 2. Since the analysis software that was available in our laboratory did not allow the removal of aggregate from the image as reported by others [40], therefore, only the porosity and the unhydrated cement were studied.
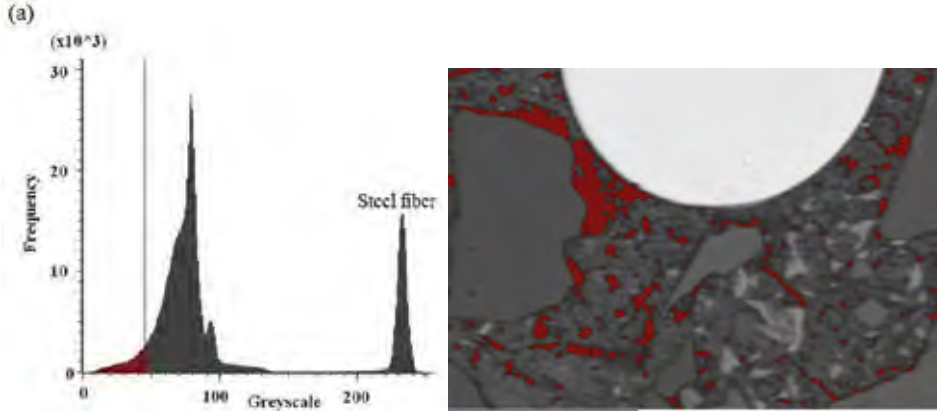

Figure 1 – A typical grayscale histogram that corresponds to a typical BSE-image, with the isolated right peak referring to the steel fiber.
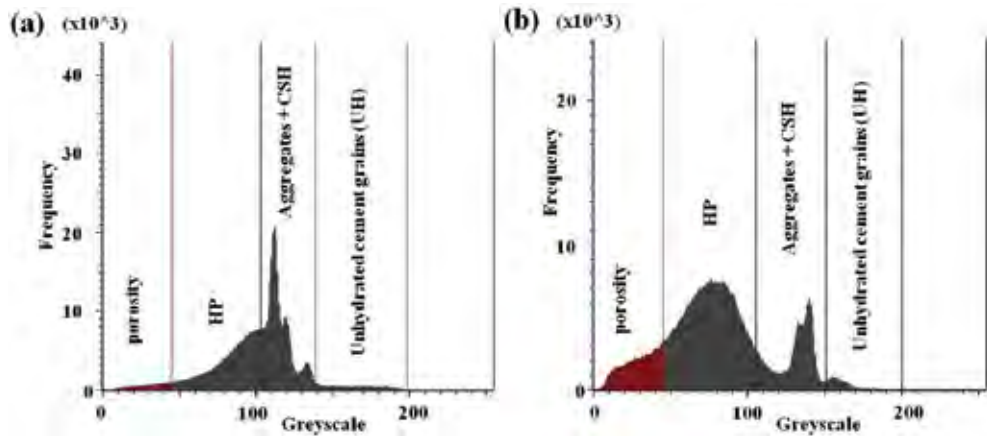

Figure 2 – Histograms for (a) w/c 0.3 and (b) w/c 0.5, with aggregates present in the image.

10-µm wide strips were cut successively from the BSE image starting at the interface of the steel fiber up to a distance of 60 µm using the magnetic lasso tool in Adobe Photoshop software. All strips were saved at 2560x1920 pixels, 8 bit greyscale mode and in jpg format. The features in the strips were segmented manually and measured in area fraction using analySIS®.

4   NANOINDENTATION TEST

Nanoindentation test is similar to macro-mechanical test, where the mechanical properties of material are tested. In nanoindentation, the mechanical properties are measured in nano scale using an indenter. Therefore, it is important to have a surface flatness less than 1 µm for the ease

of nanoindentation. The maximum load is determined so that the tip will stop indenting when the maximum load is reached, and thus, a P-h curve is obtained.

In our study, the nanomechanical properties (elastic modulus and hardness) of the cement hydrates in the ITZ between steel fiber and bulk matrix were studied using a Hysitron Triboindenter with a Berkovich indenter, which is a three-sided pyramid diamond. Fig. 3 shows a typical indentation load versus indentation displacement with the elastic modulus E and the hardness H of a sample being calculated as follows [25]:

$$S = \frac{dP}{dh} = \frac{2}{\sqrt{\pi}} E_2 \sqrt{A} \tag{1}$$

$$E = (1 - v^2)\left[\frac{1}{E_r} - \frac{(1 - v_i^2)}{E_i}\right]^{-1} \tag{2}$$

$$H = \frac{P_{max}}{A} \tag{3}$$

where S is the initial unloading stiffness; P the indentation load; h the indentation depth; E_r the reduced elastic modulus; A the projected area of the elastic contact; v Poisson's ratio for the sample; E_i and v_i are Young's modulus and Poisson's ratio for the indenter and P_{max} the peak indentation load. In our study, the elastic modulus E_i and the Poisson's ratio v_i of the adopted indenter are 1,140 GPa and 0.07, respectively.
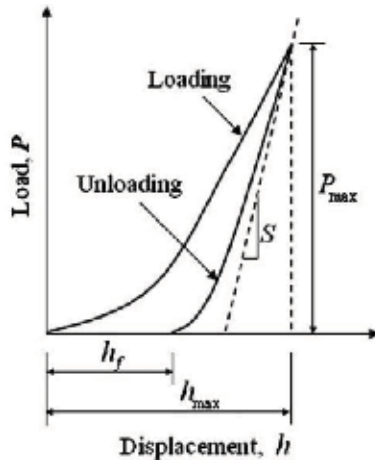
Figure 3 – A typical representation of the indentation load versus indentation displacement.

All tests were programmed in such a way that the indenter came into contact with the specimen's surface. When the indenter penetrated into the specimen, the load increased at a constant rate of 1 mN/s until it reached a maximum load of 5 mN. Then the load was held at the maximum for 2 s before unloading at the same constant rate. The protocol for the movement from one indent to the next was set as a Constant Direction Mode and the distance between two adjacent test points was set to be 10 μm.

Fig. 4 shows typical P-h curves of the nanoindentation on the steel fiber and on the matrix. Not all the P-h curves obtained from the nanoindentation on the cementitious material are valid for calculating the elastic modulus and the hardness. Irregular P-h curves that exhibited large displacement jump at any portion of the loading portion were discarded, see Fig. 5. The irregular nature of those curves may be due to the presence of a large void [34] or the surface cracking during the indentation [30]. Since the contact stiffness is measured only at the peak load, and no restrictions are placed on the unloading data being linear during any portion of the unloading [25], curves showing nonlinear characteristic in the unloading portion were adopted, see Fig. 6.
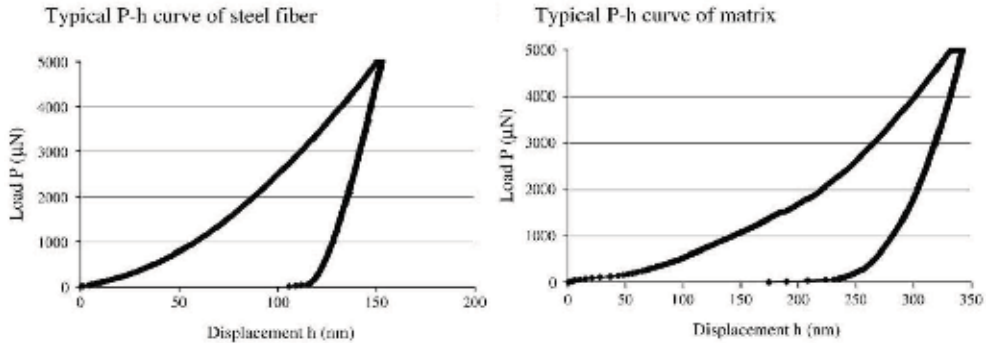
Figure 4 – Typical P-h curves of steel fiber and matrix.
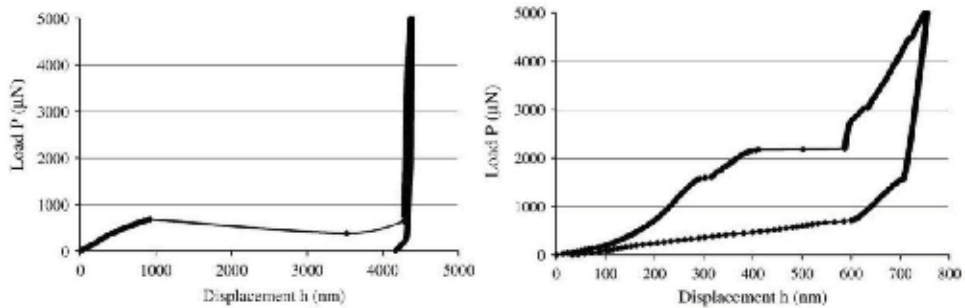
Figure 5 – Irregular curves showing a big pop-in on the loading portion.
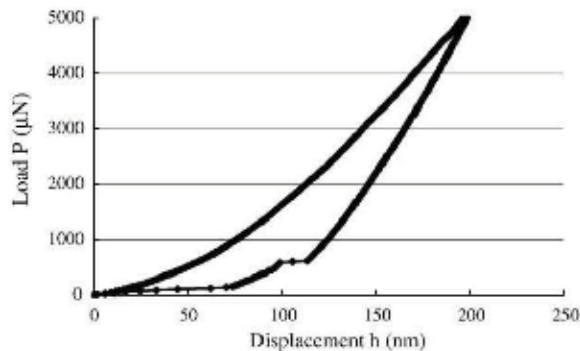
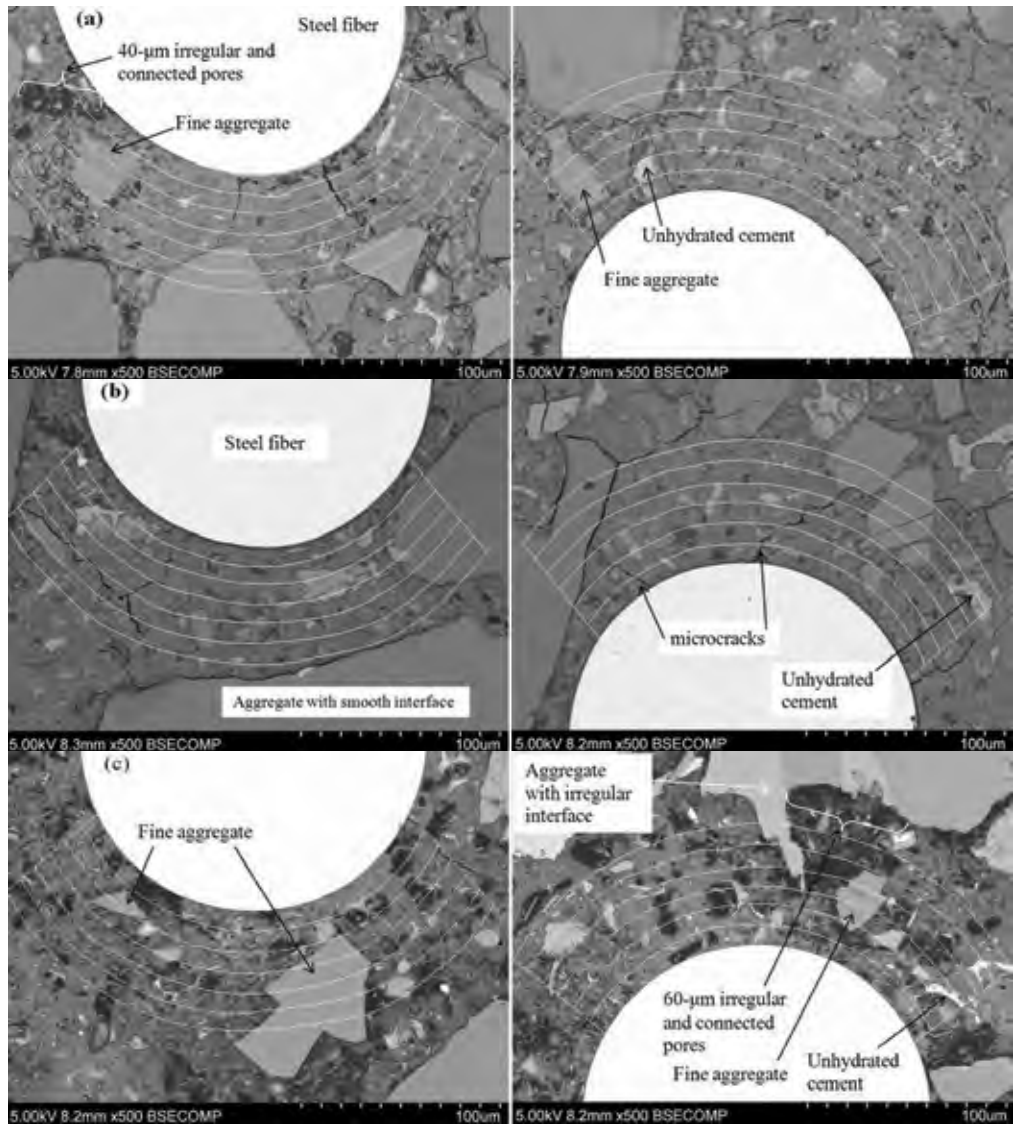*Figure 6 – Nonlinearity on the unloading portion.*

Figure 7 – BSE images of ITZ between steel fiber and bulk paste for 0.3 vol% steel fiber-reinforced mortar with (a) w/b 0.3, 0 % silica fume, (b) w/b 0.3, 10 % silica fume, (c) w/b 0.5, 0 % silica fume. Left is the bottom side and right is the top side of steel fiber. The bright half-round object is steel fiber.

5   RESULTS AND DISCUSSION

5.1   Pores and microcracks

From the BSE images shown in Fig. 7, two phenomena are found in the ITZ between steel fiber

and matrix, which are pores and microcracks. Under the magnification of 500x, the pores looked round, tube-like or irregular either in individual or connected shapes. The similar disconnected pores at the top side of steel fiber were found at the bottom side of steel fiber, indicating that no bleeding during the curing of fresh mortar [41]. For both w/b, irregular and connected pores of around 40 μm and of around 60 μm in width formed either in the area between the aggregate and steel fiber or at the aggregate with a irregular interface, not a straight interface, see Fig. 7(a) and (c). This indicated that the irregular interface of aggregate had higher possibility in disturbing the microstructure packing during mixing and this led to the build-up of connected pores.

From Fig. 7, microcracks with the width of 1 to 2 μm were more in w/b 0.3 than in 0.5, and more in the specimen with 10 % silica fume than 0 % silica fume. Microcracks originated from the steel fiber's interface, propagated into bulk paste and reached the aggregate's interface. Fine aggregates around 20 to 30 μm in size at the distance of around 20 to 50 μm from the steel fiber's interface had an effect in arresting the microcracks see Fig. 7(a), or changing the direction of crack propagation. Since the BSE images were only taken after the final polishing, it was hard to say that if all the microcracks were an artifact of the grinding and polishing process. Hsu et al. [42] reported that the diamond cutting and grinding produced no appreciable cracking on the surface and no crack was observed in bulk paste before compression when the specimen was examined with a stereoscopic microscope under 40x magnification. In our study, microcracks in bulk paste were found especially more in mortars with w/b 0.3 than those with w/b 0.5, see Fig. 7. Therefore, the appearance of microcracks in bulk paste mainly comes from the autogenous shrinkage that happened during the hydration of cement paste. The thermal shrinkage due to the oven drying in the sample preparation could possibly increase the length and the width of microcracks in the bulk paste.

5.2   Area % of porosity and unhydrated cement at ITZ

Fig. 7 shows the BSE images of 0.3 vol% steel fiber-reinforced mortars at three different w/b: (a) with w/b 0.3 with 0 % silica fume, (b) with w/b 0.3 with 10 % silica fume, and (c) w/b 0.5 with 0 % silica fume. Fig. 8 shows the area % of porosity and unhydrated cement versus the distance from the steel fiber's interface, corresponding to the BSE images in Fig. 7. In this paper, the top and bottom side refer to the arrangement of steel fiber in horizontal or in 90 degree angle to the direction of the fresh mortar being poured into the steel mould.

Fig. 8 shows that w/b 0.3 has a lower area % of porosity than w/b 0.5, indicating that a higher cement-hydrate packing in the ITZ in w/b 0.3. This is also in line with what is expected in [35] that w/b 0.3 has higher compressive strength than w/b 0.5. Regardless of w/b, the area % of porosity was high at the distance of 10 μm from the steel fiber's interface, and it reduced and reached a plateau after the distance of 30 μm away from the steel fiber's interface. Therefore, the thickness of the ITZ of steel fiber with diameter 0.16 mm is around 30 μm. Fine aggregates that found within the distance of 30 μm from the steel fiber's interface could disturb the cement-hydrate packing, see Fig. 7(c), and the trend of the porosity curve, see Fig. 8. Depending on the geometry and arrangement of the neighbouring aggregate, aggregate with irregular shape tends to have high pores at the interface, see Fig. 7(c). This explains an increase in the trend of porosity at the distance 50 μm away from the steel fiber's interface in Fig. 8. Aggregate with smooth shape has better cement-hydrate packing and shows less porosity at the interface, see Fig. 7(b). Therefore, no sharp increases in the trend of porosity at the distance 50 μm away from

the steel fiber's interface.

For unhydrated cement, w/b 0.5 with 0 % silica fume and w/b 0.3 with 10 % silica fume showed a low and constant value of area %; while w/b 0.3 with 0 % silica fume shows an increase at the distance of 20 or 30 μm from the steel fiber's interface, see Fig. 8(b). Higher area % of unhydrated cement in w/b 0.3 compared to w/b 0.5 indicated not enough water to complete the hydration in w/b 0.3. A low area % of unhydrated cement found near the steel fiber's interface for the specimen of w/b 0.3 was mainly caused by a locally high w/b formed near the surface of the steel fiber due to the wall effect. For w/b 0.5, we believe that a locally high w/b formed at the steel fiber's interface compared to the matrix. However, due to the high water content in w/b 0.5, almost all the cement grains were hydrated, and thus a low and constant area % of unhydrated cement was observed both in the ITZ and bulk paste. Fig. 7 shows that the microcracks do not propagate through the unhydrated cement, instead, they propagate surrounding the unhydrated cement because the unhydrated cement has higher young modulus [34] and hardness [43] than the hydrated product. Therefore, the presence of unhydrated cement in cement paste was an advantage as it could arrest and force the crack passing through a tortuous path. However, the disadvantage is that the unhydrated cement does not fully contribute to adhesion that is more needed in cement based materials.
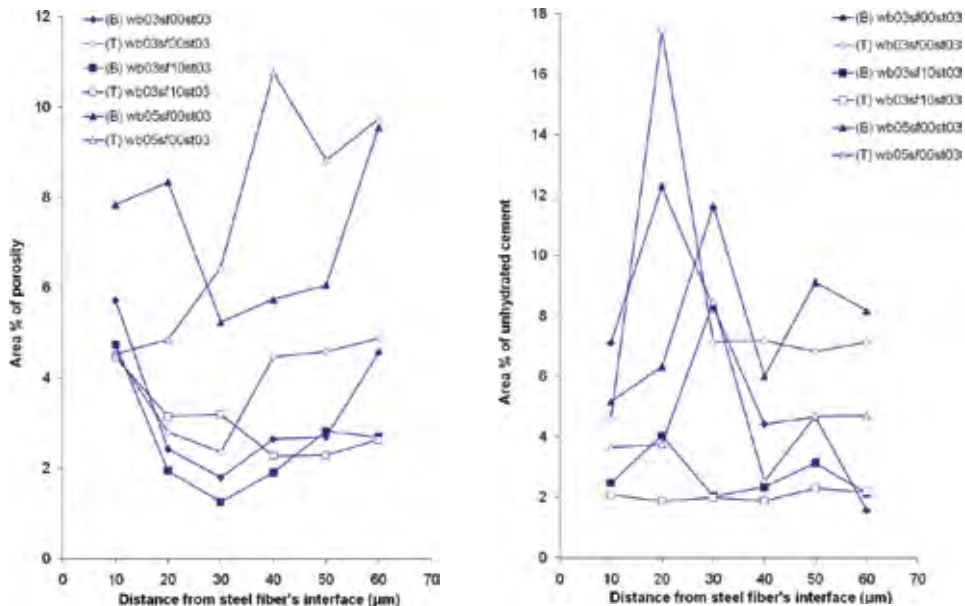

Figure 8 – The area % of porosity and unhydrated cement with each point corresponds to each strip in the BSE images in Figure 7. w/b = water/binder, sf = silica fume, st = steel fiber, with two digits after sf and st refer to quantity in % and vol%, respectively.

Fig. 8 shows that 10 % silica fume does not reduce the area % of porosity by densifying the ITZ between steel fiber and bulk paste. Caliskan [44] showed that only up 20 % silica fume replacement of cement could improve the interfacial bond strength by densifying the microstructures in the ITZ and produced thinner ITZ. On the other hand, silica fume also has a significant influence in increasing the shrinkage compared to plain mortar [45]. The microcracks found in our mortars with 10 % silica fume could be due to the high autogeneous shrinkage

during setting. These microcracks were interpreted as pores in the BSE-IA, and thus a higher area % of porosity is shown in mortars with 10 % silica fume. Although this was the case, 10 % silica fume also increased the content of calcium silicate hydrate (CSH) in the mortars. And thus, a higher compressive strength of mortars with 10 % silica fume compared to mortars with 0 % silica fume were reported in [35], where the same mortars were used in both studies.

5.3   Elastic modulus and hardness at ITZ

Fig. 9 is a typical BSE image that shows the nanoindentation from the steel fiber extending to the matrix in our experiment. Fig. 10 shows the hardness and E modulus profiles of the steel fiber-ITZ-matrix of mortars with (a) w/b 0.3 with 0 % silica fume, (b) w/b 0.3 with 10 % silica fume, and (c) w/b 0.5 with 0 % silica fume. In Fig. 10, the vertical axis indicates the steel fiber's interface and the horizontal axis indicates the distance from the steel fiber's interface. A comparison of the hardness profile was made between our data and Igarashi et. al [20], who reported that a microhardness gradient is shown in the vicinity of the inclusion and it becomes relatively constant in the bulk matrix, with the trends of the gradients can be classified into four types as shown in Fig. 11. The type I curve shows an exponential increase in the microhardness when approaching the inclusion's interface. The reasons may be that the inclusion and the matrix are well bonded at the interface and the region closed to the inclusion is rich in massive CH [20]. Deviations from these conditions can lead to changes in the shape of the curve such as II, III, and IV in Fig. 11.

For the specimen with w/b 0.3 with 0 % silica fume, the hardness profile of the ITZ between steel fiber and matrix shows a similar trend as the type I in Fig. 11. An obvious increase in hardness and elastic modulus are seen in the distance 5-35 μm away from the steel fiber's interface. In the 35-65 μm zones, the nano-mechanical properties become relatively constant and a plateau is reached. The lowest hardness value is 0.1636 GPa, which occurs approximately 56 μm away from the steel fiber's interface. Overall, the bonding across the ITZ for mortar with w/b 0.3 with 0 % silica fume is quite efficient.

For the specimen with w/b 0.3 with 10 % silica fume, the hardness profile of the ITZ between steel fiber and matrix is similar to type III in Fig. 11. A relatively low hardness is observed just in the 10-30 μm zones. The lowest hardness value is 0.2391 GPa, which occurs 30 μm away from the steel fiber's interface. The nano-mechanical properties become relatively constant beyond this zone. Overall, for the mortar at w/b 0.3, the bond behavior for that with 10 % silica fume is good, but not as efficient as that with 0 % silica fume.

For the specimen with w/b 0.5 with 0 % silica fume, the hardness profile of the ITZ shows a typical characteristic of type IV in Fig. 11. Comparing with the hardness profile in the specimen with w/b 0.3 with 0 and 10 % silica fume, a relatively lower hardness profile is seen in the mortar with w/b 0.5. This is mainly due to a larger water/binder ratio, as pointed out by Sun et al. [19]. The lowest hardness is observed near the steel fiber's interface, just 25.6 μm from the steel fiber's interface. This value is 0.1452 GPa, indicating a decrease of the hardness at the weakest point owing to the increase of the water/binder ratio. A trough is shown in the 0-35 μm zones. This indicates that the interfacial bonding in the specimen with w/b 0.5 is poor and not as effective as that obtained in the specimen with w/b 0.3.
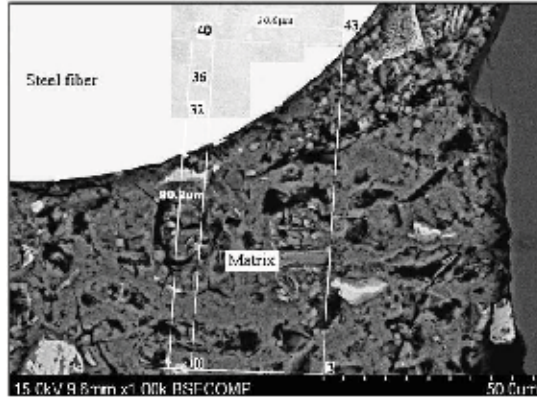
Figure 9 – Image of steel fiber-matrix interfacial zone, where the dimension of the indendted area is 30 μm x 80 μm.
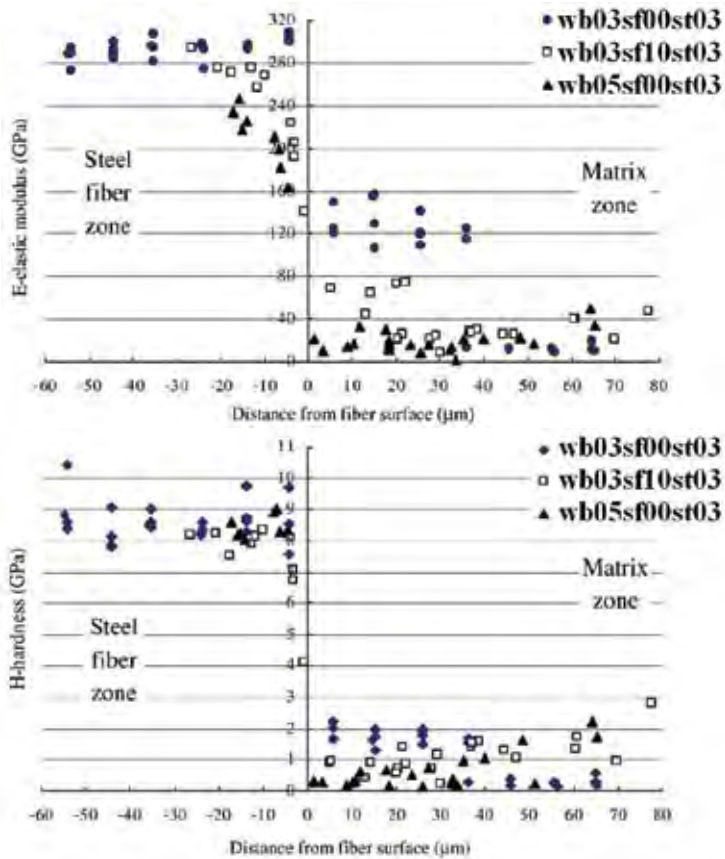

Figure 10 – Elastic modulus and hardness profile of ITZ between steel fiber and matrix for 0.3 vol% steel fiber-reinforced mortars with (a) w/b 0.3 with 0 % silica fume, (b) w/b 0.3 with 10 % silica fume, and (c) w/b 0.5 with 0 % silica fume.
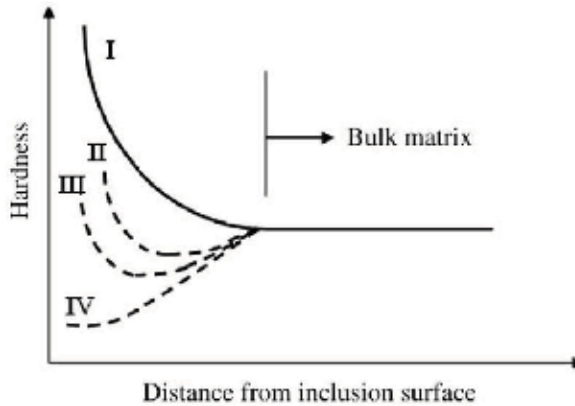
Figure 11 – Classification of microhardness profile in the ITZ around a rigid inclusion and cement paste matrix [20].

6   CONCLUSIONS

The study of backscattered electron image analysis and nanoindentation on the ITZ of steel fiber with diameter 0.16 mm at mortars with three different w/b ((a) w/b 0.3 and 0 % silica fume, (b) w/b 0.3 and 10 % silica fume, and (c) w/b 0.5 and 0 % silica fume) leads to the following conclusion:

1) The BSE-IA shows that the thickness of ITZ for steel fiber with 0.16 mm diameter is around 30 μm, regardless of w/b. Fine aggregates with sizes around 20 to 30 μm that packed at the distance of 20 to 50 μm not only has abilities in arresting the microcracks, changing the direction of crack propagation but also disturbing the microstructure packing at the ITZ of steel fiber.

2) For mortars with w/b 0.3 with 0 % silica fume, an efficient bonding across the steel fiber matrix is shown by an increase in the hardness profile when the interface of steel fiber is approached. For mortars with w/b 0.5 with 0 % silica fume, due to the presence of higher area % of porosity at the ITZ, the steel fiber-matrix bond is not very good. In addition, the hardness value at the weakest point in the ITZ of w/b 0.5 is smaller than that in w/b 0.3. This indicated that the w/b has effect on the ITZ quality.

3) The area % of porosity, the elastic modulus and the hardness profile of the ITZ of steel fiber are also influenced by the addition of silica fume. In mortars with w/b 0.3 with 10 % silica fume, when the steel fiber's interface is approached, a rise in the hardness profile is observed and this indicates a good interfacial bonding across the ITZ. However, the rise is comparatively low compared to mortars with w/b 0.3 with 0 % silica fume. On top of that, the BSE-IA also showed that mortars with 10 % silica fume has higher area % of porosity than that with 0 % silica fume. Both studies support the conclusion that the bonding across the steel fiber-matrix interface in mortars with 10 % silica fume is not as efficient as that with 0 % silica fume. However, silica fume increases the content of calcium-hydrate-silicate (CSH), which gives strength to the mortars, and this compensates the increase in area % of porosity in the ITZ. This study explains the flexural strength and the compressive strength obtained in [35], where the same mortars were used. Mortars with 0 and 10 % silica fume showed similar flexural strength, as the failure was

caused by the steel fiber pulled-out, involving mainly the properties in the ITZ. However, the compressive strength of mortars with 10 % silica fume were higher than 0 % silica fume, mainly because the failure in compression occurred through any weak point in the paste matrix, not just the ITZ.

ACKNOWLEDGMENTS

REFERENCES

1. Scrivener, K.L., Crumbie, A.K., Laugesen, P., "The interfacial transition zone (ITZ) between cement paste and aggregate in concrete", *Interface Science*, Vol.12, 2004, pp. 411-421.
2. Chan, Y.-W., Li, V.C., "Effect of transition zone densification on fiber/cement paste bond strength improvement", *Advanced Cement Based Materials*, Vol. 5, 1997, pp. 8-17.
3. Redon, C., Chermant, J.-L., "Compactness of the cement microstructure versus crack bridging in mortars reinforced with amorphous cast iron fibers and silica fumes", *Applied Composite Materials*, Vol. 8, 2001, pp. 149-161.
4. Chan, Y.-W., Chu, S.-H., "Effect of silica fume on steel fiber bond characteristics in reactive powder concrete", *Cement and Concrete Research*, Vol. 34, 2004, pp. 1167-1172.
5. Kayali, O., "Effect of high volume fly ash on mechanical properties of fiber reinforced concrete", *Materials and Structures*, Vol. 37(5), 2004, pp. 318-327.
6. Cwirzen, A., Penttala, V., "Aggregate-cement paste transition zone properties affecting the salt-frost damage of high-performance concretes", *Cement and Concrete Research*, Vol. 35, 2005, pp. 671-679.
7. Horne, A.T., Richardson, I.G., Brydson, R.M.D., "Quantitative analysis of the microstructure of interfaces in steel reinforced concrete", *Cement and Concrete Research*, Vol. 37, 2007, pp. 1613-1623.
8. Chen, H., Sun, W., Zhao, Q., Sluys, L.J., Stroeven, P., "Effects of fiber curvature on the microstructure of the interfacial transition zone in fresh concrete", Frontiers of Architecture and Civil Engineering in China, Vol. 1(1), 2007, pp. 99-106.
9. Katz, A., Bentur, A., "Effect of matrix composition on the aging of CFRC", *Cement and Concrete Composites*, Vol. 17, 1995, pp. 87-97.
10. Stucke, M.S., Majumdar, A.J., "Microstructure of glass fibre-reinforced cement composites", Journal of Materials Science Letters, Vol. 11, 1976, pp. 1019-1030.
11. Nilsen, A.U., Monteiro, P.J., "Concrete: A three phase material", Cement and Concrete Research, Vol. 23(1), 1993, pp. 147-151.
12. Akşaoğlu, T., Tokyay, M., Çelik, T., "Effect of coarse aggregate size and matrix quality on ITZ and failure behavior of concrete under uniaxial compression", Cement and Concrete Composite, Vol. 26(6), 2004, pp. 633-638.

13. Akşaoğlu, T., Tokyay, M., Çelik, T., "Assessing the ITZ microcracking via scanning electron microscope and its effect on the failure behavior of concrete", Cement and Concrete Research, Vol. 35(2), 2005, pp. 358-363.

14. Diamond, S., Huang, J., "The ITZ in concrete – A different view based on image analysis and SEM observations", Cement and Concrete Composition, Vol. 23(2-3), 2001, pp. 179-188.

15. Gatty, L., Bonnamy, S., Feylessoufi, A., Clinard, C., Richard, P., Damme, H. Van, "A transmission electron microscopy study of interfaces and matrix homogeneity in ultra-high-performance cement-based materials", Journal of Materials Science, Vol. 36(16), 2001, pp. 4013-4026.

16. Scrivener, K.L., "Backscattered electron imaging of cementitious microstructures: understanding and quantification", Cement and Concrete Composites, Vol. 26, 2004, pp. 935-945.

17. Brough, A.R., Atkinson, A., "Automated identification of the aggregate-paste interfacial transition zone in mortars of silica sand with Portland or alkali activated slag cement paste", Cement and Concrete Research, Vol. 30(6), 2000, pp. 849-854.

18. Zhu, W., Bartos, P.J.M., "Application of depth-sensing microindentation testing to study of interfacial transition zone in reinforced concrete", Cement and Concrete Research, Vol. 30(8), 2000, pp. 1299-1304.

19. Sun, W., Mandel, J.A., Said, S., "Study of the interface strength in steel fiber-reinforced cement-based composites, ACI Journal, Proceeding, Vol. 83(4), Title No. 83-53, 1986, pp. 597-605.

20. Igarashi, S., Bentur, A., Mindess, S., "Microhardness testing of cementitous materials", Advanced Cement Based Materials, Vol. 4(2), 1996, pp. 48-57.

21. Zhu, W., Bartos, P.J.M., "Assessment of interfacial microstructure and bond properties in aged GRC using a novel microindentation method", Cement and Concrete Research, Vol. 27(11), 1997, pp. 1701-1711.

22. Trtik, P., Bartos, P.J.M., "Micromechanical properties of cementitious composites", Materials and Structures, Vol. 32(5), 1999, pp. 388-393.

23. Cross, W.M., Sabnis, K.H., Kjerengtroen, L., Kellar, J.J., " Microhardness testing of fiberreinforced cement paste", ACI Materials Journal, Vol. 97(2), 2000, pp. 162-167.

24. Velez, K., Sorrentino, F., "Characterization of cementitious materials by nanoindentation", In M. Gawlicki W. Kurdowski, editor, *Kurdowski Symposium-Science of Cement and Concrete*, Krakow, June 2001, pp. 67-77.

25. Oliver, W.C., Pharr, G.M., "An improved technique for determining hardness and elastic modulus using load and displacement sensing indentation experiments", Journal of Materials Research, Vol. 7(6), 1992, pp. 1564-1583.

26. Velez, K., Maximiliena, S., Damidotb, D., Fantozzia, G., Sorrentinob, F., "Determination by nanoindentation of elastic modulus and hardness of pure constituents of portland cement clinker", Cement and Concrete Research, Vol. 31, 2001, pp. 555-561.

27. Constantinides, G., Ulm, F.-J., "The effect of two types of C-S-H on the elasticity of cement-based materials: results from nanoindentation and micromechanical modeling", Cement and Concrete Research, Vol. 34(1), 2004, pp. 67-80.

28. Jennings, H.M., Thomas, J.J., Gevrenov, J.S., Constantinides, G., Ulm, F.-J. "A multitechnique investigation of the nanoporosity of cement paste", Cement and Concrete Research, Vol. 37, 2007, pp. 329-336.

29. Zhu, W., Hughes, J.J., Bicanic, N., Pearce, C.J., "Nanoindentation mapping of mechanical properties of cement paste and natural rocks", Materials Characterization, Vol. 58(11-12), 2007, pp. 1189-1198.

30. DeJong, M.J., Ulm, F.-J., "The nanogranular behavior of C-S-H at elevated temperatures up to 700°C", Cement and Concrete Research, Vol. 37, 2007, pp. 1-12.
31. Mondal, P., Shah, S.P., Marks, L., "A reliable technique to determine the local mechanical properties at the nanoscale for cementitious materials", Cement and Concrete Research, Vol. 37(10), 2007, pp. 64-90.
32. Constantinides, G., Ulm, F.-J., "The nanogranular nature of C-S-H", Journal of the Mechanics and Physics of Solids, Vol. 55, 2007, pp. 64-90.
33. Zhu, W., Sonebi, M., Bartos, P.J.M., "Bond and interfacial properties of reinforcement in self-compacting concrete", Materials and Structures, Vol. 37, 2004, pp. 442-448.
34. Mondal, P., Shah, S.P., Marks, L.D., "Nanoscale characterization of cementitious materials", ACI Materials Journal, Vol. 105, 2008, pp. 174-179.
35. Lee, S.F., Wang, X.H., Jacobsen, S., "Mix design and effect of silica fume and steel fiber on rheological and mechanical properties of mortars", *Nordic Concrete Research*, No. 41-03, 2010, pp. 33–50.
36. Kim, J.Y., Lee, J.J., Lee, Y.H., Jang, J., Kwon, D., "Surface roughness effect in instrumented indentation: A simple contact depth model and its verification", Journal of Materials Research, Vol. 21(12), 2006, pp.2975-2978.
37. Lee, S.F., Jacobsen, S., "Sample preparation, image acquisition and image analysis on interfacial transition zone of steel fiber-reinforced mortar", *Nordic Concrete Research*, No. 41-02, 2010, pp. 15–32.
38. Yang, R., Buenfeld, N.R., "Binary segmentation of aggregate in SEM image analysis of concrete", Cement and Concrete Research, Vol. 31, 2001, pp. 437–441.
39. Head, M.K., Buenfeld, N.R., "Measurement of aggregate interfacial porosity in complex, multi-phase aggregate concrete: Binary mask production using backscattered electron, and energy dispersive X-ray images", Cement and Concrete Research, Vol. 36, 2006, pp. 337–345.
40. Wong, H.S., Head, M.K., Buenfeld, N.R., "Pore segmentation of cement-based materials from backscattered electron images", Cement and Concrete Research, Vol. 36, 2006, pp. 1083-1090.
41. Igarashi, S., Bentur, A., Mindess, S., "The effect of processing on the bond and interfaces in steel fiber reinforced cement composites", Cement and Concrete Composites, Vol. 18, 1996, pp. 313-322.
42. Hsu, T.T.C., Slate, F.O., Sturman, G.M., Winter, G., "Microcracking of plain concrete and the shape of the stress-strain curve", ACI Journal, Proceeding, Vol. 60(2), Title No. 60-14, 1963, pp. 209-224.
43. Sorelli, L., Constantinides, G., Ulm, F.-J., Toutlemonde, F., "The nano-mechanical signature of ultra high performance concrete by statistical nanoindentation techniques", Cement and Concrete Research, Vol. 38, 2008, pp. 1447–1456.
44. Caliskan, S., "Aggregate/mortar interface: influence of silica fume at the micro-and macro-level", Cement and Concrete Composites, Vol. 25, 2003, pp. 557–564.
45. Rao, G.A., "Long-term drying shrinkage of mortar -influence of silica fume and size of fine aggregate", Cement and Concrete Research, Vol. 31, 2001, pp. 171–175.

Applications for Numerical Simulation of Self-Compacting Concrete

Annika Gram
PhD Student
Swedish Cement and Concrete Research Institute, CBI
Drottning Kristinas väg 26, SE - 100 44 Stockholm
E-mail: annika.gram@cbi.se

Johan Silfwerbrand
Professor, Managing Director
Swedish Cement and Concrete Research Institute, CBI
Drottning Kristinas väg 26, SE - 100 44 Stockholm
E-mail: johan.silfwerbrand@cbi.se

ABSTRACT

This paper, presenting practical applications for numerical simulation, is divided into two parts: 1. Verification and application of the numerical concrete model presented here and 2. Introduction of an on-site rheology assessment tool, the Rheo-Box, which is to be used for the concrete acceptance test in order to verify rheological parameters of the concrete as feedback to obtain satisfactory form filling. It is shown that simulated values correspond well to both analytical and experimental results for concrete flow. In the future, numerical simulation will be a more common tool for predictions of possibly complicated SCC castings.

Key words: Numerical simulation, analytical channel flow solution, SCC, casting, Rheo-Box.

1.   INTRODUCTION

Self-Compacting Concrete, SCC, flows under its own weight and consolidates in the formwork without any additional vibration. The high potential of SCC, its excellent form filling abilities and fluidity in its fresh state are investigated and numerically simulated employing Computational Fluid Dynamics. The simulations are compared to theory as well as experimental data from industrial castings in order to test predictability of the material model presented here.

A correct prediction of SCC flow behaviour will increase control over complex castings which, without specific care, may otherwise lead to poor form filling, surface imperfections and aggregate blocking. Advance problem detection can give valuable data input for the requirements concerning on-site workability acceptance tests.

This paper is presenting a numerical model for self-compacting concrete followed by an industrial application and the introduction of a rheological measurement tool. It is divided into

two parts: 1. 'Verification and Application of the Numerical Material Model' by comparison to an analytical solution and an example of industrial application and 2. The Introduction of 'An on-Site Rheology Assessment Tool', the Rheo-Box. It can be used as a concrete acceptance test in order to evaluate the rheological parameters of the delivered concrete with that of the desired concrete needed to obtain satisfactory form filling.

Workability of SCC was studied and modelled assuming adequate stability and no blocking during casting, since the concrete is modelled as a homogeneous Bingham fluid. Form filling abilities were simulated for a double-tee slab and the results were compared to the castings of double-tee slabs in a precast concrete plant.

Here, a model for flow pattern is presented. It includes the shape at flow stoppage, which may serve as an aid in achieving complete form filling and surface perfection with possible feedback to on-site test requirements for the freshly delivered concrete.

Since form filling ability can be related to the rheological Bingham parameters of fresh concrete, rheological parameters may be of interest on the construction site. The here introduced elongated rheological box (the Rheo-Box) presents a possible acceptance test for on-site SCC with the opportunity to give instant feedback to the concrete plant based on rheological results during the casting process. In this paper, the rheological box is first verified by numerical simulation and then successfully tested for four real concrete batches.

2.   LITERATURE STUDY ON SIMULATION OF CONCRETE FLOW

With the development of SCC, the wish to predict both flow and especially blocking has led to the selection of a particle flow code in order to model concrete flow [2, 3, 4]. Various types of software and simulation methods, such as continuous formulations [5, 6, 7], modelling of particles only [8, 9, 10], or simulating particles in a liquid phase [11], have been employed in order to model mortar and concrete. Extensive previous work on numerical simulation of concrete shearing flow in a viscometer can be found [12], as well as numerical simulation showing high details of the material and the effects of particle shape on flow properties, e.g. [13]. Simulation of full scale castings showing more than details or sections, concrete flow was previously investigated in a full scale wall casting, showing flow patterns of the concrete during form filling [14]. The simulation software used for this paper is called OpenFOAM (Field Operation And Manipulation). The code is an object-oriented numerical simulation toolkit for continuum mechanics written in C++, released by OpenCFD Ltd and available for free (https://www.opencfd.co.uk).

3.   THEORETICAL ASPECT OF FLOW MODELLING

For Pascalian liquids, meaning incompressible fluids (such as concrete), we have the continuity equation for incompressible fluid with fluid velocity vector $\mathbf{u}$:

$$\nabla \cdot \mathbf{u} = 0 \tag{1}$$

The governing equation for non-Newtonian fluid flow, called Cauchy's equation of motion [17], is given by:

$$\rho \frac{D\mathbf{u}}{Dt} = \nabla \cdot \boldsymbol{\sigma} + \rho \ \mathbf{g} \tag{2}$$

Where $\mathbf{g}$ is the gravitational acceleration vector acting on the system, ρ is the material density and the stress tensor $\boldsymbol{\sigma} = -p\,\mathbf{I} + \mathbf{T}$. Here, p denotes pressure, $\mathbf{I}$ is the unit dyadic and $\mathbf{T}$ is the extra stress tensor, associated with the apparent viscosity η of the fluid. As concrete is a viscoplastic material, the relation used for $\mathbf{T}$ is [18]:

$$\mathbf{T} = 2\eta\dot{\boldsymbol{\varepsilon}} \tag{3}$$

with $\dot{\boldsymbol{\varepsilon}}$ being the tensor of rate of deformation as can be found in [19]:

$$\dot{\boldsymbol{\varepsilon}} = \frac{1}{2}(\nabla\mathbf{u} + (\nabla\mathbf{u})^{\top}) \tag{4}$$

In [12] it has been shown that Eq. (2) is not only applicable for homogeneous fluids, but from a fundamental physical point of view it can also be applied on coarse granular systems like fresh concrete.

Concrete and other concentrated suspensions are often modelled as a Bingham material. It is a plastic material, showing little or no deformation up to a certain level of stress. Above this yield stress τ_0, the material flows. These materials are called viscoplastic or Bingham plastics after E.C. Bingham, who was the first researcher to use this description on paint in 1916, [20]. With τ and γ being the shear stress and shear deformation of the material, respectively, and G the shear modulus, we can now write:

$$\begin{aligned}
\tau &= G\gamma & \text{for} \quad \tau < \tau_0 \\
&\text{and} \\
\tau &= \tau_0 + \mu_{pl}\dot{\gamma} & \text{for} \quad \tau \geq \tau_0
\end{aligned} \tag{5}$$

Concrete is assumed to behave as a Bingham material during shear, Eq. (5). To fit the Cauchy equation, the apparent viscosity η going into Eq. (3) is written as:

$$\eta = \frac{\tau_0}{\dot{\gamma}} + \mu_{pl} \tag{6}$$

As yield stress is low the apparent viscosity is mostly governed by the plastic viscosity (Eq. (6)). Without the effects of inertia, the shape of the material at flow stoppage is determined by the yield stress τ_0.

The shear rate $\dot{\gamma}$ must not equal zero, but is fixed in numerical simulations to obtain a minimum numerical value even at flow stoppage. As defined in most rheology text books, e.g. [19] the shear rate is

$$\dot{\gamma} = \sqrt{(2\dot{\boldsymbol{\varepsilon}} : \dot{\boldsymbol{\varepsilon}})} \tag{7}$$

Computationally, Eq. (6) is implemented by adding a small numerical value m to $\dot{\gamma}$ [21], even at flow stoppage ($\dot{\gamma} = 0 + m$). The set of equations defining the non-compressible viscosity model for the simulations are given by Eqs. (1) to (4) and Eqs. (6) to (7). To track the fluid interface, a high resolution differencing scheme for Volume of Fluid (VOF) method was employed, [22]. Meshing and computing were done according to 'Best Practice Guidelines' for CFD, [23], further details may be found in [24].

4. VERIFICATION OF THE NUMERICAL MATERIAL MODEL

4.1 Yield Stress

The simulation model described above is compared to a theoretical channel-flow solution. Given flow that spreads slowly without inertia effects, the final flow spread at flow stoppage is directly correlated to the yield stress of the material, assuming that material density and volume are known. Gently pouring of 6 liters of concrete from a bucket (lasting 30 seconds to avoid inertia effects) into a channel-type box will result in different spreads dependent on the yield stress τ_0. A volume 6 liters is approximately 1000 or sometimes even 4000 times the volume of the largest particle in the concrete, thus this amount is considered to be sufficient to be representative for the material [25].

Once the density ρ of the concrete is known, the yield stress can be determined according to Eqs. (8) and (9). With w being the channel width, h_{max} the maximum height of the poured concrete in the channel and x the propagation coordinate of the concrete, the tested volume V will be equal to [25]:

$$V = w \int_0^{h_{max}} x\mathrm{dh} = \frac{w^3}{4A}\left(\ln(1+u) + \frac{u(u+2)}{2}\right)$$

$$\text{with} \quad A = \frac{2\tau_0}{\rho g w} \quad \text{and} \quad u = \frac{2h_{max}}{w} \tag{8}$$

The final maximum height h_{max} of the concrete at the pouring end of the channel can be linked to final spread length l at flow stoppage:

$$l = \frac{h_{max}}{A} + \frac{w}{2A}\ln\left(\frac{w}{w+2h_{max}}\right) \tag{9}$$

For the theoretical solution of τ_0, inertia effects of the material are disregarded and a non-slip condition is assumed. For concrete of density 2300 kg/m^3 one obtains according to theory (Eqs. (8) and (9)) for $\tau_0 = 50$ Pa and $\tau_0 = 12.5$ Pa a final spread length of $l = 702$ mm and $l = 1160$ mm respectively. This has also been simulated based on Equations (1) through (7). The numerically calculated lengths for the channel flow are $l = 708$ mm and $l = 1130$ mm respectively, differing only by 1.7% from the theoretical values for spread lengths obtained by Eqs. (8) and (9), [24] for the two concretes with different levels of yield stress. It can therefore

be concluded that the numerical model shows good agreement between the material yield stress and the final shape at flow stoppage.

4.2   Viscosity

The speed of flow v is associated with the apparent fluid viscosity. Depending on the viscosity, a certain stress level on the fluid will result in a particular shear rate, as can be understood from Eq. (5). Inertia effects might affect the final shape of flow once the typical inertia stress ($I = \rho v^2$, [6]) is not considerably smaller (in the order of tenths) than the yield stress of the material.

Simulation of a different case, the regular L-box was compared for 18 different types of concrete and correlated to videotaped L-box tests together with their measured Bingham parameters and density, [24]. The flow time from gate opening until reaching the end of the box (t_{600}) was both measured and simulated. The correlation factor between the measured and simulated time duration is $R^2 = 0.62$. The flow is point wise slower (~1.0 - 1.5 seconds) or just slightly slower (~0.5 seconds) in the lab tests than in the simulated case, as shown in Figure 1.
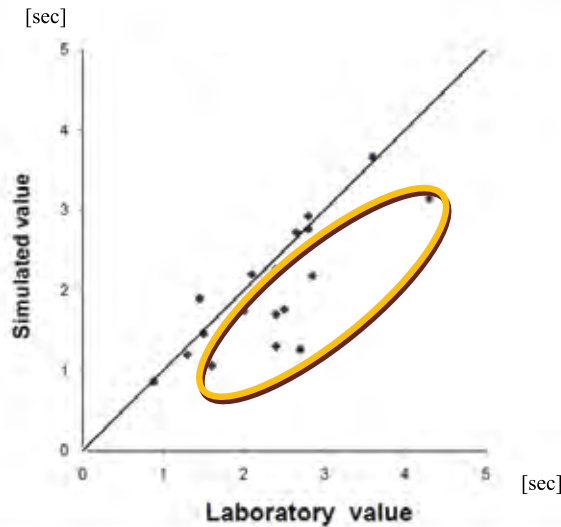

Figure 1 - L-box tests compared to simulated values of t_{600} for 18 different types of concrete, the delayed laboratory values can be found within the marked area.

This delay is most likely due to the fact that gate opening time (averaged to about 1 second) was not accounted for in the simulation. The delay in flow is apparently of importance [26] when calculating for the plastic viscosity. Thus, the simulation model here is considered to be reliable including plastic viscosity calculations.

5. APPLICATION OF THE NUMERICAL MATERIAL MODEL – FORM FILLING OF A PRECAST ELEMENT

A precast double-tee slab manufactured at Strängbetong's precast factory in Kungsör, Sweden, was modelled.

5.1 The Double-Tee Slab

A waffled type of double-tee slab, which is manufactured for roofing and precast indoors under stable conditions in lengths up to 32 meters, has been simulated at its heavily reinforced ends (see Figure 2). Nine prestressed reinforcement cables, diameter 12.9 mm, are surrounded by stirrups spaced at 70 mm. The lower set of reinforcement is partially resting on top of metal plates.
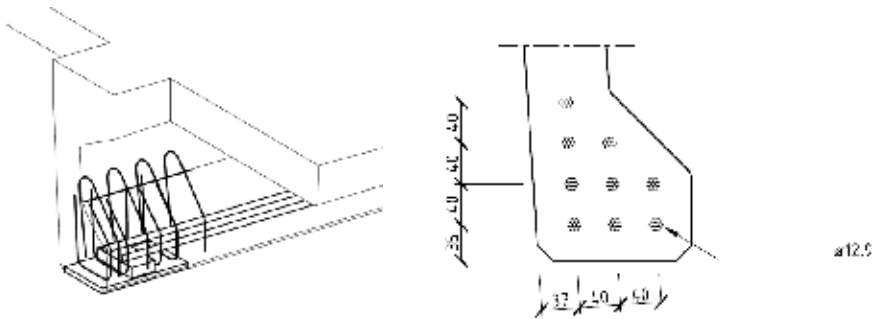

Figure 2 - The waffled double-tee slab in perspective view (left) and its cross sectional view (right), dimensions in [mm].

The concrete has a low yield stress τ_0, a consistent level of apparent viscosity is monitored through power consumption measurements during mixing of every single batch. Production of the concrete is performed under stable, constant and predictable conditions when it comes to SCC recipe (i.e. mixing, timing, temperature, placing and formwork design). The manufacturing has been trimmed and optimized over several years in order to minimize man hours as well as material and environmental resources. The slab is carefully filled by slowly pouring the concrete from the bucket into one tee at a time. The mix slowly flows ahead in the tee from one end to the other end. This allows the concrete to 'de-air', i.e. loose air bubbles along the way, resulting in high quality surfaces. Ends are then top filled before casting the body of the slab. The slump flow with the Abram's cone for the mixed batches is about 800 mm with a t_{500} of 2 seconds.

5.2 Assumptions Made for the Model

In order to calculate the worst-case scenario, the top filled 70 mm thick end section is simulated showing the nine prestressed cables of the tee. For simplicity, the round cables are modeled as square voids, which to a certain extent hinder the concrete (lighter liquid) as seen in Figure 3

from reaching the bottom of the tee. The case is simulated with four different levels of yield stress (τ_0 = 25 Pa, τ_0 = 12.5 Pa, τ_0 = 5 Pa and τ_0 = 1.0 Pa) to be compared. The concrete is gently poured from a vessel located right above the tee, eliminating inertia effects. The front and back of the simulated section are smooth, but rigid, walls. They represent the end wall on one side and a stirrup on the other side. In case of top filling the end section, the front and back walls here serve to emphasize the simulation of a worst scenario occurrence. For the same reason, the metal plates at the bottom of the tee are included in the model.

5.3   Results

As can clearly be seen from the results in Figure 3, the geometry of the modelled tee with the rebars is tricky to fill completely.

Figure 3 – End section of tee filling for τ_0 = 25 Pa, τ_0 = 12.5 Pa, τ_0 = 5 Pa and τ_0 = 1.0 Pa.

Dark spots in the lighter fluid represent air pockets. These are more distinct and larger for higher yield stress levels. Air pockets occur at the bottom, around the voids representing the rebars and along the right-hand tilted wall. Even with a yield stress as low as only 1.0 Pa, a few shadows are still observed. This corresponds well with the fact that in order to ensure complete form filling at both end sections of the tees in the factory, a poker vibrator is dipped into the concrete for just a few seconds, short enough as to not force the mix to segregate. A low amount of mechanical vibration will ensure a high quality product, thoroughly filling in the form giving a smooth surface. Accordingly, it is worth noting that a real life problem is also detected numerically.

6.   AN ON-SITE RHEOLOGY ASSESSMENT TOOL – THE RHEO-BOX

Using the verified material model, simulations were performed on the so called Rheo-Box in order to link concrete speed and spread length in the box to the rheological parameters of plastic viscosity and yield stress. The Rheo-Box can be used on the construction site for control and verification of the delivered concrete in order to ensure quality of the fresh concrete and its required rheology. The Rheo-Box is a unique assessment tool for the job-site since both yield stress and plastic viscosity may be evaluated.

6.1   Geometry of the Rheo-Box

Figure 4 shows the rheological measuring box, the so called Rheo-Box. It is a 1.2 m long channel of 0.2 m width. Attached to this is a 0.3 m high container holding the concrete, which has an opening of 0.2 m × 0.15 m facing the channel. A volume of 6 liters of concrete is filled and released into the channel when opening the gate. Numerically, the gate opening time is zero, since the fluid release is modelled as being instantaneous. In addition to measuring the final spread length at flow stoppage, time t_{400} is measured from gate opening time to the point when the concrete flow has reached a travelling distance of 0.4 m.
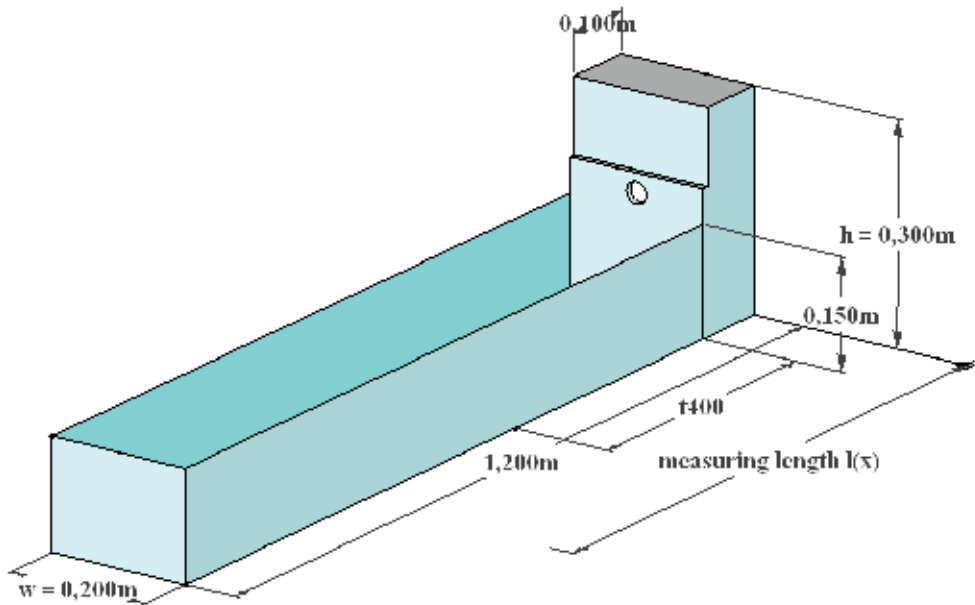

Figure 4 - Geometry of the Rheo-Box, with travelling distance for t_{400} and measuring length l.

6.2   Rheological Input Data

Altogether, 45 different simulations of flow in the Rheo-Box were performed, as well as 4 lab tests using a ConTec-4 SCC viscometer (http://www.contec.is) producing the following rheological input data shown in Table 1. The concrete measured in the ConTec-4 SCC viscometer was also visually recorded when tested in the Rheo-Box for detailed evaluation of the travelling speed at t_{400} and its length at flow stoppage. It was observed that gate opening time for the Rheo-Box can be averaged at 0.2 seconds, thanks to the low friction guides of the gate. Before gate opening, the box was scarcely wetted and the concrete was carefully rodded in the container of the Rheo-Box 20 times to avoid thixotropic effects.

Table 1 – Input data adequately mapping the self-compacting zone suggested by [27]

μ_{pl} [Pa s]	$\rho = 2100$ kg/m³ τ_0 [Pa]	$\rho = 2250$ kg/m³ τ_0 [Pa]	$\rho = 2400$ kg/m³ τ_0 [Pa]	μ_{pl} [Pa s]	τ_0 [Pa]	ρ [kg/m³]
	Simulated Values			**Lab Test Cases**		
10	30, 55, 70	30, 40, 50, 60, 70	30, 55, 70	11.1	52	2196
20	30, 40, 55	20, 40, 50, 60, 70	30, 40	39.45	81.5	2380
30	5	40, 50, 55, 60, 65	5	49.15	23	2380
40	45	40, 45	45	59.25	40.5	2370
50		15, 50				
60	10	10	10			
70	20	25	20			
90	15	15	15			
130	10		10			

6.3 Results

A high correlation factor R^2 was achieved for the simulated yield stress and viscosity relations.

Yield Stress
The relation between the yield stress and final spread length at flow stoppage is plotted in Figure 5. Simulated values (y = 412 e$^{-3.736x}$) and theoretical values are compared to the 4 lab test cases, showing adequate model correspondence. As can be seen, simulated values give a higher yield stress than theoretical values for smaller spreads (inertia effects are more pronounced for small spreads, as the concrete speed is higher close to its point of release). These effects are negligible for large spreads where the simulated relation given is closer to the theoretical solution.
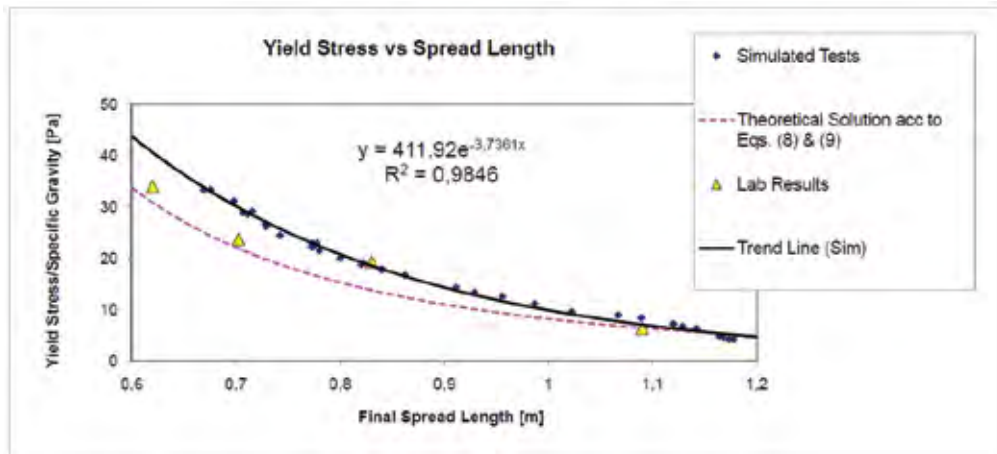

Figure 5 - Output data compared to lab test results and theoretical solution according to Eqs. (8) and (9).

Viscosity

A linear relation for the plastic viscosity of the simulated concrete was found according to Figure 5, linking the plastic viscosity linearly to the product of the final spread at flow stoppage and t_{400}. Previously, a similar linear relation between the ratio viscosity to yield stress and the time to final spread was established [28]. The average travel distance of the fluid in the Rheo-Box, according to the geometry in Figure 4, is approximately: (0.3 m + 1.2 m)/2 = 0.75 m at average flow duration of (maximum flow duration)/2 ≈ 5 s. This gives an average fluid flow speed of 0.15 m/s and yields for a concrete density ρ = 2300 kg/m^3 an inertia stress of I = 51.75 Pa (see Section 4.2), which is definitely not considerably lower than any of the yield stress levels presented here. A delayed gate opening time of 0.2 seconds will however not affect the calculated viscosity more than 2 Pa s for plastic viscosities ranging between 5 Pa s and 130 Pa s according to the relation y = 7.2x + 2.03 given in Figure 5, the trend line from the lab tested concrete showing this particular small shift.
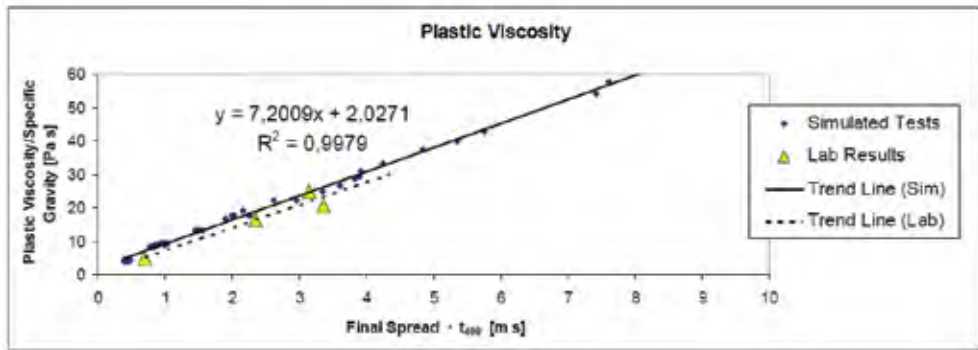

Figure 5 - Output data linking the product of t_{400} and final spread to material viscosity.

The trend lines for any type of Rheo-Box and their correlation to a particular viscometer can always be calibrated for a more elaborate real concrete test series if found necessary.

7. CONCLUSIONS

It has been shown that numerical simulation of concrete modeled as a Bingham material correlates well to the theoretical solution of the channel flow. Yields stress τ_0 determines spread length in the box, plastic viscosity μ_{pl} is a parameter related to speed of flow. Simulation of castings, such as an end section of the presented double-tee slab show high conformity with the real world form filling.

A new test device was introduced, the Rheo-Box, allowing measurement of both yield stress and plastic viscosity of a Bingham fluid. Promising results shown indicate that the Rheo-Box could produce reliable rheological parameters when calibrated for a large lab test series. Finally, it can be concluded that these types of flow tests are not as accurate as rheological parameters produced using a viscometer in a lab environment. However, parameters obtained with the Rheo-Box can present complementary information of practical use for the construction site.

It is the authors' belief that in the future, numerical simulation will be a more common tool used for predictions of possibly complicated SCC castings.

ACKNOWLEDGEMENTS

REFERENCES

1. Weller, H., Tabor, G., Jasak, H, Fureby, C., A tensorial approach to computational continuum mechanics using object oriented techniques, *Computers in Physics*, 12 (1998) 620-631.
2. Chu, H., Machida, A., Numerical simulation of fluidity behaviour of fresh concrete by 2D distinct element method, Transaction of the Japan Concrete Institute 18.
3. Noor, U. A., Uomoto, T., Three-dimensional discrete element method of rheology tests of self-compacting concrete, in: Proceedings, First International RILEM Symposium in Self-Compacting Concrete, Stockholm, Sweden, 1999.
4. Petersson, Ö., Hakami, H., Simulation of SCC – laboratory experiments and numerical modelling of slump flow and L-box tests, in: Proceedings, 2nd International SCC Conference, Tokyo, Japan, 2001.
5. Uebachs, S., Brameshuber, W., Numerical simulation of the flow behaviour of self-compacting concretes using fluid mechanical methods, in: Proceedings, 4th International RILEM Symposium, Chicago, USA, 2005, pp. 597-604.
6. Roussel, N., Coussot, P., "Fifty-cent rheometer" for yield stress measurements: from slump to spreading flow, *Journal of Rheology*, 49 (2005) 705-718.
7. Nyholm Thrane, L., Szabo, P., Geiker, M., Stang, H., Pade, C., Simulation and verification of flow in test methods, in: Proceedings, 4th International RILEM Symposium, Chicago, USA, 2005, pp. 551-556.
8. Petersson, Ö., Simulation of self-compacting concrete – laboratory experiments and numerical modelling of testing methods, slump flow, J-ring and L-box tests, in: Proceedings, 3rd International RILEM Symposium, Reykjavik, Iceland, 2003, pp. 202-207.
9. Mechtcherine, V., Shyshko, S., Simulating the behaviour of fresh concrete using distinct element method, in: Proceedings, 5th International RILEM Symposium, Ghent, Belgium, 2007, pp. 467-472.
10. Gram, A., Farhang, A., Silfwerbrand, J., Computer-aided modeling and simulation of self-compacting concrete flow, in: Proceedings, 5th International RILEM Symposium, Ghent, Belgium, 2007, pp. 455-460.
11. Dufour, F., Pijaudier-Cabot, G., Numerical modelling of concrete flow: homogeneous approach, *International Journal for Numerical and Analytical Methods in Geomechanics* 29 (2005) 395-416.

12. Wallevik, J., Rheology of particle suspensions, Ph.D. thesis, NTNU, Trondheim, Norway (2003).
13. Flatt, R., Martys, N., Bergström, L., The rheology of cementitious materials, MRS Bulletin (2004) 314-318.
14. Nyholm Thrane, L., Form filling with self-compacting concrete, Ph.D. thesis, Danish Technological Institute (2007).
15. Roussel, N., A thixotropy model for fresh fluid concretes: theory, validation and applications, *Cement and Concrete Research* 36 (2006) 1797-1806.
16. Billberg, P., Form pressure generated by self-compacting concrete- influence of thixotropy and structural behaviour at rest, Ph.D. thesis, Royal Institute of Technology, Sweden (2006).
17. Malvern, L.E., Introduction to the mechanics of a continuous medium, Prentice-Hall, 1969.
18. Mase, G.E., Continuum mechanics, Schaum's Outlines, McGraw-Hill, 1970.
19. Goldstein, R.J. (ed.) Fluid Mechanics Measurements, Taylor & Francis, 1996.
20. Macosco, C.W., Rheology Principles, Measurements and Applications, CVCH Publishers Inc., 1994.
21. Papanastasiou, T. C., Flow of material with yield, *Journal of Rheology*, 31 (1987) 385-404.
22. Hirt, C., Nichols, B., Volume of fluids (VOF) method for the dynamics of free boundaries, *Journal of Computational Physics* 39 (1981) 201-225.
23. Best Practice Guidelines, European Research Community on Flow, Turbulence and Combustion, Turbulence and Combustion, 2000.
24. Gram, A., Numerical modelling of self-compacting concrete flow – discrete and continuous approach, Lic. Thesis, Royal Institute of Technology, Stockholm, Sweden (2009).
25. Roussel, N., The LCPC-box, a cheap and simple technique for yield stress measurements of SCC, *Materials and Structures*, 40 (2007) 889-896.
26. Nyholm Thranem L., Simulation of the test method "L-box" for self-compacting concrete. Annual Transactions of the Nordic Rheology Societey, 12:47–54, 2004.
27. Nielsson, I. and Wallevik, O.. Rheological evaluation of some empirical test methods - preliminary results. In O. Wallevik and I. Nielsson, editors, Third International RILEM Symposium, PRO 33, pages 59–68, Reykjavik, Iceland, 2003.
28. Tregger, N., Ferrara, L., Shah, S., Identifying viscosity of cement paste from mini-slump-flow test, *ACI Materials Journal*, 105 (2008) 558-564.

Flexural behaviour of members with a combination of steel fibres and conventional reinforcement

Anette Jansson, PhD student
Kent Gylltoft, Professor
CHALMERS University of Technology
Dep. of Civil- and Environmental Engineering,
Div. of Structural Engineering
412 96 Göteborg, Sweden
E-mail: anette.jansson@chalmers.se
        kent.gylltoft@chalmers.se

Ingemar Löfgren, Ph.D. Thomas Concrete Group AB,
Göteborg, Sweden
E-mail: ingemar.lofgren@tcg.nu

ABSTRACT

The purpose of the presented work was to investigate the flexural behaviour of members with a combination of steel fibres and conventional reinforcement. A systematic approach for material testing and structural analysis, based on fracture mechanics, was used and covers (1) material testing, (2) inverse analysis and (3) structural analysis based on FEM. In addition, the average crack spacing from the FE analyses was compared with experimental results and with two analytical approaches. The results suggest that the approach used for the material testing provides the properties necessary to perform analyses based on non-linear fracture mechanics. The structural behaviour could be predicted with good agreement with FEM using both bi-linear and multi-linear stress-crack opening (σ-w) relationships. When comparing peak loads obtained in the experiments with results from the analyses, the agreement was good. The crack spacing from the experiments was predicted with good agreement using both the analytical approach by Löfgren and the multi-linear FE approach.

Keywords: fibre-reinforced concrete, fracture mechanics, stress-crack opening relationship, inverse analysis, crack spacing.

1.   INTRODUCTION

The number of practical applications of fibre-reinforced concrete (FRC) is increasing, as FRC offers a possibility to greatly simplify in-situ cast concrete construction. However, if FRC is to be a more widely used material, general design guidelines are needed which take into account the material properties characteristic of FRC. Moreover, with reduction of crack width being one of the main benefits of FRC, it seems necessary to develop methods which predict crack width and fracture process with acceptable accuracy.

In order to account for the positive effects of the fibres, in the design proposals for FRC by RILEM TC 162-TDF [1] and by CNR DT 204-2006 [2] (Italian design standard), a modification has been suggested to adapt the crack-width calculation formulas for regular concrete found in ENV 1992-1-1 [3]. The modification made by RILEM considers the fibre-aspect ratio (L_f / d_f), where the original formula in [3], for crack spacing in plain concrete, is multiplied by a factor ($50 \, d_f$ / l_f) with 1.0 as upper limit; see Eq. 1.

$$s_{rm} = \left(50 + 0,25 \cdot \kappa_1 \cdot \kappa_2 \cdot \frac{\phi}{\rho_{eff}} \right) \left(\frac{50}{L_f / d_f} \right)$$

$$\text{with} \quad \left(\frac{50}{L_f / d_f} \right) \leq 1,0$$

(1)

The modification according to the Italian proposal [2] is similar, but here there is also a lower limit for the multiplication factor. However, considering that increased fibre volume fraction will give a larger contribution to the crack arrest, the above proposed modifications for calculation of crack width/spacing seem incomplete, as also pointed out by Chiaia et.al. [4]. Hence, a different approach is suggested by Löfgren [5] where the residual strength is considered which includes the effect of both fibre amount, fibre type and aspect ratio. This approach is described in section 4 below.

A more comprehensive approach is to use finite element analysis based on non-linear fracture mechanics. With this approach it is possible to predict and simulate the fracture process – a necessity for materials like FRC, which has a significantly different cracking behaviour compared to plain concrete, when design requirements for the serviceability state govern.

The tests reported in this paper were carried out on beams reinforced with a combination of steel fibres and conventional continuous steel reinforcement. The material properties for the post-cracking behaviour of the steel fibre-reinforced concrete, in terms of stress-crack opening relationship, were determined through inverse analysis of results from wedge-splitting tests (WST). Since especially the cracking behaviour was of interest, two kinds of stress-crack opening relationship were tested (bi-linear and multi-linear, see Figure 1) to investigate if any of the two is better suited for studying of the cracking process than the other.
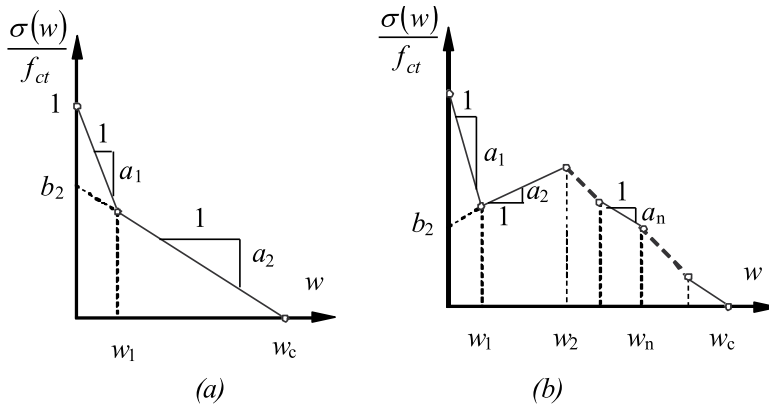

Figure 1 – General shape of the two types of simplified stress-crack opening relationships used for the FE-analyses: a) bi-linear and b) multi-linear.

2. EXPERIMENTAL PROGRAMME

2.1 Materials

The concrete used was self-compacting (a slump flow spread of 500 to 650 mm) and had a water cement-ratio of 0.55. The fibre content was 0%, 0.25 vol-% (19.6 kg/m^3), 0.5 vol-% (39.3 kg/m^3) and 0.75 vol-% (58.9 kg/ m^3). For fibre reinforcement a hooked-end steel fibre with yield limit 1100 MPa was used, Dramix® RC65/35. The mix compositions can be found in [6] and in Table 1. Rebars of sizes $\phi 6$ and $\phi 8$ were used for the conventional steel reinforcement. Their material properties, in terms of stress-strain curves, are shown in Figure 2, where the stresses are based on average measured diameter; 5.7 and 7.7 mm, respectively. The $\phi 6$ re-bars had a yield-strength f_{sy} of 660 MPa and a tensile strength f_{su} of 766 MPa. The $\phi 8$ re-bars had a yield strength f_{sy} of 640 MPa and a tensile strength f_{su} of 748 MPa.

Table 1. Concrete composition of the different mixes.

Series	Cement Bygg Skövde	Water	Sand 0 - 4 mm	Sand 0 - 8 mm	Gravel 4 - 8 mm	Gravel 8 - 16 mm	Filler (lime)	Super plasticizer	Stabilizer	Fibre,Dramix ®RC 65/35
1-V_f0-ϕ8	325	179	633	158	235	549	188	3.9	3.2	00.0
2-V_f05-ϕ8	325	179	627	156	233	545	188	3.9	3.2	39.3
3-V_f025-ϕ6	325	179	630	157	234	547	188	3.9	3.2	19.6
4-V_f05-ϕ6	325	179	627	156	233	545	188	3.9	3.2	39.3
5-V_f075-ϕ6	325	179	625	156	233	542	188	3.9	3.2	58.9

Heading for the column group: Dry content, kg/m^3
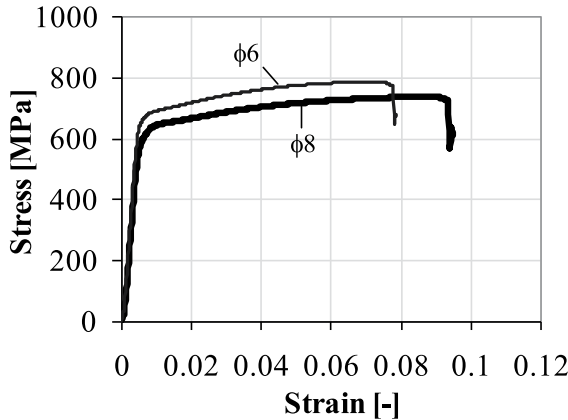

Figure. 2 – Stress-strain relationship for the longitudinal steel reinforcement in the tested beams.

2.2 Material testing – FRC

The compressive strength was determined at 28 days on water-cured cubes, 150x150x150 mm^3, according to SS-EN 12390-2 [7] and SS-EN 12390-3 [8] ; the results are presented in Table 2. The tensile fracture behaviour of the FRC (in the form of stress-crack opening (σ-w) relationships) was determined by conducting inverse analysis on results from wedge-splitting tests (WST); see Figure 3, following a procedure presented by Löfgren et al. [9]. This approach

has been shown to yield reliable results; see e.g. Meda et al. [10], Löfgren [11], and Löfgren et al. [9].

Wedge-splitting test,

WSTThe WST was performed according to NT Build 511 [12] on cubic specimens with side length 150 mm. In each specimen a cast groove in the upper part of the specimen was provided for placement of the wedge, and a starter notch was cut to ensure stable crack initiation. During a test, the vertical load, Fv, is applied and measured with a load cell and the crack mouth opening displacement (CMOD) by a clip gauge. The vertical load, Fv, is transformed into a horizontal splitting force, Fsp, which may be calculated from the vertical load Fv as:

$$F_{sp} \approx \frac{F_v}{2\tan(\alpha)},$$

(2)

where α is the angle of the wedge, see Figure 3. The result is displayed as the splitting load, Fsp, versus the crack mouth opening displacement, CMOD and can be seen in Figure 4.
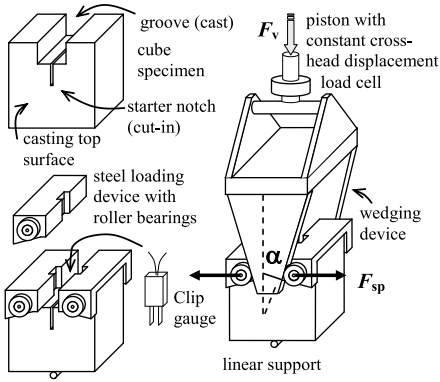

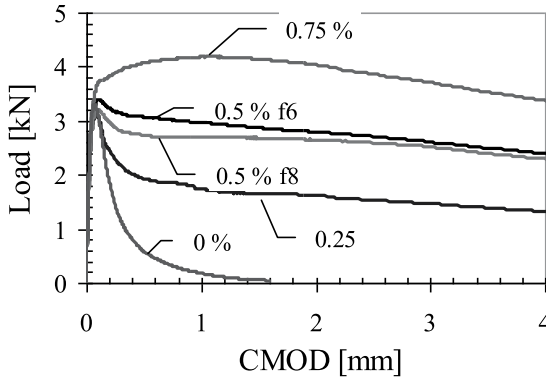*Figure. 3 – Principle of the wedge-splitting test method, from Löfgren [11].*

Figure. 4 –Average splitting load-CMOD curves for the five different mixes.

Inverse analysis

The inverse analysis is performed as a stepwise back-calculation of the splitting load-crack

mouth opening displacement (Fsp-CMOD) curves from the WST tests. Two different σ-w relationships were determined for each mix; namely bi-linear and multi-linear, see Figure 1. For the bi-linear σ-w relationships an optimisation program was used, developed at DTU by Østergaard [13], while for the multi-linear one the optimisation was achieved manually in combination with finite element analysis.

Both approaches are performed as iterative processes. The tensile strength, f_{ct}, was one of the estimated parameters in the inverse analysis based on a bi-linear σ-w relationship, along with the ultimate crack opening, w_c, and the slopes a_1 and a_2, (Figure 1). The values for f_{ct} were limited with respect to reasonable values referring to the compressive strength. For the multi-linear approach the same tensile strengths and ultimate crack openings were assumed as obtained in the bi-linear analyses. The remaining multi-linear σ-w curve was obtained by estimating values for the stress at a given crack opening. The estimated σ-w was then used as input in an FE analysis of the WST. The estimated σ-w values were changed in a "trial and error" manner until the results from the FE analysis were in close agreement with the WST experimental results. The inverse analysis was considered acceptable when the ratio of the WST-experimental load and the WST-load from the FE-results, $F_{sp.inv}/F_{sp.exp}$, in each point of the estimated curve was as close to unity as possible (best fit). The requirement was that the ratio should lie within the range 1±0.1 for the bi-linear relationship and 1±0.05 for the multi-linear relationship. Naturally for the bi-linear approach with only two varying parameters (slopes a_1 and a_2), it is not possible to achieve as good agreement as when using a multi-linear approach, where an unlimited number of points may define the σ-w relationship.

The choice of slope of the descending branch is quite sensitive. As an example see Figure 4, where three different suggestions for the beginning of a multi-linear σ-w relationship are given, (note the scale). For instance at σ=2MPa, w differs by 0.01 mm between s-w_B and s-w_D. The results from the FE analyses using the three different σ-w relationships are seen in Figure. 5, where s-w_D yields a markedly higher splitting load in the first part of the curve (FE_D Figure 5).
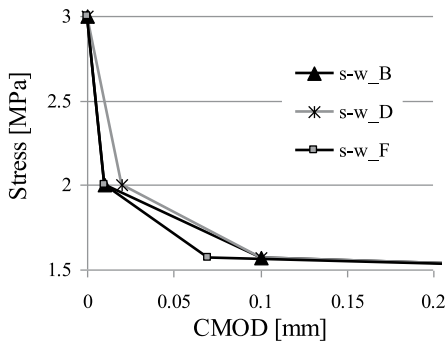

Figure. 4 – Three examples of multi-linear σ-w relationship for the mix with fibre volume fraction V_f =0.5%, (note the scale).
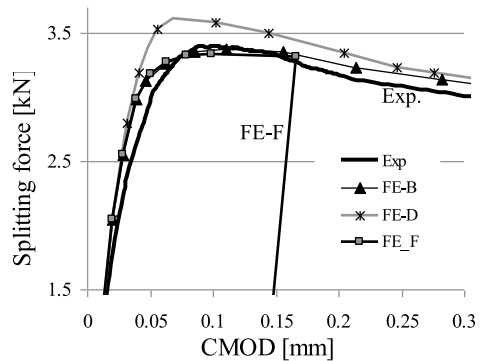
Figure. 5 – For mix with V_f =0.5%; compare WST-exp with FE results from using the three σ-w relationships suggested in Figure 4 (note the scale).

The final *σ-w* relationships for the different SFRC mixes are presented in Figures 6 and 7. Typical differences in accuracy between the inverse analysis using a bi-linear *σ-w* relationship and a multi-linear one are shown in Figures 8a-b.
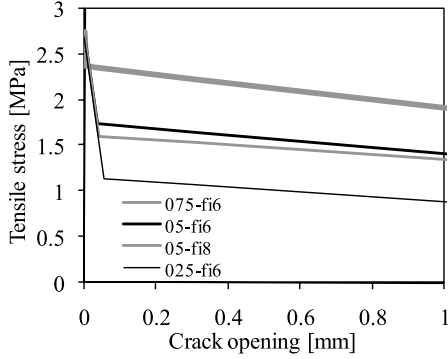

Figure. 6 – Final bi-linear σ-w relationship for the full-scale elements.
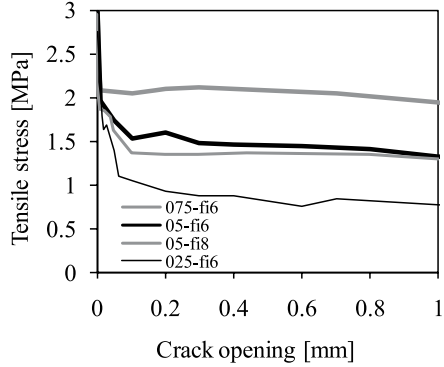
Figure. 7 – Final multi-linear σ-w relationship for the full-scale elements.
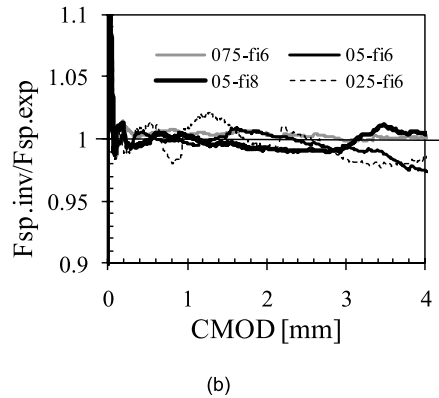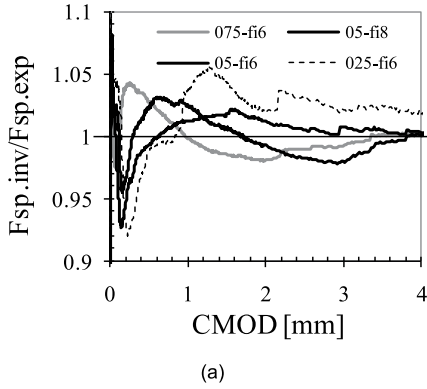
Figure. 8 – Comparison of ratio splitting load from wedge splitting test / splitting load from FE analysis ($F_{sp.exp}/F_{sp.inv}$); (a) bi-linear and (b) for multi-linear σ-w relationship.

2.3   Tests on beams with conventional bar reinforcement

The tested beams had a geometry and test set-up according to Figure 9. The experimental programme, listed in Table 2, consists of five series with three beams in each, resulting in a total of fifteen beams. The beams had a geometric reinforcement ratio ρ of 0.25% or 0.45%. The compressive strength (determined at 28 days on water-cured cubes, 150x150x150 mm^3) varied with the fibre content (as a result of differences in the entrained air content) and can be seen in Table 3; for details see [6].

In section 3 below the experimental results of the tested beams are presented as the average of the three beams that were tested for each mix (Figures 11-15).

Table 2. Experimental programme.

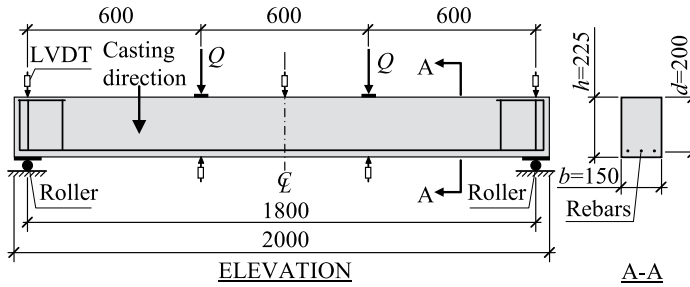| Series	Rebars	Fibre dosage[*] [vol-%] ([kg/m³])	$f_{cc.28d}$ [MPa] (Min/Max)
1-V_f0-ϕ8	3 ϕ 8 (ρ=0.45%)	0% (0)	47.7 (45.7/49.4)
2-V_f05-ϕ8	3 ϕ 8 (ρ=0.45%)	0.5% (39.3)	38.2 (37.4/39.1)
3-V_f025-ϕ6	3 ϕ 6 (ρ=0.25%)	0.25% (19.6)	39.2 (37.7/40.2)
4-V_f05-ϕ6	3 ϕ 6 (ρ=0.25%)	0.5% (39.3)	37.7 (36.4/38.6)
5-V_f075-ϕ6	3 ϕ 6 (ρ=0.25%)	0.75% (58.9)	36.8 (36.6/37.0)

Figure. 9 – Test set-up for the structural beam tests.

3.   RESULTS FROM EXPERIMENTS AND ANALYSES

To achieve a deeper understanding of the structural and fracture behaviour, non-linear fracture mechanics was applied, using the finite element method. The general finite element program Diana was used in all analyses; see TNO [14]. The concrete was modelled with four-node quadrilateral isoparametric plane stress elements. For the reinforcement, truss elements were used, and the interaction between the reinforcement and the concrete was modelled by using special interface elements describing the bond-slip relation; see TNO [14]. The bond-slip relationship was chosen according to CEB-FIP MC90 [15], and confined concrete with good bond conditions was assumed.

To model the cracks a smeared crack approach was used. This means that the crack process zone should be "smeared out" over a distance - the crack-band width. The stress-crack opening curve represents the energy that is consumed/dissipated during the fracture process and the crack-band width is used to convert the crack width (or displacement) to a strain. When modelling concrete without fibre reinforcement and assuming complete interaction between concrete and rebars, the crack-band width is chosen as the average crack spacing. If instead allowing slip between concrete and rebars, the crack-band width is usually chosen as the width (or average width) of one mesh element, assuming that the crack should localize in this element row only. For fibre reinforced concrete, on the other hand, this choice is not as straight forward. Conventional reinforcement in combination with fibre reinforcement may create a densely distributed reinforcement which gives rise to diffusion and distortion in the neighbourhood of the

reinforcement and lead to a diffuse crack pattern. The reason for this is that the fibres are able to transfer significant stresses across the crack. This means that even if the elements neighbouring the actual crack might not be subjected to localised cracking, they are subjected to large stresses due to the stress transfer across the crack, and micro cracks may be present. Due to this the crack pattern in analyses of fibre-reinforced concrete becomes more diffuse than for concrete with no fibres added, and the assumption of crack localization in one element row does not hold. It then seems reasonable that the crack band width for FRC materials with combined reinforcement instead could be chosen closer to the average crack spacing. In order to ensure the toughness to be correctly modelled the energy, needed to crack one unit area, is thus averaged out over several element widths (i.e. a larger crack-band width is used). This is also necessary in order to make sure that the load bearing capacity, i.e. the stress transfer over the crack is not over estimated. If the crack band width is chosen too small, the load bearing capacity will be over estimated. This is a difficulty when modelling FRC materials and further investigations regarding this matter are necessary.

For the reference series with no fibres added, Series 1, a non-linear tension softening curve according to Cornelissen et. al was used, see [16]. The basic shape of this curve is pre-defined in the FE software Diana [14] and is determined by the tensile strength, f_{ct}, Young's modulus, E_c, and fracture energy, G_f. For Series 1 the fracture energy was determined from the WST results to G_f=136 Nm/m^2 and the crack-band width was chosen to the width of one mesh element = 5 mm.

The results from the tested beams are presented in Figures 11-15 together with results from the FE analyses. In general, the peak-load was predicted with good agreement for the FE-analyses, using both a bi-linear and a multi-linear σ-w relationship; see Table 3 and Figure 10.
The correlation was good; 0.994 for the FE analyses using a bi-linear σ-w relationship and 0.996 using a multi-linear one. In addition, the average crack spacing in the analyses (measured on the cracks located in between the two load points) show acceptable agreement with the experimental ones, see Table 4. Furthermore, the load-deflection curves were predicted with good agreement for both types of σ-w relationship; although the models predicted a somewhat stiffer pre-yield response, see Figures 11, 14 and 15. This could possibly be explained by not having obtained the optimum parameters for the σ-w relationships, and could also be related to difficulties in determining the yield value for the reinforcement bars. Furthermore, the bond-slip relationship used for the analyses was based on a proposal for plain concrete and might have to be adjusted when analyzing fibre-reinforced concrete. Additionally it can be said that numerical problems were encountered in the analyses of the beams with 0% and 0.75% fibre content and, especially for the latter, the FE program had difficulties reaching convergence at initialized yielding of the rebars.

When looking at the crack patterns there are indications that the analyses where a multi-linear σ-w relationship was used, seem to better follow the experimental results where an increase in fibre content yields a decrease in crack spacing. Hence, this relationship is promising for future analyses aiming at crack-width prediction in the serviceability limit state.

Table 3. Maximum loads from experiments and analyses.

	Q_{max} [kN]				
	$V_f 0 \phi 8$	$V_f 0.5 \phi 8$	$V_f 0.25 \phi 6$	$V_f 0.5 \phi 6$	$V_f 0.75 \phi 6$
Exp average	28.2	31.9	18.6	19.7	21.5
(Exp min / Exp max)	(27.4/ 29.0)	(30.6/ 33.5)	(18.0/ 19.1)	(19.0/ 20.5)	(20.6/ 22.3)
FE bi-lin	28.9*	31.7	18.6	19.6	22.8
FE multi		31.8	19.5	20.2	22.9

* For Series V_f 0-ϕ8 a non-linear tension-softening relationship according to Cornelissen et al. was used; see TNO [11].

Table 4. Average crack spacing, exp. vs. analysis.

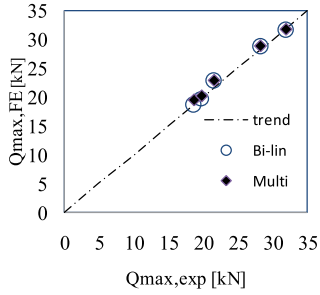|	Average crack spacing [mm]				
	$V_f 0 \phi 8$	$V_f 0.5 \phi 8$	$V_f 0.25 \phi 6$	$V_f 0.5 \phi 6$	$V_f 0.75 \phi 6$
Exp average	78	59	71	66	55
(Exp min / Exp max)	(75/80)	(57/63)	(66/77)	(65/68)	(53/58)
FE bi-lin	80*	64	88	87	48
FE multi		51	69	57	40

Figure. 10 − Comparison of maximum load from experiments and from the finite element analyses.
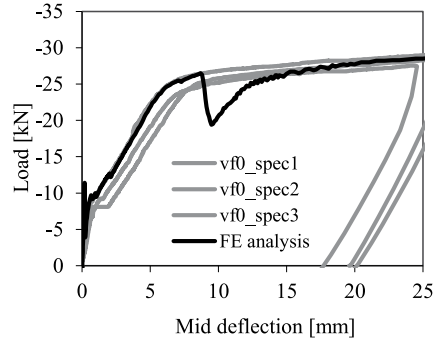
Figure. 11 − Comparison of load-deflection relationships for full-scale elements and analyses. No fibres added, rebar diameter 8 mm.
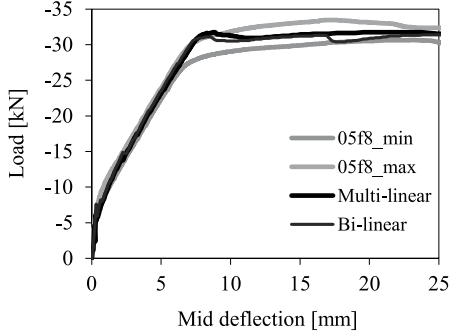
Figure. 12 – Comparison of load-deflection relationships from experiments and analyses, for the FE analyses using two types of σ-w relationship. V_f =0.5% and rebar diameter 8 mm.
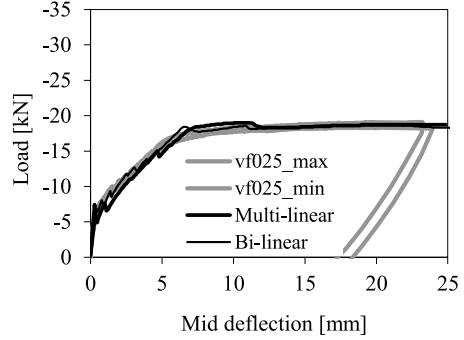
Figure. 13 – Comparison of load-deflection relationships from experiments and analyses, for the FE analyses using two types of σ-w relationship. V_f =0.25% and rebar diameter 6 mm.
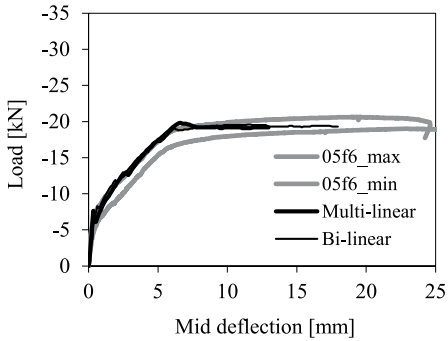
Figure. 14 – Comparison of load-deflection relationships from experiments and analyses, for the FE analyses using two types of σ-w relationship. V_f =0.5% and rebar diameter 6 mm.
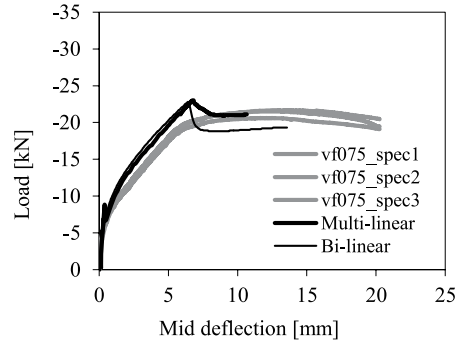
Figure. 15 – Comparison of load-deflection relationships from experiments and analyses, for the FE analyses using two types of σ-w relationship. Fibre volume V_f=0.75% and rebar diameter 6 mm.

4. ANALYTICAL APPROACH FOR CRACK SPACING

The crack spacing in reinforced concrete structures (without fibres) can be calculated using the following expression presented in EN-1992-1-1 [17].

$$s_{r.max} = k_3 \cdot c + k_1 \cdot k_2 \cdot k_4 \cdot \frac{\phi}{\rho_{s,eff}} \ [mm] \tag{3}$$

where:

c is the concrete cover

ϕ is the bar diameter

$\rho_{s,eff}$ is the effective reinforcement ratio, $\rho_{s,eff} = A_s / A_{c,eff}$

and $A_{c,eff}$ is the effective area of concrete in tension surrounding the reinforcement

$k_1 = 0.8$ for high bond bars and 1.6 for bars with an effectively plain surface

$k_2 = 0.5$ for bending, 1.0 for pure tension, or $(\varepsilon_1 + \varepsilon_2)/(2 \cdot \varepsilon_1)$ for eccentric tension

$k_3 = 3.4$

$k_4 = 0.425$

For a section with combined reinforcement, a similar expression can be derived, which takes the contribution from the fibre reinforcement into account; see Gustafsson Karlsson [6] or Löfgren [5]. Consider a reinforced tension prism loaded with the crack load, Ncr, according to Figure 16. The rod is reinforced with fibres and a centrally placed reinforcement bar, with an area of As. The force equilibrium in the region between two cracks with the maximum crack distance s$_{r,max}$ = 2·l$_{t,max}$ is analysed. At the crack, the fibre-reinforced concrete transfers a stress f$_{ft.res}$. At the midpoint between the two cracks, the concrete is about to crack and the stress is thus $\sigma_{ct} \approx$ f$_{ctm}$. The increase of stress is a result of stresses being transferred from the reinforcement to the concrete through bond. The bond stress τ$_b$ varies along the transmission length and has an average value of τ$_{bm}$ which can be calculated as:

$$\tau_{bm} = \frac{\int_0^{l_{t,max}} \tau_b(x)dx}{l_{t,max}} \tag{4}$$
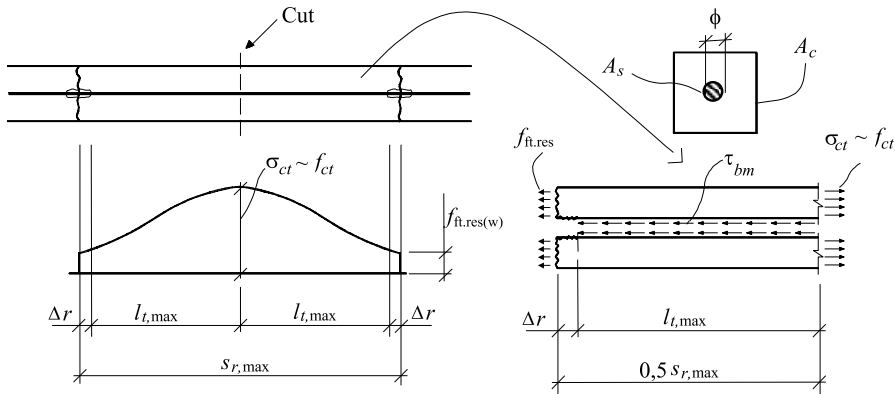

Figure. 16 – Equilibrium of forces for a tension prism.

If the tension prism is cut in the middle between the two cracks and along the interface between the reinforcement and concrete, the following equilibrium condition can be formulated:

$$\tau_{bm} \cdot \pi \cdot \phi (0.5 \cdot s_{r,max} - \Delta r) + f_{ft.res} \cdot A_c = f_{ctm} \cdot A_c \tag{5}$$

Since tensile forces are not transferred to the whole concrete area, A_c, the effective concrete area is used instead, $A_{c.eff}$, in accordance with EC2 [3]. Then the following expression may be used:

$$A_{c,eff} = A_s \cdot \frac{A_{c,eff}}{A_s} = \frac{A_s}{\rho_{eff}} \tag{6}$$

where ρ_{eff} is the reinforcement ratio. Using (6) in (5) leads to:

$$\tau_{bm} \cdot \pi \cdot \phi \left(0.5 \cdot s_{r,max} - \Delta r \right) = \frac{\pi \phi^2}{4 \rho_{eff}} \left(f_{ctm} - f_{ft.res} \right) \Rightarrow$$

$$s_{r,max} = 2\Delta r + \frac{1}{2} \cdot \frac{\left(f_{ctm} - f_{ft.res} \right)}{\tau_{bm}} \cdot \frac{\phi}{\rho_{eff}} \tag{7}$$

Assuming $S_{r,min} = 0.5\ S_{r,max}$, the average crack spacing S_{rm} may be obtained by taking the average value of the two as:

$$s_{rm} = 1.5\Delta r + \frac{3}{8} \cdot \frac{\left(f_{ctm} - f_{ft.res} \right)}{\tau_{bm}} \cdot \frac{\phi}{\rho_s} \tag{8}$$

The stress transfer from the reinforcement to the surrounding concrete depends partly on the surface properties of the reinforcement, and partly on the properties of the concrete. Based on experimental results, it has been found that the average bond stress can be calculated as:

$$\tau_{bm} = \frac{3}{2 \cdot k_1} \cdot f_{ctm} \tag{9}$$

If the expression for the average bond stress is introduced into (8) and the zone Δr is assumed to 30 mm, the following expression is obtained for the crack spacing of a tension rod:

$$s_{rm} = 50 + 0.25 \cdot k_1 \frac{\left(f_{ctm} - f_{ft.res} \right)}{f_{ctm}} \cdot \frac{\phi}{\rho_{eff}} \Rightarrow$$

$$s_{rm} = 50 + 0.25 \cdot k_1 \left(1 - \frac{f_{ft.res}}{f_{ctm}} \right) \cdot \frac{\phi}{\rho_{eff}} \qquad \text{[mm]} \tag{10}$$

If the effect of concrete cover, the spacing of the reinforcement, and type of loading (tension or flexural) are considered, the following expression can be used to calculate the crack spacing:

$$s_{r,max} = k_3 \cdot c + k_1 \cdot k_2 \cdot k_4 \cdot k_5 \cdot \frac{\phi}{\rho_{s,eff}} \quad \text{[mm]} \tag{11}$$

$$s_{rm} = \frac{1}{1.7} \cdot \left(k_3 \cdot c + k_1 \cdot k_2 \cdot k_4 \cdot k_5 \cdot \frac{\phi}{\rho_{s,eff}} \right) \text{[mm]} \tag{12}$$

The conclusion is that, for calculating the crack spacing, the basic formula as suggested in EC2 [17] can be used but it has to be modified with the relationship between the residual tensile strength and the tensile strength with the introduced variable as follows:

$$k_5 = \left(1 - \frac{f_{ft.res}}{f_{ctm}}\right) \qquad (0 \le k_5 \le 1) \qquad\qquad (13)$$

An early suggestion by Löfgren for the average crack spacing, s_{rm}, which also considers the concrete cover, c, is seen in Eq. (14), and this was the formula used when calculating the crack spacing in Section 5:

$$S_{rm} = c + 3 \cdot \phi + 0.25 \cdot k_1 \cdot k_2 \cdot k_5 \frac{\phi}{\rho_{eff}} \qquad\qquad (14)$$

with k_1, k_2 and k_5 according to above.

5. EVALUATION OF THE METHODS

To evaluate the model proposed by Löfgren, in Figure 17 the calculated crack spacing from the analytical method and from the FE analysis is compared with the crack spacing obtained in the experiments. In addition, a comparison is made with the proposal according to RILEM TC 162-TDF [5], where the crack spacing is calculated as:

$$s_{rm} = \left(50 + 0.25 \cdot k_1 \cdot k_2 \cdot \frac{\phi_b}{\rho_r}\right)\left(\frac{50}{l_f / \phi_f}\right) \qquad\qquad (15)$$

As can be seen in Eq. 12, the proposal by RILEM does not consider the effect of increased fibre content, whereas the proposal according to the analytical approach by Löfgren takes into account the residual tensile strength of the fibre-reinforced concrete. Hence the latter is able to predict that the crack spacing decreases with increased fibre content V_f, or with increased fibre slenderness as this also increases the residual tensile strength; see Figure 17. In the same figure it can also be seen that, for the FE analyses, the bi-linear results fluctuate more than the multi-linear results in predicting the crack spacing. The latter seem to better follow the experimental trend where an increase in fibre content results in a decrease in crack spacing.
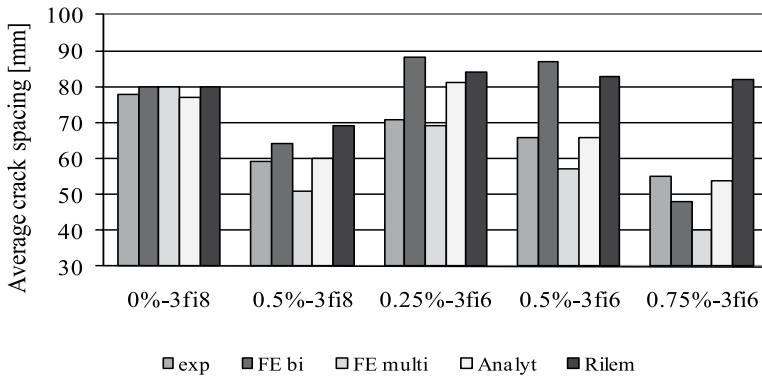

Figure. 17 – Comparison between calculated crack spacing and the crack spacing obtained in the experiments. (For simplicity the series with no fibres added also has two columns from FEM even though only one approach was used, see comment in Table 3.)

6. DISCUSSION

With the addition of fibres, in combination with conventional reinforcement, the response both during and after the cracking process became stiffer and the crack spacing decreased. When comparing the two series with the ϕ 8 mm bars (i.e. with no fibres and with V_f =0.5%) it was found that the ultimate load increased with about 13% (28.2 kN vs. 31.9 kN), the deflection at peak load was smaller for the fibre reinforced beam, and the crack spacing was reduced by approximately 15% (from 78 mm to 63 mm), see Figure 18 a). Of course it should be kept in mind that when adding fibres to the mixture, keeping the same amount of longitudinal reinforcement, the total steel area will increase, in this case, to almost the double (from 2.37 kg to 5 kg). Hence an increase in load carrying capacity is expected. For these moderate fibre volume fractions (V_f=0.25%-0.75%), the conventional reinforcement is more effective when it comes to load carrying capacity. Hence, the main benefit from fibre reinforcement is the reduced crack spacing, which leads to a larger number of cracks and consequently, to reduced crack width. A second aspect is the larger moment capacity that is obtained from adding fibres, i.e. for the same deflection/curvature SFRC beams can sustain a larger moment compared to beams without fibre reinforcement. It can be seen that the fibre reinforced beams exhibit a more stable behaviour both during the cracking process and after the same. Furthermore, in the SFRC beam, yielding in the conventional reinforcement occurs for a higher load compared to the beam without fibre reinforcement.
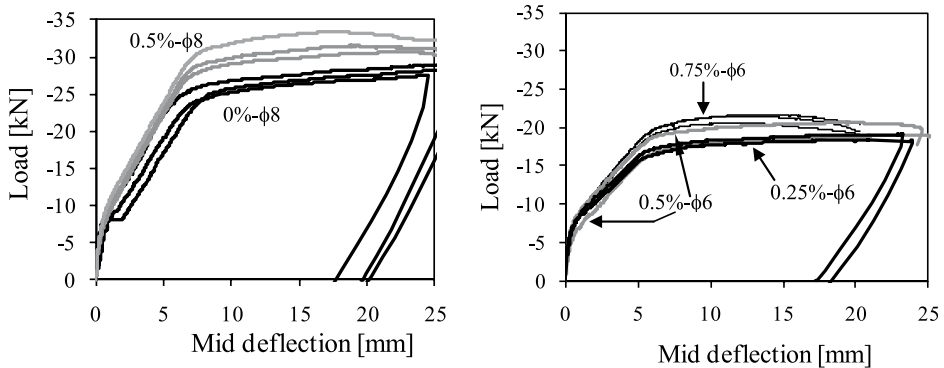
Figure. 18 – a) Load-deflection for the series with ϕ8 rebars, b) all three results for Series 0.75, and max/min load-deflection for Series 0.25 and 0.5, all with ϕ6 rebars.

One purpose of the present work was to investigate whether a multi-linear σ-w relationship could better describe the cracking process in flexural beams compared to a bi-linear σ-w relationship, which was used in an earlier work; see [18].

When studying the results it can be observed that for the overall behaviour, in terms of load-deflection curves and maximum loads, both relationships show equal agreement with the experimental results. When studying the crack patterns, though, and also the average crack spacing, it is indicated that the analyses using multi-linear σ-w relationships yield more distinct crack patterns, with reasonable agreement between analysis and experiment regarding average crack spacing.

In general, with the approach based on fracture mechanics it is possible to determine the 5 relationship and use this to predict the structural behaviour of reinforced FRC beams; this was done with acceptable agreement and correlation between experiments and analyses. Good agreement between experiments and analyses was found for fibre contents 0.0–0.5%, while for fibre content 0.75% the agreement was less satisfactory.

The analytical model by Löfgren, for calculation of crack spacing, proved to yield results in very good agreement with the experimental ones. Especially the decrease in average crack spacing with increasing fibre content was well captured. As pointed out earlier, the approach by RILEM does not consider the residual strength. This can be seen in Figure 17, where, besides results from the approach by RILEM, the analytical approach by Löfgren and the FE analyses are compared with the experimental results. It can be seen that the bi-linear FE approach is not able to capture the decreasing crack spacing with increasing fibre content, while the multi-linear approach seems more effective in this respect.

The load-deflection curve for conventional reinforced concrete (see Figure 19) is generally characterised by an initial almost linear response (O-C) until cracking starts (C). The cracks continue to grow and form as the load increases; in the load–displacement curve this is indicated in a region of decreasing stiffness (C-Y) until yielding occurs (Y). At onset of yielding (Y) the deflection increases more rapidly (Y-P) until the peak load is reached (P). When fibres are used in combination with conventional reinforcement different load deflection behaviours can be identified and these will depend on the amount of conventional reinforcement, amount of fibres, and the fibre length. Generally, with the addition of fibres the initial linear response may be prolonged and the stiffness after cracking (C) increases – see Figure 19. With moderate fibre additions the general shape of the load-deflection curve will not change – see Figure 18 – but with increased fibre amount the peak load (P) will occur earlier for a smaller deflection. When large amount of fibres are added (still strain softening) and/or with a small amount of conventional reinforcement (curve RFRC-3), see e.g. Löfgren [11] who tested beams with a geometric reinforcement ratio of 0.075% to 0.121% in combination with a fibre dosage of 0.5 and 0.75%, the peak load will almost coincide with the onset of yielding (Y&P) and the load decreases afterwards. The reason for this change in behaviour is that this type of FRC has a softening behaviour where the stress carrying capacity decreases with increasing crack width. Moreover, the shorter the fibres are the more rapidly the stress will decrease.
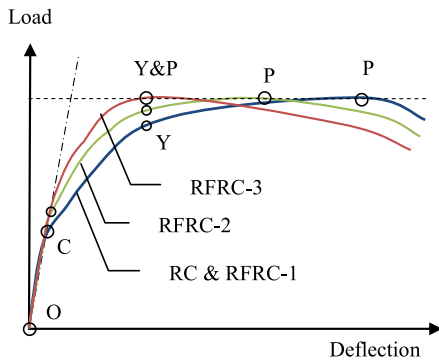

Figure. 19 – Schematic load-deflection curves for reinforced concrete (RC) and reinforced fibre concrete (RFRC) – a strain-softening FRC. With the lowest fibre content in RFRC-1 and the highest for RFRC-3.

7. CONCLUSIONS

Based on the test results and the analyses, the following conclusions may be drawn:

- the WST method provided adequate information regarding the post-cracking behaviour of the fibre-reinforced concrete (in terms of σ-w relationship);
- for overall response a bi-linear σ-w relationship was sufficient;
- a multi-linear σ-w relationship tended to describe the cracking process slightly better than a bi-linear one with regard to the average crack spacing;
- for the same deflection a higher load can be sustained with the FRC compared to non fibrous concrete;
- addition of fibres leads to reduced crack spacing;
- the bending stiffness after cracking was increased by fibre reinforcement;
- with addition of fibres an increase in load carrying capacity was obtained, although for this matter conventional reinforcement is more effective;
- the analytical approach by Löfgren [5] was used to predict the experimental crack spacing with good accuracy, and especially the decreasing crack spacing with increasing fibre content was well captured;
- with FEM the structural behaviour (load-deflection and crack spacing) could be predicted with acceptable agreement;
- however, more research is needed regarding the parameters governing the cracking process, e.g. influence of the bond-slip relationship and the σ-w relationship, and also regarding modelling aspects such as the crack band width.

8. REFERENCES

1. RILEM TC 162-TDF, *Test and design methods for steel fibre reinforced concrete, σ-ε design method.(Chairlady L. Vandewalle). . Materials and Structures / Matériaux et Constructions,*, 2003. **36**: p. 560-567.

2. CNR-DT 204/2006, *Istruzioni per la Progettazione, l'Esecuzione ed il Controllo di strutture di Calcestruzzo Fibrorinforzato.* Draft 2006: Rome. p. 59.

3. ENV-1992-1-1, *Eurocode 2: Design of Concrete Structures, Part 1-1: General Rules and Rules for Buildings. .* 1991.

4. Chiaia, B., P.A. Fantilli, and P. Vallini, *Evaluation of crack width in FRC structures and application to tunnel linings.* Materials and Structures, 2009. **42**: p. 339-351.

5. Löfgren, I., *Calculation of crack width and crack spacing*, in *Nordic Mini Seminar "Fibre reinforced concrete".* 2007: Trondheim, Norway.

6. Gustafsson, M. and H. Karlsson, *Fibre-reinforced concrete structures-analysis of crack spacing and crack width (In Swedish: Fiberarmerade betongkonstruktioner-Analys av sprickavstånd och sprickbredd)*, in *Dep. of Structural Engineering.* 2006, Chalmers University of Technology: Göteborg. p. 102.

7. SIS - Bygg, o., anläggning, *SS-EN 12390-2*, in *SVENSK STANDARD* 2001.

8. SIS - Bygg, o., anläggning, *SS-EN 12390-3*, in *SVENSK STANDARD.* 2002.

9. Löfgren, I., H. Stang, and J.F. Olesen, *The WST method, a fracture mechanics test method for FRC. Materials and Structures*, 2008. **41**: p. 197-211.

10.   Meda, A., G.A. Plizzari, and V. Slowik. *Fracture of fiber re-inforced concrete slabs on grade. Fracture Mechanics of Concrete Structures*. in *Proceedings of FRAMCOS-4*. 2001: Swets & Zeitlinger. Lisse, the Netherlands.

11.   Löfgren, I., *Fibre-reinforced Concrete for Industrial Construction-a fracture mechanics approach to material testing and structural analysis*, in *Dep. of Civil and Environmental Engineering*. 2005, Chalmers University of Technology: Göteborg. p. 268.

12.   Nordic Innovation Centre, O., *NT BUILD 511: Wedge Splitting Test method (WST) – fracture testing of fibre-reinforced concrete (Mode I)*. 2005.

13.   Østergaard, L., et al., *A method for fast and simple interpretation and inverse analysis of the wedge splitting test*. 2003

14.   TNO, *DIANA - Finite Element Analysis, User's Manual release 9.*. 2005.

15.   CEB/FIP Model Code 90, *Textbook on behaviour, Design and Performance Updated knowledge-bulletin 1*. 1993.

16.   Cornelissen, H.A.W., D.A. Hordijk, and H.W. Reinhardt, *Experimental determination of crack softening characteristics of normal-weight and lightweight concrete*. Heron, 1986. **31**(2).

17.   EN-1992-1-1, *EUROPEAN STANDARD. Eurocode 2: Design of concrete structures - Part 1-1: General rules and rules for buildings*. 2004.

18.   Jansson, A., I. Löfgren, and K. Gylltoft. *Applying a fracture mechanics approach to material testing and structural analysis of FRC beams*. in *Proceedings of FRAMCOS-6*. 2007. Catania Italy.

Laboratory Parametric Study of Moisture Condition in Covered Underfloor heated concrete slabs

Anders Sjöberg
Ph.D. Assistant Professor
Division of Building Materials, Lund University
P.O. Box 118, 221 00 Lund
anders.sjoberg@byggtek.lth.se

Lars-Olof Nilsson
Professor
Division of Building Materials, Lund University
P.O. Box 118, 221 00 Lund
lars-olof.nilsson@byggtek.lth.se

ABSTRACT

This study was performed on 42 floor slabs where the moisture was measured at several occasions and the effect of cast in under floor heating was evaluated. A simulation model of moisture redistribution is present.

Major finding was that the drying time decreases when the floor heating is started early under the drying process and moisture measurement should be made right between the heating pipes at 40% of the depth of the concrete slab.

There seems only to be a small risk of enhanced moisture conditions in the wood flooring if the underfloor heating is turned off during the first year.

Key words: Concrete slab, Moisture, Underfloor heating, Wooden floor

INTRODUCTION

For reasons of comfort, the use of underfloor heating in concrete floors is increasingly common. In newly built single family houses, it is more the rule than the exception for the heating system to be installed as underfloor heating. The main intention is to avoid "cold floors"; even when wood floors are used which are traditionally regarded as pleasantly warm, underfloor heating is often specified.

From the standpoint of moisture, a construction with underfloor heating has several advantages, but there are also a number of points which must receive special attention if moisture damage and moisture problems are to be avoided.

Most of these are relatively well known, but some aspects require research to elucidate the issues more fully, so that specifications may be drawn up for practical and safe treatment of underfloor heating at the design and construction stages. Thermal insulation, thicker than normal for energy conservation reasons, that is installed below the heating pipes provides very good protection against soil moisture in the vapour phase owing to the large temperature gradient across the thermal insulation. If underfloor heating can be used during the construction stage, moisture of construction can also dry out sooner since the concrete slab can be warmed up.

It is found that wood floors normally have a relatively low moisture resistance, compared with the moisture resistance of the concrete subfloor and the moisture resistance of the adhesive used to bond the wood floor to the subfloor. Because of this, the upward moisture transfer from the concrete subfloor passes through the wood floor without causing major wetting of the underside of the wood floor, provided that the subfloor is not <u>too</u> moist and the moisture resistance of the wood floor is not <u>too</u> high.

Matters are more difficult if the room climate is humid. When RH is 60%, it is difficult to prevent RH at the underside of the wood floor exceeding 65%. This needs research so that the manufacturers limiting value of 65% RH may be raised.

Underfloor heating below a wood floor provides very high temperatures in the subfloor so that the surface temperature of the wood floor may be raised. The reason for this is that wood is a relatively good thermal insulator, i.e. it has a relatively large resistance to heat transfer.

The thermal resistance of a wood floor is of the same order as the surface resistance between a surface and the air. This means that the temperature difference between the top and bottom of the wood floor must be of the same order as the desired temperature difference between the wood floor and the air. With a room temperature of +20°C and a desired surface temperature of +27°C, the temperature below the wood floor must therefore be +34°C. A thick wood floor requires even higher temperatures in the concrete subfloor.

Some of the questions that have been raised in conjunction with the bonding of wood floors to concrete subfloors containing construction moisture are

- How dry must it be before the wood floor is bonded on?
- Does the construction function without a polyethylene foil as moisture insulation?
- What happens when the heating is turned off?
- Are conditions different for different wood floors?

2.   METHODS

2.1   Materials

Two types of concrete based on ordinary Portland cement were used as a substrate to the floorings. These were normal structural concrete (NSC) with a water cement ratio (w/c-ratio) of 0.6 and a self desiccating concrete (SDC) with w/c-ratio of 0.4. By varying the w/c-ratio different sets of properties of the substrate were obtained according to Sjöberg (1). For instance, a concrete with a low w/c ratio is more alkaline and more impervious to e.g. moisture than the one with high w/c ratio , provided that they are based on the same type of cement.

120 mm thick concrete slabs (1200×800 mm) were cast in moulds of extruded cellular plastic, see figure 1. The walls of the mould were 100 mm thick and its bottom 200 mm. On the inside of the mould a vapour barrier of double plastic sheeting was laid to prevent undesired downward drying of the concrete slab. After application of the flooring the plastic sheets were sealed against the edges of the flooring materials with aluminium tape.

Figure 1.   Mould (batch 1) with cast in heating pipes and console for thermo element.

Four different floor covering materials were used in this study, one rubber based flooring (R) and three types of wood based floor coverings (W1-3). Moisture depended material parameters has been determined in this study and are described in section 5.1.

The rubber flooring was attached to the substrate with 0.33 kg/m^2 of an acrylic based adhesive [proff solid 3480]. The open time from applying the adhesive until the flooring was attached was about 13 minutes at 20°C and 60% RH. The wood floor was attached with 1 m^2/litre MS-polymer adhesive with no actual open time.

2.2   Test setup

This study was performed on 42 specimens divided into three batches. All batches included both NSC and SDC. All times and data are summarised in tables 1 & 2.

Directly after casting the concrete surface was covered with a plastic sheet allowing a period of sealed curing. Thereafter the plastic sheets were removed, allowing the concrete to dry from one side only, up through the free surface, for a period of time before the floorings were attached. One week prior to the application of flooring, the concrete surface was screeded with ca 3 mm of a cement based self levelling compound.

The first batch consists of 18 specimens, all with rubber based flooring, conditioned at 20°C and 60% RH. The parameters studied were the influence of w/c-ratio, the depth of the underfloor heating pipes and the drying time prior to flooring. The second batch consists of 12 specimens, all with wood based flooring, conditioned at 20°C and 60% RH. The parameters studied were the influence of w/c-ratio, different types of wood floor coverings, and the drying time prior to flooring. The third batch consists of 12 specimens who were identical to the second batch with the exception that they were conditioned at 20°C and 30% RH.

2.3   Measurements

Temperature and moisture conditions were measured in the specimens on several important occasions. Temperature measurements were performed with cast-in Type T thermocouples.

Moisture measurement was performed on concrete samples removed from several depths in the slab and placed in a sealed test tube according to the regulations specified in RBK (2). A carefully calibrated RH probe was placed in the test tube and the readings were noted after two days when the system had reach its equilibrium, Sjöberg (1). In a pre-study the RH probes were put in holes drilled directly in the concrete slab according to Nilsson (3). This trial method was abandoned as it results in condensation problems on the probes and unreasonably large uncertainties concerning temperature effects.

The first moisture measurement was made at the same time as the application of the flooring, the second measurement during the redistribution of construction water, and the third measurement when the moisture level beneath the flooring had reached its peak value.

3.   RESULT OF MEASUREMENTS

3.1   Temperature

The temperature of the cast-in heating pipes was continuously adjusted relative to a maximum temperature of 27°C on top of the flooring, in order to correspond to the maximum temperature gradient allowed in an underfloor heated construction. Measured temperature profiles for four different cases are shown in figure 2. The solid lines represent the temperature profile through the concrete slab near the heating pipe and the dashed lines the profile between these. The labelled cases in figure 2 are based on the type of flooring used and the depth of the cast-in heating pipes. Case 1 represents the mean value of the specimens with rubber based flooring and heating pipes at 30 mm depth, case 2 the specimens with rubber based flooring and heating pipes at 100 mm depth, case 3 the specimens with 14 mm multi layer parquet, and case 4 the specimens with 20 mm solid board. Cases 3 and 4 have the heating pipes cast in at 100 mm depth.
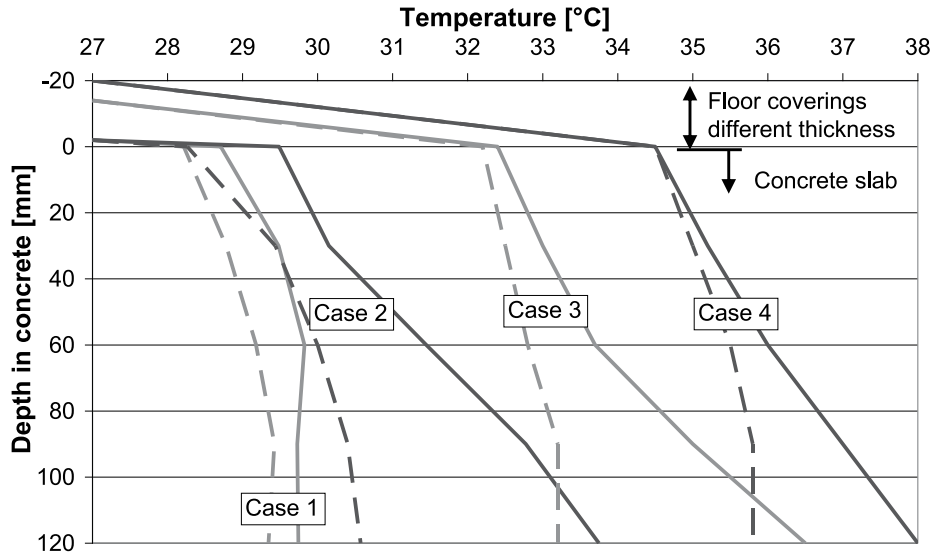
Figure 2.   Measured temperature profiles (mean values) through concrete slab and flooring for four cases.

It is clearly shown in figure 2 that the temperature in the concrete rises owing to the greater thermal resistance of the thicker flooring material. Case 1 with heating pipes at 30 mm gives a lower temperature above the pipe (solid lines) than case 2. This difference occurs because the temperature in the heating pipe is adjusted relative to the temperature between the pipes, represented as the top of the dashed lines.

3.2   Relative humidity

Moisture measurements on the samples removed from 5-10 different depths in 42 samples on 3 occasions provide the study with hundreds of moisture profiles. All these moisture profiles are fully shown in Sjöberg & Nilsson (4,5). The mean value of each measured moisture profile is summarised in tables 1, 2 & 3.

Table 1a.   *Times and data for batch 1.*

Specimens	1	2	3	4	5	6	7	8	
Drying climate	60	60	60	60	60	60	60	60	% RH in 20°C
Flooring	R	R	R	R	R	R	R	R	Types of flooring material
Concrete	0.4	0.4	0.4	0.4	0.6	0.6	0.6	0.6	W/C-ratio
Depth-pipe	30	30	100	100	30	30	100	100	Depth, mm from surface
Sealed curing	28	28	28	28	28	28	28	28	Days (time of period)
Drying time	14	28	13	28	14	28	5	28	Days between curing and flooring
Heat start	16	30	15	30	16	30	7	30	Days between curing and heating
Measure 1	1	1	2	1	1	1	2	1	Days from flooring to first measure
RH middle	87.8	87.0	85.4	88.2	92.3	91.8	93.1	94.3	% Relative humidity
RH pipe	88.2	-	-	88.8	92.8	-	93.6	93.3	% Relative humidity
Measure 2	139	124	141	125	139	124	141	125	Day from flooring to second measure
RH middle	84.3	83.7	81.9	83.2	87.2	88.2	86.5	87.0	% Relative humidity
RH pipe	84.3	84.0	81.0	83.0	86.7	88.2	86.2	86.5	% Relative humidity
Measure 3	323	309	321	309	323	309	321	309	Days from flooring to third measure
RH middle	81.2	81.3	77.5	83.0	84.0	86.3	83.0	85.5	% Relative humidity
RH pipe	80.2	82.2	76.2	80.7	82.8	87.0	79.8	84.3	% Relative humidity

Table 1b.   *Times and data for batch 1.*

Specimens	10	11	12	13	14	15	16	17	18	
Drying climate	60	60	60	60	60	60	60	60	60	% RH in 20°C
Flooring	R	R	R	R	R	R	R	R	R	Types of flooring material
Concrete	0.4	0.6	0.6	0.4	0.4	0.6	0.6	0.4	0.6	W/C-ratio
Depth-pipe	-	-	-	30	100	30	100	-	-	Depth, mm from surface
Sealed curing	28	28	28	1	28	1	28	28	28	Days (time of period)
Drying time	28	14	28	113	92	113	92	92	92	Days between curing and flooring
Heat start	-	-	-	0	0	0	0	-	-	Days between curing and heating
Measure 1	2	1	2	-57	-64	-57	-64	-64	-64	Days from flooring to first measure
RH middle	87.8	95.3	92.3	80.5	87.3	83.5	90.0	90.2	94.8	% Relative humidity
RH pipe	87.8	92.8	93.2	80.0	87.2	81.6	91.8	-	-	% Relative humidity
Measure 2	139	141	139	47	1	47	1	1	1	Day from flooring to second measure
RH middle	84.8	89.7	91.2	81.8	82.2	85.8	86.7	85.3	89.7	% Relative humidity
RH pipe	85.3	89.8	91.3	81.3	83.0	83.3	85.3	85.2	90.3	% Relative humidity
Measure 3	349	324	349	249	241	249	241	241	241	Days from flooring to third measure
RH middle	81.2	86.0	85.5	78.3	80.3	82.8	82.3	82.8	87.3	% Relative humidity
RH pipe	81.8	86.0	86.2	77.5	79.5	81.5	81.0	83.2	88.3	% Relative humidity

Table 2. *Times and data for batch 2.*

Specimens	19	20	21	22	23	24	25	26	27	28	29	30
Drying climate	60	60	60	60	60	60	60	60	60	60	60	60
Flooring	W1	W2	W3	W1	W2	W3	W1	W2	W3	W1	W2	W3
Concrete	0.6	0.6	0.6	0.6	0.6	0.6	0.4	0.4	0.4	0.4	0.4	0.4
Depth-pipe	100	100	100	100	100	100	100	100	100	100	100	100
Sealed curing	1	1	1	1	1	1	1	1	1	1	1	1
Drying time	94	94	94	127	127	127	74	74	74	106	106	106
Heat start	101	101	101	137	137	137	83	83	83	118	118	118
Measure 1	-1	-1	-1	-3	-3	-3	-1	-1	-1	-1	-1	-1
RH middle	87.3	87.7	88.8	86.8	87.3	88.5	83.8	83.2	84.8	80.3	81.8	81.7
RH pipe	87.3	87.7	88.8	86.8	87.3	88.5	83.8	83.2	84.8	80.3	81.8	81.7
Measure 2	31	31	31	23	23	23	50	50	50	31	31	31
RH middle	86.5	87.7	87.2	87.3	87.5	86.5	78.0	77.2	78.3	77.0	77.7	77.5
RH pipe	86.2	87.2	88.3	87.8	88.2	85.2	75.7	77.0	77.8	76.7	77.8	77.8
Measure 3	56	56	56	51	51	51	63	63	63	59	59	59
RH middle	84.8	85.8	82.2	82.8	85.3	86.2	77.5	77.3	77.0	77.7	77.8	78.3
RH pipe	84.0	84.8	82.8	82.5	84.2	81.8	76.3	75.5	76.8	77.3	77.0	76.8

Table 3.   Times and data for batch 3.

Specimens	31	32	33	34	35	36	37	38	39	40	41	42
Drying climate	30	30	30	30	30	30	30	30	30	30	30	30
Flooring	W1	W2	W3	W1	W2	W3	W1	W2	W3	W1	W2	W3
Concrete	0.6	0.6	0.6	0.6	0.6	0.6	0.4	0.4	0.4	0.4	0.4	0.4
Depth-pipe	100	100	100	100	100	100	100	100	100	100	100	100
Sealed curing	1	1	1	1	1	1	1	1	1	1	1	1
Drying time	45	45	45	80	80	80	46	46	46	81	81	81
Heat start	52	52	52	87	87	87	53	53	53	87	87	87
Measure 1	-1	-1	-1	0	0	0	-1	-1	-1	-1	-1	-1
RH middle	90.6	88.9	89.7	83.6	83.9	85.6	82.4	82.2	82.1	78.4	76.9	77.2
RH pipe	90.6	88.9	89.7	83.6	83.9	85.6	82.4	82.2	82.1	78.4	76.9	77.2
Measure 2	-	-	-	-	-	-	-	-	-	-	-	-
RH middle	-	-	-	-	-	-	-	-	-	-	-	-
RH pipe	-	-	-	-	-	-	-	-	-	-	-	-
Measure 3	81	81	81	83	83	83	81	81	81	81	81	81
RH middle	83.2	83.5	84.3	80.4	81.6	81.3	73.1	73.6	74.1	73.3	76.6	73.0
RH pipe	80.5	82.2	82.8	78.0	81.4	79.3	71.1	74.3	73.8	72.9	73.2	70.8

4.   STATISTIC EVALUATION

A statistical factorial evaluation of the measured values in Tables 1 & 2 is performed according to Box et al (6). This evaluation points out the significant influence of several of the tested variables. Some of the variables had a large influence on the RH-level during the first measurements, which were made when the flooring was laid, and decreased with time. These decreasing factors were the influence of w/c-ratio that gives a mean reduction of 6.0% RH in the moisture profile over the time of measurement when the w/c-ratio is 0.4; the effect of starting the heating early before the flooring is laid (mean reduction of 4.7% RH); and an increase in the length of the period of drying before laying the flooring (mean reduction of 1.3% RH).

There were four significant factors, increasing with time, which have an influence on the RH-level. These increasing factors were the influence of the drying climate that gives a mean reduction of 2.4% RH in the moisture profile over the time of measurement when specimens were kept at 30% RH and 20°C; the depth of heating pipes in the concrete where 30 mm gave a mean reduction of 0.9% RH; the use of a homogeneous wooden floor with a lower resistance to water vapour than a less tight parquet flooring (mean reduction of 0.5% RH); and the location of the measurement: near the heating pipe (mean reduction of 0.5% RH) vs. right between the pipes.

5.   NUMERICAL SIMULATION

5.1   Model

Calculations of moisture redistribution have been performed by a computer simulation based on a two dimensional finite difference calculation. The simulation is made for a cross section of the specimens divided into 20*20 elements of optional size. The simulation solves the moisture flow equation (ekv.1) for every time step:

$$g = -\delta \, \frac{\partial v}{\partial x} - \frac{k_p}{\eta} \cdot \frac{\partial P_w}{\partial x} \qquad\qquad \left[kg/(m^2 \cdot s) \right] \qquad \text{Ekv.1}$$

where g is the moisture flow, δ (m^2/s) is the diffusion coefficient for water vapour transport, v (kg/m^3) is the vapour content, x (m) is the size of the element, kp (kg/m) is the water permeability, η (Ns/m^2) is the dynamic viscosity and P_w (Pa) is the pore water pressure.

The change in moisture content for each element is calculated in every time step by:

$$\Delta w = \frac{\Delta g}{\Delta x} \Delta t \qquad\qquad \left[kg/(m^2 \cdot s) \right] \qquad \text{Ekv.2}$$

where w (kg/m^3) is the moisture content and t (s) is the length of the time step.

The moisture flow during the following time step is based on the new calculated moisture content. The vapour content at the beginning of the next time step is for instance calculated as:

$$v = v_{old} + v_{sat}(T) \frac{\Delta w}{\Delta w / \Delta RH} \qquad\qquad \left[kg/(m^3) \right] \qquad \text{Ekv.3}$$

where v_{old} *(kg/m³)* is the vapour content at the beginning of the previous time step, $v_{sat}(T)$ *(kg/m³)* is the vapour content at saturation as a function of temperature T and *Δw/ΔRH* *(kg/m³·%RH)* is the moisture capacity of the material evaluated as the gradient of a sorption isotherm.

5.1   Evaluated material properties

Moisture depended material parameters
The determination of parameters of concrete is based on the measured moisture profiles and thoroughly described in Sjöberg & Nilsson (7). Moisture depended material parameters used in this simulation are summarised in table 4

Table 4.   Moisture depended material properties used at simulations

	RH	%	10	30	50	70	85	90	95	99
Wood	W	kg/m³	29	42	60	79	103	116	134	152
	δ	m²/s	2.0 E-07	5.5 E-07	1.1 E-06	2.0 E-06	3.3 E-06	3.9 E-06	5.2 E-06	6.5 E-06
	Kp	kg/m	1.0 E-26	1.0 E-26	1.0 E-26	1.0 E-26	1.0 E-26	1.0 E-26	1.0 E-26	1.0 E-26
Con.	W	kg/m³	20	27	40	60	83	95	115	140
	δ	m²/s	3.0 E-07	3.0 E-07	3.0 E-07	3.0 E-07	2.9 E-07	2.9 E-07	2.9 E-07	2.3 E-07
	Kp	kg/m	1.0 E-26	1.0 E-26	1.0 E-19	9.9 E-18	9.6 E-17	1.3 E-15	2.4 E-15	6.2 E-15

Rubber based flooring
The rubber based floor covering (R) used in the experiments is 2 mm thick and provides a moisture tight seal on the surface. The flow resistance to water vapour, Z = 2.4·10⁶ s/m. In the simulations the rubber based flooring is assumed to be completely moisture tight and to have a thermal conductivity of 0.14 W/(m·K). The thermal conductivity of wood is 0.07 W/(m·K) and that of concrete 1.7 W/(m·K).

Wood floor
The various wood floor coverings provide a semi-tight seal of the surface in the experiments. The vapour tightness of material W1-3 was determined by using the cap method according to McLean et al (8) and CEN/ISO (9). The first wood floor (W1) was made of a 20 mm homogeneous tongued and grooved board of pinewood, Z = 51·106 s/m at 20°C and Z = 90·106 s/m at 30°. The second wood floor (W2) was a 14 mm multi layer parquet with a top layer of about 3,5 mm oak board, Z = 44·10⁶ s/m at 20°C and Z = 80·10⁶ s/m at 30°.The third wood floor (W3) was a 14 mm multi layer parquet with a top layer of about 3,5 mm oak divided into three parallel boards, Z = 57·10⁶ s/m at 20°C and Z = 98·10⁶ s/m at 30°.In the simulations moisture depended material parameters according to table 3 was used.

5.2   Results of simulations

The result from simulations is illustrated in figure 3 together with results from all measurements. It is shown in figure 3 that there is almost no difference in the moisture levels near vs. between the heating pipes during the first measurement. The difference increases in the second measurement and is largest in the third measurement. The results from the simulation correspond to the values of the third measurement and the agreement is acceptable. The results from the measurement also show that the moisture level decreases with time as the concrete slab is slowly drying out through the flooring.
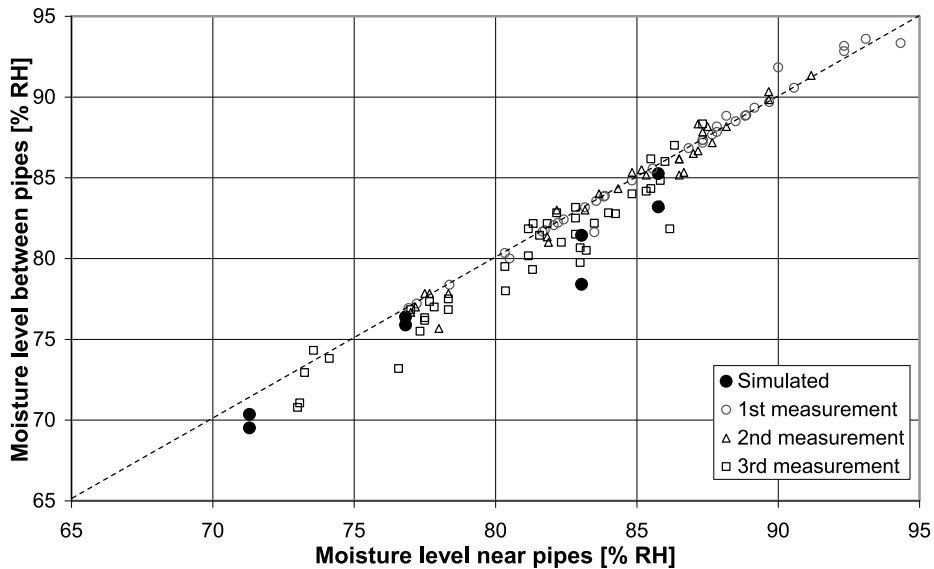

Figure 3.   Measured RH-levels near vs. between pipes and simulated RH levels.

The next simulation was performed to sort out how to make a measurement before laying the flooring, in order to ascertain the highest moisture level the floorings and adhesive will be exposed to after redistribution of the remaining construction water. It was assumed in the simulation that all remaining construction water in the concrete at the time the flooring is laid will be trapped and have no opportunity to dry out. The moisture in the middle of the concrete will then be redistributed and will remoisten the dryer top part. It was found in this simulation of 6 different cases that the moisture condition between the heating pipes at 40% depth of the concrete slab was similar to the highest moisture value that later occurred at any time in contact with the flooring. See figure 4. Of the six simulated cases, three had the heating pipes at 30 mm depth and three at 100 mm. For each of these the flooring was simulated after 3, 6 and 12 months of drying period. The underfloor heating was turned on at the same time as the flooring was laid. For every case a "measured" value is shown for the time of flooring and 3, 6 and 12 month thereafter to illustrate the variation with time at the point of measurement. The drying time has by far the greatest influence on the moisture condition, according to figure 4. Whether the heating pipe is cast in at 30 or 100 mm makes no significant difference whatever. Nor does

the moisture condition at the point of measurement at 40% depth of the concrete slab fluctuate during the period when moisture is redistributed n the rest of the slab.
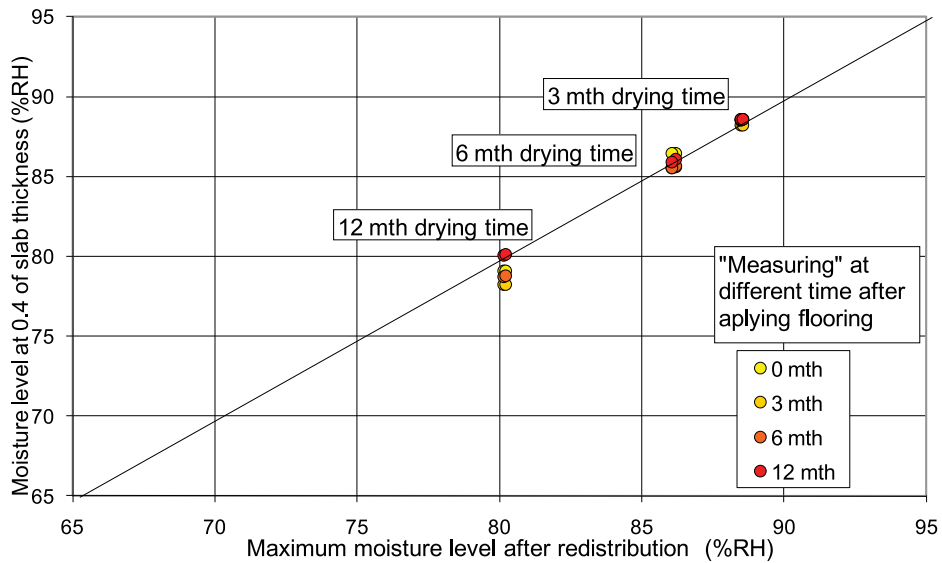

Figure 4.   Simulated RH-level at 0.4 depth before flooring vs maximum RH-levels after redistribution.

The third simulation demonstrates the drying process in the concrete floor when a wooden floor is attached after an initial drying. In figure 5 the line labelled "start" shows the moisture distribution in the uncovered concrete slab after two weeks' drying at 60% RH and 20°C. The initial distribution is calculated and shows very good agreement with the measured values.

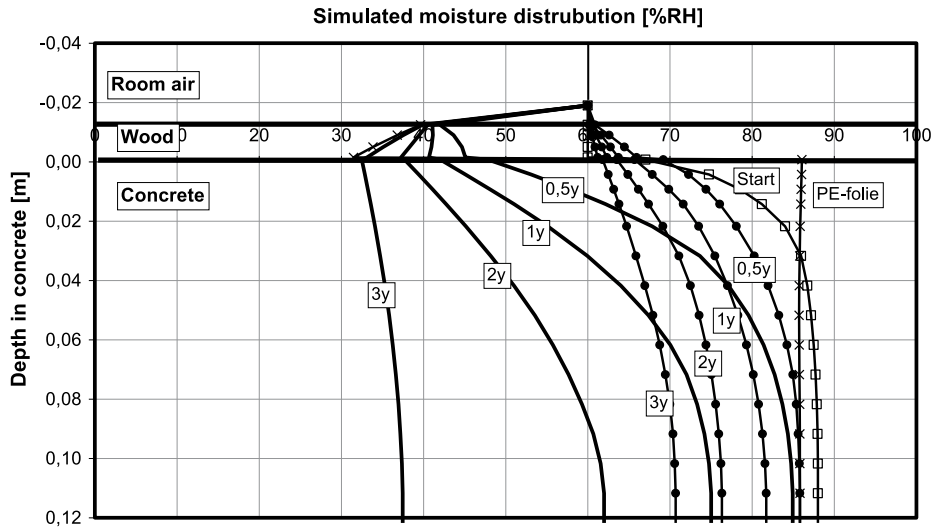**Simulated moisture distrubution [%RH]**

Figure 5.   Simulated moisture distribution during three year of drying for three cases. Heating pipes at 100 mm temperature profile according to case 3 in figure 2.

The lines with dots in figure 5 represent the moisture distribution profiles when the slab has an attached wooden floor but no heating. The distribution decreases with time 0.5, 1, 2 and 3 years after the wooden floor is applied. The equilibrium moisture level which the distribution profile will reach after a long time is 60% RH.

The solid lines represent the moisture distribution profiles that occur when the concrete slab has an attached wooden flooring and heating pipes at 100 mm depth. The temperature in the heating pipes is adjusted to produce 27°C at the floor surface. Because of the increased temperature, the relative humidity at the floor surface will almost immediately decrease to approx. 40% RH. There will be a decreasing moisture distribution profile through the wooden flooring and the moisture level of the distribution profile in the concrete will reach an equilibrium at approx. 30% RH after a long time.

The line marked with "x" shows the distribution profile when a moisture barrier, eg a polyethylene (PE) foil, is placed between the concrete slab and the wooden floor. In that case the moisture level in the wood floor will almost immediately reach the same distribution profile as it only does after a long time without the PE foil. The equilibrium moisture level in the concrete will be ca 85% RH. This is the same level as that of the initial profile at 25% of the depth. In Nilsson (7) this equilibrium depth is shown to be 40% when a concrete slab with single sided drying is covered with a tight seal, e.g. a PVC or rubber based flooring. The depth in Nilsson (7) is considered to be on the safe side compared to this study.

In figure 6 the redistribution of the moisture distribution profile is shown when the underfloor heating is turned off 6 months after the wooden flooring was attached. After just a couple of days the moisture level in the surface of the wooden floor has increased from just over 40% RH to nearly 60% RH. After a week the moisture level at the top of the concrete starts to rise. 3-6

months later the system is at its new equilibrium with a significantly higher moisture level in the wood floor at the top of the concrete. The moisture level in the bottom part of the concrete slab is lower than before since it has had time to dry upwards through the whole process.
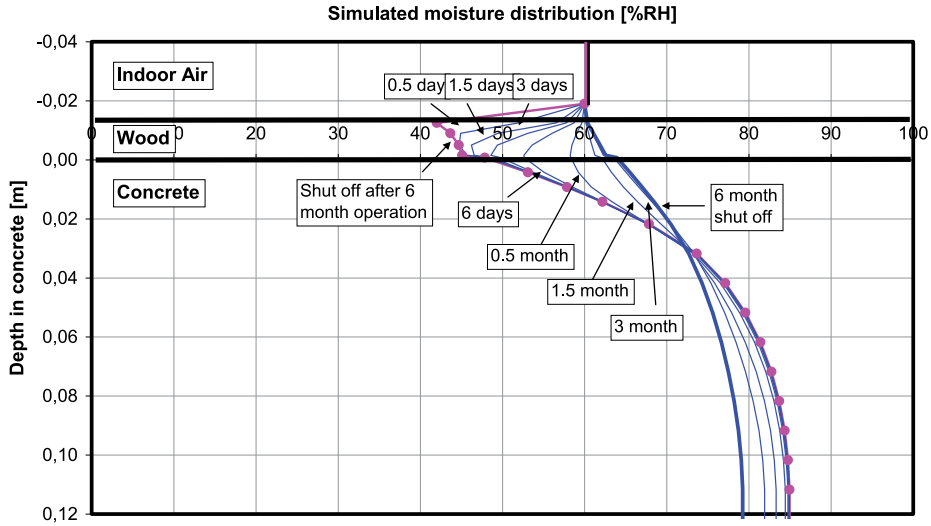

Figure 6.   *Simulated moisture distribution during six month shut off. Heating pipes at 100 mm temperature profile according to case 3 in figure 2.*

6.   SUMMARY AND CONCLUSIONS

This study concludes that there is an advantage in making use of the cast-in underfloor heating during the construction phase to speed up the drying of the concrete slab. The influence of starting the underfloor heating early, in practice as soon as possible after the building envelope is closed, was almost 5% RH in this study. At the construction site this may represent a reduction of the drying period by several weeks, maybe months. This is especially the case if the aim is to reach such moisture levels in the concrete substrate that vapour tight PVC or rubber based floorings may be attached without the risk of degradation.

There is only a small difference in relative humidity (RH) level near *vs.* between the heating pipes. In this study the mean difference increased a little, from almost nothing at the time the flooring was laid to near 1% RH after one year. This may indicate that the diffusion of water vapour from hot to cold areas is of the same magnitude as the capillary suction of pore water back to the hot areas.

When floorings are attached on top of the concrete slab the drying process is disturbed. Tight floorings such as PVC or rubber based materials will practically terminate the drying process and initiate redistribution of the remaining construction water. Less tight floorings such as wood will allow a limited drying. The magnitude of the drying through the flooring is dependent on

material parameters such as the flow resistance of the materials and conditions such as ambient RH and the temperature profile through the construction.

There seems to be a small risk of enhanced moisture conditions in the wood flooring if the underfloor heating is turned off during the first year. But, on the other hand, this condition will only be the same as if there had been no heating in the first place. No additional water will accumulate in the wooden flooring due to the heat being turned off. A moisture barrier under the wooden floor may not prevent moisture damages, it is most likely it instead will contribute to drying and shrinkage damages in the wood.

A polyethylene (PE) foil placed between the concrete slab and the wooden floor increases the moisture level in the concrete surface and reduces it in the wooden floor. The PE foil may reduce the risk of wetting underneath the wooden floor but may also cause a new risk if the moisture level in the concrete surface exceeds the critical value for e.g. mould growth in the remaining sawdust. The positive effect of the PE foil may be finite since there will only be a minor increase for a short period of time in the moisture level of the wood.

Any measurement before the flooring is laid, in order to ascertain the highest moisture level the floorings and adhesive will be exposed to after redistribution, should be made right between the heating pipes at 40% of the depth of the concrete slab if the slab can only dry out upwards. If the concrete slab can dry out both upwards and downwards, the measurement may be performed at 20% depth.

REFERENCES

1   Sjöberg A. 2001. Secondary emission from concrete floors with bonded flooring materials. Department of Building Materials, Chalmers University of Technology, Göteborg. P-01:2. 188 pages

2   The Advisory Council for Building Competence (RBK) (2005): Measuring of moisture in concrete (in Swedish). Operational manual published by The Swedish Construction Federation (BI)

3   Nilsson LO (1980). Heated concrete floors. Pilot tests (In Swedish: Värme i betonggolv. Pilotförsök) Lunds University, division of Building Materials. Internal report.

4   Sjöberg A, Nilsson LO (2007.1) (In Swedish) Fuktmätning i betonggolv med golvvärme, Etapp II: Täta golvbeläggningar. Lunds University, division of Building Materials. Report TVBM-3140

5   Sjöberg A, Nilsson LO (2007.2) (In Swedish) Fuktmätning i betonggolv med golvvärme, Etapp III: Limmade trägolv. Lunds University, division of Building Materials. Report TVBM-3141

6   Box G, Hunter W, Hunter S. 1978. Statistics for Experimenters. An Introduction to Design, Data Analysis, and Model Building. John Wiley & Sons, USA. 653 pages.

7   Nilsson LO (1977) Excess moisture in concrete slabs on grade. Drying and measuring methods. Part 2: Moisture measurements (in Swedish: Byggfukt i betongplatta på mark. Torknings- och mätmetoder. Del 2: Fuktmätning). Building Materials and Moisture Research Group, Lund Institute of Technology. Report TVBM-3008.

8   McLean RC, Galbraith GH, Sanders CH. 1990. Testing building materials, moisture transmission testing of building materials and the presentation of vapour permeability values. Building research and Practice. The journal of CIB. No 2 2990.

9   CEN/ISO (2002) Hygrothermal performance of building materials. Determination of water absorption coefficient. prEN ISO 15148:2002.